Mass cytometry of the developing mouse nervous system

Amy Lynnette Van Deusen

Charlottesville, VA

B.S. Biochemistry, University of Virginia, 2005

M.S. Biological Sciences, University of California Irvine, 2008

A Dissertation presented to the Graduate Faculty of the University of Virginia in Candidacy for the Degree of Doctor of Philosophy

Neuroscience Graduate Program

University of Virginia

May 2024

Abstract

For more than a century, various technological and biological limitations have hindered attempts to comprehensively taxonomize cells present in the mammalian nervous system. Although single-cell transcriptomics (scRNA-seq) are rapidly expanding our appreciation of the cellular diversity of neural tissues, the numerous mechanisms involved in translating RNA into functional and properly trafficked proteins means these results provide only a recipe for individual cell identities and states. To better understand the molecular profiles driving neural cell identity and functions, protein-based measurements are necessary. Herein, we generated the first single-cell protein-based atlases of the developing mouse brain (Chapter II) and dorsal root ganglia (DRG, Chapter III) by using mass cytometry, a cutting-edge technique similar to flow cytometry that employs metal-conjugated antibodies and time-of-flight detection to quantify expression of up to 50 biomarkers. Our results quantify simultaneous expression of neurofilaments, transcription factors, surface receptors, adhesion molecules, enzymes, glycoproteins, and other relevant molecules in millions of cells. By examining tissues collected at daily timepoints from embryonic day 11.5 until postnatal day 4, we surveyed how the molecular profiles and abundances of cells change in the brain and DRG during this critical period of development. The results are corroborated by immunohistochemistry (IHC) and confocal fluorescence microscopy of brain and DRG tissue slices. We also evaluated the relationship between mRNA and protein expression by comparing our single-cell protein measurements with scRNA-seq data published in La Manno, et al. [*Nature* (596):92–96*,* 2021] and Sharma, et al. [*Nature* (577):392–398, 2022] for mouse brain and DRG, respectively. The results, which were confirmed by IHC and RNAscope for select makers, indicate discordances between mRNA and protein during mouse nervous system development. Pseudotime-based trajectory analyses employing the URD algorithm replicate canonical molecular transitions for cortical excitatory neurons, somatosensory neurons, glial precursors, oligodendrocytes, and Schwann cells; moreover, they predict two distinct pathways for producing oligodendrocyte progenitor cells in the forebrain. Our findings provide the highest resolution profile of single-cell protein expression in mouse brain and DRG available to date. Moreover, our methods and analytical strategies lay the foundation for future protein-based and multiomic approaches to precisely identify neural cells – an important step for building a complete atlas of the nervous system.

Acknowledgements

I first want to thank my thesis mentors, Chris Deppmann and Eli Zunder, who gave me the opportunity, support, and resources to do something a bit crazy. You have given me one of the greatest gifts of my life – the confidence to move forward as a scientist.

I would also like to thank my incredible colleagues who made it fun even when things got difficult, especially Austin Keeler, Irene Gadani, Kristen Fread, Corey Williams, Sarah Goggin, Sushanth Kumar, Jiachen Shi, O. Yipkin Calhan, Shayla Vradenburgh, and Mike Solga, as well as the many members of the Deppmann laboratory I have had the fortune of working alongside over the years.

I am also very grateful for my distinguished committee members Xiaowei Lu, John Lukens, Hui Zong, and especially Barry Condron, who gave their time and expertise to help me shine. In addition, I thank Sarah Kucenas, Noelle Dwyer, and Alban Gaultier for their invaluable expertise and generosity with resources.

I am also thankful for the amazing UVA Neuroscience Graduate Program coordinators Nadia Cempré and Kim Knotts, whose patience and persistence was unwavering.

I would also like to thank the mentors whose past encouragement led me to pursue and continue a career in scientific research, especially Ed Perez-Reyes, Charles Ribak, Tilo Kunath, Mike McConnell, and Michael McGary.

Dedication

First and foremost, this is for my mom, Karen Largen, and sister, Kelly Van Deusen. Their unconditional love and support have made everything possible for me.

It is also for Robb Burgess, the love of my life.

And for Dustin French, my partner in crime since my journey at UVA began in 2001.

And finally, it is for those who I have lost along the way. Most of all my treasured grandparents Morrison & Elsie Largen and Helen & Bill Roudabush, without whose support and guidance I would have never made it this far. And for my beloved dogs, Jefferson and Lynn, who always provided unconditional love, support, and slobber.

Table of Contents

List of Figures

Appendix I

Appendix II

Abbreviations and Acronyms

Aδ-LTMR	Aδ low-threshold mechanoreceptors
ALDH1A1	Aldehyde dehydrogenase 1A1
ASD	Autism spectrum disorder
BFABP	Brain fatty acid-binding protein (also known as BLBP)
BLBP	Brain lipid-binding protein (also known as BFABP)
BSA	Bovine serum albumin
C-LTMR	C-low-threshold mechanoreceptors
CGRP	Calcitonin gene-related peptide
CNS	Central nervous system
CSM	Cell staining medium
DCX	Doublecortin
DMEM	Dulbecco's Modified Eagle's Medium
DRG	Dorsal root ganglia
EMPs	Erythromyeloid progenitors
GABA	γ-aminobutyric acid
GAD65	Glutamic acid decarboxylase 2
GFAP	Glial fibrillary acidic protein
GLAST	Sodium-dependent glutamate/aspartate transporter 1
ICP-MS	Inductively coupled plasma mass spectrometry
iGC	Intermediate glial cell
IHC	Immunohistochemistry
IMC	Imaging mass cytometry
INP	Intermediate neuronal progenitor
k-NN	k-nearest neighbors
Ly6C	Lymphocyte antigen 6C
Ly6G	Lymphocyte antigen 6G
MAP2	Microtubule-associated protein 2
MBP	Myelin-binding protein
MCAM	Melanoma cell adhesion molecule
MIBI	Multiplex ion beam imaging
N-cad	N-cadherin
NCC	Neural crest cell
NDS	Normal donkey serum

NF-H	Neurofilament heavy subunit
NSC	Neural stem cell
NPC	Neural progenitor cell
NP	Non-peptidergic
OCT	Optimal Cutting Temperature Compound
OligoO4	Oligodendrocyte marker O4
OPC	Oligodendrocyte progenitor cell
p75NTR	p75 neurotrophic receptor
PBS	Phosphate-buffered saline
PCA	Principal component analysis
PDGFRα	Platelet-derived growth factor receptor alpha
PDGFRβ	Platelet-derived growth factor receptor alpha
PECAM	Platelet endothelial cell adhesion molecule
PEP	Peptidergic neurons
PFA	Paraformaldehyde
PNS	Peripheral nervous system
PSA-NCAM	Polysialylated neural cell adhesion molecule
RA-LTMR	Rapidly adapting low-threshold mechanoreceptor
RGC	Radial glial cells
RNA-seq	Transcriptomic sequencing
RTK	Receptor tyrosine kinase
SA-LTMR	Slowly adapting low-threshold mechanoreceptor
scRNA-seq	Single-cell transcriptomic sequencing
SEM	Standard error of the mean
SGC	Satellite glial cell
SPADE	Spanning-Tree Progression Analysis of Density-Normalized Events
SSEA-1	Stage-specific embryonic antigen 1
SVZ	Subventricular zone
t-SNE	t-Stochastic Neighbor Embedding
TH	Tyrosine hydroxylase
TOF-MS	Time-of-flight mass spectrometry
UMAP	Uniform Manifold and Approximation
VCAM	Vascular cell adhesion molecule
VSMC	Vascular smooth muscle cell
VZ	Ventricular zone

Chapter I: Building an Atlas of Nervous System Development

FUNDAMENTAL PRINCIPLES

A Brief Historical and Evolutionary Perspective

For millennia, identifying the composition of the nervous system was beyond our technological capabilities. This changed in the late nineteenth century when Santiago Ramón y Cajal employed light microscopy and an innovative staining technique devised by his mentor, Camillo Golgi, to catalog the morphology of individual neural cells throughout the central nervous system (CNS) and peripheral nervous system (PNS) (Garcia-Lopez et al., 2010). His findings, built from an enormous collection of drawings, led him to conclude that neurons were individual units with distinct connections – a controversial concept that contradicted both his mentor and the dogma widely accepted by the field at the time, namely, that neuronal processes form a continuous web or "reticulum". Cajal's contributions, which earned him the title of "Father of Modern Neuroscience", provide the foundation upon which all neural cells are classified.

Since then, classification of neural cells has vastly expanded beyond morphology to include ultrastructural features (Gray, 1959), electrophysiological properties (Adrian, 1954; Curtis and Cole, 1940; Eccles et al., 1957; Renshaw et al., 1940; Woldring and Dirken, 1950), metabolic properties (Magistretti and Allaman, 2015), nucleic acid expression (Gall and Pardue, 1969; Macaulay et al., 2017), protein expression (Coons et al., 1941), and developmental lineage (Rakic, 1982). Some of the key milestones in efforts to classify neural cells are shown in Figure 1.

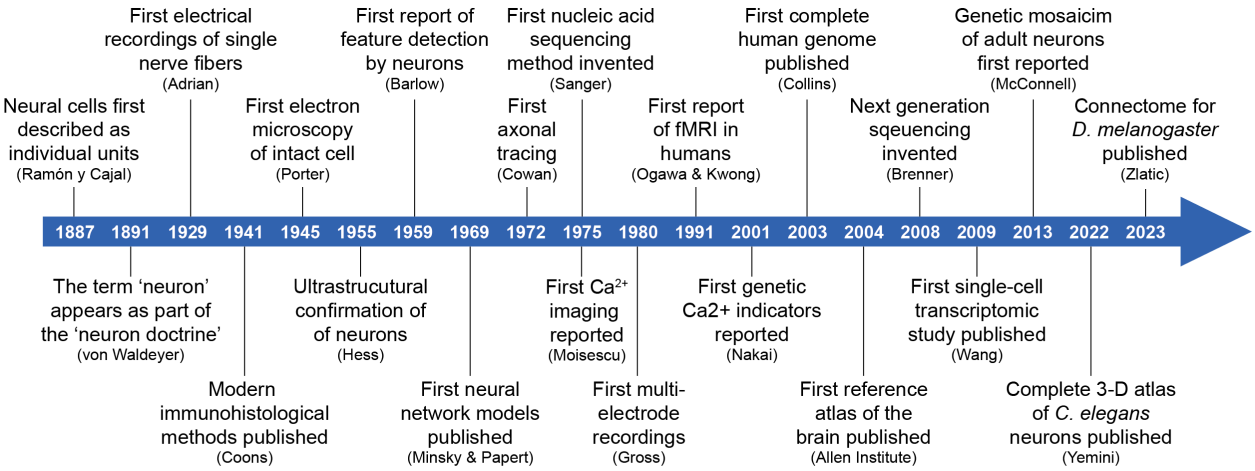

Figure 1. **Milestones of neural cell identification.** Select events key to our ability to understand and classify neural cell types are shown. The primary researcher or institute to which each milestone is attributed is shown in parentheses.

In one of the simplest species with a centralized nervous system, *Caenorhabditis elegans* (worm), the specific identity of each neuron has been characterized (http://www.wormatlas.org/). However, as organisms evolved to become more complex and undertake more complicated tasks, neural networks became more extensive in size, specialized in function, and diverse in composition (Geisler, 2018; Wilsch-Bräuninger et al., 2016). Therefore, in many invertebrates (e.g., echinoderms, arthropods, nematodes, mollusks, and annelids) and nearly all vertebrates (e.g., fish, amphibians, reptiles, birds, and mammals), the vast cellular diversity and sheer magnitude of cell numbers has thus far prevented such comprehensive classification. Notably, several databases are maintaining growing lists of neuronal subtypes, including the Allen Brain Institute (http://celltypes.brain-map.org/) and Hippocampome (http:///hippocampome.org).

The human brain is large [86 billion neurons and 85 billion non-neuronal cells (Azevedo et al., 2009)] and contains a far more heterogeneous population of neural cells compared

with other species. In particular, the human neocortex supports a wide array of highly specialized activities that form the basis for higher functions such as perception, language, and emotion. Indeed, the increased relative size and gyrated structure of the human cortex compared with other primates is what affords humans our “higher” intelligence (Geisler, 2018; Wilsch-Bräuninger et al., 2016), including an advanced prefrontal cortex that permits “executive control” of complex behaviors such as planning, personality, decision making, and modulation of social interactions (Domenech and Koechlin, 2015; Miller, 2000).

Because of these vast evolutionary differences, it is important to consider the conservation and divergence of neural cell types and network properties when approaching neuroscience-related questions and interpreting data from model systems used in the laboratory. This is perhaps most important when considering hypotheses related to human health and neurological disease.

Significance for Human Health

Development of the nervous system involves a highly regulated symphony of intrinsic and extrinsic cues that guide cells into their proper fates, functions, and locations. Disruption of this symphony by genetic or metabolic disorders, nutrient deprivation, immune dysfunction, infectious disease, or physical trauma is associated with a wide array of debilitating neurological disorders.

Clinically, neurodevelopmental disorders can be divided into four general categories: structural malformations, cognitive and neuropsychiatric disorders, localized cortical

dysplasias, and motor disorders. However, from a research perspective, it is often more useful to consider the developmental origin of these disorders, i.e., defects in cell proliferation, specification, migration, and/or survival (Manzini and Walsh, 2011). For example, microcephaly (reduced brain size and volume) occurs because of proliferation-related defects in neural progenitors (Dwyer et al., 2016; Romero et al., 2018; Sun and Hevner, 2014), while lissencephaly (loss of gyral patterning and normal laminar structure) arises from defective neuronal migration (Pilz et al., 1998; Romero et al., 2018). Thus, neurodevelopmental disorders, which are primarily classified by clinical symptoms, often comprise multiple disorders with slightly varying causes but similar symptomatic output. For this reason, many disorders thought to originate during cortical development are classified as “spectrum” disorders, perhaps most notably autism (Lauritsen, 2013), which encompasses a broad range of genetic etiologies and clinical manifestations.

Neurodevelopmental disruptions have also been implicated in several neurological disorders that manifest during adulthood, including schizophrenia (Nour and Howes, 2015; Owen et al., 2011), Alzheimer’s disease (Arendt et al., 2017; Bothwell and Giniger, 2000), and epilepsy (Bozzi et al., 2012; Nickels et al., 2016). Therefore, as both the average age of the global population (World Bank Group, http://data.worldbank.org) and incidence of neurodegeneration (McGovern Institute for Brain Research, https://mcgovern.mit.edu) continue to increase, roles for neurodevelopment in neurodegenerative disorders are of growing importance. Accordingly, it is more important than ever to increase our understanding of how the nervous system develops so that we

might intervene as early as possible to prevent disease and improve human health outcomes.

Modeling Mammalian Development in the Laboratory

Use of *in vitro* and *in vivo* models has greatly enhanced understanding of the molecular and cellular processes essential for nervous system development. Generally, such models employ cells from three sources: immortalized cell lines, pluripotent stem cells, and primary neural tissue – each with its own unique benefits and limitations (Azari and Reynolds, 2016). Primary cell models, including cells and tissue slices, are directly harvested from animal neural tissues. Outside of performing *in vivo* studies, this source of cells provides the best approximation of *in vivo* physiology. However, it remains of utmost importance to consider conserved and divergent properties when applying the results of studies performed in model systems to interpretation of human functions and disease mechanisms – especially for the brain. For brevity, we will limit further discussion of this topic to mouse models of nervous system development.

First, in terms of neuroanatomy, humans exhibit an extensively folded gyrencephalic brain, while mice have a lissencephalic (smooth) brain lacking gyrations. This expansion and gyration of the human brain compels differentiating neurons to migrate along longer paths, which has been correlated with an increased number of transit-amplifying basal progenitors [including neural progenitors cells (NPCs) and radial glial cells (RGCs)] in humans compared with mice and small primates (De Juan Romero and Borrell, 2015; Wilsch-Bräuninger et al., 2016; Romero et al., 2018). In addition, although essential

features of cortical lamination appear to be preserved between mice and humans, layers II and III are greatly expanded in humans, which has enormous implications on intellectual function (DeFelipe, 2011). As such, it is especially important to consider mechanisms underlying cortical growth and folding when abstracting information about human cortical disorders from mouse model results.

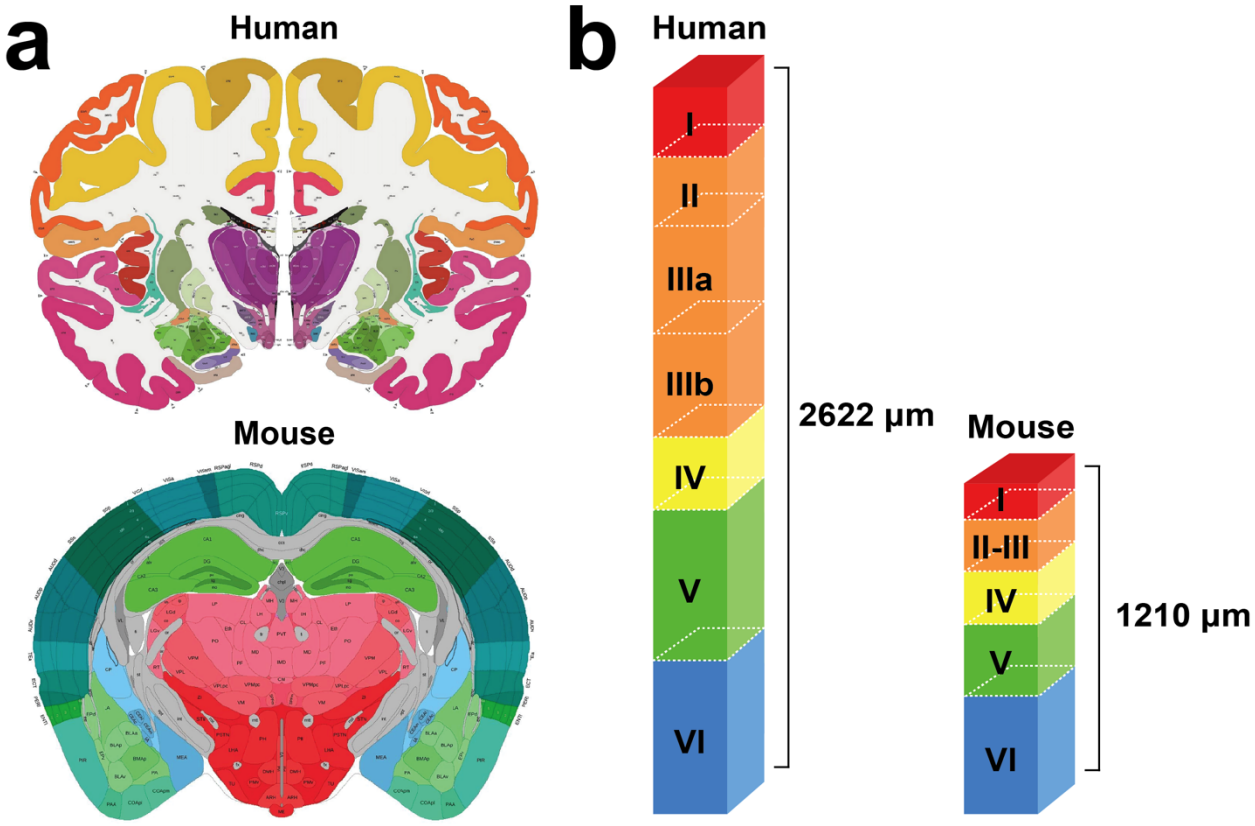

Figure 2. **Comparison of human and mouse brain anatomy. a**) Coronal sections of human and mouse brain from the Allen Institute's Human Brain Atlas (https://human.brain-map.org) and Mouse Brain Atlas (https://mouse.brain-map.org). **b**) Comparison of cortical layer thicknesses between humans and mice. Adapted from DeFelipe, 2011. The evolution of the brain, the human nature of cortical circuits, and intellectual creativity. *Frontiers Neuroanatomy*.

Second, species-specific patterns in the temporal progression of developmental neurogenesis and gliogenesis must be taken into account. As shown in Figure 8, human

cortical development takes much longer and displays an amplified period of neurogenesis for layer II/III neurons compared with mice. These expanded features increase the chance for developmental perturbations that cause cortical dysfunction in humans (Ross and Walsh, 2001; Romero et al., 2018).

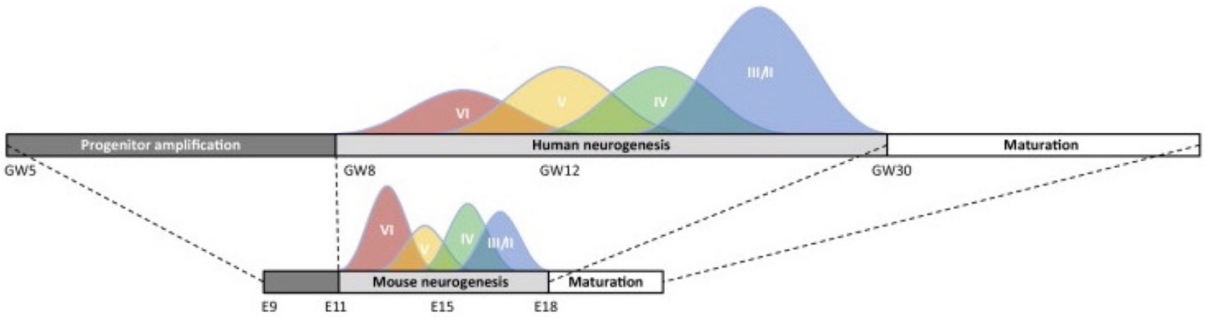

Figure 3. **Timeline of key events during human and mouse cortical development.** Figure and legend originally published in van den Ameele, et al, 2014. Thinking out of the dish: what to learn about cortical development using pluripotent stem cells. *Trends in Neuroscience*. Reprinted with permission from Elsevier (License No. 5678150511157).

Finally, molecular and cellular differences between mice and humans must be considered. A ratio of approximately 50% neurons and 50% glia is conserved amongst rodents (Herculano-Houzel et al., 2006), primates, and humans (Herculano-Houzel et al., 2014, 2007). However, numerous theories have been put forward to describe how discrete changes in the development of neurons, astrocytes, and/or oligodendrocytes result in enhancement of specific functions/behaviors in mice or humans (Oberheim et al., 2009; Miller et al., 2010; Oberheim et al., 2012; Molnár and Pollen, 2014). In terms of gene expression in neural tissues, the Allen Institute (https://portal.brain-map.org/) provides one of the most comprehensive databases of results from mouse and human studies, while the Gene Expression Omnibus/Sequence Read Archive and other

databases are rapidly accruing microarray, RNA sequencing, and other high-throughput gene expression data (https://www.ncbi.nlm.nih.gov/geo/). However, differences in protein expression – an essential driver of cell identity and function – and cellular compositions are not as well catalogued.

CELLULAR COMPONENTS OF THE NERVOUS SYSTEM

Although the mammalian brain contains an enormous diversity of neural cells, they remarkably arise from just two types of cells: neural stem cells (NSCs) in the CNS and neural crest cells (NCCs) in the PNS. In response to an array of intrinsic and extrinsic factors (e.g., morphogens, pro-neural transcription factors, and cell cycle kinetics), these cells proliferate, differentiate, migrate, or die to ultimately produce the nervous tissue structures observed in adults (Edlund and Jessell, 1999). This process also involves many nonneural cell types, such as microglia and vascular cells, which perform essential functions to ensure proper nervous system development (Morimoto and Nakajima, 2019; Vogenstahl et al., 2022). In this section, the major classes of neural and nonneural cells found in the mammalian nervous system are briefly overviewed.

Neural Cells

Neural Stem Cells and Progenitors

The term “neural stem cell” is applied to self-renewing cells with the multipotent capacity to differentiate into all three major classes of neural cells: neurons, astrocytes, and oligodendroglia (Gage, 2000). In practice, the term NSCs is applied to neuroepithelial

cells, radial glial cells (RGCs), adult neural stem cells, and even NCCs *in vivo*, as well as pluripotent stem-cell derived cells biased towards a neural phenotype *in vitro*.

In vertebrates, NSCs arise from the neural tube and ultimately generate virtually all the neural cells found in the brain and spinal cord. Molecularly they can be identified by their expression of the intermediate filament nestin and transcription factor Sox2 (Hutton and Pevny, 2011). In addition, they can be further classified by their location, polarity, and expression of factors responsible for their patterning and identity [e.g., Pax6 for cortical neural progenitors (Heins et al., 2002) and Mnx1 for spinal cord motor neurons (Lee et al., 2004)].

As indicated by their name, NCCs arise from the neural crest, which initially forms the border between the neural plate and ectoderm. These cells are highly migratory and eventually form a wide range of cell types, including neurons and glia of the PNS, as well as melanocytes, smooth muscle, and craniofacial cartilage and bone (Le Douarin et al., 2004). In addition to nestin and Sox2, NCCs express the transcription factor Sox10, which is essential for maintaining their multipotency (Kim et al., 2003).

As development proceeds, the ability of NSCs/NCCs to produce different progeny is spatiotemporally restricted by cell intrinsic programs and extrinsic cues (Yoon et al., 2018). As shown in Figure 4, NSCs ultimately terminate neurogenesis in favor of gliogenesis. During this progression, NSCs display increased expression of astroglial genes such as brain lipid-binding protein [BLBP, also known as fatty acid-binding protein 7 (FABP7)], astrocyte-specific glutamate transporter (GLAST), and glial fibrillary acidic

protein (GFAP) (Hartfuss et al., 2001; Heins et al., 2002; Kriegstein and Alvarez-Buylla, 2009; Noctor et al., 2002). In addition, a quiescent subset of NSCs give rise to adult neural stem cells (Fuentealba et al., 2015; Furutachi et al., 2015; Hu et al., 2017; Merkle et al., 2004; Yuzwa et al., 2017), which retain their core transcriptional identity (Yuzwa et al., 2017) and express vascular cell adhesion molecule (VCAM) to maintain their stem-like properties (Hu et al., 2017).

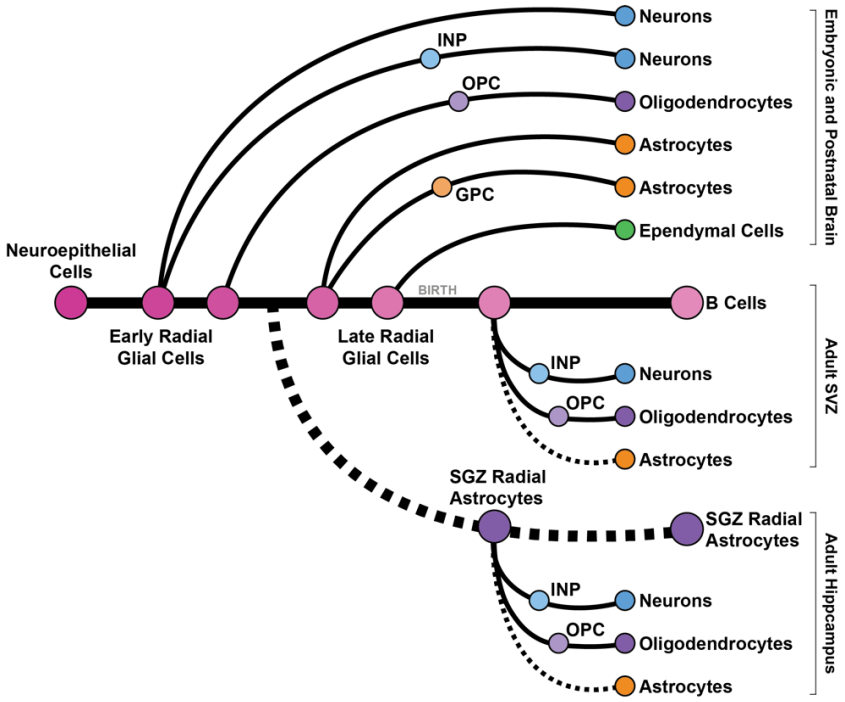

Figure 4. Lineage tree of neural stem cells. Lineages of neural stem cells in the embryonic and postnatal brain are shown in the upper half, while lineages in the adult SVZ and hippocampus are shown in the bottom half. Solid lines indicate experimentally validated lineages, while dashed arrows indicate hypothetical pathways. INP, intermediate neuronal progenitor; GPC, astroglial progenitor cells; OPC, oligodendrocyte progenitor cell; SGZ: subgranular zone; SVZ, subventricular zone. Adapted from Kriegstein and Alavarez-Buylla, 2009. The glial nature of embryonic and adult neural stem cells. *Annual Review of Neuroscience*. Reprinted with permission from Annual Reviews, Inc. (License No. 1472119-1).

Neural progenitor cells (NPCs) represent an intermediate cell state in which cells retain a limited capacity for self-renewal but no longer have the multipotency of NSCs to generate

all neural cell types. Instead, NPCs can be subclassified at their most basic level as either “neuronal” or “glial” according to their biomarker expression profile, proliferative capacity, polarity, and lineage restriction.

In the neocortex, a key event in the transition from NSC to intermediate neuronal progenitor (INP) is downregulation of Pax6 and upregulation of Tbr2 (Englund et al., 2005; Sessa et al., 2017), which serves as a specific biomarker of INPs. Similarly, Sox10 expression is downregulated in favor of neurogenins 1/2 and Islet1 in during early specification of sensory neuronal progenitors in the dorsal root ganglia (DRG) (Ma et al., 1999; Sun et al., 2008), a collection of sensory ganglia found along the spinal cord (Figure 5).

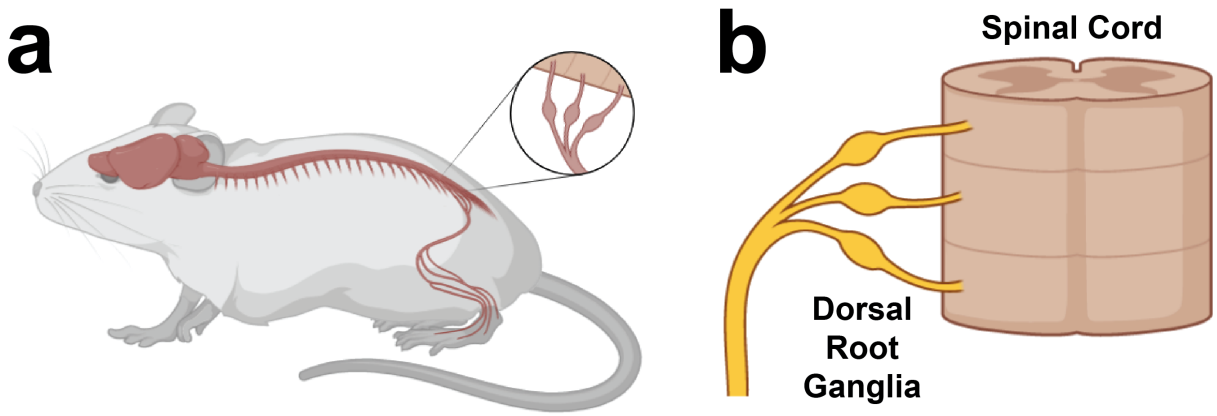

Figure 5. Anatomy of the mouse dorsal root ganglia. a, Location of dorsal root ganglia (DRG) along the spinal cord in relationship to a peripheral nerve. **b**, Illustration of DRG connections to the spinal cord. Figure generated using BioRender (http://www.biorender.com).

Expression of pro-neuronal transcription factors like Tbr2 and Islet1 occurs in response to a symphony of instructive and permissive cues. These factors act to suppress gliogenesis of NSCs [considered the default differentiation pathway (Doetsch, 2003)],

thus permitting a tightly regulated window of neurogenesis (Florio and Huttner, 2014; Kriegstein and Alvarez-Buylla, 2009).

Excitatory Neurons

Neurons are specialized cells that transmit information throughout the body via electrochemical signaling. To achieve this, they express a diverse range of proteins (such as ionotropic and metabotropic channels, electrogenic pumps, and vesicular transporters) that maintain dynamic stability of specific ions and metabolites within the cell, thus generating an electrical potential across the cell membrane. However, signaling by neurons is highly refined throughout the CNS and PNS in a geographic and cell type-specific manner, resulting in enormous complexity of neuronal cell types, especially in the brain.

For example, in the cerebral cortex, neurons with similar projection patterns are frequently dispersed across multiple laminar layers and organized into ontogenetic columns (or “cortical fields”) responsible for different functions (Arai and Pierani, 2014; Mountcastle, 1997). As information about cortical connectivity and the molecular profile of these cells has expanded, it has become clear that hodological and laminar criteria are insufficient to define all excitatory projection neuron subtypes (Franco and Müller, 2013). Moreover, although NPCs are thought to be pre-destined for specific neuronal and laminar fates (Bedogni et al., 2010; Chen et al., 2008; Leone et al., 2008; Zimmer et al., 2004), the developmental mechanisms underlying specification and integration of distinct neuronal subtypes are only beginning to be understood (Ohtaka-Maruyama and Okado, 2015).

Neuronal cell diversity is first established by the location in which the neuronal progenitor was born. For example, in the cerebral cortex, neuronal progenitors in the pallium almost exclusively generate glutamatergic excitatory neurons, while those arising more ventrally in the medial ganglionic eminence almost exclusively produce GABAergic inhibitory neurons (Lavdas et al., 1999; Miyoshi et al., 2010; Xu et al., 2004). Similarly, in the PNS, the identity of cells derived from NCCs is heavily influenced by their original position along the anterior-posterior axis, as shown in Figure 6.

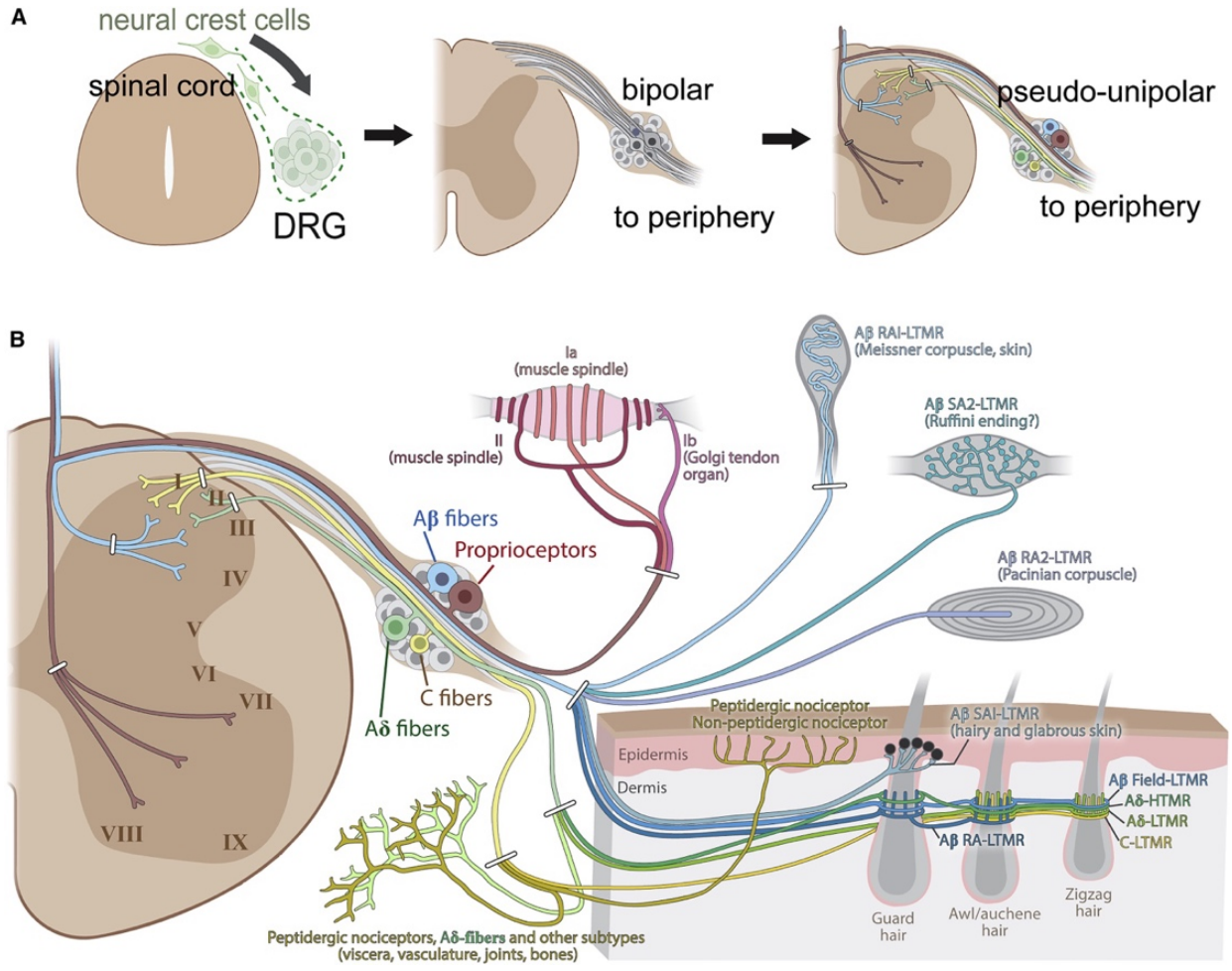

Figure 6. Overview of early development, anatomy, and the major DRG somatosensory neuron subtypes. (A) Dorsal root ganglia (DRG) neurons derive from neural crest cells that delaminate from the dorsal neural tube and coalesce to form DRGs. Rodents typically have 30 or 31 pairs of DRGs; 8 pairs of cervical, 13 pairs of thoracic, 5 or 6 pairs of lumbar, and 4 pairs of sacral DRGs. Nascent DRG neurons assume a spindle-shaped, bipolar morphology, with axons emanating from opposite sides of the cell body. A stem axonal protrusion containing the two axonal branches then forms and refines to assume the mature T shape pseudo-unipolar morphology by birth. (B) Somatosensory neuron cell bodies reside in DRG, adjacent to the spinal cord. DRG neurons have a pseudo-unipolar morphology with axonal branches extending into both the periphery and the spinal cord. The major peripheral end organs formed by DRG neuron subtypes are illustrated on the right, and the general, albeit oversimplified spinal cord lamination patterns of their central projections are also shown. Note that Aβ LTMR fibers and proprioceptors also have central branches with multiple collaterals extending along the rostral-caudal axis of the spinal cord and an additional branch that ascends via the dorsal column, often reaching the dorsal column nuclei of the brainstem. Figure and legend originally published in Meltzer, et al., 2021. The cellular and molecular bases of somatosensory neuron development. *Neuron*. Reprinted with permission from Elsevier (License No. 5678160104207).

Subsequent mechanisms of neuronal specification are far more complicated, involving changes in epigenetics, gene expression, cell polarity, cytoskeletal dynamics, adhesion properties, and a host of other factors, as well as interactions with nonneural cells. Evaluating gene and protein expression of neurons at the single-cell level promises to significantly increase our understanding of these mechanisms, as well as provide an answer to the question: how many types of neurons exist?

Generally, cortical neuronal precursors and early neurons can be identified by their expression of specific surface antigens [e.g., CD24 and polysialylated neural cell adhesion molecule (PSA-NCAM)], pro-neuronal transcription factors (e.g., NeuroD1 and Tbr1), and neurofilaments (e.g., doublecortin and beta III tubulin). More mature neurons can be identified by their expression of various neurofilaments [e.g., mitogen-activated

protein 2 (MAP2)], the nuclear proteins Rbfox3 (NeuN) and ELAV3/4 (HuC/HuD), as well as numerous other markers specific for individual neuronal subtypes. Mature neurons can be classified as either excitatory (glutamatergic) or inhibitory (GABAergic), in addition to further classification by their expression of a range of neurotransmitters and/or receptors. For example, dopaminergic neurons express receptors specific for dopamine, while serotonergic neurons express receptors that specifically bind serotonin.

Inhibitory Neurons

Unlike excitatory neurons, which frequently make long-range projections, interneurons participate in localized circuit regulation to inhibit signaling of target neurons. This inhibitory function is produced by the inhibitory neurotransmitter γ-aminobutyric acid (GABA) (McCormick, 1989). Accordingly, inhibitory neurons can be molecularly identified by their expression of proteins related to GABA synthesis and transmission, such as glutamic acid decarboxylases 1 and 2 (GAD67 and GAD65, respectively) and vesicular GABA transporter, respectively.

In the cerebral cortex, cortical interneurons arise from NPCs in the subpallium (Yuste et al., 2020), while cortical excitatory neurons are born in the ventricular zone (VZ) and subventricular zone (SVZ). Similar spatial restriction of inhibitory and excitatory neurogenesis in other regions of the brain (e.g., cerebellar ventricular zone and rhombic lip, respectively) initially led researchers to believe that these two main lineages of neurons diverge at the level of NPC or even RGC. However, it was recently shown that individual NPCs in the embryonic mouse cerebellum are capable of generating both

excitatory and inhibitory neurons (Zhang et al., 2021), suggesting that specification of these cell types may occur later during neuronal differentiation.

Astroglia

Named for their unique star-shaped morphologies, astrocytes are a glial cell subtype found in the CNS that is important for brain structure, metabolic support, neurotransmission, and regulation of the extracellular space surrounding neurons and oligodendroglia (Khakh and Sofroniew, 2015; Sofroniew and Vinters, 2010). Satellite glial cells (SGCs) are the equivalent of astrocytes in sensory, parasympathetic, and sympathetic ganglia. They display similar expression profiles, morphologies, and functions as astrocytes (Hanani and Spray, 2020). Originally thought to primarily function as support cells for neurons, the neuroscience community has recognized more important roles for astroglia and SGCs during development (Molofsky et al., 2012), neuroinflammation (Colombo and Farina, 2016), and neurotransmission (Cornell-Bell and Finkbeiner, 1991; Perea et al., 2009). Moreover, astrocytes have been implicated in neurological disorders such as epilepsy (Coulter and Steinhäuser, 2015) and multiple sclerosis (Ponath et al., 2018).

All glial cells are thought to arise from a common glial-restricted progenitor, although discrete lineage pathways underlying astroglia development are less clear. Indeed, it has been exceptionally difficult to fully elucidate the developmental specification and/or spatiotemporal diversification of astrocytes and SGCs because there is not a single biomarker or method to characterize different subtypes. That is, expression of numerous

“glial” markers by astrocytes has not been satisfactorily correlated to their identity, as opposed to their signaling state (e.g., activation in response to injury or inflammation). However, the existence of an “O2A” neural progenitor with the capacity to generate type 2 astrocytes and oligodendrocytes has been reported (Baracskay et al., 2007; Hart et al., 1989). These cells express a mix of NSC, astroglia, and oligodendrocyte progenitor cell markers, including A2B5, GLAST, and platelet-derived growth factor α (PDGFRα).

Morphologically, three types of astrocytes exist: fibrous, protoplasmic, and radial. Although astrocytes exhibit regional heterogeneity in the CNS (Chai et al., 2017), which is important for synaptogenesis and repair (Tsai et al., 2012), how this is achieved and maintained remains unknown. In the PNS, as many as five distinct SGC subtypes have been identified, including SGCs “transcriptionally tuned” to accommodate sensory and sympathetic ganglia-specific functions (Mapps et al., 2022).

To achieve better understanding of the identity and functional characteristics of astrocytes and SGCs, approaches capable of measuring an increased number of biomarkers are necessary, such as single-cell transcriptomic or proteomic techniques.

Oligodendroglia

As neural circuitry became more refined, it became necessary to develop strategies to increase the speed and fidelity of certain types of neuronal transmission. To achieve this, the majority of bilaterian species evolved oligodendroglia and/or Schwann cells, which

form myelin sheaths around the axons of specific neurons to insulate signals in the CNS and PNS, respectively (Hartline, 2011; Salzer, 2015).

In the CNS, oligodendrocyte progenitor cells (OPCs) are initially specified from glial-restricted NPCs by downregulation of NSC markers such as Sox2 and sequential upregulation of Sox8, Sox9 (Wegner and Stolt, 2005), and Olig2, which induces expression of Sox10 and PDGFRα (Hart et al., 1989; Kuhlbrodt et al., 1998; Noble et al., 1988; Richardson et al., 1988). In mice, the first wave of oligodendrogenesis originates in the SVZ of the medial ganglionic eminence at E12.5, followed by two rounds arising from the lateral and caudal ganglionic eminences commencing at E15.5 (Fancy et al., 2009; Kessaris et al., 2006), and a final wave at P0 in the dorsal SVZ (Kessaris et al., 2006; Rowitch and Kriegstein, 2010). OPCs originating from these waves migrate throughout the cerebral cortex, whereby they begin to differentiate and mature, generating non-myelinating oligodendrocytes characterized by O4 glycoprotein expression in addition to OPC markers (Sommer and Schachner, 1981). As oligodendrocytes mature and become myelinating cells, they begin to express myelin-associated markers such as myelin-binding protein (MBP) and myelin oligodendrocyte glycoprotein (Linington and Lassmann, 1987).

In the PNS, Schwann cell precursors are specified from NCCs through upregulation of Sox2 and Egr1 (Svaren and Meijer, 2008). Initial differentiation occurs around E12.5 in mice and by E15.5, immature Schwann cells expressing can be observed (Jessen et al.,

2015). During the postnatal period, subsets of immature Schwann cells begin to express Egr2, Olig1, and myelin-associated proteins (Svaren and Meijer, 2008).

Notably, although distinct waves and discrete locations of oligodendrogenesis have been described in the brain (Jakovcevski et al., 2009; van Tilborg et al., 2018), how and whether this spatiotemporal restriction produces functionally distinct OPC or oligodendrocyte subtypes remains unknown. Investigating such questions is important because OPCs and oligodendrocytes play important roles in the maintenance of normal CNS function and have been implicated in traumatic brain injury (Dent et al., 2015) and neurological disorders such as multiple sclerosis (Patel and Balabanov, 2012). Similarly, relatively little is known about potential ganglia-specific subsets of Schwann cells, although these cells have been implicated in chronic pain (Wei et al., 2019), peripheral neuropathies (Lehmann and Höke, 2010), and other PNS disorders (Kamil et al., 2019).

Ependymal Cells

Ependymal cells, a type of glial cell that lines the ventricles of the brain, play an important role in production and regulation of cerebral spinal fluid. Notably, while a few studies identified ependymal cells to be a source of adult NSCs (Carlén et al., 2009; Johansson et al., 1999), these cells lack the capacity to regenerate; thus, ependymal cells do not satisfy one of the key criteria for NSCs: self-renewal. Regardless, ependymal cells express several markers associated with NSCs and NPCs including S100B, CD133, and CD124. In rats, the majority of ependymal cells arise from between E14 and E16, and it does not appear that these cells proliferate during adulthood (Spassky et al., 2001).

Nonneural Cells

Microglia and Macrophages

Derived from yolk sac-primitive macrophages (Ginhoux et al., 2013, 2010), microglia are considered to be tissue-resident macrophages of the CNS, whose role is protecting the brain against infection and injury (Gehrmann et al., 1995; Kreutzberg, 1996). To achieve this, microglia constantly survey the brain parenchyma for signals indicating damage or infection (Davalos et al., 2005; Lehnardt, 2010; Nimmerjahn et al., 2005). Detection of such signals stimulate microglia to adapt either a pro-inflammatory or anti-inflammatory state, which allows them to clear pathogens, protect neural cells from inflammation-induced damage, and repair injury (Goldmann and Prinz, 2013; Minghetti and Levi, 1998).

Microglia begin to invade the CNS during early development (Alliot et al., 1999; Ransohoff and Perry, 2009) and thereafter comprise 5%–15% of all cells in the brain (Pelvig et al., 2008). Colonization of the early embryonic brain is a conserved feature among vertebrate species (Hanisch and Kettenmann, 2007; Herbomel et al., 2001; Schlegelmilch et al., 2011; Swinnen et al., 2013; Verney et al., 2010), suggesting an essential role for microglia in brain development. Indeed, during CNS development, the balance of microglial activation can significantly impact NSC differentiation (Alliot et al., 1999; Osman et al., 2019; Ransohoff and Perry, 2009), neuronal survival (Bessis et al., 2007), and circuit integration (Squarzoni et al., 2014). Moreover, CNS infection or injury during development results in microglial activation and concomitant release of a variety of pro- and/or anti-inflammatory factors that can profoundly affect neurogenesis and gliogenesis (Shigemoto-Mogami et al., 2014).

The functions and surface marker expression profile of microglia and myeloid cells is extremely similar, with both expressing integrin alpha M (CD11b), protein tyrosine phosphatase receptor type C (CD45), and the surface glycoproteins Ly6C, Ly6G, and F4/80 (Korzhevskii and Kirik, 2016). However, much less is known about the functions and expression profile of tissue-resident macrophages in the PNS. Although they reportedly display similar transcriptional profiles with CNS microglia, some regional specificity was observed between tissue-resident macrophages of the brain, spinal cord, DRG, sciatic nerve, fascia, and vagus nerve (Wang et al., 2020). Considering the increasing number of functions attributed to microglia, research to better understand the functions of tissue-resident macrophages in the PNS seems a very worthwhile endeavor.

Vascular Cells

Vascularization of the CNS begins around E9.5 when endothelial cells form primitive vessels by interacting with pericytes (specialized cells that wrap around vessels) in a process chaperoned by yolk sac-derived tissue macrophages (microglia precursors) (Fantin et al., 2010; Schmidt and Carmeliet, 2010). By E11, neighboring radial vessels anastomose the ventral and dorsal forebrain (Fantin et al., 2010; Tata et al., 2015; Vasudevan et al., 2008) under the guidance of neuroepithelial cells and NPCs, which directly and indirectly attract sprouting vessels towards the VZ (Engelhardt and Sorokin, 2009; Fantin et al., 2010; Tata et al., 2016). As endothelial cells mature, they form specialized interactions (tight junctions) with pericytes and the end feet of astrocytes to establish a blood–brain barrier, the integrity of which is essential for spatially restricting blood flow and controlling the brain's interactions with the circulatory system throughout

life (Engelhardt and Liebner, 2014; Ruhrberg and Bautch, 2013; Tata et al., 2015). Notably, proper vascularization is also essential for proper OPC migration (Tsai et al., 2016).

Key markers for brain endothelial cells include platelet endothelial cell adhesion molecule 1 (PECAM), PDGFRβ, melanoma cell adhesion molecule (MCAM), and VCAM (He et al., 2016; Zeisel et al., 2015). Thus, to fully comprehend how interactions between vascular cells and neural cells drive differentiation, migration, and survival during CNS development, an approach incorporating a broad range of markers for both neural and nonneural cell types is required.

Fibroblasts

Fibroblasts serve as the main cellular component of connective tissues that support various organs and tissues throughout the body. They achieve this function by secreting collagen to maintain the extracellular matrix (P. Lu et al., 2011). In the CNS, fibroblasts are an important component of the meninges, which stabilize the brain and spinal cord to prevent injury. In addition, the meninges support functions of the neurovasculature, nerves, lymphatics, and cerebrospinal fluid (Decimo et al., 2012). In the PNS, fibroblasts form the meninges that envelop the spinal roots and serve as a constituent of other connective tissues (e.g., epineurium, perineurium, and endoneurium) (Richard et al., 2012). All fibroblasts characteristically express collagens (typically A1 and A2). In addition, they may express p75 neurotrophic receptor (p75NTR), PDGFRα, vimentin, and a range of other markers (Muhl et al., 2020).

THE SINGLE-CELL OMICS REVOLUTION

Genomics and Transcriptomics

Technology is essential for expanding our knowledge about the nervous system. Although a multitude of approaches have been applied to evaluate mechanisms responsible for nervous system development and disease in species ranging from worms to humans, progress has been stymied by low-throughput and/or low-resolution methods, which restrict the number of cells or biomarkers that can be examined.

Fortunately, recent advances in high-throughput sequencing technology permit high-resolution methods, such as genomic sequencing and transcriptomic sequencing (RNA-Seq), that provide quantifiable data about millions of molecular targets (Adams et al., 1991; Shendure and Ji, 2008). Collectively, such techniques are referred to as “omics” technologies (e.g., genomics, epigenomics, transcriptomics, and proteomics) and their goal is to define all the molecular constituents within a sample. Further refinement led to single-nuclei and single-cell versions of these techniques (C. Chen et al., 2017; Chu et al., 2017; Fu et al., 2015; Lister et al., 2008; Tang et al., 2009; Xing et al., 2021; Zong et al., 2012), which are quickly revolutionizing our understanding of the molecular and cellular complexity of a wide range of tissues.

Indeed, in the few short years since the advent of these techniques, the number of distinct neural cell types thought to exist in the CNS has vastly increased (Cuevas-Diaz Duran et al., 2017). In the hypothalamus alone, there are currently predicted to be at least 62

neuronal subtypes (Romanov et al., 2017) – a number that pales in comparison with the distinct number of neurons in the neocortex. Accordingly, high-resolution, single-nuclei or single-cell techniques are required to distinguish the potentially thousands of neurochemically and physiologically distinct cell types in the mammalian nervous system.

Single-cell transcriptomics (scRNA-seq) is particularly informative for distinguishing neural cell types (La Manno et al., 2016; Kee et al., 2017; Frazer et al., 2017; Bifari et al., 2017; Y.-J. J. Chen et al., 2017; Yuzwa et al., 2017; Mayer et al., 2018; Rosenberg et al., 2018; Tiklová et al., 2019; Wizeman et al., 2019; Guo and Li, 2019; Zhang et al., 2020; Romanov et al., 2020; Zhou et al., 2020; Kim et al., 2020; Li et al., 2020; Lee et al., 2022). The accumulating results are producing a high-dimensional atlas of distinct neural cell types in the adult brain and shedding light on the dynamic molecular profiles of cells during nervous system development.

scRNA-seq has been especially useful for refining classifications of inhibitory neurons. Previously, it was noted that use of only three markers (parvalbumin, somatostatin and the ionotropic serotonin receptor 5HT3a) can account for nearly all neocortical GABAergic neurons (Rudy et al., 2011). However, a recent scRNA-seq study identified a range of cell-adhesion molecules, transmitter-modulator receptors, ion channels, signaling proteins, neuropeptides, vesicular release components, and transcription factors related to cellular communication as essential for GABAergic neuronal identity (Paul et al., 2017). Moreover, transcriptomic profiling demonstrates the existence of as many as 16 distinct

interneuron subtypes in the developing and juvenile mouse cortex and hippocampus (Yuzwa et al., 2017; Zeisel et al., 2015).

It should be noted that because measurements of mRNA transcripts are still several steps removed from protein function (e.g., translation, post-translational modification, and subcellular trafficking), scRNA-seq provides only a limited view of cellular identity and function. Moreover, it remains a low-throughput and expensive technique with the inherent potential for dropouts (AlJanahi et al., 2018; Kharchenko et al., 2014). Regardless, these studies provide an enormously valuable unbiased set of information about individual cells, meaning improved analytical and intersectional methods are now needed to evaluate the functional outcomes of scRNA-seq and other omics findings.

Methods to Analyze Single-Cell Omics Data

Early attempts to characterize high-dimensional data sets employed principal component analysis (PCA), a statistical method that reduces the dimensionality of data by calculating a small number of “principal components” that preserve the variability of the original data while displaying it in a reduced number (usually two or three) of dimensions (Bendall et al., 2011; Gewers et al., 2021; Newell et al., 2012). However, because PCA assumes that inputs have linear relationships, it is of limited utility for analyzing complex biological processes, which exhibit more dynamic activities.

To overcome challenges associated with high-dimensional data, several methods have been developed. As shown in Figure 8, Spanning-Tree Progression Analysis of Density-

Normalized Events (SPADE) outputs a minimal-spanning tree consisting of “nodes” representing clusters of cells with similar phenotypes (Qiu et al., 2011). However, because nodes represent multiple cells, use of SPADE eliminates the single-cell resolution of input data. To enhance visual interpretation of data, nonlinear dimensionality can be reduced using methods such as t-Distributed Stochastic Neighbor Embedding (t-SNE) and Uniform Manifold and Approximation (UMAP) (McInnes et al., 2018), which output data as a two- or three-dimensional scatter plot (Figure 7). Briefly, cells are first clustered by their pairwise molecular similarity for all data points before an iterative process to evaluate differences between high- and low-dimensional matrices is performed. This is achieved using the k-nearest neighbors (k-NN) algorithm (Fix and Hodges, 1989), which predicts the groupings of individual cells in high-dimensional space. The results provide a visualization of local and global relationships between cells, including local and global structures.

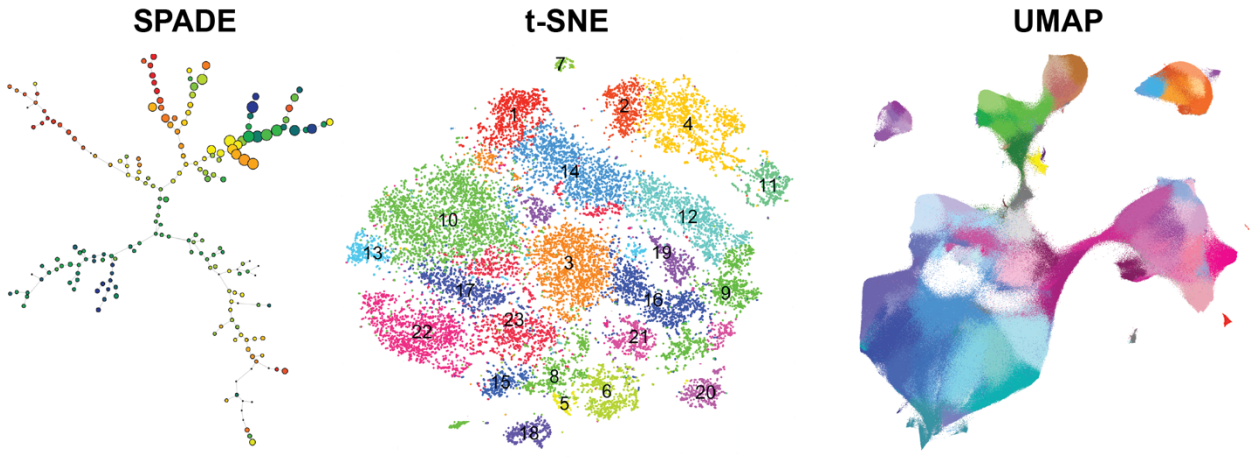

Figure 7. Example outputs of high-dimensional analysis for mouse brain samples. Spanning-Tree Progression Analysis of Density-Normalized Events (SPADE), t-distributed Stochastic Neighbor Embedding (t-SNE), and Uniform Manifold and Approximation (UMAP) are shown.

Neither t-SNE nor UMAP assign cells to specific clusters, but this can be achieved with manual gating, PhenoGraph (Levine et al., 2015) or CITRUS (Polikowsky and Drake, 2019) software, or publicly available algorithms for R or Python. At present, the Leiden algorithm (Traag et al., 2019) is the premier choice for single-cell clustering analyses. As shown in Figure 8, the algorithm uses the k-NN graph to compute local communities and calculate partitions between these communities until an aggregate network is generated. Application of these tools can be useful for identifying the presence, absence, or change in abundance of specific subpopulations.

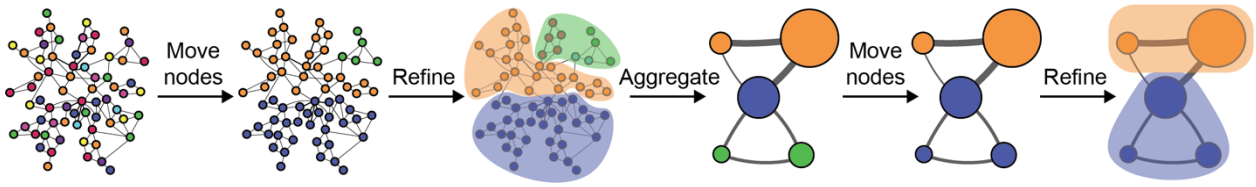

Figure 8. Schematic of how the Leiden algorithm functions. The algorithm moves individual nodes between communities to identify partitions, each of which is then refined and aggregated into a network based on the refined partition (the non-refined partition is used to create an initial partition for the aggregate network). Subsequently, the algorithm moves individual nodes in the aggregate to determine the best partition. These steps are iterated until no further improvements can be made. Adapted from Traag, et al., 2019. From Louvain to Leiden: guaranteeing well-connected communities. *Scientific Reports.*

In addition to providing insights into cell identity, high-dimensional data can be exploited to make predictions about the molecular dynamics underlying changes in cell state or identity. For example, by restricting connections between cells from different time points to cells in the immediately preceding or proceeding time point, Wanderlust (Bendall et al., 2014) and FlowMap (Ko et al., 2020; Zunder et al., 2015b) offer the ability to examine the progression of high-dimensional molecular phenotypes over time. Similarly, the URD

algorithm predicts molecular trajectories underlying cell differentiation and specification by “simulating diffusion” of molecular factors (Farrell et al., 2018).

The ability to evaluate molecular changes in cells in a high-dimensional manner is particularly useful in the context of examining developmental or disease progression, as it permits high-resolution fate mapping. At present, the abovementioned techniques have almost exclusively been applied to single-cell transcriptomic data, which provide only a limited view of cell functions. In the future, employing these analytical approaches to protein-based data promises to yield further insights into the molecular expression and signaling that drive cellular identity and functions.

EMERGENCE OF MASS CYTOMETRY

Overview of Mass Cytometry Technology

Mass cytometry is a technique combining inductively coupled plasma mass spectrometry (ICP-MS) with time-of-flight mass spectrometry (TOF-MS) to detect metal ions present in single cells with high sensitivity (Bandura et al., 2009; Bendall et al., 2011). By using standard immunochemistry techniques to label cells with antibodies conjugated to rare earths metals (i.e., not endogenously found in cells), mass cytometry can be used to quantify expression of proteins and nucleic acids, as well as post-translational and epigenetic modifications important for cell signaling (Frei et al., 2016).

As shown in Figure 9, to prepare cells for mass cytometry, they are dissociated into a single-cell suspension, cross-linked with a fixative solution, incubated with metal-conjugated primary antibodies against surface epitopes, permeabilized, incubated with metal-conjugated primary antibodies against intracellular epitopes, and then exposed to an iridium (Ir191 and Ir193) DNA intercalator. For subsequent data acquisition, cells are suspended in water and then pumped through a capillary tube, which forms a stream of single cells that is nebulized into droplets and passed through an argon plasma flame (7500 K). This process (ICP-MS) ionizes the cell and antibodies into an “ion cloud”, which is filtered by mass-to-charge ratio so that only ions with an atomic mass greater than 80 reach the TOF detector (necessary to prevent the detector from being bombarded with ions common in organic material such as carbon, hydrogen, and oxygen). Quantities of individual ion types present in each ion cloud are resolved according to their relative velocity (TOF-MS), a feature determined by their mass and kinetic energy. Using this method, expression levels of up to 50 antibodies can be simultaneously measured in single cells at a rate of up to 2×10^6 cells per hour (Bandura et al., 2009; Bendall et al., 2011).

The chemistry enabling immunocytochemical measurements by mass cytometry involves labeling antibodies with heavy metals that are not endogenously present in animal cells. To achieve this, an isotopically pure metal from the lanthanide series is mixed with polyethylene glycol polymers (each containing 16–22 chelating sites); meanwhile, the antibody is subjected to a reducing agent in the presence of maleimide linker molecules, which typically bind to reduced cysteine residues within the constant (Fc) region. By

subsequently incubating the metal-labeled polymers with maleimide-linked antibodies, the antibodies are metal-conjugated through a cross-linking reaction. Notably, the metal-conjugation process is incompatible with labeling of IgM antibodies, typically expressed during development, as their constant regions are exclusively linked by cysteine residues. Therefore, the reduction process would destroy the structure and function of these antibodies.

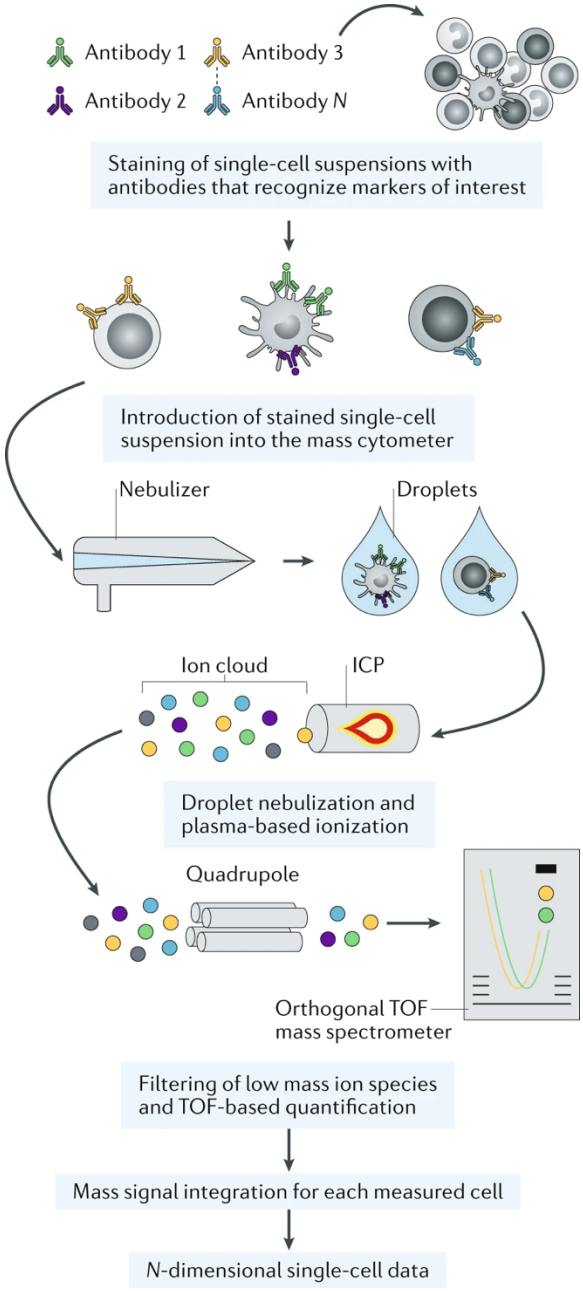

Figure 9. Schematic overview of mass cytometry method. Figure originally published in Hartmann and Bendall, 2019. Immune monitoring using mass cytometry and related high-dimensional imaging approaches. *Nature Reviews Rheumatology*. Reprinted with permission from Springer Nature (License No. 5678641033568).

Mass cytometry can also be used to detect nucleic acids using metal-conjugated oligonucleotides (Frei, 2016), iridium-based DNA intercalators (Ir191 and Ir193), and live-cell impermeant cisplatin (Pt195 or Pt198), which serve as useful markers of cell identity and viability, respectively. Thus, mass cytometry offers a uniquely intersectional approach to examine molecular mechanisms underlying fundamental cellular processes.

Methods to Analyze Mass Cytometry Data

As mass cytometry imparts the ability to acquire quantified data for up to 50 markers in millions of individual cells (Bandura et al., 2009; Bendall et al., 2011), a high-dimensional approach is necessary to maximize interpretation of the data. Luckily, software capable of handling copious amounts of data are increasing in number and features.

The mass cytometer instrument outputs a specialized file type (.fcs) that can be read by R packages or software specifically created for cytometric measurements, such as FlowJo (https://www.flowjo.com) and CytoBank (http://community.cytobank.org). Data in these files can be visualized by examining a single parameter against another single parameter in the form of biaxial plots, or in high-dimensional space. Similar to analyses presented for flow cytometry, cells can then be divided into subpopulations that are high, low, or negative for a given marker by drawing “gates”. However, as mass cytometry of 50 markers results in data sufficient for 1225 unique biaxial plots, manual gating is an inefficient method to handle the data. For example, a manual gating strategy for isolating single viable cells and identifying major cell types in P4 telencephalon is shown in Figure 10.

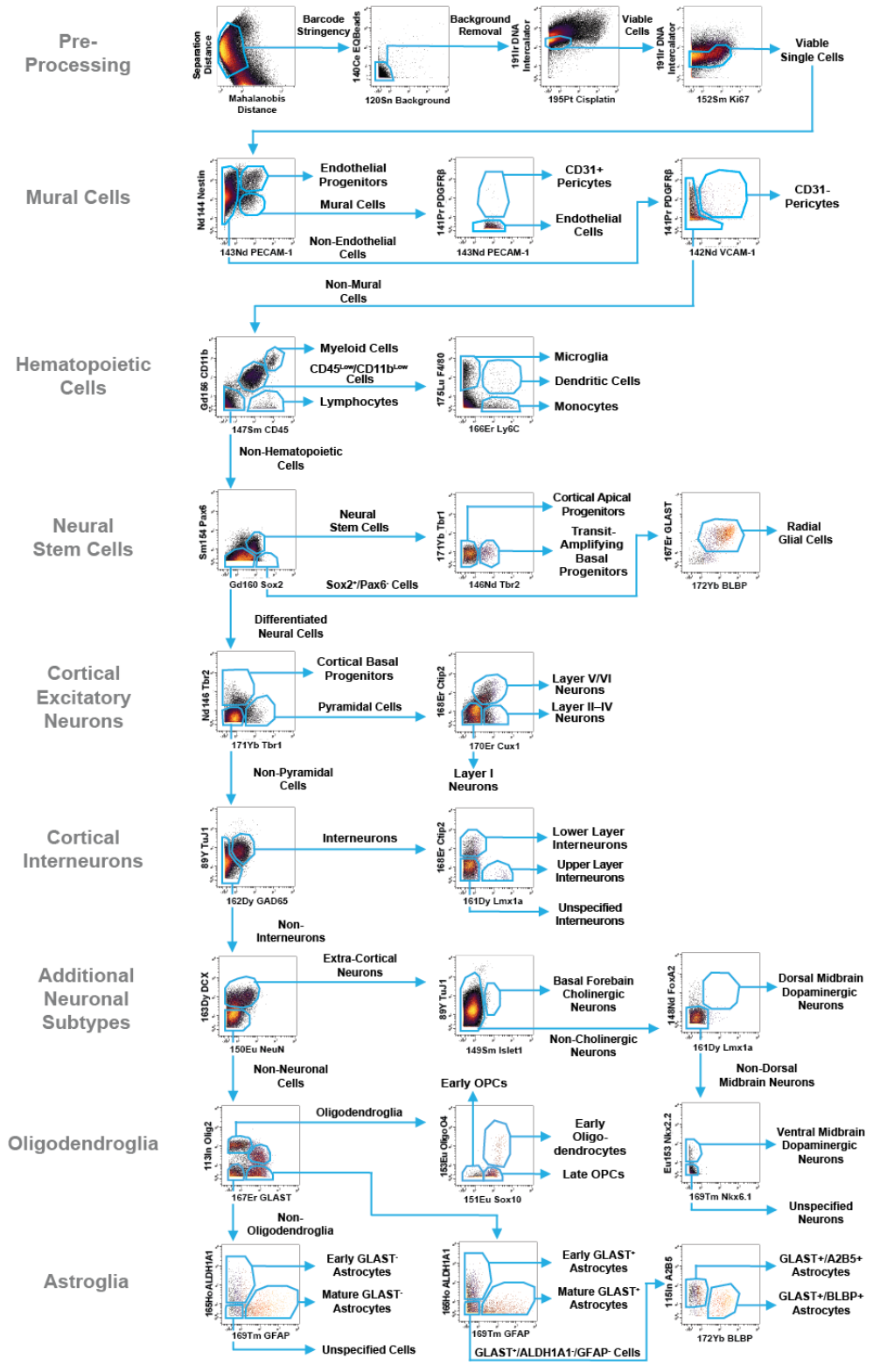

Figure 10. Manual gating strategy to isolate single viable cells and identify major cell types in P4 mouse telencephalon. Manual gating (cytobank.org) of biaxial plots can be performed in sequence to isolate single cell events (Pre-Processing) and identify cell populations.

To overcome this challenge, automated gating or high-dimensional clustering can be performed on expression data for cells. Indeed, many of the algorithms developed to analyze and visualize scRNA-seq data are readily adaptable for mass cytometry data, including UMAP and Leiden clustering algorithms, which we described above. One of the primary benefits for using such software packages is that algorithm-based gating removes many potential errors or bias resulting from manual gating (Mair et al., 2016).

Advantages and Limitations of Mass Cytometry

Advantages of Mass Cytometry

There are several key advantages for using mass cytometry to analyze cells. Compared with other immunocytochemical techniques, such as those involving microscopy or other optically based measurements, mass cytometry affords the ability to examine up to 50 markers simultaneously – an up to 16-fold increase (Bandura et al., 2009; Bendall et al., 2011). Moreover, the method by which mass cytometry data is acquired is quantitative, incredibly sensitive, and has low background.

In addition to being relatively high-throughput (currently, only flow cytometry has higher single-cell throughput), mass cytometry has expanded potential to simultaneously measure protein expression across multiple samples by barcoding cells (Zunder et al., 2015a). By processing samples together (i.e., barcoding cells, pooling them for staining in the same antibody cocktail, and acquiring data simultaneously), errors resulting from sample-to-sample variability are greatly reduced. Notably, although barcoding strategies have previously been applied for flow cytometry (Krutzik et al., 2011), this requires use of

one or more of the limited number of channels available for analysis. In contrast, the barcoding strategy used for mass cytometry employs palladium metals (Pd^{102}, $Pd^{104–106}$, Pd^{108}, and Pd^{110}) in a 3-on/3-off system, resulting in 20 available barcodes that do not interfere with measurements of lanthanide metal-conjugated antibodies (Zunder et al., 2015a). Thus, mass cytometry is a high-resolution immunocytochemical method for quantifying protein expression in single cells with enhanced utility for direct comparison of samples.

Mass cytometry can be used to quantify virtually any target for which there is an available antibody (Bandura et al., 2009; Bendall et al., 2011), including post-translational modifications (Teh et al., 2020), as well as RNA transcripts (Frei et al., 2016). Moreover, innovative chemistry techniques are being employed to generate an increased variety of reagents compatible with mass cytometry. For example, a lanthanide-chelated, azide-containing probe was recently developed to perform copper-catalyzed azide-alkyne Huisgen cycloaddition (also known as “click chemistry”) on EdU for quantification of DNA synthesis by mass cytometry (Shaklee et al., 2018). Importantly, as the click chemistry approach is applicable to a broad range of molecular targets, this opens the door for increased diversity of tools suitable for mass cytometry. Thus, while mass cytometry may have slightly lower throughput than flow cytometry and far lower resolution compared with scRNA-Seq in terms of the number of markers quantified per cell, it permits examination of a much broader range of biological targets and is superior in terms of deep profiling of cellular functional states.

Alternative single-cell approaches for multiplex protein detection exploit sequencing technologies like those used for scRNA-seq to measure both mRNA and protein expression levels, however each has its own limitations. For example, a method employing oligonucleotide-conjugated antibodies with strain-promoted alkyne–azide cycloaddition (SPAAC) (Gong et al., 2016) is only suitable for measuring surface proteins. Another method using Cas9 programmed with single-guide RNAs (CITE-seq) (Stoeckius et al., 2017) has similarly only been used to investigate surface proteins. In contrast, a method combining scRNA-seq with proximity extension assays (SPARC) (Reimegård et al., 2021) can only measure intracellular protein levels. In addition, all these methods have the general limitations of scRNA-seq, such as relatively low throughput and high cost.

Limitations of Mass Cytometry

General limitations of working with antibodies also apply to mass cytometry, including issues related to antigen availability, specificity, and signal-to-noise ratio (Ivell et al., 2014). Generally, antibodies that work for immunofluorescence will also work for mass cytometry. However, the process of metal-conjugating antibodies has the potential to affect their variable region (Fv), which is responsible for antigen specificity and binding. Thus, the specificity of antibodies should be compared before and after metal conjugation. Notably, it can be difficult to directly compare metal-conjugated antibodies by mass cytometry and other immunocytochemistry-based methods requiring use of a secondary antibody, as the Fc region typically bound by secondary antibodies may be blocked by the metal-polymer tag. Moreover, the metal-conjugation process is incompatible with

labeling of IgM antibodies, further restricting the availability of antibodies suitable for this technique.

As mass cytometry is a variation of flow cytometry, it shares many of the same general limitations – perhaps the most prominent being a requirement for samples to be in a single-cell suspension. Indeed, both cytometric methods have been widely applied to analyze hematopoietic cell lineages, which naturally occur in suspension *in vivo*, but are rarely applied to cells from solid tissues because of the loss of spatial information.

To obtain single-cell suspensions from solid tissue, mechanical and/or enzymatic dissociation is necessary. As these processes occur over several minutes or hours, the *in vivo* signaling state of most proteins is lost and replaced by their response to dissociation. This could be overcome by fixing cells prior to dissociation, however using paraformaldehyde to fix cells makes it difficult to dissociate tissue and obtain intact single cells. In addition, mass cytometry requires the use of fixed cells and destroys them during the data acquisition process, unlike flow cytometry, which can even be used to sort live cells for clinical applications.

In addition to technological restrictions, there are specific limitations for using mass cytometry to analyze neural cells. First, neural cells have polarized morphologies that are vital to their identity and function. The process of dissociating neural cells, whether from *in vitro* or *in vivo* sources, into a single-cell suspension has a dramatic impact on their morphology; namely, it “chops off” neurites and/or causes cells to retract their processes

and adapt a more spherical shape. Although this processing results in viable cells (at least until fixation) that maintain their essential molecular identity, it limits analysis of neural cells to components present within the cell soma. For example, proteins associated with synaptic transmission, which are localized and/or translated peripherally in neuronal processes, are inaccessible for analysis by mass cytometry. Thus, designing antibody panels to address specific hypotheses must take into consideration whether this technique is feasible.

Imaging mass cytometry (or multiplexed ion beam imaging) (Angelo et al., 2014; Giesen et al., 2014), an emergent technology combining mass cytometry with laser-scanning microscopy, restores the ability to resolve spatial information and *in vivo* signaling states in cells with intact morphologies. Importantly, the same metal-conjugated antibodies can be used for both methods, allowing for parallel cytometric and microscopic studies.

Reported Applications of Mass Cytometry

Mass cytometry has previously been applied to molecularly characterize pluripotent stem cell reprogramming in *in vitro*-cultured cell lines (Lujan et al., 2015; Zunder et al., 2015b), perform lineage mapping of myogenic cells (Porpiglia et al., 2017), and examine the pathogenesis of a wide range of cancers (Fisher et al., 2017; Kaiser et al., 2017; Knapp et al., 2017; Krieg et al., 2018; Spitzer and Nolan, 2016). In addition, several studies have used mass cytometry to evaluate hematopoietic cells in the CNS. For example, comparison of CNS immune cell profiles of healthy adult mice, geriatric mice, and multiple sclerosis (experimental autoimmune encephalomyelitis) model mice distinguished

several subsets of CNS dendritic cells and revealed previously uncharacterized subsets of border-associated microglia (Mrdjen et al., 2018). Additional studies have investigated rodent models of multiple sclerosis (Ajami et al., 2018; Böttcher et al., 2019, 2020b), Huntington's disease (Ajami et al., 2018), and major depressive disorder (Böttcher et al., 2020a), as well as human glioma tissues (Fu et al., 2020b; Goswami et al., 2020; Koch et al., 2022; Mueller et al., 2020; Robinson et al., 2020; Simonds et al., 2021; Vasquez et al., 2017; Yao et al., 2021).

Collectively, the results of these studies demonstrate the power of mass cytometry to identify and molecularly characterize cell subsets in the nervous system. However, only a single previous study (using seven neural markers) employed mass cytometry to actually assess neural cells (Ogrodnik et al., 2019). Therefore, the utility of mass cytometry for analyzing neural cell types has not been thoroughly described.

Herein, the potential of mass cytometry to provide high-throughput, high-resolution proteomic analyses of single neural cells during mouse CNS and PNS development is described. In addition, the utility of this technique for resolving key neurodevelopmental questions and strategies, as well as challenges for its application, are discussed. Use of mass cytometry enables a highly intersectional approach capable of accounting for numerous factors associated with neural cell proliferation, differentiation, function, and disease.

Chapter II: Mass Cytometry Analysis of Mouse Brain Development

The contents of this chapter have been accepted for publication as “A developmental atlas of the mouse brain by single-cell mass cytometry.” Amy Van Deusen, Sushanth Kumar, O. Yipkin Calhan, Sarah Goggin, Jiachen Shi, Corey Williams, Austin Keeler, Kristen Fread, Irene Gadani, Christopher Deppmann, Eli Zunder. *Nature Neuroscience* [Accepted Jan 8 2024].

Abstract

Development of the mammalian brain requires precisely controlled differentiation of neurons, glia, and nonneural cells. To investigate protein-level changes in these diverse cell types and their progenitors, we performed single-cell mass cytometry on whole brain (E11.5/E12.5) and microdissected telencephalon, diencephalon, mesencephalon, and rhombencephalon (E13.5–P4) collected daily from C57/BL6 mice. Measuring 24,290,787 cells from 112 sample replicates with a 40-antibody panel, we quantified 85 molecularly distinct cell populations across embryonic and postnatal development, including microglia/macrophages putatively phagocytosing neurites, neural cells, and myelin. Differentiation trajectory analyses emulate canonical molecular pathways underlying cortical neurogenesis and gliogenesis, and predict two distinct pathways for oligodendrogenesis. Differences in cell abundances measured by mass cytometry, immunohistochemistry, scRNA-Seq, and RNAscope affirm the value of protein-level measurements for identifying functional cell states in the developing brain. Overall, our findings demonstrate the utility of mass cytometry as a high-throughput, scalable platform for single-cell profiling of brain tissue.

Introduction

While numerous studies have cataloged cells present in the brain at maturity (Yuste et al., 2020), many fundamental questions about their development remain unresolved. In particular, the molecular profiles, timing of appearance, and cell-lineage relationships of neural stem cells (NSCs) and intermediate progenitors remain poorly characterized. Mapping the molecular trajectories and cell fate decisions underlying brain development promises to enhance our understanding of developmental disorders such as autism spectrum disorder (Courchesne et al., 2007) and epilepsy (Bozzi et al., 2012; Nickels et al., 2016), as well as mature-onset diseases that may originate during development, such as schizophrenia (Owen et al., 2011; Nour and Howes, 2015) and Alzheimer's disease (Bothwell and Giniger, 2000; Arendt et al., 2017).

Previous efforts to identify and characterize cell populations in the central nervous system (CNS) primarily relied on either immunofluorescence microscopy, which detects a small number of proteins simultaneously, or single-cell RNA sequencing (scRNA-seq), which detects a large number of transcripts simultaneously. scRNA-seq and the related technique single-nuclei RNA sequencing have been applied to characterize the molecular diversity of cells in a wide range of embryonic and postnatal mouse brain tissues (La Manno et al., 2016; Kee et al., 2017; Frazer et al., 2017; Bifari et al., 2017; Y.-J. J. Chen et al., 2017; Yuzwa et al., 2017; Mayer et al., 2018; Rosenberg et al., 2018; Tiklová et al., 2019; Wizeman et al., 2019; Guo and Li, 2019; Zhang et al., 2020; Romanov et al., 2020; Zhou et al., 2020; Kim et al., 2020; Li et al., 2020; Lee et al., 2022). However, no previous study has molecularly profiled single cells from every brain region at daily time points

across embryonic and postnatal development, and no single-cell omics study to date has quantified protein instead of mRNA abundance levels in the developing brain.

In this study, we leveraged the high throughput (1×10^6 cells/hour) of single-cell mass cytometry to profile four regions of the developing brain: telencephalon diencephalon, mesencephalon, and rhombencephalon, with daily time points from embryonic day 11.5 (E11.5) to postnatal day (P4). Mass cytometry is a variation of flow cytometry in which abundances of proteins and other biomolecules are quantified at the single-cell level using rare earth metal isotope-labeled antibodies and other affinity reagents (Bandura et al., 2009; Bendall et al., 2011). Commercially available reagents permit over 40 molecular markers to be measured and quantified simultaneously in each cell by mass cytometry, including cell surface receptors, transcription factors, cytoskeletal proteins, and markers of cell cycle status and viability.

The antibody-based measurements from mass cytometry can directly read out functional biomolecules, unlike mRNA transcripts that do not necessarily correlate with protein abundance – a disconnect most pronounced during dynamic cell transitions (Liu et al., 2016; Reimegård et al., 2021) like those occurring in early brain development. Mass cytometry was previously employed to investigate glioma (Galdieri et al., 2021; Hu et al., 2019; Kondo et al., 2020; Leelatian et al., 2020, 2017; Sankowski et al., 2019; Shaim et al., 2021; Yan et al., 2021), microglia(Ajami et al., 2018; Mrdjen et al., 2018; Böttcher et al., 2019, 2020a; Ormel et al., 2020; Zilkha-Falb et al., 2020; Li et al., 2021; Xie et al., 2022), and dorsal root ganglia(Keeler et al., 2022), but this approach has yet to be applied

to study neural cell types in the brain, except for one limited analysis with seven neural-specific markers in a study of obesity-inhibited adult neurogenesis (Ogrodnik et al., 2019).

To adapt mass cytometry for neural cells from embryonic and postnatal brain tissue, we developed a 40-antibody panel of markers relevant to CNS development and optimized cell dissociation techniques. Once this iterative development and optimization process was complete, we profiled brains of C57/BL6 mouse embryos and pups from E11.5, shortly after the secondary vesicles have formed and cortical neurogenesis begins, to P4, when the brain regions have assumed their final morphology, mature neural cell types are present, and synaptic connections begin to form(V. S. Chen et al., 2017).

Using this neural mass cytometry approach, we identified and quantified 85 molecularly distinct cell populations across embryonic and postnatal development in the telencephalon, diencephalon, mesencephalon, and rhombencephalon. These cell populations generally show complementary overlap with those previously identified by scRNA-seq studies (La Manno et al., 2016; Kee et al., 2017; Frazer et al., 2017; Y.-J. J. Chen et al., 2017; Yuzwa et al., 2017; Mayer et al., 2018; Mi et al., 2018; Rosenberg et al., 2018; Carter et al., 2018; Tiklová et al., 2019; Wizeman et al., 2019; Guo and Li, 2019; Zhang et al., 2020; Romanov et al., 2020; Zhou et al., 2020; Kim et al., 2020; Li et al., 2020; Ruan et al., 2021; Di Bella et al., 2021; La Manno et al., 2021; Sarropoulos et al., 2021; Turrero García et al., 2021; Lee et al., 2022), although our time-course comparison reveals that mRNA transcript levels do not necessarily predict protein abundance during early brain development. Application of URD pseudotime analysis (Farrell et al., 2018) to

map cell differentiation captures classical neuronal and oligodendroglial trajectories, and predicts two potentially distinct cell-lineage hierarchies for producing embryonic OPCs. Additionally, our measurements detected putative phagocytic cargo within individual microglia/macrophages, highlighting their dynamic functions during early brain development. Collectively, our findings, methods, and analytical strategies establish mass cytometry as a platform to identify cell types in the developing brain, as well as the transition states and molecular trajectories underlying their specification.

Materials and Methods

Animals

All animal husbandry and experiments were carried out in accordance with guidelines of the Association for Assessment of Laboratory Animal Care and approved by the University of Virginia Animal Care and Use Committee (Deppmann Protocol No. 3795). Mice were harvested from C57/BL6 females (Jackson Labs, 000664) bred in house from embryonic day 11.5 (E11.5) to postnatal day 4 (P4). For timed pregnancies, animals were mated overnight and removed the following day, and pregnancy was confirmed by the presence of a plug and consistent weight gain after 1 week. Animals were housed with a 12-h light/dark cycle with food and water *ad libitum*.

Dissection

For collection of embryonic mice, timed-pregnant mice were anesthetized and subjected to cervical dislocation before surgically removing all embryos. Postnatal pups were placed on ice before decapitation. Subsequently, whole brains were removed from mice aged

E11.5 to P4 and placed in 35-mm Petri dishes containing Dulbecco's phosphate-buffered saline (PBS; Thermo Fisher Scientific, 14190) on ice.

Single-cell dissociation of brain tissue

Following decapitation of embryonic and postnatal mice, dissociation of viable single cells from brain tissue was optimized similar to a previously reported strategy (Volovitz et al., 2016). After dissection of whole brains (E11.5/E12/5) or microdissection into cortex, diencephalon, midbrain, and cerebellum/hindbrain (E13.5–P4) (Fig. 1a), tissues were separated, meninges were removed, and samples from mice in a single litter were pooled into Eppendorf tubes as follows: 1–2 telencephalons, 3–5 diencephalons, 3–5 mesencephalons, or 2–3 rhombencephalons. Preliminary experiments using flow and mass cytometry (described below) revealed that enzymatic dissociation was necessary to generate preparations with high levels of viable single cells and minimal cellular debris. As shown in Extended Data Figure 1a, flow cytometry demonstrates that mechanical dissociation alone (No Enzyme) yielded roughly half the single cells produced by our optimized protocol (as indicated by the percentage of cells in the gate) and far less TuJ1-Ax488-positive cells negative for DRAQ7 (nuclear stain; Biolegend) debris. Mass cytometry analysis of the same samples with a DNA intercalator (DNA-Ir191) and metal conjugated form of the same antibody (TuJ1-Pr141) produced similar results, although the extra filtration and dilution steps used for mass cytometry appeared to enrich for singlet cells (Extended Data Fig. 1b). Further quantification of singlet viable cells using DNA-Ir191 and cisplatin (Pt195, described in detail below) demonstrates that enzymatic dissociation vastly improved viability of cells in final preparations (Extended Data Fig. 1c),

while analysis with an antibody against histone H3 (a core nuclear protein) confirmed that events positive for TuJ1 and negative for DNA intercalator were indeed cellular debris without cell nuclei (Extended Data Fig. 1d). Although we tested collagenases II and IV, dispase II, papain, and Accutase™ at various concentrations and in different combinations (data not shown), we ultimately chose a combination of collagenase IV and dispase II, as well as small amounts of DNAse-I and hyaluronidase, which were found to be essential to prevent samples from taking on a mucus-like viscosity that thwarted cell recovery. Specifically, a P1000 micropipette was used to add 1 mL of Dulbecco's Modified Eagle's Medium containing 4.6 mg/mL dispase II (Sigma-Aldrich, D4693), 1 mg/mL collagenase type IV (Worthington, LS004186), 0.2 mg/mL DNAse-I (Sigma-Aldrich, 11284932001), and 0.2 mg/mL hyaluronidase (Sigma-Aldrich, H3884) to each dish. Tissue was immediately mechanically dissociated by mincing with forceps and gently pipetting up and down five times with a P1000 micropipette, before transferring the resulting cell slurry to a microcentrifuge tube. After incubation at 37ºC in a water bath for 20 min, the cell suspension was passed through a 75-µm sieve and 45-µm sieve (Thermo Fisher Scientific, 50871316 and 50871319) with a P1000 micropipette. Tubes were then centrifuged at 300 × g for 3 min at 4ºC, the supernatant was discarded, and cells were washed by adding 1.5 mL of PBS containing 0.5% bovine serum albumin (BSA; Sigma-Aldrich, A9418) and gently pipetting. After centrifugation at 300 × g for 3 min at 4ºC, cells were resuspended in 100 µL of PBS.

Cisplatin staining and fixation of single-cell suspensions

Resuspended cells were mixed with 100 µL of 2× cisplatin solution (10 µM in PBS; Sigma Aldrich, P4394) with a P1000 micropipette, incubated at room temperature for 30 sec, and then quenched with 1.3 mL of PBS containing 0.5% BSA. Following centrifugation at 300 × g for 3 min at 4ºC, supernatants were removed, and the resulting cell pellets were washed once with PBS containing 0.5% BSA. Subsequently, cells were fixed for 10 min at room temperature in 1 mL of 1.6% PFA solution (Electron Microscopy Services, CAS 30525-89-4) in PBS. Following fixation, the cell suspension was centrifuged at 600 × g for 3 min at 4ºC, washed once with PBS, centrifuged again, and resuspended in 1 mL of cell staining medium (CSM; 0.5% BSA, 0.02% NaN_3 in PBS). A 100-µL aliquot of each sample was placed in a separate tube (for flow cytometry analysis) before storing samples and aliquots at -80ºC until use for analysis.

Cell counts and visual inspection by light microscopy

To preliminarily confirm the quality of dissociation, fixed cells were visually inspected in bright field mode at 4×, 10×, and 20× using an EVOS AMF4300 microscope (Thermo Fisher Scientific). Samples exhibiting a preponderance of single cells with low levels of debris and cell clumps were counted using a Bio-Rad TC20 Automated Cell Counter.

Immunocytochemistry and flow cytometry

To further validate the quality of dissociated cell preparations, we quantified the presence of cell singlets, aggregates, and neurite debris in each sample that passed visual inspection using flow cytometry with the fluorescent nuclear stain DRAQ7 and an Alexa

Fluor™ 488-conjugated antibody against the neuronal intermediate filament TuJ1. Briefly, aliquots of each cell sample were thawed on ice, pelleted by centrifugation at 600 × g for 3 min at 4ºC, and the supernatant was discarded. Next, cells were permeabilized with ice-cold 100% methanol and incubated on ice for 10 min with vortexing every 2 min. After centrifugation at 600 × g for 3 min at 4ºC, the supernatant was discarded and cells were washed once with CSM before blocking in a solution of 10% normal donkey serum (NDS; Millipore, S30-100ML) in CSM. Cells were incubated with TuJ1 antibody (1:1000 in CSM; Biolegend) for 1 h at room temperature on a shaker. After incubation, cells were centrifuged at 600 × g for 3 min at 4ºC, the supernatant was discarded, and DRAQ7 (1:5000 in PBS) was added for 5 min. Samples were immediately measured on an Attune™ NxT flow cytometer (Thermo Fisher Scientific) and analyzed using CytoBank (community.cytobank.org).

Mass cytometry antibody panel design

The 40-antibody panel for mass cytometry was designed to capture virtually all cell types present in the mouse brain during development and therefore included established markers of neural and nonneural cell identity, as outlined in Extended Data Table 1. Metal labels were chosen with consideration for antigen abundance, variations in instrument sensitivity for isotopes, signal spillover, environmental background, and the purity of available metal isotopes, as described in the manufacturer's technical support information (Fluidigm, 2015). Additional technical constraints were also taken into consideration during panel design. For example, the loss of cell processes (e.g., neuronal axons and dendrites, astrocytic end feet, and myelin sheaths) during single-cell dissociation is an

important caveat for analyses of neural tissues by flow/mass cytometry and scRNA-seq. Therefore, peripherally expressed proteins that are also synthesized in the cell body and can be detected there at lower levels (e.g., DCX, TuJ1, and MAP2) were chosen for the antibody panel. Cell dissociation and sample processing may also cause fragments of cells or sheared processes to stick to the surface of other cells, resulting in cells appearing positive for markers of two discrepant cell types. This appears to be the case for the mural cells observed in the present study, which are positive for both the mural cell marker MCAM and neural cell markers such as TuJ1. Once we observed this phenomenon, we chose to keep MCAM in the antibody panel to be able to exclude these cells from analysis as neural cells.

Metal conjugation of antibodies

Purified antibodies (lyophilized or in buffer free of BSA and gelatin) were conjugated to isotopically pure metals (listed in Table 1) for mass cytometry analysis using Maxpar® Antibody Labeling Kits (Standard BioTools) according to the manufacturer's instructions. Immediately following conjugation, stock solutions were prepared for long-term storage at 4°C by diluting conjugated antibodies at least two-fold with Candor PBS Antibody Stabilization Solution (Candor Bioscience GmbH). Final concentrations of antibodies in stock solutions ranged from 0.05–0.4 mg/mL.

Validation of antibodies

Following metal conjugation, each antibody was titrated to determine the optimal concentration for mass cytometry analysis. To define the antibody concentration providing

the highest signal-to-noise ratio, we employed positive and negative counterstains (e.g., TuJ1 for neurons, BLBP for glial cells, CD45 for hematopoietic cells) to evaluate cell samples from mouse brain, a mouse embryonic stem cell line (E14Tg2a, ATCC, CRL-1821), two mouse neuroblastoma cell lines [N1E-115 (ATCC, CRL-2263) and Neuro-2a (ATCC, CCl-131)], one mouse glioma cell line (GL261, National Cancer Institute Division of Cancer Treatment and Diagnosis Tumor Repository, Glioma 261), two mouse OPC cell lines (OPC-1052 and OPC-8173, gift from Prof. Hui Zong, University of Virginia), and a human embryonic kidney cell line (293T, ATCC, CRL-3216). The optimal concentration of each metal-conjugated antibody preparation was defined as the concentration providing the highest signal-to-noise ratio between appropriate positive and negative controls (Extended Data Fig. 1g,h). Antibodies were considered specific and reliable if they produced signal in DNA intercalator-positive cells exhibiting one or more positive counterstains, and were absent in cells exhibiting a negative counterstain (Extended Data Fig. 1i). Notably, although signal compensation is possible (Chevrier et al., 2018), it is not standardly applied in the field or this experiment because minimal overlap occurs between signals for individual metals and each antibody was titrated to an optimal concentration.

Sample barcoding, staining, and intercalation for mass cytometry

To prepare samples for mass cytometry, frozen cells were thawed and pelleted by centrifugation at 600 × g for 3 min at 4ºC. After removing the supernatant, cells were washed once with CSM and resuspended in 0.5 mL of cold saponin solution (0.02% in PBS) containing one of the twenty 6-choose-3 combinations of 1 mM palladium barcoding reagents, as previously described (Zunder et al., 2015a; Fread et al., 2017).

Following incubation on a shaker at 800 rpm for 15 min at room temperature, samples were centrifuged at 600 × g for 3 min at 4ºC and the supernatant was discarded. The resulting cell pellet was washed three times with CSM and then pooled with other samples into a total of seven barcoded sets for antibody staining (Supplementary Table 1).

Prior to staining of surface epitopes, each barcoded set was blocked in CSM containing 10% (v/v) NDS for 30 min at room temperature. After blocking, antibodies indicated as "Surface" in Extended Data Table 1 were diluted in CSM and added to cells (100 µL staining volume per 1 × 10^6 cells). Following incubation at room temperature on a shaker at 800 rpm for 30 min, samples were centrifuged at 600 × g for 3 minutes at 4ºC and the supernatant was discarded. After washing the cell pellet three times with CSM, cells were permeabilized for intracellular staining by filling the sample tube with ice-cold 100% methanol and incubating on ice for 10 min with vortexing every 2 min. Next, samples were centrifuged at 600 × g for 3 min at 4ºC, the supernatant was discarded, and cells were washed once with CSM. Samples were then incubated with primary antibodies listed as "Intracellular" in Extended Data Table 1 (diluted in CSM) for 1 h at room temperature on a shaker at 800 rpm. After incubation, samples were centrifuged at 600 × g for 3 min at 4ºC, the supernatant was discarded, and cells were washed three times with CSM.

After primary antibody staining, cells were stained with 0.1 µM Cell-ID™ Intercalator-Ir (201192, Standard BioTools) in 1.6% PFA containing for 15 min overnight at 4ºC. After intercalation, cells were washed once with CSM, once with water, once with 0.05% Tween-20 (in water), and again with water. Finally, cells were pelleted by centrifugation

at 600 × g for 3 min at 4ºC and then samples were kept on ice until measurement on the mass cytometer. As outlined in Supplemental Table 1, the 112 samples analyzed in this study were prepared as seven barcoded sets, which were stained with fresh antibody solutions and run on the mass cytometer on three occasions (first run included barcode sets 1–3, second included sets 4–6, and third included set 7).

Mass cytometry

Immediately before analysis, cells were resuspended in Maxpar® Cell Acquisition Solution (approximately 1 mL per 1 × 10^6 cells, Standard BioTools) containing 1:20 EQ™ Four Element Calibration Beads (Standard BioTools) and pipetted through a 40-µm nylon mesh filter. Cells were analyzed in multiple runs on a Helios™ CyTOF® 2 System (Standard BioTools) at a rate of 500 cells per second or less.

Normalization and debarcoding

To control for variations in instrument signal sensitivity across individual mass cytometry runs, raw .fcs data files were normalized using EQ Four Element Calibration Beads as described in Finck et al. 2013 (https://github.com/nolanlab/bead-normalization) (Extended Data Fig. 2a). The resulting normalized .fcs files from each run were concatenated for each sample set and then debarcoded using software described in Fread et al., 2017 (https://github.com/zunderlab/single-cell-debarcoder) to deconvolute palladium metal expression on single cells, thus permitting identification of individual samples according to a 6-choose-3 combinatorial system (Zunder et al., 2015a) (Extended Data Fig. 2b–d). The modified version adds a new parameter for barcode

negativity (bc_neg) that is the sum of the counts for the three barcode metals expected to equal zero based on the barcode deconvolution assignment. High values of this parameter signify events likely containing two or more cells.

Isolation of single-cell events with two-dimensional gating

To isolate single cells from debris and clumps of multiple cells, .fcs files processed as described above were uploaded to CytoBank (community.cytobank.org) and gated according to the strategy illustrated in Extended Data Figure 2e–j. First, an additional debarcoding process was performed by gating out events with a low barcode separation distance, high Mahalanobis distance, and/or high signal for non-barcode metals (Extended Data Fig. 2e). Subsequently, singlets were isolated by gating out events with exceptionally high or low lengths or widths relative to the center (Extended Data Fig. 2f).

To remove non-viable cells, events with high Pt195 signal (indicating high cisplatin uptake before fixation) were removed (Extended Data Fig. 2g). Next, events with a high cerium (Ce140) signal, indicating potential failure to remove a calibration bead during normalization, were removed (Extended Data Fig. 2h). Finally, gating was applied to remove events exhibiting high spectral overlap between metal isotopes (Extended Data Fig. 2i) and cellular debris (Extended Data Fig. 2j). Isolated single-cell events for individual timepoints were exported to .fcs files for further analysis.

Batch correction

To account for changes in antibody signals between barcode sets and remove the potentially negative influence of aberrant signals from debris or cell clumps on normalization of signals from individual markers, batch correction was performed after isolating single-cell events as described above. To correct for differences in signal intensities of individual markers across the seven barcoded sets (batch effects), debarcoded .fcs files were processed as described in Schuyler et al., 2019 (https://github.com/CUHIMSR/CytofBatchAdjust). Briefly, each barcoded set contained a universal sample (mixture of all ages and brain regions examined). Antibodies that produced Gaussian distributions and mean signals with variance greater than 1% for this universal sample were corrected at the 50th percentile, including: A2B5, BLBP, CD24, Cux1, DCX, NeuroD1, PSA-NCAM, Sox2, Sox10, and TuJ1 (Extended Data Fig. 2k). Mean signals for ALDH1A1, CD11b, and SSEA-1 had 2%–3% variance and normal distributions with truncated lower tails. Batch correction of these markers at 80th and 95th percentiles was determined to be ineffective at reducing the variance of mean signal, while correction at the 50th percentile resulted in overcorrection (ALDH1A1 and SSEA-1) or a non-zero mean (CD11b); therefore, these markers were not batch corrected. The remaining markers were not batch corrected because the variance of their mean signal was determined to be less than 1%. Protein expression levels of each marker in the universal sample for the seven barcoded sets are shown for all cells and positive cells in Extended Data Figure 2l,m, respectively. Positive cells were manually thresholded for expression using the values listed in Extended Data Figure 6b.

ArcSinH scaling

To minimize background signal levels and provide the greatest signal-to-noise ratio, ArcSinH values were manually scaled for each antibody using CytoBank. Default (ArcSinH = 5) and final ArcSinH transformation values are shown in Extended Data Fig. 2n. The default value was used for markers not shown.

Clustering of high-dimensional data

To reduce the effect of differences in tissue and sample size on clustering, 5×10^5 cells were randomly selected from each age/region for the global analyses shown in Figures 1–4, yielding a total of 5.75×10^6 (~24%) cells from the original dataset (2.43×10^7 cells). For analyses shown in Figure 5, clustering was performed on all $Sox2^{high}nestin^{high}$ cells (isolated by the manual gating strategy in Fig. 5a), yielding a total of 3,253,641 cells (~13%) from the original dataset. For analyses of the telencephalon shown in Figure 6, clustering was performed on 1.25×10^5 cells randomly sampled from each replicate (n = 2 per age), yielding a total of 3.25×10^6 cells (~47%) from the 6,855,672 telencephalon cells in the original dataset. For analyses shown in Figure 7, clustering was performed on all CD45-positive cells (defined by the manual gating strategy shown in the inset in Fig. 7a and Extended Data Fig. 9a), yielding a total of 1,345,841 cells (~5.5%) of the original dataset.

To identify discrete cell populations within the developing mouse brain, isolated single cells were subjected to two rounds of high-dimensional analysis. For both rounds of clustering, all markers were included for generation of UMAP layouts to distinguish major

classes (i.e., NSCs, neuronal progenitors, glial progenitors, neurons, astrocytes, oligodendrocyte progenitors, hematopoietic cells, and mural cells).

To analyze potential artifacts related to our use of seven barcoded sets, which were stained with three freshly prepared antibody cocktails and run on the mass cytometer on three different days (as described above), a UMAP layout was generated from 5×10^5 cells randomly selected from each of the seven universal samples included in each run (Extended Data Fig. 3b).

Assignment of cluster identities

The cell-type specificity of each antibody used in the panel is outlined in Extended Data Table 1. Accordingly, cells were organized into major classes by their molecular profile as follows: 1. Neural stem cells (NSCs): positive for Sox2 and nestin with or without Pax6, Sox1, Olig2, CD133, and CD24; negative for mature neural markers. 2. Intermediate neuronal progenitors: positive for Tbr2. 3. Neurons: positive for DCX, TuJ1, and/or MAP2, with low levels of the postmitotic neuronal marker NeuN. 4. Inhibitory neurons: positive for GAD65. 5. Radial glial cells/glial precursors: high expression GLAST and BLBP, with or without GFAP. 6. OPCs: variable levels of Olig2, PDGFRα, and Sox10; two clusters also expressed low levels of OligoO4, suggesting differentiation into early oligodendrocytes. 7. Neuronal progenitors: combined expression of markers associated with NSCs and mature neurons, negative for glial markers. 8. Glial progenitors: combined expression of markers associated with NSCs, RGCs/glial precursors, and astroglial cells, with or without Olig2; negative for neuronal markers. 9. Endothelial cells: positive for

platelet endothelial cell adhesion molecule-1 (PECAM1) with or without Ly6C. 10. Mural cells: positive for MCAM or PDGFRβ; notably, mural cell clusters also contain several neural markers, but do not have elevated DNA-intercalator levels, indicating that these are not cell doublets or aggregates. Instead, the most likely explanation is that neural cell debris is sticking to their cell surfaces. 11. Non-neural cells: negative for virtually all neural cell markers, although the presence of markers such as PDGFRα, P75NTR, Cux1, CD24, and VCAM suggest the presence of putative fibroblasts among these clusters. 12. Microglia/macrophages: low expression of canonical markers CD45 and CD11b, as well as positive expression of F4/80. 13. Other hematopoietic cells: high expression of CD45 and CD11b. 14. Neural crest-derived cells: high expression of Sox10 and negative for Olig2. Two putative non-brain populations appeared to contaminate early embryonic dissections, a cluster exhibiting low expression of P75NTR, BLBP, and some stem cell markers presumably representing developing cranial ganglia; and a cluster exhibiting ALDH1A1 expression presumably representing a population of developing glial cells. 15. "Apoptotic" cells: high expression of cleaved caspase 3; notably, cells with low to moderate expression were observed in numerous clusters (especially glial progenitors). 16. Low-complexity cells: one small cluster of cells was negative for expression of all panel proteins, representing 2.16% of total cells analyzed. Cluster numbers presented in the manuscript have been reordered to improve readability. Original and reordered cluster numbers are provided in the Source Data for Figures 1 and 5–7.

Visualization of high-dimensional data with UMAP

Mass cytometry datasets were visualized by uniform manifold approximation and projection (UMAP, https://github.com/lmcinnes/umap) (McInnes et al., 2018) using the following parameters: nearest neighbors = 15, metric = Euclidean, local connectivity = 1, N components layout = 2 (3 for UMAP in Fig. 7a), N components cluster = 2, N epochs = 1000.

Leiden clustering

Community detection with the Leiden algorithm (Traag et al., 2019) was performed to partition cells into clusters according to molecular profile similarity using Python. To improve computational speed and scalability, the hnswlib package (https://github.com/nmslib/hnswlib) was incorporated into this process (https://github.com/zunderlab/VanDeusen-et-al.-CNS-Development-Manuscript/blob/main/02_UMAP_and_Leiden_Clustering/03_Leiden.py) using the following parameters: Hierarchical Navigable Small World Graphs (HNSWG) space = 12, HNSWG $EF_{Construction}$ = 200, HNSWG M = 16, HNSWG EF_{Set} = 20.

Immunohistochemistry

Following dissection of whole brains, they were immersed in 4% PFA overnight before cyroprotection in 30% sucrose in PBS for 2 days, all at 4°C. Subsequently, brains were embedded in Optimal Cutting Temperature Compound (VWR, 25608-930), frozen on dry ice, and stored at -80ºC until cryosectioning into 40-µm sections. Mounted sections were warmed to room temperature, washed with 1× PBS three times for 5 minutes each, and

subjected to antigen retrieval by microwave boiling slides/sections in 10 mM sodium citrate buffer (pH 6.0). After cooling sections to room temperature, the sodium citrate buffer was replaced with 1× PBS and sections were microwaved until boiling again. Next, sections were washed three times with 1× PBS and incubated in blocking solution (0.2% Triton X-100 and 3% NDS) for 1 hour at room temperature. Subsequently, sections were incubated with primary antibodies diluted in blocking solution overnight at 4 °C. Primary antibodies used for IHC were the same clones as used for mass cytometry except for rabbit anti-BFABP (Abcam, ab281734, 1:250, RRID: unknown). Following primary antibody staining, sections were washed with 1× PBS three times for 5 minutes each, incubated with secondary antibodies for 1 hour at room temperature protected from light, and washed with 1× PBS three times for 5 minutes each. Secondary antibodies used in this study included: Alexa Fluor 488 donkey anti-mouse (Thermo Fisher Scientific, A21202, 1:500, RRID: AB_141607), Alexa Fluor 568 donkey anti-rabbit (Thermo Fisher Scientific, A10042, 1:500, RRID: AB_2534017), and Alexa Fluor 647 donkey anti-goat (Thermo Fisher Scientific, A21447, 1:500, RRID: AB_2535864). Following secondary staining, sections were mounted in Fluoromount-G with DAPI (SouthernBiotech, 0100-20).

In situ hybridization assay by RNAscope

Following dissection, E13.5, E15.5, and E17.5 brain tissues were immersed in 4% PFA overnight before cyroprotection in 30% sucrose in PBS for 2 days, all at 4°C. Subsequently, brains were embedded in Optimal Cutting Temperature Compound, frozen on dry ice, and stored at -80ºC until cryosectioning into 20-µm sections onto positively

charged slides (Shandon Superfrost Plus, Thermo Fisher Scientific, 6776214). After air drying sections overnight in the dark, they were twice washed for 2 minutes in PBS, incubated for 10 minutes in H_2O_2 (RNAscope H_2O_2 and Protease Reagents Kit, Advanced Cell Diagnostics, 322381), and washed again twice for 2 minutes with distilled water. Next, sections were incubated with protease IV solution (RNAscope H_2O_2 and Protease Reagents Kit) for 30 minutes at 40°C in a HybEZ II oven (Advanced Cell Diagnostics, 321710/321720), washed twice with distilled water for 2 minutes each, and incubated in one of two probe master mixes for 2 hours at 40°C [Mix 1: Mm-Fabp7 (414651-C1) and Mm-Sox2 (401041-C2); Mix 2: Mm-Eomes (429641-C1) and Mm-nestin (313161-C2); Advanced Cell Diagnostics]. After washing sections twice with 1 × wash buffer (RNAscope Wash Buffer Reagents, Advanced Cell Diagnostics, 310091), amplification was performed by sequential incubations with AMP1, AMP2 and AMP3 solutions (RNAscope Multiplex Fluorescent Detection Kit Version 2, Advanced Cell Diagnostics, 323110) for 30 minutes at 40°C, with two 2-minute washes with wash buffer between solutions. Next, sections were incubated with horseradish peroxidase (HRP)-channel 1 (HRP-C1) (RNAscope Multiplex Fluorescent Detection Kit Version 2) for 15 minutes at 40°C, washed twice for 2 minutes each in wash buffer, and incubated in fluorescent dye for 30 minutes at 40°C [1:750 dilution; Tyramide Signal Amplification (TSA) Cyanine 3, Akoya, TS000202]. After washing sections with wash buffer twice for 2 minutes each, they were blocked with HRP blocker for 15 minutes at 40°C. The same HRP steps were repeated for channel 2 by applying a second fluorescent dye (1:750 dilution; TSA Fluorescein, Akoya, TS000200). Finally, 10–20 mL of DAPI was applied at room temperature to stain cell nuclei (Fluoromount-G) and slides were sealed with coverslips.

Confocal microscopy

Brain sections were imaged on a laser-scanning confocal Zeiss 980 NLO at 40× resolution in Z-stacks at 1-µm intervals for automated quantification using QuPath. Ratios of positive cells and expression levels in cells were evaluated using the Positive Cell Detection feature in QuPath with the following parameters: requested pixel size = 0.4 µm, background radius = 8 µm, medium filter radius = 0 µm, sigma = 1.5, minimum area = 10 µm, maximum area = 100 µm, threshold (DAPI) = 5, cell expansion = 2 µm. Thresholds for identifying positive cells (Extended Data Fig. 4b) were manually adjusted for each batch of images to minimize the effects of variations in staining or background levels. Plotting and statistical analysis of confocal microscopy results was performed with R.

Comparison of protein and RNA expression profiles

To compare protein and RNA expression levels, we chose one of the largest scRNA-seq datasets describing nervous system tissue published to date (La Manno et al., 2021). Samples were first matched for microdissected regions and ages for the two datasets (Extended Data Fig. 6a). Expression counts matrix for the scRNA-seq data were downloaded from mousebrain.org and preprocessed according to the original publication (La Manno et al., 2021). Differences in the processes used to dissociate single cells from embryonic brain tissues are outlined in Extended Data Fig. 6c for each dataset. To calculate percentages of expressing cells for scRNA-seq and mass cytometry data, cells in scRNA-seq data were considered ‘expressing’ if their value was above zero. For mass cytometry data, which typically exhibits low background for individual markers compared with antibody-based techniques, thresholds for labeling cells as positive were manually

assessed as the 99th percentile of expression in low-complexity cells (Extended Data Fig. 6b). To evaluate expression levels by cell class for each brain region, our clusters (shown in Fig. 1c,d) were manually matched with those identified using scRNA-seq, resulting in 17 distinct cell classes (Extended Data Fig. 6d). Mean expression was then calculated for the identified population of cells expressing each gene/marker for each brain region. For both datasets, the calculated mean expression values were finally per-feature range-normalized to fall between 0 and 1. Percentages of cells expressing each marker, normalized mean expression values, and expression values for individual cells were then examined for each RNA-protein pair in each brain region and plotted using R (Fig. 4a).

Identification of developmental cell trajectories with URD

To model the cell fate decisions involved in developmental cell trajectories, the R package URD (Farrell et al., 2018) was adapted for use with mass cytometry data. “Root” and “tip” cells were manually chosen as the beginning and end points for construction of a map based on diffusion of protein expression levels (Fig. 5a and Fig. 6b). All markers were used for analysis with the following URD parameters: floodPseudotime n= 500, minimum.cells.flooded = 2, max.frac.NA = 40, knn = 15. Because of computational limitations, both the Sox2^{high}nestin^{high} cell dataset and telencephalon dataset were randomly and proportionally (with regard to sample age and cluster, respectively) sampled to a total 61,000 cells. The URD algorithm assigned each cell a pseudotime value based on its distance from the root, indicating its relative position along the differentiation trajectory from root to tip. By identifying intersecting paths from thousands of random walks from each tip back to the root, URD constructs a dendrogram from which

molecular trajectories and branchpoints can be derived. Pax6^{high} NSCs present at E11.5 were chosen as the root for both URD analyses, while clusters chosen as tips were selected because their molecular profile suggest a mature differentiation status (i.e., relatively high expression of mature neural markers and low expression of stem/immature markers relative to subclusters of similar identity). To ensure proper representation of neurogenic Sox2^{high}nestin^{high} subpopulations that became sparse postnatally, cells in tip subclusters from P0–P4 samples were included in this analysis and selected irrespective of their origin in the brain.

Quantification of cell doublets/aggregates by flow cytometry and mass cytometry

As described above in the Flow Cytometry section, cells were stained with DRAQ7 (a DNA intercalator) and TuJ1 conjugated to Alexa Fluor 488. Positive cells exhibiting increased ratios of forward- or side-scatter area to width were considered doublets/cell aggregates, as verified by increased DRAQ7 positivity. To approximate this approach using mass cytometry, proportions of cells exhibiting high positivity for non-barcode-specific palladium isotopes, low barcode separation distance (indicating cell aggregates/doublets occurring because of immunocytochemical processing), and/or off-center signals (indicating abnormally dense metal ion contents of potential doublets/aggregates occurring in the original “single-cell” suspension) were quantified.

To test the robustness of our method to identify (and exclude) cell doublets and aggregates by mass cytometry, differences between relative abundances of doublets quantified by flow and mass cytometry were compared for ages and brain regions using

Student's t-test. Of the 42 ages/brain regions analyzed (four were excluded because of a lack of paired samples), none exhibited a significant difference ($p > 0.09$) in proportions of doublets identified by mass or flow cytometry. Moreover, Wilcoxon test of all paired samples revealed no significant difference between proportions of doublets/cell aggregates identified by flow cytometry and mass cytometry ($p = 0.078$, Fig. 7h).

Statistics and reproducibility

No statistical method was used to predetermine sample size. No data were excluded from analyses and experiments were not randomized. The investigators were not blinded to allocation during experiments or outcome assessments.

Results

Classification of cells in the developing mouse brain by mass cytometry

To characterize single cells in the developing brain by their protein expression signatures, we first adapted mass cytometry for brain tissue by optimizing dissection and cell dissociation techniques for single-cell analysis (Methods, Extended Data Fig. 1a–f), and developed a 40-antibody staining panel for specific cell types in the brain (Extended Data Table 1). The antibody panel includes general markers of neural identity (CD24, N-cadherin, Cux1), neuronal development [doublecortin (DCX), β-tubulin III (TuJ1), NeuN, microtubule-associated protein 2 (MAP2), glutamic acid decarboxylase 65 (GAD65), Tbr2, NeuroD1, Ctip2, Tbr1], glial development [A2B5, brain lipid-binding protein (BLBP), glial fibrillary acidic protein (GFAP), glutamate/aspartate transporter 1 (GLAST), Olig2, OligoO4, Sox10, platelet-derived growth factor α (PDGFRα)], leukocytes and microglia

(CD45, CD11b, Ly6C, F4/80), and vascular cells (CD31, vascular cell adhesion molecule (VCAM), melanoma cell adhesion molecule (MCAM), PDGFRβ]. We also included markers of NSCs and progenitor cells (Sox1, Sox2, nestin, Pax6, polysialylated-neuronal cell adhesion molecule (PSA-NCAM), CD133, stage-specific embryonic antigen-1 (SSEA1)], cell signaling and proliferation [Ki67, TrkB, p75 neurotrophic receptor (p75NTR)], and apoptosis (cleaved caspase 3). As annotated in Extended Data Table 1, many of these markers are not restricted to a single cell type, such as BLBP, which is expressed in radial glial cells (RGCs) as well as astrocytes. Antibodies for each marker were conjugated to unique rare earth metal isotopes with Maxpar® X8 Antibody Labeling Kits (Standard BioTools, South San Francisco, CA), and then titrated to identify their optimal staining concentrations using known-positive and known-negative control cells on a CyTOF® Helios™ mass cytometer (Standard BioTools) (Extended Data Fig. 1g–i). Additional details are provided in the Methods section.

Brain samples from C57/BL6 mouse litters were collected at daily timepoints from E11.5 to P4 by dissection of timed-pregnant females (embryonic) and newborn pups (postnatal). Because E11.5 and E12.5 brains are difficult to reliably microdissect, we analyzed whole brain samples for these early ages. Brains aged E13.5 and older were microdissected into the telencephalon, diencephalon, mesencephalon, and rhombencephalon; for each litter, tissues from each brain region were pooled prior to dissociation as shown in Figure 1a. Following mechanical and enzymatic dissociation (Methods), single-cell suspensions were briefly incubated with cisplatin as a non-cell-permeant viability stain(Fienberg et al., 2012), fixed with 1.6% paraformaldehyde (PFA), and stored at -80°C. For mass cytometry

analysis, cell samples were thawed and labeled with palladium barcodes (Zunder et al., 2015a), followed by pooling into barcode sets for uniform antibody staining.

After mass cytometry measurement, the resulting 37,913,425 cell events were pre-processed to isolate viable single cells. Briefly, pre-processing steps included: 1) bead normalization (Finck et al., 2013) (Extended Data Fig. 2a); 2) debarcoding (Zunder et al., 2015a; Fread et al., 2017) (Extended Data Fig. 2b–d); 3) clean-up gating to remove cell doublets, aggregates, dead cells, debris, calibration beads, and other metal contaminants (Extended Data Fig. 2e–j; www.cytobank.org); 4) batch correction(Schuyler et al., 2019) (Extended Data Fig. 2k–m); and 5) marker scaling (Extended Data Fig. 2n). As detailed in the Methods section, batch correction was necessary to correct for minor variability in antibody signals resulting from the use of three separate antibody cocktails to stain the seven barcoded sets, which varied slightly in total numbers of cells. These preprocessing steps resulted in 24,290,787 high-quality, viable, singlet cells from 112 samples of C57/BL6 mice, with at least two biological replicates (n = 2–4 litters) analyzed for each age and brain region (Supplementary Table 1). Kruskal-Wallis testing of marker variances in the processed sample replicates reveals that expression of an individual marker significantly varied ($p < 0.05$) in 94 (5.1%) of 1840 comparisons (40 markers × 46 sample types; Extended Data. Fig. 2o).

To identify and categorize cell populations in the mouse brain throughout development and across brain regions, we performed Leiden clustering (Traag et al., 2019) on all samples and visualized the results on a 2D Uniform Manifold Approximation and

Projection (UMAP) layout (McInnes et al., 2018). An initial round of Leiden clustering yielded 22 clusters (Extended Data Fig. 3a–d), which were manually grouped by protein expression profile into six subsets: NSCs and progenitors, neurons and neuronal progenitors, glial progenitors and precursors, oligodendroglia and contaminating non-brain neural cells, endothelial and other nonneural cells, and hematopoietic cells. A second round of Leiden clustering on these six subsets yielded 85 distinct clusters in total (Fig. 1b; Extended Data Fig. 3e), each with a unique age profile [Fig. 1b (left inset), Extended Data Fig. 3f], distribution throughout the brain [Fig. 1b (right inset), Extended Data Fig. 3g], and protein expression pattern (Fig. 1c). As outlined in the Method**s** section, these properties were used to identify the following major cell classes: NSCs (4.99%), intermediate neuronal progenitors (INPs, 4.45%), neuronal progenitors (8.56%), putative excitatory neurons (14.45%), inhibitory neurons (17.45%), RGCs/glial precursors (5.65%), Olig2^{mid} neural progenitor cells (Olig2^{mid} NPCs, 5.01%), Olig2^{mid} glial precursors (13.19%), OPCs (2.61%), nonneural cells (5.96%), endothelial cells (5.18%), mural cells (0.03%), microglia/macrophages (8.37%), other hematopoietic cells (0.56%), non-brain-derived neural cells (0.39%), apoptotic cells (0.99%). Overall, 97.84% of all cells examined were classified as specific cell types, with the remaining 2.16% categorized as low-complexity cells (Methods). Consistent overlap of biological replicates in UMAPs for each sample type (Extended Data Fig. 3h) indicates that the layout was not overtly biased by any individual sample. Moreover, overlap of replicates in a UMAP generated using only the seven universal samples (Extended Data Fig. 3i–k) suggests technical variability only occurred in a subset of early neuronal cells.

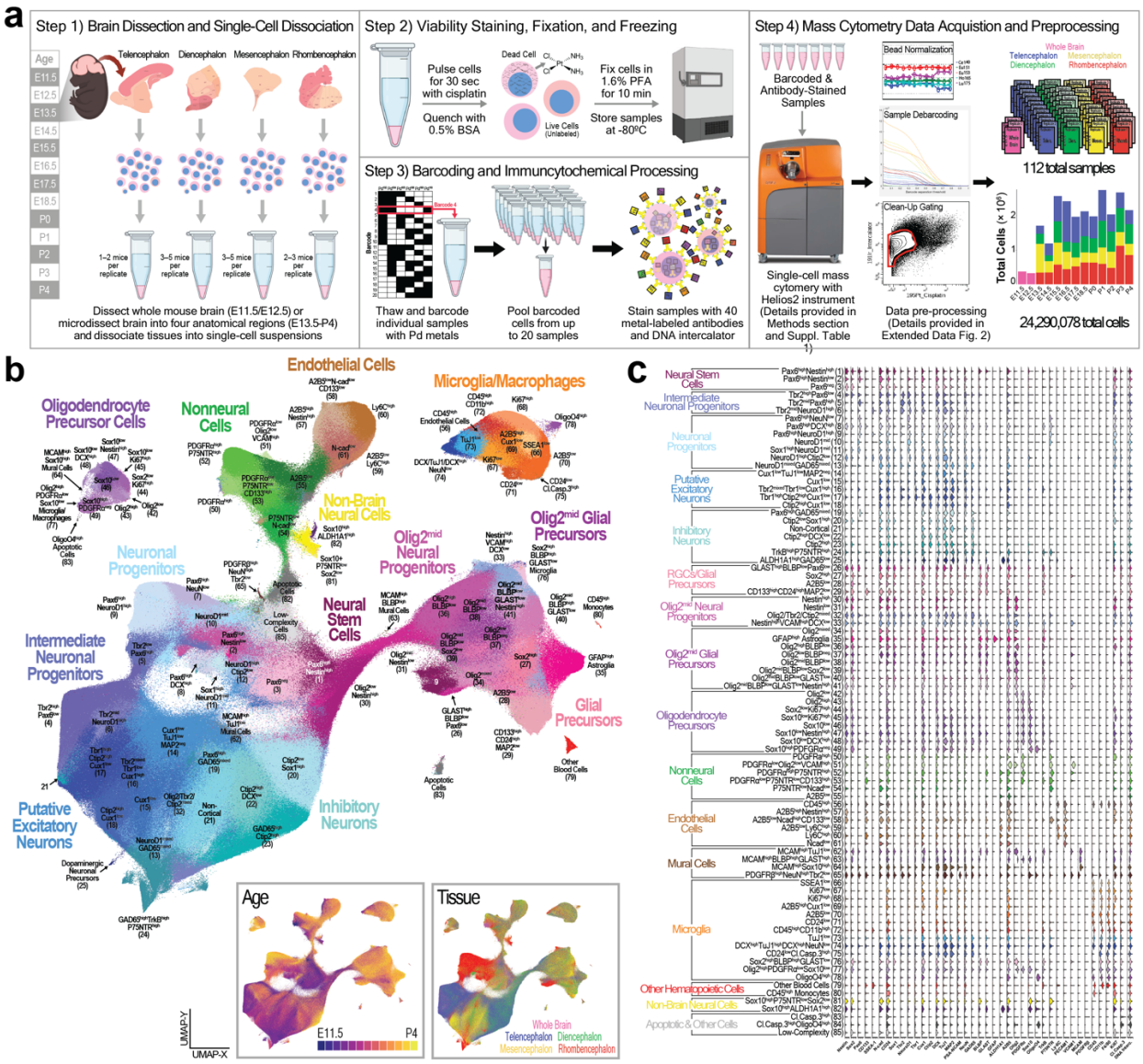

Figure 1. Classification of cells in the developing mouse brain by mass cytometry. a, Overview of workflow for isolating and processing single cells from developing mouse telencephalon, diencephalon, mesencephalon, and rhombencephalon for mass cytometry and high-dimensional analysis. Inset bar graph shows numbers of cells analyzed for each age (E11.5–P4) and brain region (n = 2–4 litters per age, 112 samples, 24,290,078 cells total). **b**, UMAP of Leiden clustering of all samples colored by cluster with insets colored by developmental age and tissue origin. An equal number of randomly sampled cells (1.25×10^5) was analyzed for each sample type, yielding a total of 5.75×10^6 cells. **c**, Violin plot showing expression of all 40 markers in the 85 identified clusters. Clusters are arranged according to class and molecular profile.

Corroboration of mass cytometry protein measurements by immunohistochemistry

To validate our ability to reliably identify brain cells and evaluate the potential for systemic bias resulting from cell enrichment or loss during single-cell dissociation, we compared relative abundances of cells positive for BLBP, Ctip2, Olig2, or Sox2 assessed by mass cytometry with those quantified using immunohistochemistry (IHC) and confocal fluorescence microscopy. Both UMAPs overlaid with expression of individual markers and representative IHC images show that protein expression varies considerably across cell types and ages (Fig. 2a, Extended Data Fig. 4a). Quantification of the relative percentages of cells positive for each marker (Fig. 2b–e) was performed by dividing the number of cells whose expression exceeded a threshold value (Extended Data Fig. 4b) by the total number of cells using customized R scripts and QuPath (Bankhead et al., 2017) software.

Proportions of cells expressing BLBP, Ctip2, Olig2, and Sox2 measured by mass cytometry and IHC (Fig. 2b–e) were largely congruent. Although trends for proportions of Olig2-expressing cells were nearly identical, values for IHC were slightly lower than those measured by mass cytometry, likely because the former represents quantification of a dorsal region of cortical tissue slices while the latter represents quantification of Olig2-expressing cells distributed throughout both dorsal and ventral areas of the cortex. Similarly, the relatively low proportions of Sox2-expressing cells measured by mass cytometry compared with IHC at E13.5 reflect that the imaged regions of cortical tissue slices contain large areas of ventricular/subventricular zones, which are enriched for

Sox2-expressing cells at this age, whereas mass cytometry results again reflect the entire tissue.

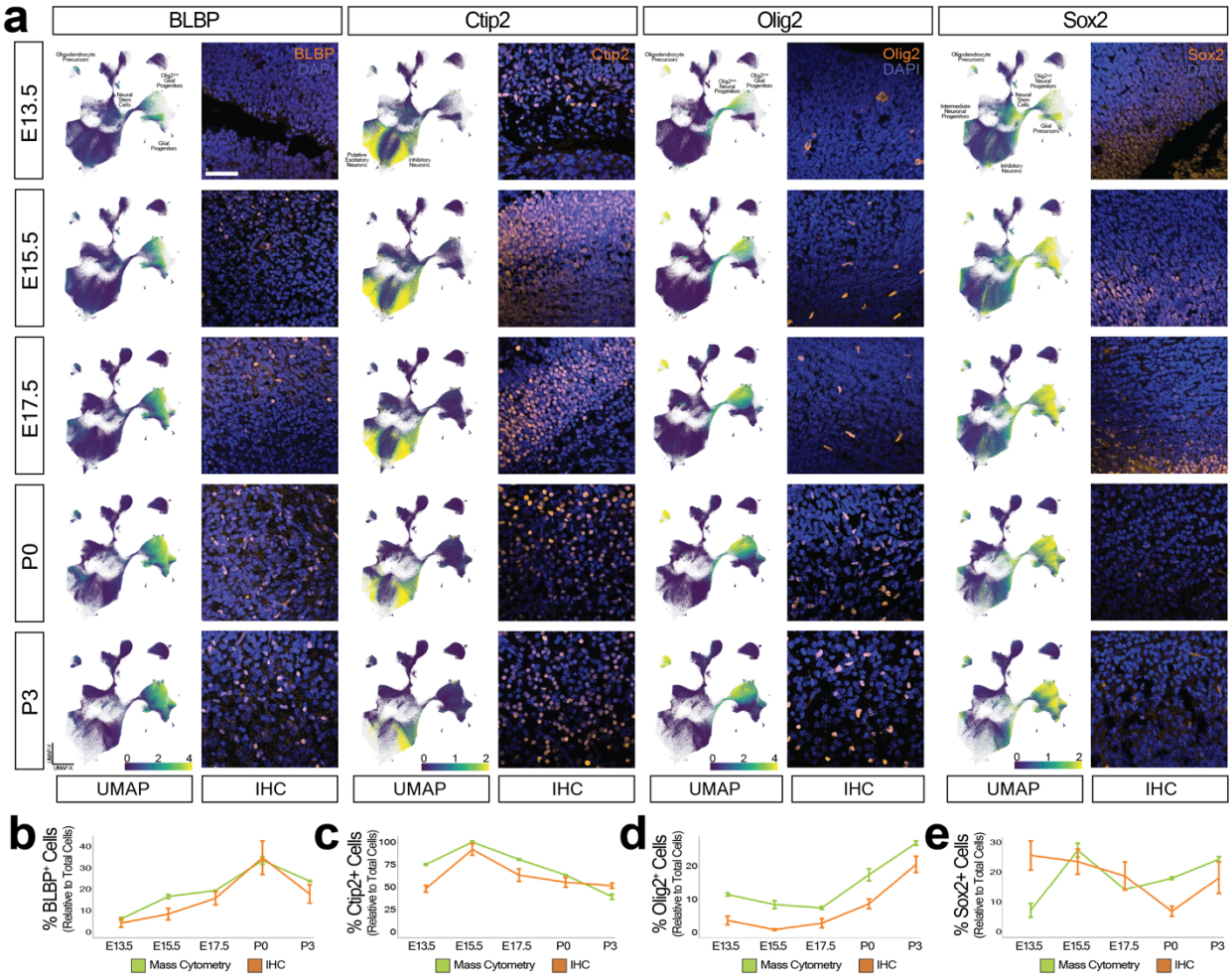

Figure 2. Corroboration of mass cytometry protein measurements by immunohistochemistry (IHC). **a**, Representative IHC of mouse telencephalon stained for BLBP, Ctip2, Olig2, or Sox2 at E13.5, E15.5, E17.5, P0, and P3. IHC images are paired with mass cytometry UMAP layouts from the corresponding age, colored by expression of the same marker. Scale bar, 20 μm. **b–e**, Proportions of cells positive for BLBP (**b**), Ctip2 (**c**), Olig2 (**d**), and Sox2 (**e**) across matching timepoints between IHC and mass cytometry. Data are presented as mean values ± s.e.m. Mass cytometry data include n = 2 litters per age, 3.75×10^5 cells total. IHC data include n = 3 litters per age, 2.07×10^6 cells total.

In combination with our previous evaluation of mouse dorsal root ganglia (Keeler et al., 2022), these corroboratory results provide evidence that mass cytometry can accurately quantify protein expression of key markers for identification of neuronal, glial, and nonneural cells in the developing mouse nervous system.

Spatiotemporal profile of cell abundances in the developing mouse brain

Transformation of the neural tube from a sheet of polarized cells (~E8.5) into the complex structure of the mouse brain (~90% of adult brain volume achieved by P14) (Orr et al., 2016) is accomplished by rapid proliferation and diversification of cells embryonically and postnatally. To explore these changes, we first used UMAPs to visualize cells present in the mouse telencephalon, diencephalon, mesencephalon, and rhombencephalon from E11.5 to P4 (Fig. 3a). Changes in the abundances of major cell types (Fig. 3b, Extended Data Fig. 5a) provide evidence for the following general trends: large proportions of NSCs and neuronal cells during embryonic ages, vast proliferation of glial cells perinatally, and steady expansion of nonneural cells across embryonic and postnatal development. In contrast to other brain regions, populations of neuronal progenitors steadily increase in the rhombencephalon, consistent with previous reports of prolonged neurogenesis in the cerebellum postnatally (Carter et al., 2018; Wizeman et al., 2019).

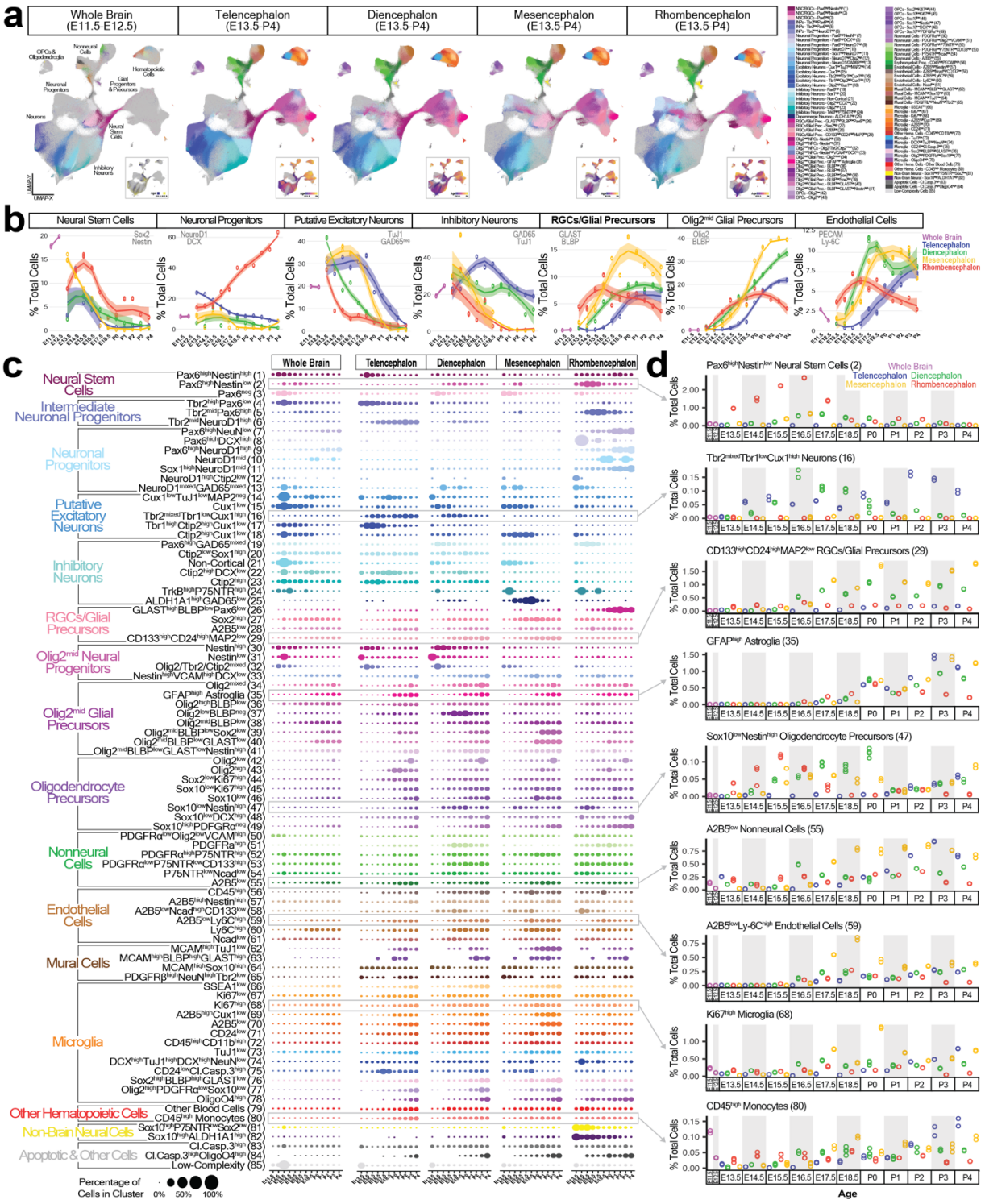

Figure 3. Spatiotemporal profile of cell abundances in the developing mouse brain. a, UMAP of Leiden clustering (from Fig. 1b) colored by cluster for indicated brain regions and ages. Insets show the same UMAP colored by age. For all UMAPs, cells from other brain regions/ages are colored gray. **b**, Relative abundances of major cell classes in each brain region from E11.5–P4. Individual replicates are

shown along with Loess curve fitting of the data. **c**, Dot plots showing relative cluster abundances at each developmental age. Results for E13.5–P4 in the whole brain plot represent the mean for all four brain regions. Results for E11.5 and E12.5 are replicated in each regional plot to facilitate comparison. **d**, Scatter plots showing relative abundances of select clusters for each sample type. Plots for all clusters are shown in Extended Data Figure 5d,e. For a–d, an equal number of randomly sampled cells (1.25×10^5) was analyzed for each sample type, yielding a total of 5.75×10^6 cells (n = 2–4 litters per age, 112 samples). The data used to generate plots in b–d are available in .csv format in the Source Data for this figure.

To further evaluate developmental trends, relative percentages of each cell type cluster were visualized in Figure 3c. Among NSCs and INPs, we observed a $Pax6^{neg}$ subset in the embryonic diencephalon and mesencephalon, while populations expressing Pax6 and Tbr2 are enriched in the telencephalon and rhombencephalon, where they ultimately produce glutamatergic neuronal lineages (Götz et al., 1998; Englund et al., 2005; Luo et al., 2021). A small fraction of $Tbr2^{mid}Pax6^{high}$ INPs in the rhombencephalon is positive for Olig2 (Fig. 1c), consistent with reports of Olig2-expressing cells in the embryonic cerebellar ventricular zone and rhombic lip (Schüller et al., 2008; Ju et al., 2016).

In line with the cerebellum containing as many as 70% of total neurons in the adult mouse brain (Herculano-Houzel and Lent, 2005), six of the seven neuronal progenitor populations are observed almost exclusively in the rhombencephalon (Fig. 3c). Although the majority presumably go on to produce cerebellar granule cells, the rare $Ctip2^{high}NeuroD1^{high}Olig2^{low}$ population observed at the earliest ages likely corresponds to early Purkinje cell progenitors, which were previously shown to express both Olig2 and NeuroD1 (Seto et al., 2014). Other putative glutamatergic and inhibitory neuron populations are distinguished by positive or negative GAD65 expression, respectively (Fig. 1c), although GAD65 is expressed by GABAergic (Kaufman et al., 1991),

dopaminergic (González-Hernández et al., 2001), and cholinergic neurons (Lozovaya et al., 2018). Two waves of Cux1^{low}TuJ1^{low}MAP2^{neg} neurons in the telencephalon (Fig. 3c) suggest that this is a transitional population [presumably derived from waves of direct and indirect neurogenesis around E13.5 and E18.5, as previously observed by Dwyer *et al*. (Dwyer et al., 2016)] that ultimately matures into the observed Cux2^{low}, Cux1^{high}, and Ctip2^{high} populations.

Three of the six GABAergic inhibitory neuron populations are predominantly observed in the forebrain and express Ctip2 (Fig. 1c), a classical marker of deep layer subcerebral projection neurons that is also expressed by Purkinje cells in the cerebellum (Leid et al., 2004) and parvalbumin, somatostatin, and 5-HT3 inhibitory neurons in layers I–V of the neocortex (Nikouei et al., 2016). Of the four observed Ctip2^{neg} GABAergic subtypes, Pax6^{high}GAD65^{mixed} cells in the embryonic diencephalon and rhombencephalon (Fig. 3c) likely correspond to inhibitory neurons in the developing dorsal white matter, which were previously found to express Pax6 (Riccio et al., 2012). Similarly, the observed ALDH1A1^{high}GAD65^{low} population likely corresponds to ventral mesencephalic dopaminergic neuron precursors, which were previously found to localize within the substantia nigra pars compacta (Tiklová et al., 2019).

RGCs/glial precursors (Olig2^{neg} cells expressing stemness markers such as Sox2, BLBP, and GLAST, but not mature neuronal or glial markers; Fig. 1c) gradually increase in proportion as the brain develops, except for a GLAST^{high}BLBP^{low}Pax6^{low} population observed almost exclusively in the rhombencephalon that rapidly expands immediately

after birth (Fig. 3c). Sox2^{high} and A2B5^{low} RGCs/glial precursors generally exhibit caudal-to-rostral expansion across the four brain regions, while a CD133^{high}CD24^{high}MAP2^{low} population [likely containing ependymal cells (Pfenninger et al., 2007)] is primarily observed in the diencephalon and mesencephalon.

The four Olig2^{mid} neural progenitor clusters likely represent cells that can give rise to neuronal and glial lineages. Two of these populations, Olig2^{mid}nestin^{high} and Olig2^{mid}nestin^{low} NSCs, express no mature neural markers (Fig. 1c) and are principally observed in the forebrain (Fig. 3c). An Olig2/Tbr2/Ctip2^{mixed} population most abundant at E14.5 likely corresponds to a mixed population of early neuronal progenitors, including early basal forebrain cholinergic neuronal progenitors regulated by Olig2 (Furusho et al., 2006). Finally, a nestin^{high}VCAM^{high}DCX^{low} population exhibiting caudal-to-rostral expansion corresponds to uncommitted Olig2-expressing neural progenitors.

Eight molecularly similar glial precursor clusters expressing Olig2 are designated as Olig2^{mid} glial precursors, including a GFAP^{high} population that expands from E16.5 in all brain regions (Fig. 3c), consistent with previous observations of “Olig2-lineage” or “OPC-derived” astrocytes (Ono et al., 2008; Huang et al., 2014; Tatsumi et al., 2018; H. Wang et al., 2021). Thus, these cells likely represent various states of intermediate glial cells (iGCs), which were previously shown to have distinct astrocytic or oligogenic potentials (Weng et al., 2019). Interestingly, only BLBP^{low}nestin^{low} Olig2^{mid} glial precursors highly expressed the proliferation marker Ki67 (Fig. 1c).

OPCs and oligodendrocytes are characterized by high Olig2 and PDGFRα expression, although one PDGFRα^{neg} OPC population expressing Sox10 was also identified, in agreement with previous reports (Spassky et al., 2001; Zheng et al., 2018). Consistent with multiple waves of OPC generation in distinct ventricular zones during embryonic development (Kessaris et al., 2006), expansion of OPC populations varies spatiotemporally (Fig. 3c). However, the eventual presence of OPCs with similar protein expression profiles by P4 in all microdissected brain regions is consistent with previously reported transcriptional uniformity of postnatal OPCs (Marques et al., 2018).

Nonneural cells (generally defined by a lack of Sox2 and neural cell markers, Fig. 1c) could not be precisely identified by our CNS-focused antibody panel, but likely contain brain fibroblasts, vascular smooth muscle cells, and other cerebrovascular cells. All six endothelial cell populations generally exhibit caudal-to-rostral expansion (Fig. 3c), including a rare subset of CD45^{low}PECAM^{high} cells resembling erythromyeloid progenitors (EMPs), a cell type previously shown to be capable of producing erythroid, myeloid, and endothelial cell lineages (Plein et al., 2018). Mural cells, characterized by MCAM and PDGFRβ expression, were sparsely present at all ages but also contain neural markers, likely due to incomplete removal of neural debris from the surface of these adhesive cells (Fig. 1c).

Microglia/macrophages displaying characteristic CD45 and CD11b expression gradually increase in proportion throughout the brain (Fig. 3c). However, many subsets also contain various neural markers (Fig. 1c), which we believe result from the established phenomena

of microglial phagocytosis (VanRyzin, 2021), as discussed below. Finally, we observed two Sox10^{high} populations exclusively in the whole brain and rhombencephalon (Fig. 3c), likely representing contaminating spinal cord and neural crest-derived cells.

To evaluate biological and technical variability in our clustering results, we evaluated the variability of identified clusters across each brain region (Fig. 3d; Extended Data Fig. 5b–d). Although some intralitter and interlitter variation is expected because of slight differences in the timing of fertilization and intrauterine environment, analysis of variance for biological replicates suggests high consistency of results overall. Generally, the highest variances are observed in neuronal populations from E11.5–P0 and glial populations from P0–P4, corresponding with periods during which these cells vastly increase in number; in contrast, low variances were observed for OPC populations at all ages. Notably, most of the smallest clusters identified (< 1000 cells or 0.016% of 5.75 × 10^6 cells; clusters 25, 56, 62–65, and 84) appeared to be mural cell doublets or nonneural cells. Because of the low abundances of these clusters and our lack of additional identifying markers, our ability to reliably detect and quantify such populations is limited.

Comparison of protein and mRNA expression patterns in the developing mouse brain

Because protein and mRNA are each subject to numerous regulatory mechanisms that control their synthesis and degradation, there is no universal method to accurately predict protein abundances from mRNA expression levels, or vice versa (Liu et al., 2016). To investigate how well mRNA expression predicts protein abundance for various classes of cells in the developing brain, we compared our antibody-based mass cytometry

measurements with age-matched (from E11.5–E18.5) and tissue-matched scRNA-seq measurements from Linnarsson and colleagues (La Manno et al., 2021) (Extended Data Fig. 6a). Our antibody panel has 34 proteins with directly comparable cognate mRNAs in the Linnarsson dataset, but other markers are not directly comparable, such as cleaved caspase 3 and the ganglioside A2B5 (Extended Data Fig. 6b). Moreover, there were minor differences in the enzymes, buffers, mechanical filtration methods, incubation times, and centrifugation speeds used to dissociate single cells for mass cytometry and scRNA-seq analyses (Extended Data Fig. 6c).

To evaluate expression levels by cell class, we first manually matched our clusters (shown in Fig. 1b,c) with those identified using scRNA-seq, resulting in 17 distinct cell classes (Extended Data Fig. 6d). Next, we evaluated percentages of cells expressing each protein-mRNA cognate pair and their normalized mean abundance levels in each class (Fig. 4a). As indicated by the size of dots in the plot, percentages of cells expressing key markers for each class are generally in agreement between mRNA and protein expression with a few notable exceptions. Although INPs are present from E11.5–P4 in all four brain regions according to protein expression, no INPs expressing Pax6, Tbr2, or NeuroD1 mRNA are observed in the mesencephalon or rhombencephalon after E12.5. In contrast, many NSCs, RGCs, and glial precursors express GLAST mRNA but not GLAST protein, and more early oligodendrocytes express Sox10 mRNA than Sox10 protein.

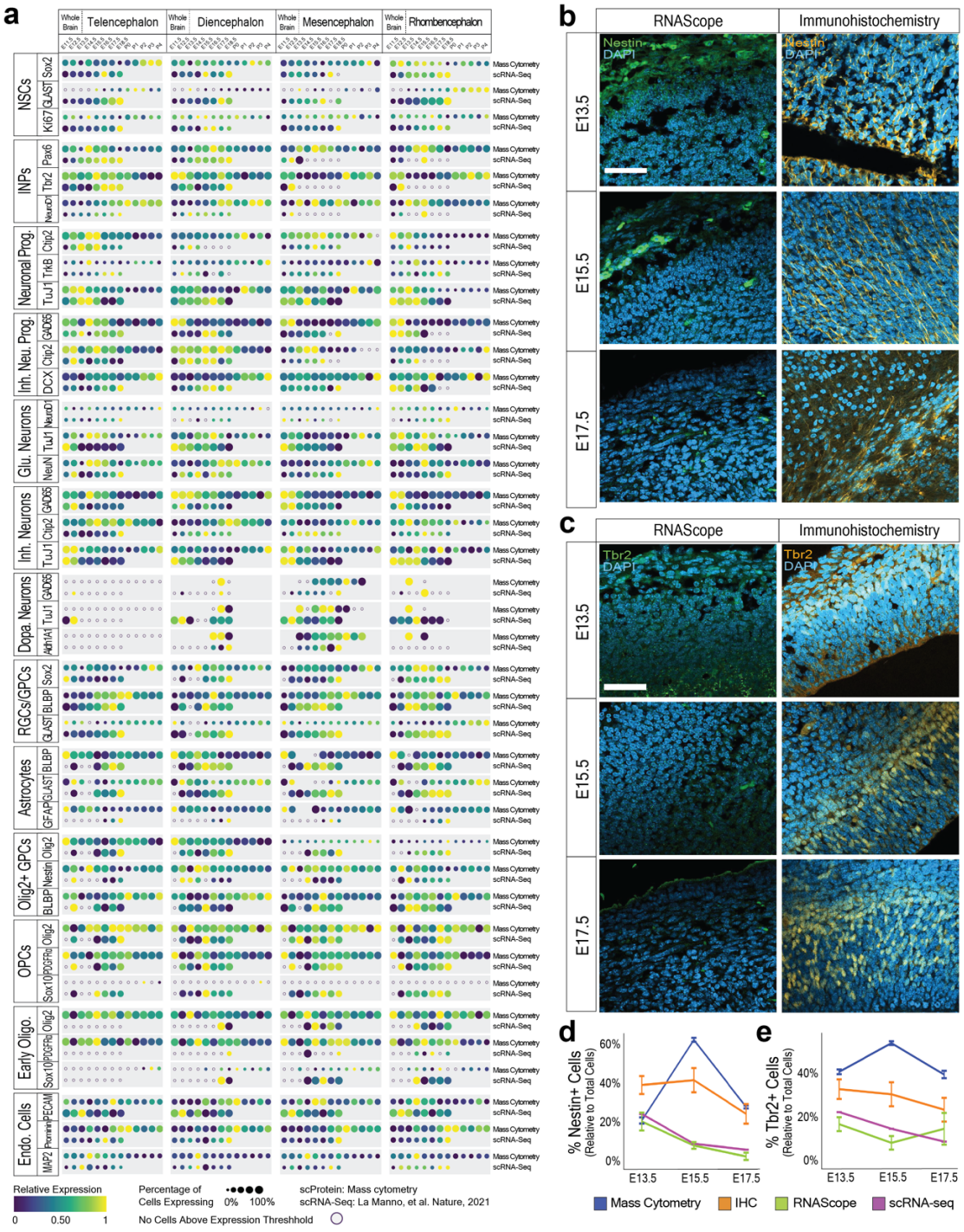

Figure 4. Comparison of protein and mRNA expression patterns in the developing mouse brain. a, Dot plot comparing protein expression evaluated by mass cytometry and RNA expression evaluated by scRNA-seq (published by La Manno et al. Nature, 2021). Select genes important for classifying cell type identities are shown. For mass cytometry data, results for E11.5 and E12.5 are replicated in each plot because they were normalized separately for comparison with each region; n = 2–4 litters per age for a total of 5.75 × 10^6 cells from 112 samples were analyzed. For scRNA-seq data, n = 1–3 litters per age for

a total of 1.92 × 10^5 cells from 75 samples were analyzed. Overlapping samples and clusters are outlined in Extended Data Figure 6. **b**,**c**, Representative images of RNAScope™ and IHC of nestin (b) and Tbr2 (c) in mouse telencephalon at E13.5, E15.5, and E17.5. Scale bar, 50 µm. **d**,**e**, Quantification of proportions of nestin-positive cells (c) and Tbr2-positive cells (d) in mouse telencephalon at E13.5, E15.5, and E17.5 by mass cytometry, IHC, RNAScope, and scRNA-seq. For d and e, mass cytometry (CyTOF) data include n = 2 litters per age, 3.75 × 10^5 cells total; IHC data include n = 3 litters per age, 1.33 × 10^5 cells total; RNAScope data include n = 3 litters per age, 3.87 × 10^4 cells total; and scRNA-seq data include n = 1–3 litters per age, 2.27 × 10^4 cells total.

The highest levels of mRNA expression tend to precede or coincide with the highest levels of protein expression for many markers (Fig. 4a). In particular, mRNA and protein expression levels of certain transcription factors (e.g., Pax6 and Ctip2), neurofilaments (e.g., DCX, MAP2, and TuJ1), and enzymes (e.g., ALDH1A1 and GAD65) are concordant. In contrast, mRNA and protein expression levels of most cell surface markers (e.g., GLAST, PDGFRα, PECAM, and TrkB) are poorly related, potentially due to biological factors (e.g., numerous cellular processes involved in generating and properly localizing cell surface receptors) or technical artifacts (e.g., dropout of low-abundance RNA transcripts).

To investigate whether the differences we observed in mRNA and protein expression at the single-cell level are corroborated by alternative methods, we analyzed nestin and Tbr2 expression in the mouse telencephalon by IHC and RNAscope™ (Fig. 4b,c), and compared percentages of cells expressing nestin and Tbr2 measured by mass cytometry, IHC, scRNA-seq, and RNAscope. At E13.5, both mass cytometry and IHC indicate that higher proportions of cells express nestin protein compared with nestin mRNA measured by RNAscope and scRNA-seq (Fig. 4d). Both mass cytometry and IHC results exhibit a

trend of increasing proportions of cells expressing nestin protein from E13.5 to E15.5, followed by a substantial decline of 25%–50% between E15.5 and E17.5. In contrast, percentages of cells expressing nestin mRNA assessed using scRNA-seq and RNAscope demonstrate a consistent decrease from E13.5 onwards. Similar to nestin, percentages of cells expressing Tbr2 protein were consistently higher than percentages expressing Tbr2 mRNA at all ages examined (Fig. 4e). The microscopy-based IHC and RNAscope measurements corroborate single-cell measurements and comparison between cognate protein and mRNA levels, even though these would not be expected to match perfectly, because they only measure tissue sections rather than the entire tissue with characteristic heterogeneity of spatial organization.

Differentiation trajectories of Sox2^{high}nestin^{high} cells in the developing mouse brain

We next investigated how the molecular profile of NSCs, RGCs/glial precursors, and intermediate progenitors changes over the course of development and between brain regions. Because cells positive for stem cell markers were distributed across a large number of clusters (Extended Data Fig. 4a), this subset of cells was isolated by gating on two canonical NSC markers: Sox2 (Avilion et al., 2003; Ellis et al., 2004; Hutton and Pevny, 2011; Okita et al., 2007; Suh et al., 2007; Yu et al., 2007) and nestin (Lendahl et al., 1990; Mignone et al., 2004; Park et al., 2010) (Fig. 5a). Sox2^{high}nestin^{high} cells display the highest abundance at E14.5, reach a nadir around E18.5/P0, and increase postnatally (P1–P4) in all brain regions, although relative proportions of postnatal NSCs and RGCs/glial precursors vary between regions (Fig. 5b). The first embryonic wave of NSCs expresses neurogenic markers such as Tbr2, NeuroD1, DCX, and TuJ1; while the second

postnatal wave expresses glial markers such as BLBP, GLAST, and GFAP (Fig. 5c), consistent with a neurogenic to gliogenic switch of NSC fates in the developing brain before birth (Qian et al., 2000; Gao et al., 2014).

To identify cell populations in the NSC/RGC/glial precursor compartment, we performed two rounds of Leiden clustering on Sox2^{high}nestin^{high} cells (first round results are shown in Extended Data Fig. 7a,b). The resulting 43 neural cell populations include three distinct clusters of NSCs (Pax6^{high}, Olig2^{low}, and Pax6^{neg}), two INP clusters (Tbr2^{high}Pax6^{low} and Tbr2^{high}NeuroD1^{low}), 17 clusters of neuronal progenitors, and 22 clusters representing various glial progenitors (Fig. 5d; Extended Data Fig. 7c–e). In addition, three PECAM^{high} populations and small populations of mural cells, microglia/macrophages, apoptotic cells, and contaminating non-brain cells were observed. Generally, these clusters molecularly resemble those described in Figure 1.

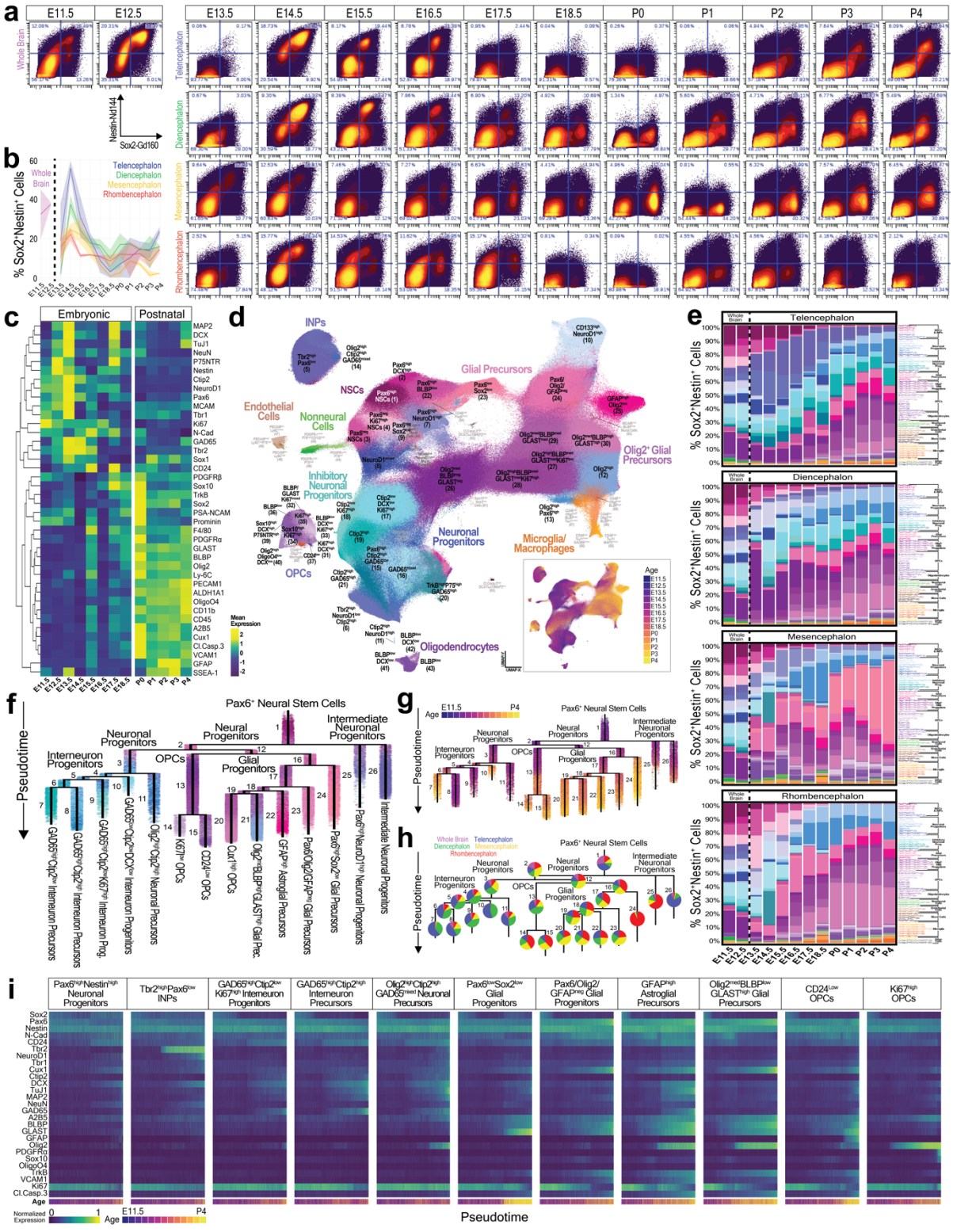

Figure 5. Differentiation trajectories of Sox2^{+}Nestin^{+} cells in the developing mouse brain. **a**, Biaxial plots showing gating of Sox2^{+}Nestin^{+} cells with CytoBank. Percentages of cells in each quadrant are shown. n = 2–4 litters per age for a total of 2.53 × 10^{7} cells from 112 samples. Cells in the upper right quadrant

were included in subsequent analyses. **b**, Relative abundances of $Sox2^{+}Nestin^{+}$ cells in each brain region from E11.5–P4. Mean (solid line) shown along with range. **c**, Heatmap showing mean expression levels of all 40 markers in the antibody panel for each developmental age. **d**, UMAP of Leiden clustering of $Sox2^{+}Nestin^{+}$ cells colored according to cluster identity. Inset shows UMAP colored according to developmental age. For **c**–**e**, n = 2–4 litters per age, 3.25×10^5 cells total from 112 samples. **e**, Stacked bar graphs showing relative abundances of $Sox2^{+}Nestin^{+}$ clusters in each brain region from E11.5–P4. Note that results for E11.5 and E12.5 are replicated in each plot to facilitate comparison with that region. The data used to generate these plots is available in .csv format in the Source Data for this figure. n = 2–4 litters per age for a total of 3.25×10^5 cells in 112 samples. **f**,**g**, URD dendrogram colored according to Leiden clustering (**f**) and developmental age (**g**). Numbers indicate branch numbers. **h**, URD dendrogram with pie charts showing relative abundances of cells from each brain region for that branch. **i**, Heatmaps colored by marker expression for select trajectories identified by URD analysis. For **f**–**i**, n = 2–4 litters per age, 6.10×10^4 cells from 112 samples.

Evaluation of relative $Sox2^{high}nestin^{high}$ cluster abundances across brain regions (Fig. 5e) reveals that uncommitted $Pax6^{high}$, $Pax6^{low}$, and $Olig2^{mid}$ NSC-like cell populations are maintained in all brain regions from E11.5 to P4, although at relatively low proportions postnatally. The forebrain exhibits similar cell population dynamics with two major exceptions: 1) expansion of Olig2-expressing neuronal and glial progenitors begins two days earlier in the diencephalon, around E15.5; and 2) more than 30% of cells in the telencephalon from E13.5–E18.5 are $Tbr2^{high}$ INPs, a cell population not observed in other brain regions (Fig. 5e). Unlike the forebrain, which contains numerous $GAD65^{high}$ neuronal cell populations at all ages examined, GAD65-expressing neuronal progenitors are far less prevalent in the mesencephalon and rhombencephalon during late embryonic and postnatal ages, consistent with observed maturation of Purkinje cells (Beekhof et al., 2021) and expansion of other cerebellar inhibitory neuron populations after P5 (Leto et al., 2006; Miale and Sidman, 1961; Weisheit et al., 2006). Moreover, in the mesencephalon, a $VCAM^{high}Pax6^{mixed}Sox2^{mid}$ population not observed in other brain

regions rapidly expands from E17.5 to comprise over 50% of all Sox2^{high}nestin^{high} cells by P4. Similar VCAM^{high} cells reported at this stage have been described as quiescent NSCs that persist until adulthood in the lateral ventricles (Fuentealba et al., 2015) and neocortex (Yuzwa et al., 2017). At the cell-subtype level, our clustering analysis recapitulates the progressive switch from neurogenic to gliogenic NSCs (Fu et al., 2021). However, our results also demonstrate that an array of glial progenitors are already present at E13.5 and neuronal progenitors persist until after P0, albeit at much lower relative abundances in the forebrain and mesencephalon (Fig. 5e). These findings are consistent with previous reports (La Manno et al., 2016; Yuzwa et al., 2017; Rosenberg et al., 2018; Carter et al., 2018; Wizeman et al., 2019; Zhang et al., 2020; Romanov et al., 2020; La Manno et al., 2021; Sarropoulos et al., 2021), including clonal neuron, astrocyte, and oligodendrocyte progeny arising from individual RGCs genetically labeled between E10 and E13 (Gao et al., 2014).

To explore the molecular dynamics underlying specification of NSC/RGCs into intermediate progenitors, we applied URD pseudotime analysis (Farrell et al., 2018) to predict differentiation trajectories of Sox2^{high}nestin^{high} cells (excluding endothelial cells, nonneural cells, and microglia/macrophages) from all brain regions and ages (Extended Data Fig. 7f–i). We chose Pax6^{high} NSCs from E11.5 whole brain as root cells because Pax6 expression commences at the earliest point of CNS development (~E8) and acts upstream of many other factors defining neural fates [including Tbr2 (Englund et al., 2005), Olig2 (Jang and Goldman, 2011), and BLBP (Arai et al., 2005)], while neural cell

populations with mature expression profiles at P0–P4 were chosen as tip cells (Extended Data Fig. 7f).

In the resulting URD dendrogram (Fig. 5f–h), the first branchpoint separates two neuronal trajectories (cortical INPs destined to generate pyramidal neurons and Pax6^{high}NeuroD1^{high} neuronal progenitors destined to produce cerebellar granule cells) from all other neural progenitors, while the second branchpoint separates the remaining neuronal progenitors from glial progenitors. The neuronal branch (segment 3) splits further into Olig2^{high}Ctip2^{high} neuronal precursors and various inhibitory progenitor/precursor populations. Paradoxically, GAD65^{high}Ctip2^{low} and GAD65^{high}Ctip2^{high} inhibitory neuron precursors (segments 7 and 8) were NeuN^{high} embryonically and NeuN^{low} postnatally (Extended Data Fig. 7k). One possible explanation is that phosphorylation or protein-protein interactions of NeuN masked the epitope targeted by our NeuN antibody (Gusel'nikova and Korzhevskiy, 2015). Analysis of the contribution of each brain region to URD branches (Fig. 5h) predicts distinct regional biases of these neuronal progenitors: INPs (segment 26) are primarily located in the telencephalon, Pax6^{high}NeuroD1^{high} INPs (segment 25) are primarily located in the rhombencephalon, and all GAD65^{high} inhibitory neurons (segments 3–11) are primarily located in the forebrain. Differences in marker expression underlying each branchpoint are shown in Extended Data Figure 7k,l.

The glial branch (segment 12) of the URD lineage hierarchy splits into two sub-branches: Olig2^{high} cells predicted to only give rise to OPCs, and Olig2^{low} cells predicted to

differentiate into both OPC and astroglial lineages (Fig. 5f). Olig2^{high} committed OPC progenitors (segment 13) only branch again much later in pseudotime, while Olig2^{low} glial cells (segment 16) branch early in pseudotime to separate Pax6^{high}Sox2^{high} glial precursors from the remaining glial cells. These remaining glial cells subsequently branch into Pax6/Olig2/GFAP^{neg} glial progenitors, GFAP^{high} glial precursors, Olig2^{mid}BLBP^{high}GLAST^{high} glial precursors, and Cux1^{high} OPCs (Fig. 5f). By this analysis, cells in segments 16–18 are predicted to be bipotent iGCs capable of producing both astrocytes and oligodendrocytes (Cai et al., 2007; Fu et al., 2021). In contrast to neuronal progenitors, cells in glial trajectories (segments 12–23) are predicted to more evenly represent the four microdissected brain regions, with the exception of BLBP^{high}GLAST^{high} RGCs/glial progenitors (segment 24), which were observed almost exclusively in the rhombencephalon (Fig. 5h) and likely represent Bergmann glia, as previously described by Heng *et al*. (Heng et al., 2017). Proportions of OPCs in three of the four terminal OPC branches (segments 14, 15, and 21 but not 20) display a pattern of rhombencephalon > mesencephalon > diencephalon > telencephalon, therefore predicting a generally caudal-to-rostral pattern of early OPC maturation that mimics myelination patterns in mouse (Kanfer et al., 1989; Verity and Campagnoni, 1988) and human brain (Inder and Huppi, 2000; Jakovcevski and Zecevic, 2005).

Analysis of protein expression levels along URD pseudotime trajectories predicts the relative timing and sequence of molecular transitions contributing to cell specification (Fig. 5i, Extended Data Fig. 7m). As expected, the INP trajectory is defined by Tbr2 expression; inhibitory neuron trajectories are distinguished by GAD65 and neuronal filaments

(commencing with DCX); and glial precursors sequentially express A2B5, BLBP, and GLAST, followed by GFAP in $GFAP^{high}$ glial precursors and Olig2 in $Olig2^{med}BLBP^{high}GLAST^{high}$ glial precursors. α

Differentiation trajectories and molecular dynamics in the telencephalon

Expanding our trajectory analysis beyond progenitors to include the maturation of neuronal and glial cells, we performed Leiden clustering on E11.5–E12.5 whole brain and E13.5–P4 telencephalon (Fig. 6a,b; Extended Data Fig. 8a–f), and analyzed the neural cells by URD using $Pax6^{high}$ NSCs from E11.5 as the root, and twelve terminal populations from P4 telencephalon as tips (Extended Data Fig. 8g–j). The predicted cell lineage hierarchy first separates neuronal cells from glial cells (Fig. 6c), with enrichment of the former during embryogenesis and the latter postnatally (Fig. 6d).

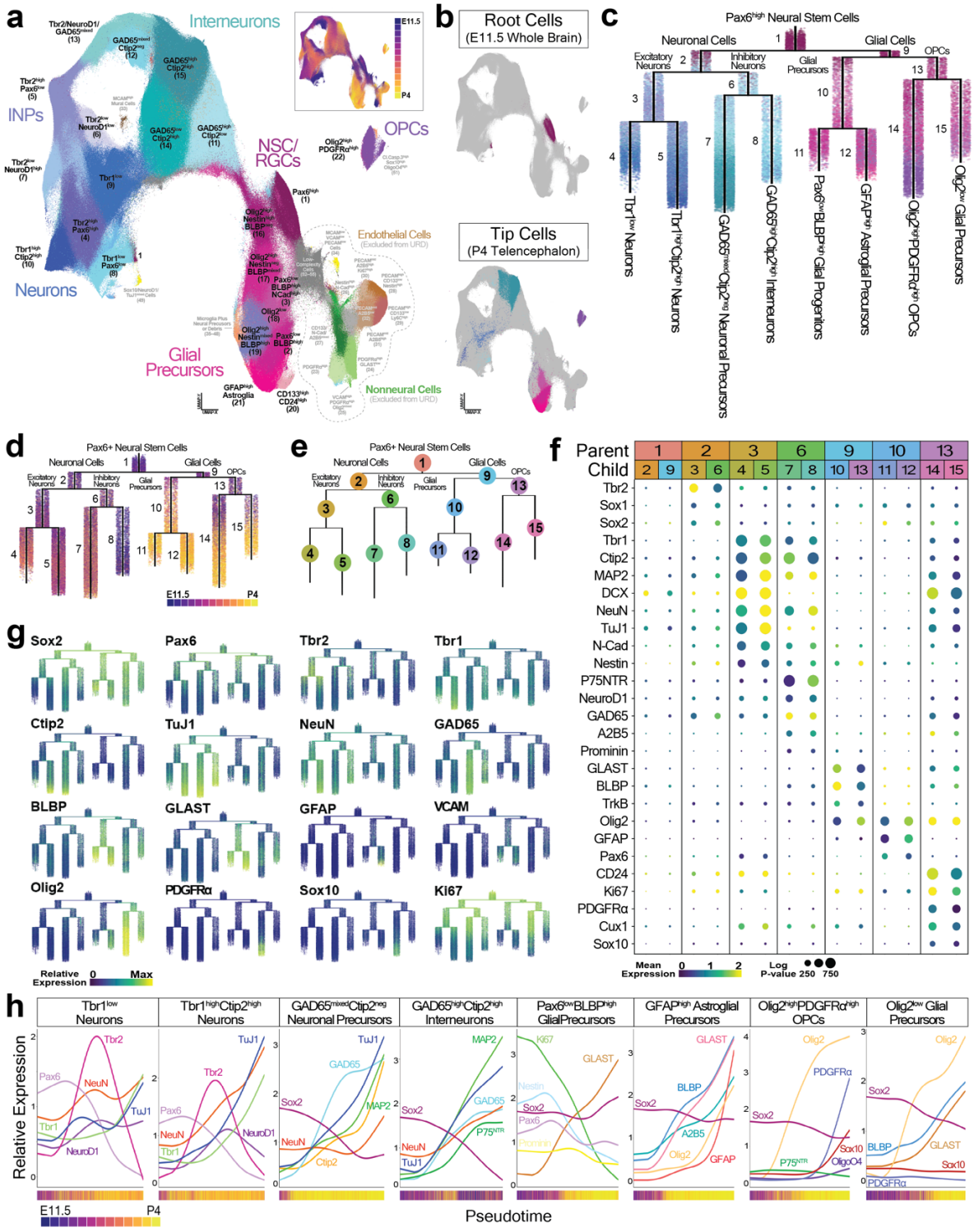

Figure 6. Differentiation trajectories and molecular dynamics in the telencephalon. **a**, UMAP of Leiden clustering of cells in the mouse telencephalon from E11.5–P4 colored according to cluster identity. Inset shows UMAP colored according to developmental age. n = 2 litters per age, 3.05 × 10^6 cells from 26 samples. **b**, UMAP of telencephalon cells chosen as the root and tips for URD analysis. **c**, URD dendrogram

colored according to Leiden cluster identity. **d**, URD dendrogram colored by developmental age. **e**, URD dendrogram with branch numbers indicated. **f**, Dot plot showing expression of markers key for the division of each branchpoint in URD analysis. **g**, URD dendrograms colored according to expression levels of select markers. **h**, Relative expression levels of proteins key for defining select molecular trajectories with URD analysis. Bars underneath graphs show median developmental ages of cells within each corresponding pseudotime bin. For **c**–**h**, n = 2 litters per age, 6.10×10^4 cells from 26 samples.

To evaluate markers underlying cell fate decisions, we evaluated the most significant differences in protein expression between child segments at each URD branch point (Fig. 6e,f). Neuronal cells (segment 2) are distinguished from glial cells (segment 9) by expression of DCX and CD24. Neuronal trajectories first separate Tbr2^{high} excitatory neurons (segment 3) from GAD65^{high}nestin^{high} inhibitory neurons (segment 6). Next, excitatory neurons split into Tbr1^{low} upper-layer neurons (segment 4) and Ctip2^{high} deep-layer neurons expressing high levels of DCX, TuJ1, and MAP2 (segment 5), consistent with inside-out formation of the cerebral cortex (Shen et al., 2006). Inhibitory neurons split further into GAD65^{mixed}Ctip2^{neg} neuronal precursors (segment 7) and GAD65^{mixed}Ctip2^{neg} interneurons (segment 8). Similar to our URD analysis of Sox2^{high}nestin^{high} cells (Fig. 5), glial trajectories were predicted to first separate into BLBP^{high}GLAST^{high} glial progenitors (segment 10) and Olig2^{mid} glial precursors (segment 13). The former trajectory branches into Pax6^{low}BLBP^{high} glial precursors (segment 11) and GFAP^{high} glial precursors (segment 12), while the latter splits into Olig2^{high}PDGFRα^{high} OPCs (segment 14) and Olig2^{mid} glial precursors (segment 15).

Inspection of key proteins across the URD pseudotime trajectories predicts their dynamics and order of expression with improved resolution. For example, sequential expression of Pax6, Tbr2, NeuroD1, and Tbr1 is observed in the two excitatory neuron

trajectories (Fig. 6g,h; Extended Data Fig. 8k), consistent with previous reports on glutamatergic neuron development in the dorsal telencephalon (Englund et al., 2005; Telley et al., 2016). On closer inspection, we observed that Pax6 does not decrease until after Tbr2 is elevated, resulting in a subset of $Pax6^{high}Tbr2^{high}$ cells. Moreover, NeuN and TuJ1 began to rise with Tbr2, but then paused and did not increase further until Tbr2 decreases, consistent with Tbr2 temporarily inhibiting neuronal maturation by transcriptionally repressing genes associated with axonal growth and dendritic complexity (Sessa et al., 2017). A similar pause in neuronal maturation was observed in the development of $GAD65^{high}Ctip2^{high}$ GABAergic neurons (Fig. 6h; Extended Data Fig. 8k). Produced by RGCs in the ventral telencephalon, these cells do not traverse through Pax6, Tbr2, and Tbr1 stages; however, their trends for GAD65, Ctip2, and MAP2 expression suggest that a similar mechanism of temporary transcriptional repression may occur during maturation of inhibitory neurons.

Sox2 expression decreases to undetectable levels during neuronal development and maturation, but expression of this stem cell-associated transcription factor was predicted to be maintained throughout $GFAP^{high}$ glial precursor and OPC differentiation trajectories (Fig. 6g,h; Extended Data Fig. 8k). In the $GFAP^{high}$ glial precursor trajectory, A2B5, BLBP, and GLAST all increased with similar kinetics, while GFAP increased at a slower rate until Pax6 levels dropped, at which point GFAP rapidly increased. While previous studies reported that OPCs sequentially express Olig2, Sox10, PDGFRα, and OligoO4 as they mature (Lu et al., 2000; Zhou et al., 2000; Tekki-Kessaris et al., 2001), our results predict

simultaneous increases in Sox10 and PDGFRα protein levels, perhaps due to translational control or protein degradation preventing earlier accumulation of Sox10.

Microglia/macrophage expansion and putative phagocytic cargoes in the developing mouse brain

To investigate subsets of microglia/macrophages in the developing brain, $CD45^{high}$ cells from all brain regions and ages were selected by two-dimensional gating (Extended Data Fig. 9a), partitioned by Leiden clustering to identify cell subtypes, and visualized with a 3D UMAP layout to improve visualization of cell clusters (Fig. 7a). Microglia/macrophages were identified as $CD45^{mid}CD11b^{high}$ cells, but our ability to further specify cell subtypes was restricted by the inclusion of only four cell type-specific markers in our antibody panel relative to the microglia-focused panels used in previous mass cytometry studies (Mrdjen et al., 2018; Ajami et al., 2018; Li et al., 2019; Böttcher et al., 2019; Fu et al., 2020b, 2020a; Ormel et al., 2020; Xie et al., 2022). However, while lacking in cell-subtype specificity, our antibody panel enables detection and quantification of putative phagocytic cargoes, allowing us to divide microglia/macrophages into two functional subtypes: “unladen” without cargo and “cargo-laden” containing neuronal or glial markers (indicated by dashed lines in Fig. 7a). Importantly, these cargo-laden microglia/macrophages were retained as cell singlets by our gating parameters and not removed from analysis as artifactual cell doublets or aggregates (Extended Data Fig. 2e–j).

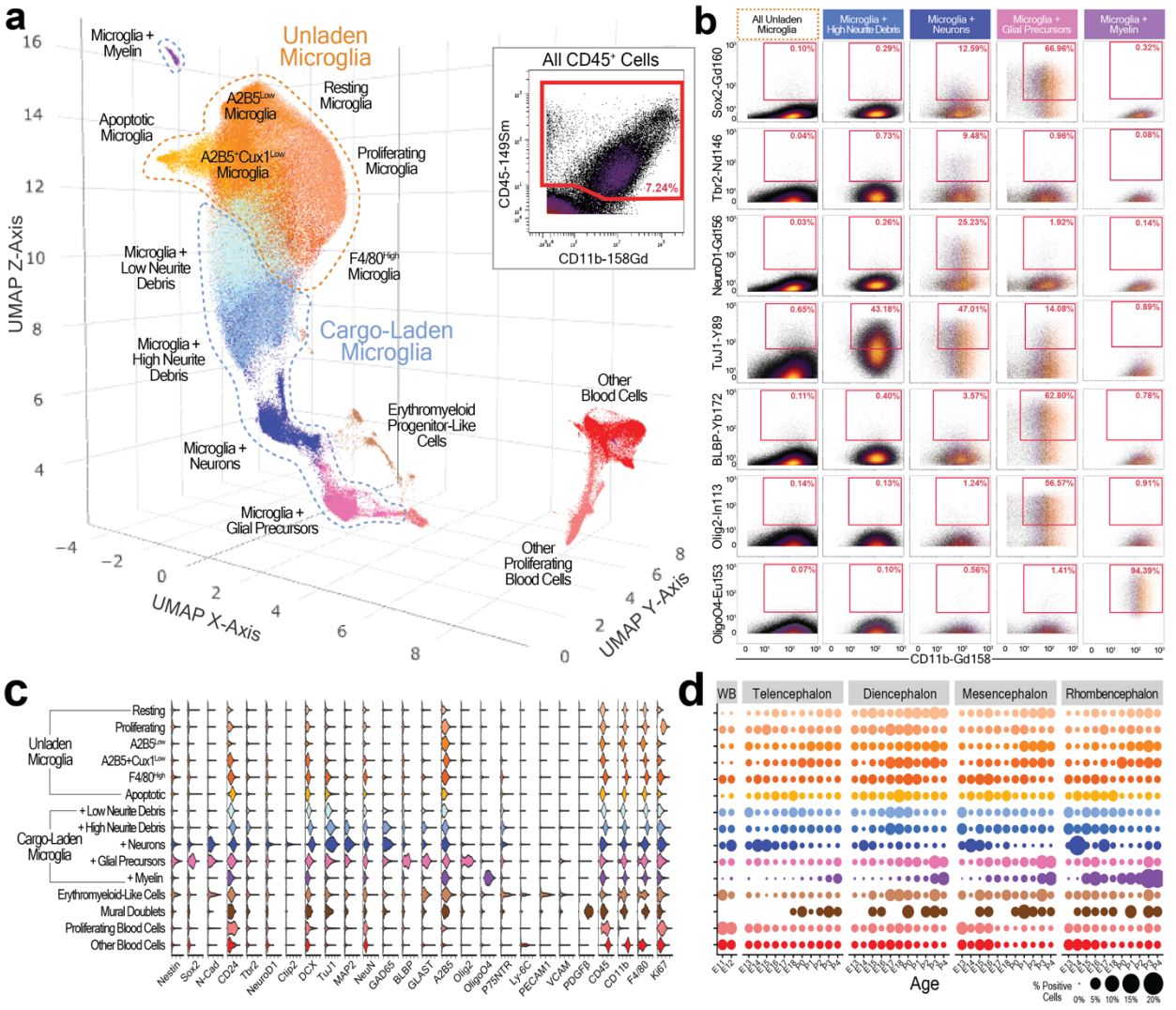

Figure 7. Microglia/macrophage expansion and putative phagocytic cargoes in the developing mouse brain. a, Three-dimensional UMAP of CD45$^+$ cells colored according to Leiden cluster identity. Dashed lines indicate grouping of microglia into non-interacting (orange) and interacting (blue) clusters. Inset shows gating of CD45$^+$ cells using CytoBank. Cells inside the red box were included in analysis. **b**, Biaxial plots showing relative abundances of cells positive for select neural proteins. **c**, Violin plot showing expression of select proteins key for distinguishing functional macrophage/microglia subpopulations in the developing mouse brain. **d**, Dot plot showing relative abundances of CD45$^+$ clusters in each brain region from E11.5–P4. n = 2–4 litters per age/brain region, 1.756 × 10^6 cells from 112 samples.

Evaluation of the microglia/macrophage marker CD11b with key markers of neuronal cells (Tbr2, NeuroD1, and TuJ1) and various glial populations (Sox2, BLBP, Olig2, and

OligoO4) reveals discrete patterns across cargo-laden microglia/macrophage clusters, whereas these markers are generally absent in all other clusters (Fig. 7b). Microglia/macrophage clusters with positive but low DCX, TuJ1, and MAP2 levels suggest engulfment of neurite debris, while clusters positive for these neurofilaments plus neuronal-related transcription factors (e.g., Tbr2, NeuroD1, Tbr1, and/or Ctip2) provide evidence for the engulfment of entire neurons (Fig. 7c, Extended Data Fig. 9b). Similarly, microglia/macrophages positive for glial and OPC markers suggest phagocytosis of these cell types, as previously reported (Li et al., 2019; Nemes-Baran et al., 2020). Microglia/macrophages positive for OligoO4 (a surface antigen of oligodendrocytes) but not other markers of OPCs/oligodendrocytes or neurites may represent myelin-engulfing microglia/macrophages (Djannatian et al., 2021; Hughes and Appel, 2020) and display caudal-to-rostral expansion mirroring reported patterns of myelination in the developing mouse brain (Kanfer et al., 1989; Verity and Campagnoni, 1988). These observations are supported by the identification of mRNAs for MBP and GFAP in P7 microglia by scRNA-seq (Li et al., 2019), as well as our previous identification of presumptive cargos in immature satellite glial cells by mass cytometry (Keeler et al., 2022).

Among unladen microglia/macrophages, we observed Ki67^{high} proliferative cells, cleaved-caspase 3^{high} apoptotic cells, and several states without further defining characteristics other than varying expression levels of F4/80, A2B5, and Cux1. Although relative abundances of unladen microglia/macrophages generally increase as brain development progresses (Fig. 7d), we observed more distinct trends for phagocytic microglia/macrophages: a consistent increase after E15.5 in the telencephalon, a plateau

after E17.5 in the diencephalon, two waves of expansion before and after birth in the mesencephalon, and one wave of expansion centered around birth in the rhombencephalon.

To investigate whether these observations represent single-cell events or cell aggregates, we quantified the extent of cell doublets and aggregates in our single-cell samples by two methods: flow cytometry with a DNA intercalator to identify cell events with greater than 4n DNA content (Extended Data Fig. 9c), and the 6-choose-3 doublet-filtering scheme used for mass cytometry barcoding (Extended Data Fig. 9d), whereby any cell event with greater than three palladium metals must contain cells from more than one barcoded sample (Zunder et al., 2015a). As measured by both methods, the frequency of cell doublets or aggregates in samples (before pre-processing) did not exhibit any noticeable trend across age or tissues (Extended Data Fig. 9e,f). In contrast, observed frequencies of both unladen and cargo-laden microglia/macrophages vary across ages and brain regions. Unladen microglia/macrophages generally increase in abundance with age in the forebrain and mesencephalon, although their numbers plateau in the rhombencephalon (Extended Data Fig. 9g). Cargo-laden microglia/macrophages increase with age in the telencephalon, plateau early in the diencephalon, display two waves centered around birth in the mesencephalon, and apex before birth in the rhombencephalon (Extended Data Fig. 9h). Notably, relative abundances of both unladen and cargo-laden microglia/macrophages were lowest in the rhombencephalon. These differences in frequency from known doublets and aggregates, coupled with the established propensity of microglia/macrophages for phagocytosis during brain

development (VanRyzin, 2021), suggest our observations represent *bona fide* phagocytic events for microglia/macrophages in the developing brain.

Discussion

In this study, we adapted mass cytometry for single-cell profiling of brain tissues to produce a protein-based cell atlas of the developing mouse telencephalon, diencephalon, mesencephalon, and rhombencephalon. Using sample replicates acquired daily across embryonic and postnatal development, we identified molecularly distinct cell populations, quantified their variability, and modeled their differentiation trajectories. As a resource, the companion dataset to this manuscript recapitulates decades of neural development research, characterizing the molecular profile and timing of appearance of virtually every major cell type, from progenitor cells, neurons, astrocytes, and oligodendrocytes, to microglia/macrophages, vascular cells, and other nonneural cell types (as summarized in Figure 8). In addition to recapitulating previous studies, our survey of the developing mouse brain provides novel insights into: 1) abundances and timing of rare neuronal and intermediate glial cell populations, 2) variations in timing between protein and mRNA levels during brain development, 3) expression of Sox2 and nestin across a wide variety of cell types, including endothelial cells, 4) two potentially distinct differentiation trajectories for generation of OPCs (direct-differentiating and iGC-derived), 5) molecular dynamics underlying specification of glutamatergic neurons in the telencephalon, and 6) cargo-laden microglia/macrophages in the developing brain.

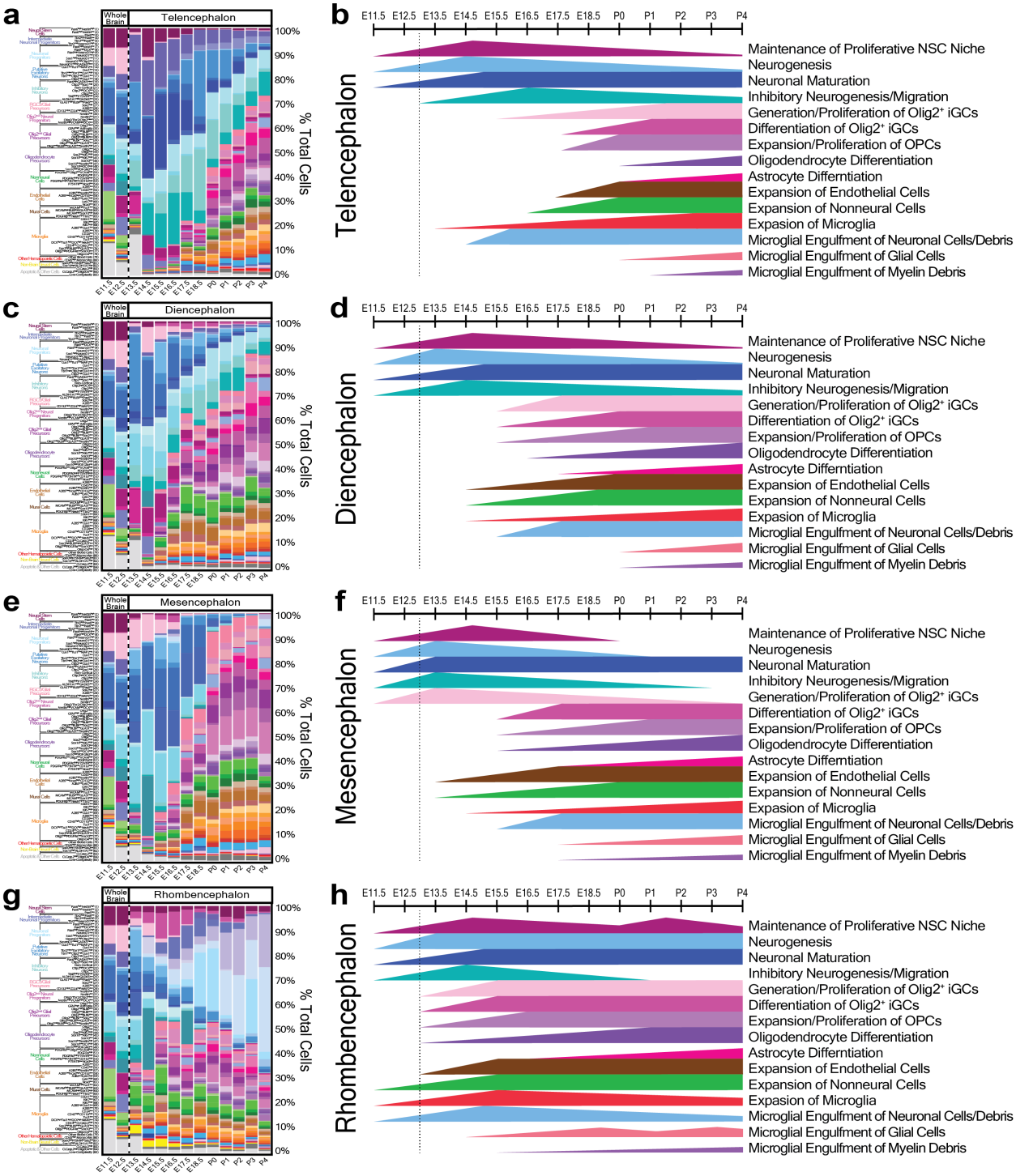

Figure 8. Overview of key processes in mouse brain development. Relative cluster abundances and schematics of major processes involved in development of the mouse telencephalon (**a**,**b**), diencephalon (**c**,**d**), mesencephalon (**e**,**f**), and rhombencephalon (**g**,**h**) from E11.5–P4. Note that results for E11.5 and E12.5 whole brain are replicated in each plot to facilitate comparison with that region.

Reminiscent of our previous observation of putative phagocytosis by satellite glial precursors in the dorsal root ganglia (Keeler et al., 2022), a fortuitous result of this study was the observation of putative phagocytic cargoes in microglia/macrophages. Phagocytosis by microglia plays an important role in brain development (Paolicelli et al., 2011; Squarzoni et al., 2014; Hughes and Appel, 2020), homeostasis (Li et al., 2019), injury (Hammond et al., 2019), and disease (Derecki et al., 2012). Notably, our findings suggesting phagocytosis of myelin by microglia/macrophages at embryonic ages represent the earliest description of this developmental phenomenon, corroborating recent findings in zebrafish, P10 mouse optic nerve, and P14 mouse brain (Hughes and Appel, 2020; Djannatian et al., 2021). Clean-up gating and doublet analysis suggest that it is unlikely the putative phagocytic cargoes observed here are due to cell doublets or larger aggregates. Future studies could provide a more detailed view of microglial subtypes and their phagocytic behavior by employing a hybrid antibody panel including additional markers to define microglial subpopulations (Mrdjen et al., 2018; Ajami et al., 2018; Li et al., 2019; Ogrodnik et al., 2019; Dusoswa et al., 2020; Zilkha-Falb et al., 2020; Li et al., 2021; Xie et al., 2022), as well as markers of phagocytic activity and cargoes. With additional validation and characterization, this approach to quantify phagocytic cargoes could be extended beyond microglia/macrophages to “non-professional” phagocytes like neural crest cells (Zhu et al., 2019). While the antibody panel used in this study was not designed to probe microglia/macrophage subtypes, the ability to quantify cargoes within these cells provides a novel method to monitor and characterize how microglia and macrophages sculpt the developing brain with their phagocytic activity.

One caveat for single-cell analysis of neural tissues is the potential for systematic bias in the quantification of relative cell-type abundances, which could be caused by lysing or depletion of specific cell populations, or resistance of specific cell populations to enzymatic/mechanical dissociation during sample processing. For example, the relatively low numbers of cleaved-caspase 3-positive cells in our study may reflect the fragility of cells undergoing apoptosis, rather than their low abundance in the developing brain. To directly estimate losses of NSCs, neurons, glia, and OPCs during the dissociation process, we performed flow cytometry to quantify relative abundances of (DAPI-positive) cells expressing Sox2, nestin, TuJ1, or Olig2 in supernatants discarded during single-cell dissociation of P3 mouse cortex (Extended Data Fig. 1e,f). The results show that cells expressing each marker were present in all five supernatants at roughly equivalent proportions to the final sample preparation, suggesting that neural populations were not selectively enriched/depleted during our single-cell dissociation process. Moreover, immunofluorescence microscopy of age-matched tissue slices corroborated trends for cell abundances measured by mass cytometry (Fig. 2). For tissue imaging with enhanced capacity for molecular profiling, the metal isotope-labeled antibodies used in this study can also be applied for mass spectrometry-based imaging, either with imaging mass cytometry (Giesen et al., 2014) or multiplexed ion beam imaging (Angelo et al., 2014).

While the cell populations we identified by protein-based measurements show general agreement with those previously identified by scRNA-seq (La Manno et al., 2016; Kee et al., 2017; Frazer et al., 2017; Y.-J. J. Chen et al., 2017; Yuzwa et al., 2017; Mayer et al., 2018; Mi et al., 2018; Rosenberg et al., 2018; Carter et al., 2018; Tiklová et al., 2019;

Wizeman et al., 2019; Guo and Li, 2019; Zhang et al., 2020; Romanov et al., 2020; Zhou et al., 2020; Kim et al., 2020; Li et al., 2020; Ruan et al., 2021; Di Bella et al., 2021; La Manno et al., 2021; Sarropoulos et al., 2021; Turrero García et al., 2021; Lee et al., 2022), the observed differences between specific protein-mRNA pairs demonstrate the value of protein measurements to characterize and quantify functional cell states. The variety of relationships we observed between mRNA and protein abundance likely arises from a combination of many factors, such as varying rates of mRNA processing and degradation, as well as varying rates of protein translation, maturation, trafficking, and degradation; all of which can differ between specific protein-mRNA pairs, across cell types, and across developmental stages within a single cell type. For example, translational control, protein degradation, and incomplete trafficking or internalization of surface proteins may result in high levels of mRNA but no protein present. Conversely, mRNA degradation may result in high levels of long-lived proteins, but no mRNA present. Investigating these mechanisms is beyond the scope of this study, but could be investigated further by split sample measurements with mass cytometry and scRNA-seq, or with CITE-seq (Stoeckius et al., 2017) to simultaneously detect protein and RNA abundances in single cells.

The neural mass cytometry approach developed in this manuscript will enable future mechanistic studies on mouse neurological disease models, enhance characterization of genetic and pharmacological perturbations of brain development, and can also be used to study *in vitro* models of neural differentiation employing embryonic or induced pluripotent stem cells. The high sample throughput and relatively low cost of mass cytometry make it particularly attractive for larger scale studies, where increased sample

numbers allow for statistical comparisons between conditions, and increased cell numbers allow for the characterization of rare, low-frequency cell populations. Indeed, the breadth of findings presented in this manuscript are derived from a single experiment run over 3 days with barcode-multiplexed samples, demonstrating the power of mass cytometry as a high-throughput platform for single-cell analyses. Potential for further optimization includes adapting the antibody panel to measure human brain cells; at present, 27 out of 40 antibodies in our mouse CNS staining panel are cross-reactive for their respective human homologs (Extended Data Table 1). The antibody panel could also be modified to focus on specific brain regions or use with imaging mass cytometry (Giesen et al., 2014), and tissue dissociation methods could be optimized for analysis of adult tissues. Collectively, our mass cytometry analyses represent a region-specific roadmap of cell specification and maturation in the mouse brain, and provide a high-throughput, multiplexed platform to investigate fundamental mechanisms of development at the protein level.

Chapter III: Mass Cytometry Analysis of Mouse Dorsal Root Ganglia Development

The contents of this chapter were previously published as “A developmental atlas of somatosensory diversification in the dorsal root ganglia by single-cell mass cytometry.” Austin Keeler*, Amy Van Deusen*, Irene Gadani, Corey Williams, Sarah Goggin, Ashley Hirt, Shayla Vradenburgh, Kristen Fread, Emily Puleo, Lucy Jin, O. Yipkin Calhan, Christopher Deppmann, Eli Zunder. *Nature Neuroscience*. 2022;25(11):1543–1558.

Abstract

Precisely controlled development of the somatosensory system is essential for detecting pain, itch, temperature, mechanical touch and body position. To investigate the protein-level changes that occur during somatosensory development, we performed single-cell mass cytometry on dorsal root ganglia from C57/BL6 mice of both sexes, with litter replicates collected daily from embryonic day 11.5 to postnatal day 4. Measuring nearly 3 million cells, we quantified 30 molecularly distinct somatosensory glial and 41 distinct neuronal states across all timepoints. Analysis of differentiation trajectories revealed rare cells that co-express two or more Trk receptors and over-express stem cell markers, suggesting that these neurotrophic factor receptors play a role in cell fate specification. Comparison to previous RNA-based studies identified substantial differences between many protein–mRNA pairs, demonstrating the importance of protein-level measurements to identify functional cell states. Overall, this study demonstrates that mass cytometry is a high-throughput, scalable platform to rapidly phenotype somatosensory tissues.

Introduction

Somatosensory neurons residing in the dorsal root ganglia (DRG) transmit diverse sensory stimuli to the central nervous system (CNS), including mechanical pressure, changes in limb position, temperature, pain and itch. Previous studies have identified up to 13 subpopulations of mature sensory neurons in the peripheral nervous system (PNS) by the first month of development in mice and up to 18 subpopulations in adulthood (Emery and Ernfors, 2020; Lallemend and Ernfors, 2012; Li et al., 2018, 2016; Usoskin et al., 2015). Although somatosensory neurons are relatively well-characterized at maturity, many fundamental questions with respect to their development remain unresolved. In particular, intermediate progenitor cell types of the DRG remain poorly characterized, and the molecular profiles that control cell type specification have not been defined. Identifying the molecular trajectories and cell fate decisions that control DRG development promises to improve understanding of sensory disorders with developmental components, such as congenital insensitivity to pain with anhidrosis (CIPA) and autism spectrum disorder (ASD) (Orefice et al., 2019, 2016; Özkaya et al., 2014).

Previous efforts to monitor the diversification and maturation of somatosensory neurons have primarily relied either on microscopy, which detects a small number of proteins simultaneously, or single-cell RNA sequencing (scRNA-seq), which detects a large number of transcripts simultaneously. scRNA-seq and the related technique, single-nuclei RNA sequencing (snRNA-seq), have been applied to characterize the molecular diversity of cell types in a wide range of adult and developing neural tissues (Darmanis et al., 2015;

Habib et al., 2016; Macosko et al., 2015; Tasic et al., 2016; Zeisel et al., 2018), including the dorsal root ganglion (Chiu et al., n.d.; Faure et al., 2020; Finno et al., 2019; Hockley et al., 2019; Kupari et al., 2021; Li et al., 2016; Nguyen et al., 2021; Rosenberg et al., 2018; Sharma et al., 2020; Usoskin et al., 2015; K. Wang et al., 2021; Wu et al., 2021), but no study to date has measured every day of development across embryonic and postnatal timepoints. Such temporal resolution is essential if we are to determine precise lineages of both abundant and rare cell types that are responsible for somatosensory perception. In this study, we leveraged the relatively high-throughput (1×10^6 cells per hour) single-cell analysis technique—mass cytometry—to exhaustively profile the composition of the DRG at every day of development from embryonic day (E) 11.5 to postnatal day (P) 4.

Mass cytometry is a flow cytometry variant that uses rare earth metal isotope-labeled antibodies and other affinity reagents to quantify the abundance of proteins and other biomolecules at the single-cell level (Bandura et al., 2009). Commercially available reagents permit over 40 molecular markers to be measured and quantified simultaneously in each cell, including cell surface receptors and intracellular signaling molecules (Bendall et al., 2011), transcription factors (Zunder et al., 2015b), cell cycle status and proliferation state (Behbehani et al., 2012) and cell viability (Fienberg et al., 2012). Mass cytometry has been used previously to characterize glioma cells and microglia in neural tissues (Ajami et al., 2018; Friebel et al., 2020; Mrdjen et al., 2018), but, until now, it has not been applied to neurons or other glial cell types in the CNS or PNS.

To investigate DRG development with mass cytometry, we developed a 41-antibody panel including key transcription factors, neurotrophic factor receptors and other protein markers known to play a critical role in the specification and maturation of DRG cell types. We applied this panel to measure single-cell DRG samples from E11.5, shortly after the DRG have coalesced from migratory neural crest cells, to P4, when somatosensory neurons have innervated their peripheral targets and have begun to mature into distinct functional types (Lallemend and Ernfors, 2012). With this approach, we identified and quantified the abundance of 30 molecularly distinct somatosensory glia and 41 somatosensory neuron subtypes across embryonic and postnatal development in the DRG.

The 41 somatosensory neuron subtypes that we identify here show complementary overlap with postnatal DRG neurons previously identified by scRNA-seq (Emery and Ernfors, 2020; Sharma et al., 2020; Usoskin et al., 2015). However, a time course comparison reveals that mRNA transcript abundance does not accurately predict protein abundance, which is the best representation of a cell's functional state. Collectively, the findings presented in this study demonstrate, to our knowledge for the first time, that mass cytometry is a high-throughput, scalable platform for single-cell analysis of neural tissues such as the DRG.

Materials and Methods

Animals

All animal experiments were carried out in compliance with policies of the Association for Assessment of Laboratory Animal Care and approved by the University of Virginia Animal Care and Use Committee (Deppmann protocol no. 3795). Mice aged E11.5 to P4 were harvested from C57/BL6 females (Jackson Labs, 000664) bred in house. For timed pregnancies, animals were mated overnight and separated after 16 hours. Animals were housed on a 12-hour light/dark cycle with food and water ad libitum at 21 °C with 45–50% humidity. For embryonic timepoints, pregnant females from single overnight (harem set up between 17:00 and 18:00 and split between 7:00 and 8:00 the next morning) timed matings were used to ensure accurate embryo age.

Validation of antibodies

After conjugation to a specific metal isotope, each antibody was titrated using a variety of cell samples and counterstains. Antibodies that generated signal in DNA intercalator-positive cells that also correlated with one or more positive counterstains, but were absent in cells with a negative counterstain, were considered to be specific and reliable. Optimal concentrations for the discernment of relative protein expression were determined by titration to identify the concentration with the greatest separation between signal in positive controls compared to signal in negative controls while minimizing background. Optimal staining concentrations for each antibody are listed in Supplementary Table 1.

Metal conjugation of antibodies

Purified antibodies were conjugated to metals (listed in Supplementary Table 1) for mass cytometry analysis using MaxPAR antibody conjugation kits (Fluidigm) according to the manufacturer's instructions. After labeling, antibodies were diluted at least 1:2 to a final concentration ranging from 0.05 mg ml^{-1} to 0.4 mg ml^{-1} in Candor PBS Antibody Stabilization solution (Candor Bioscience) for long-term storage at 4 °C.

Dissection

Spinal cords were removed from mice aged E11.5 to P4 and placed in 35-mm Petri dishes containing Dulbecco's PBS (Thermo Fisher Scientific, 14190) on ice. DRG were plucked either off the isolated spinal cord (E11.5–E15.5) or from within the ossified vertebrae (E16.5–P4), depending on age. All DRG were collected upon dissection, including the sacral, lumbar, thoracic and cervical ganglia. Total numbers of animals and cells analyzed are listed in Supplementary Table 2.

Single-cell dissociation

After dissection, all the DRG from a whole litter (6+ pups) were transferred to a 15-ml conical filled with cold DMEM/F-12. Excess media was then removed, followed by the addition of 5 ml of Enzyme Solution 1. For tissues E15.5 to P4, Enzyme Solution 1 is composed of 5 mg ml^{-1} of BSA (Sigma-Aldrich, A9418), 2 mg ml^{-1} of Collagenase Type 2 (Worthington, LS004176), 0.2 mg ml^{-1} of DNAse-I (Sigma-Aldrich, 11284932001) and 0.2 mg ml^{-1} of hyaluronidase (Sigma-Aldrich, H3884) in DMEM/F-12. For E11.5 to E14.5 tissues, Enzyme Solution 1 was prepared as above and then diluted 1:10 in DMEM/F-12.

After 20 minutes of incubation in Enzyme Solution 1 at 37 °C, this was then removed and replaced with 5 ml of Enzyme Solution 2 (trypsin in DMEM/F-12) for tissue from E15.5 to P4. Again, E11.5 to E14.5 was treated with Enzyme Solution 2 diluted 1:10 in DMEM/F-12. The tissue was incubated for 15 minutes in Enzyme Solution 2 at 37 °C before the solution was removed, leaving a residual volume of approximately 750 µl. Serial dissociation was performed with four fire-polished pipettes with decreasing pore diameter, with approximately ten triturations per pipette.

Our comparisons to IHC and scRNA-seq indicate that, generally, we were able to retain known cell types through our workflow and analysis. We also were not able to collect tissue older than P4 with enough efficiency and yield for mass cytometry analysis, due to the abundance of myelin and debris. Alternative dissociation methods or post-dissociation clean-up may make mass cytometry analysis possible for DRG past P4, including adult tissue.

Optimizing neural dissociation and antibody validation for mass cytometry of neural tissues

This study was begun without optimized protocols for cell dissociation of dissected samples and without an optimized antibody panel for neural cell types. Without a working antibody panel, it was challenging to validate and optimize our dissection and cell dissociations, but, without high-quality dissociated samples, it was challenging to validate and optimize our antibodies. To solve this ‘chicken and egg’ problem, we adopted a bootstrapping approach, starting with a few antibodies that worked relatively well (TuJ1

and Sox2) and using these to test and optimize cell dissociation techniques for samples from various timepoints. These improved-quality samples were then used to test more antibodies, and, in this iterative manner, over many back-and-forth iterations, we were able to build up our antibody panel and improve our cell dissociation techniques to identify all the DRG cell types discussed in this study.

Cisplatin staining and fixation of cells

Final cell suspensions were mixed with 100 µl of 2× cisplatin solution (10 µM in PBS; Sigma-Aldrich, P4394) and incubated for 30 seconds before quenching with 1.3 ml of PBS containing 0.5% BSA. After centrifugation at 300*g* for 3 minutes at 4 °C, resulting cell pellets were washed once with PBS with 0.5% BSA before fixation in 1 ml of 1.6% PFA solution (Electron Microscopy Services, CAS 30525-89-4) in PBS for 10 minutes at room temperature. After centrifugation at 600 × *g* for 3 minutes at 4 °C, cells were washed once with PBS before final resuspension in 1 ml of cell staining medium (CSM; 0.5% BSA and 0.02% NaN_3 in PBS), and then the cell suspension was passed through a 75-µm sieve and a 45-µm sieve (Thermo Fisher Scientific, 50871316 and 50871319) with a P1000 micropipette. Then, the cells were stored at −80 °C until all samples were collected.

Cell counts and visual inspection by light microscopy

Fixed cells were thawed and then visually inspected in bright-field mode at ×4, ×10 and ×20 on an EVOS AMF4300 microscope (Thermo Fisher Scientific) to determine if excessive amounts of cell clumping or debris were present in samples. Samples that

passed visual inspection were counted using a Bio-Rad TC20 Automated Cell Counter to determine cell number (Supplementary Table 2).

Sample barcoding, staining and intercalation

Cells were thawed on ice and pelleted by centrifugation at 600 × *g* for 3 minutes at 4 °C, and the supernatant was discarded. After washing once with CSM, cells were resuspended in 0.5 ml of cold saponin solution (0.02% in PBS) containing one of 20 specific combinations of 1 mM isothiocyanobenzyl EDTA-chelated palladium metals to barcode samples, as previously described (Fread et al., 2017; Zunder et al., 2015a). After incubation at room temperature for 15 minutes on a shaker at 800 rpm, tubes were centrifuged at 600 × *g* for 3 minutes at 4 °C; the supernatant was discarded; and the cell pellet was washed three times with CSM. At this point, individual samples were pooled into a total of three barcoded sets for antibody staining.

For staining of surface epitopes, cells were blocked in CSM containing 10% (v/v) normal donkey serum (Millipore, S30-100ML) for 30 minutes at room temperature. Next, primary antibodies indicated as ‘surface’ in Supplementary Table 1 were diluted in CSM and added to cells (100-µl staining volume per 1×10^6 cells), which were incubated on a shaker at 800 rpm for 30 minutes at room temperature. After incubation, tubes were centrifuged at 600 × *g* for 3 minutes at 4 °C; the supernatant was discarded; and the cell pellet was washed three times with CSM. For intracellular staining, cells were permeabilized by adding ice-cold 100% methanol to fill the tube and incubating on ice for 10 minutes with vortexing every 2 minutes. Next, tubes were centrifuged at 600 × *g* for

3 minutes at 4 °C, and the supernatant was discarded. After washing cells once with CSM, primary antibodies listed as 'intracellular' in Supplementary Table 1 were diluted in CSM and added to cells on a shaker at 800 rpm for 1 hour at room temperature. After incubation, tubes were centrifuged at 600 × *g* for 3 minutes at 4 °C; the supernatant was discarded; and cells were washed three times with CSM.

After primary antibody staining, cells were incubated in 1.6% PFA containing 0.1 μM Cell-ID Intercalator-Ir (201192, Fluidigm) for 15 minutes at room temperature on a shaker at 800 rpm or overnight at 4 °C without shaking. After intercalation, cells were washed once with CSM, once with water, once with 0.05% Tween 20 (in water) and again with water. Cells were pelleted by centrifugation at 600 × *g* for 3 minutes at 4 °C and then kept on ice until run on the mass cytometer.

Mass cytometry

Immediately before analysis on a Helios CyTOF 2 system (Fluidigm), cells were resuspended in water (approximately 1 ml per 1×10^6 cells) containing 1:20 EQ Four Element Calibration Beads (Fluidigm) and passed through a 40-μm nylon mesh filter. Cells were analyzed in multiple runs at a rate of 500 cells per second or less. Data were collected on a Helios CyTOF 2 using CyTOF Software version 6.7.1014.

Normalization and debarcoding

To control for variations in signal sensitivity across individual runs on the mass cytometer, raw .FCS data files were first normalized using EQ Four Element Calibration Beads

(https://github.com/nolanlab/bead-normalization) (Finck et al., 2013). Next, normalized .FCS files from each run were concatenated for each sample set. Concatenated .FCS files were then debarcoded using software to deconvolute the 6-choose-3 Pd combinatorial barcode (Fread et al., 2017; Zunder et al., 2015a), permitting identification of individual samples (https://github.com/zunderlab/single-cell-debarcoder) (Fread et al., 2017). A new parameter was added to the .FCS files: bc_neg, which is the sum of the 3 Pd measurements expected to be zero based on the cell barcode deconvolution assignment. High values for this bc_neg parameter indicate that the cell event in question is likely to contain two or more cells, and this was used for an additional clean-up gating step below.

Isolation of quality, single-cell events

To isolate single cells from fragments/debris and clumps of multiple cells, the normalized and debarcoded .FCS files described above were uploaded to Cytobank (https://community.cytobank.org), and clean-up gating was performed according to the strategy illustrated in Extended Data Fig. 2b. First, a secondary debarcoding clean-up process was performed by gating out events with high bc_neg values, followed by gating out events with a low barcode separation distance and/or high Mahalanobis distance. Next, singlets and quality events were isolated by comparing the ion count length, center and width parameters. Then, cells that were alive at the time of fixation were distinguished from debris and dissociation-damaged or destroyed cells with a gate using DNA-intercalator and cisplatin viability dye. Six unused channels (120Sn, 127I, 133Cs, 138Ba, 140Ce and 208Pb) were identified in Cytobank to contain some background levels, and

events high in these channels were then gated out. Finally, the 4th sample set exhibited an elevated background (in nearly all channels, NeuN shown) in the last third of the runtime. These events were gated out with a time gate.

Batch correction

Although sets 1 and 2 were exposed to a single master mix of antibodies, they were run independently after antibody staining. Furthermore, set 3 was run later. To account for possible batch-dependent effects, batch correction was performed on universal samples made by combining excess cells from all samples after isolating single-cell events as described above. To correct signal intensities of individual markers for batch effects, debarcoded .FCS files were subjected to the batch adjustment process described in Schuyler et al. (https://github.com/CUHIMSR/CytofBatchAdjust) (Schuyler et al., 2019). Specifically, signal intensities for the following antibodies were corrected at the 50th percentile because they yielded approximately Gaussian distributions and produced mean signals with variance greater than 1% for a universal sample included in each barcoded set: TuJ1, cMet, Connexin43, Sox2, CD9, CD117, Nestin, Sox1, CD24, NFH, CD133, CGRP, NeuN, Sox10, Ki67, Vimentin, Thy1.2, TrkC, Runx3, N-Cadherin, GAD65, Calbindin, MAP2, TrkA, MafA, Islet1, PDGFRa, Ret, Cux1, BFABP, Cleaved Caspase-3, TrkB, PGP9.5, p75NTR and IB4. Mean signals for OligO4, CD31 and CD45 had 2–3% variance and normal distributions with truncated lower tails. Batch correction of CD31 and CD45 markers at 65th and OligO4 85th percentiles was determined to be effective at reducing the variance of mean signal. As the variance of mean signal for GFAP or CD44 was less than 1%, these markers were not subjected to batch correction.

Leiden clustering

Cells were partitioned with Leiden clustering (version 0.7.0, https://github.com/vtraag/leidenalg) (Traag et al., 2019) to identify molecularly defined cell types, with the nearest neighbors parameter set to 100. In some cases, this resulted in a memory error on 240-GB High Mem compute nodes, and nearest neighbors = 15 were used instead. To assess if clusters were homogenous and unimodal, we inspected violin plots of marker expression for each cluster. To improve the homogeneity of cell populations, cell types of interest were subjected to multiple rounds of Leiden clustering. For the first round of clustering (primary clustering) and all subsequent rounds of clustering (secondary, tertiary, etc.), all 41 expression markers were used for Leiden clustering analysis. Cell cluster identities were annotated by comparison to previously reported expression profiles of DRG cell types.

UMAP dimensionality reduction

Next, 41-dimensional mass cytometry datasets (including all antibody markers) were embedded into two dimensions by UMAP (version 0.2.6.0, https://github.com/lmcinnes/umap/archive/0.2.4.tar.gz) with the following parameters: nearest neighbors = 15, metric = Euclidean, local connectivity = 1, components = 2 and epochs = 1,000 (McInnes et al., 2018).

Identification of developmental cell trajectories with URD

Code for the URD algorithm (version 1.1.1, https://github.com/farrellja/URD) (Farrell et al., 2018), originally designed to run on scRNA-seq datasets, was modified to interoperate

with mass cytometry. Code including modified functions and a script to run the full analysis is included (see 'Code availability' section). Datasets were downsampled proportionally (to ~65,000 cells) to accommodate the computational demands of URD except for the TrkB/TrkC dataset in Fig. 7, which was smaller (39,944 cells) than the computational limits encountered. The URD parameters used were floodPseudotime $n = 500$, minimum.cells.flooded = 2 and knn = 100. The sigma parameter was determined individually for each dataset with global auto-detection via Destiny in the URD pipeline.

Nearest Neighbor URD Trajectory Tool for analysis of rare cell populations

The Nearest Neighbor URD Trajectory Tool (NNUTT) was created to position a selected subset of cells on a full URD dendrogram. The code is available on GitHub at https://github.com/zunderlab/Keeler-et-al.-DRG-Development-Manuscript. The cells in this subset could (1) be included in the approximately 60,000 cells used to generate the URD dendrogram, (2) come from the larger non-downsampled original dataset or (3) come from a completely different dataset, measured separately. This tool simply maps each cell to its nearest neighbor in the 60,000-cell URD set by expression marker Euclidean distance. Subsequent analyses can then be performed to identify which dendrogram segments are best represented by each mapped subset and how protein expression in the mapped subsets compares to the original dendrogram cells for each segment.

All multi-Trk$^+$ cells on the TrkB/TrkC dendrogram come from the original URD analysis (no downsampling was used for URD construction), but most multi-Trk$^+$ cells on the

TrkA/Ret dendrogram were not in the original URD analysis (64,997 downsampled from 493,544 for URD construction). Segments were excluded from analysis with fewer than ten cells and less than 0.1% proportion of multi-Trk-expressor/all neurons or fewer than five cells regardless of proportion.

Tissue processing for IHC

Embryonic and postnatal mice were euthanized by decapitation. The lower lumbar spinal columns were dissected and fixed in 4% PFA overnight before cyroprotection in 30% sucrose in PBS for 2 days, all at 4 °C. The tissue was subsequently embedded in OCT (VWR, 25608-930) and then cryosectioned into 10-μm sections. The DRG from lower lumbar segments were analyzed at E11.5 and E12.5, immediately above the lower limb buds. The L4 DRG were analyzed at E13.5, E14.5 and P0, using the last rib as a landmark for T13.

Immunostaining

Mounted sections were warmed to room temperature and washed with 1× PBS three times for 5 minutes each. Antigen retrieval was performed for all antibodies by microwave boiling slides/sections in sodium citrate buffer (10 mM sodium citrate, pH 6.0). Sections were cooled to room temperature; sodium citrate buffer was replaced; and sections were microwaved until boiling again. Sections were then rinsed three times with 1× PBS and incubated with blocking solution (0.2% Triton X-100 and 3% normal donkey serum) for 1 hour at room temperature. Sections were incubated with primary antibodies diluted as detailed below in blocking solution overnight at 4 °C. Sections were washed with 1× PBS

three times for 5 minutes each, incubated with secondary antibodies for 1 hour at room temperature protected from light and then washed with 1× PBS three times for 5 minutes each. Sections were mounted in Fluoromount-G with DAPI (SouthernBiotech). Primary antibodies used in this study included: goat anti-TrkA (R&D Systems, AF1056, 1:200 or 0.2 mg ml^{-1}, RRID: AB_2283049), rabbit anti-TrkA (Millipore Sigma, 06-574, 1:50, RRID: AB_310180), goat anti-TrkB (R&D Systems, AF1494, 1:100 or 0.2 mg ml^{-1}, RRID: AB_2155264), mouse anti-TrkB (R&D Systems, MAB397, 1:50, RRID: AB_2298820), goat anti-TrkC (R&D Systems, AF1404, 1:500 or 1:1,000, RRID: AB_2155412), mouse anti-beta III Tubulin (TuJ1) (Covance, MMS-435P, 1:500 or 1:1,000, RRID: AB_2313773), mouse anti-Islet1/2 (DSHB, 39.4D5, 1:100, RRID: AB_528173), rabbit anti-Islet1/2 (Abcam, ab275990, 1:100, RRID: AB_10866454), goat anti-Ret (Neuromics, GT15002, 1:1,000, RRID: AB_1622006), rabbit anti-Sox10 (gift from S. Kucenas, 1:5,000), rabbit anti-BFABP [gift from C. Birchmeier and T. Müller, 1:10,000; (Kurtz et al., 1994)], rabbit anti-BFABP (Abcam, ab281734, 1:250, RRID: unknown) and rat anti-Vimentin (BioLegend, 699302, 1:250, RRID: AB_2716137). Secondary antibodies used in this study included: Alexa Fluor 488 donkey anti-mouse (Thermo Fisher Scientific, A-21202, 1:500, RRID: AB_141607), Alexa Fluor 633 donkey anti-goat (Thermo Fisher Scientific, A-21082, 1:500, RRID: AB_141493) and Alexa Fluor 568 donkey anti-rabbit (Thermo Fisher Scientific, A10042, 1:500, RRID: AB_2534017).

Cell count quantification

DRG were sectioned into fifths (five representative sets), and each section was collected and stained with the indicated marker. All tissue was imaged on the laser scanning

confocal Zeiss 780 NLO at ×20 resolution in Z-stacks at 3-μm intervals for manual quantification in Fiji (Schindelin et al., 2012). Cells expressing each marker were counted and compared to counts of all cells determined from counting DAPI-stained nuclei. To determine the percentage of Islet1^{+} and RTK^{+} cells observed by mass cytometry at these timepoints, we set a threshold value for each protein determined by the 99th percentile of expression of the low-complexity cells as a measure of background: Islet1 > 0.75, TrkA > 0.9, TrkB > 3, TrkC > 2 and Ret > 1.9.

scRNA-seq data mining

Pre-processed and annotated scRNA-seq data from Sharma et al. were downloaded from the data browser provided with their publication (https://kleintools.hms.harvard.edu/tools/springViewer_1_6_dev.html?datasets/Sharma2019/all) (Sharma et al., 2020). As our analysis was focused on DRG development, we excluded the adult mouse timepoint (P40) from our analyses. For a per-feature comparison with our mass cytometry dataset, we selected the transcripts (from within those that had passed quality control thresholds) that corresponded to our protein markers. The scRNA-seq dataset (External Resource Table 1) from Usoskin et al. was downloaded from the additional supporting data for the manuscript (http://linnarssonlab.org/drg/) (Usoskin et al., 2015).

Comparison of mRNA versus protein expression

To compare scRNA-seq and mass cytometry, neurons from both analyses were first selected by thresholding for positive neuronal marker expression. For the scRNA-seq

data, expression above zero was considered as ‘expressing’. For mass cytometry data, which typically exhibit low background for each marker similar to any antibody-based technique, thresholds for labeling cells as ‘expressing’ were determined by the 99th percentile marker expression of the low-complexity cluster 6 (Extended Data Fig. 3). For both datasets, expression values after respective pre-processing were per-feature range-normalized to fall between 0 and 1.

Visualization of high-dimensional data with FLOW-MAP

To incorporate time as a variable in inferring developmental trajectories of cell populations, graph structures incorporating the indicated timepoints from mass cytometry and scRNA-seq datasets were generated with FLOW-MAP (Ko et al., 2020; Zunder et al., 2015b). FLOW-MAP output (.graphml files) was visualized with Gephi software (http://www.gephi.org) (Bastian et al., 2009), and force-directed layout was performed with the ForceAtlas2 algorithm (Jacomy et al., 2014). For visualization, node size was adjusted to indicate cell type abundance, and the ‘prevent overlap’ option was selected in Gephi to ensure that all graph indices remained visible in the layout.

Population sorting and mRNA/protein comparison

For Trk^+ population selection and comparison between scRNA-seq and mass cytometry datasets, both were thresholded on positive expression for TrkA, TrkB or TrkC. For protein expression, we established TrkA, TrkB or TrkC expression value by the 99th percentile of expression of the low-complexity cells as a measure of background: $TrkA > 0.9$, $TrkB > 3$ and $TrkC > 2$, respectively. For RNA expression, we included any

expression value above 0 for each Trk transcript. Cells were sorted in silico based on these per-marker expression thresholds to extract 'positive' cells for the respective markers at each timepoint.

In situ hybridization assay by RNAscope

E12, E15, P0 and P4 DRG tissues were dissected from C57BL/6J mice and perfused with 4% PFA in PBS for 24 hours at 4 °C. Tissues were then incubated in 30% sucrose solution at 4 °C for 3 days. Fixed tissues were embedded in OCT compound, frozen on dry ice and stored at −80 °C. Frozen tissues were cryosectioned at 15-µm thickness, collected onto positively charged slides (Shandon Superfrost Plus, Thermo Fisher Scientific, 6776214) and air dried overnight in the dark. The next day, slides were twice washed for 2 minutes in PBS and then incubated for 10 minutes in H_2O_2 (RNAscope H_2O_2 and Protease Reagents Kit, Advanced Cell Diagnostics, 322381). Slides were then twice washed for 2 minutes with distilled water to remove H_2O_2, before incubation with protease IV solution (RNAscope H_2O_2 and Protease Reagents Kit, Advanced Cell Diagnostics, 322381) for 30 minutes at 40 °C in a HybEZ II oven (Advanced Cell Diagnostics, 321710/321720) and two additional 2-minute washes in distilled water. Tissues were then incubated in probe master mix for 2 hours at 40 °C (Probe1: Mm-Ntrk1, 435791; Probe2: Mm-TUBB3-C2, 423391-C2; Advanced Cell Diagnostics) and then washed twice in 1 × wash buffer (RNAscope Wash Buffer Reagents, Advanced Cell Diagnostics, 310091). After amplification by sequential incubations with AMP1, AMP2 and AMP3 solutions (RNAscope Multiplex Fluorescent Detection Kit version 2, Advanced Cell Diagnostics, 323110) for 30 minutes at 40 °C (separated with two 2-minute washes with wash buffer

between solutions), slides were incubated for 15 minutes at 40 °C with horseradish peroxidase (HRP)-channel 1 (HRP-C1) (RNAscope Multiplex Fluorescent Detection Kit version 2, Advanced Cell Diagnostics, 323110), before an additional two washes for 2 minutes in wash buffer. Slides were then incubated in a fluorescent dye for 30 minutes at 40 °C [1:750 dilution; Tyramide Signal Amplification (TSA) Cyanine 3, Akoya, TS000202] before two 2-minute washes with wash buffer and blocking with HRP blocker for 15 minutes at 40 °C. The same HRP steps were repeated for channel 2 by applying a second fluorescent dye (1:750 dilution; TSA Fluorescein, Akoya, TS000200). Finally, 10–20 ml of DAPI was applied at room temperature to stain the nuclei (Fluoromount-G, SouthernBiotech, 0100-20), and then slides were sealed with coverslips.

Statistics and reproducibility

No statistical method was used to predetermine sample size. No data were excluded from the analyses. The experiments were not randomized. The investigators were not blinded to allocation during experiments and outcome assessment. Data distribution was assumed to be normal, but this was not formally tested.

Results

DRG cell type characterization by protein expression

To identify and characterize cell types in the DRG by their protein expression signatures, we first adapted mass cytometry methods for neural tissues. This involved optimizing tissue dissection and cell dissociation techniques (Methods) and developing a 41-antibody staining panel for specific neuronal and glial subtypes (Supplementary Table 1)

(Lallemend and Ernfors, 2012). Each antibody was conjugated to a unique rare earth metal isotope (Ornatsky et al., 2008) and then titrated to identify its optimal staining concentration using known-positive and known-negative control cells (Extended Data Fig. 1a,b). Mouse DRGs were collected at daily timepoints from E11.5 to P4 to provide a continuous molecular expression profile (Fig. 1a and Supplementary Table 2). For embryonic timepoints, DRGs from a single litter were pooled for cell dissociation and mass cytometry analysis. For postnatal timepoints, the pups were first separated by sex, and then DRGs were combined to generate a pooled male and female sample from each litter. At least two biological replicates (that is, pooled litters) were used for each developmental timepoint (Supplementary Table 2). After dissection, the pooled DRGs were dissociated into a single-cell suspension (Wheeler et al., 2014) and then briefly incubated with cisplatin as a non-cell permeant viability stain (Fienberg et al., 2012), followed by paraformaldehyde (PFA) fixation and storage at −80 °C (Fig. 1a).

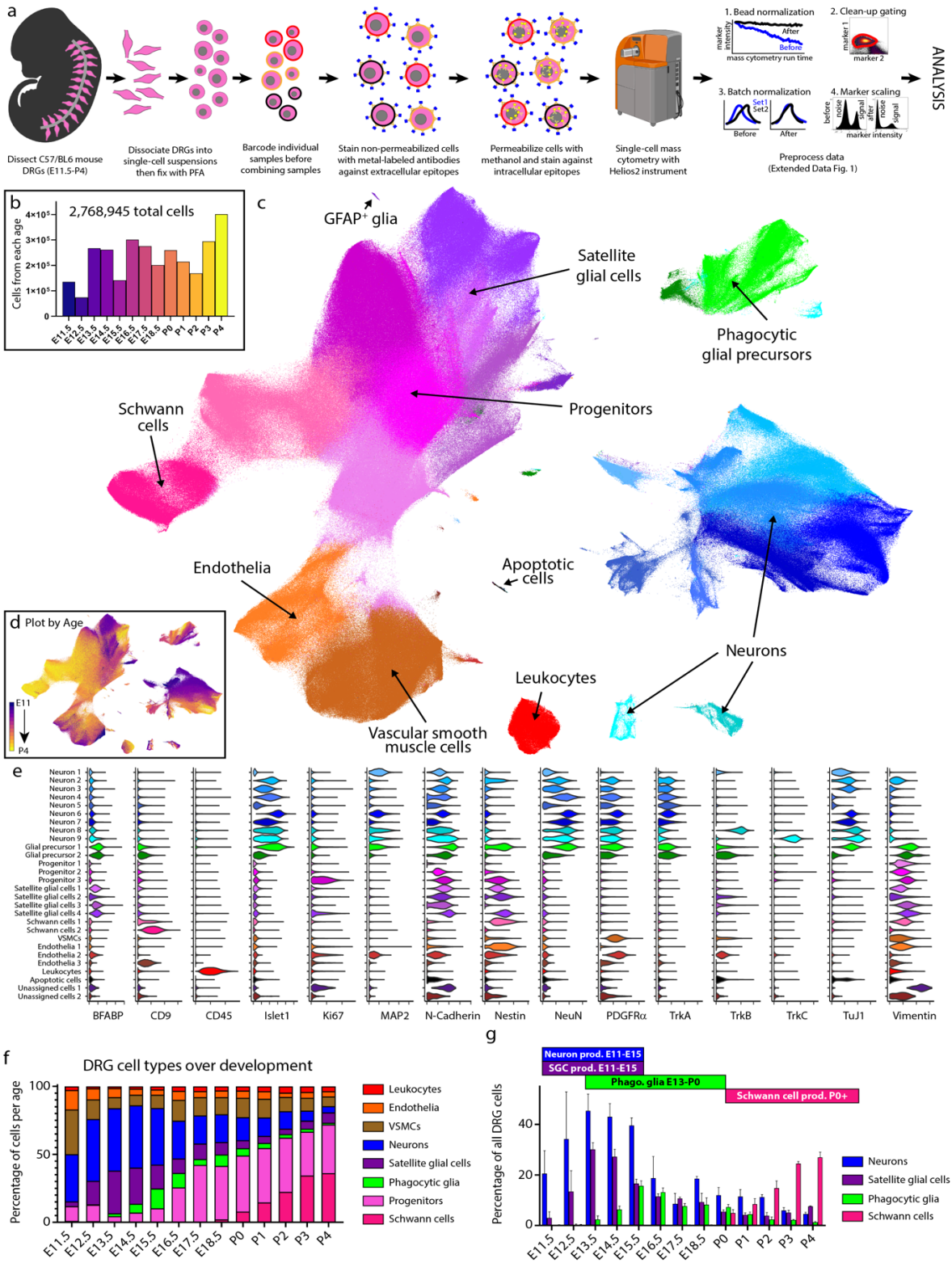

Figure 1. Characterization of DRG cell types from E11.5 to P4 by mass cytometry. a, Neural mass cytometry workflow. Created with BioRender. **b**, Total number of clean-up gated and pre-processed cells analyzed at each day of DRG development. These show the sum of 2–4 separately analyzed litters

(biological replicates) at each timepoint, for 43 samples in total. Bars are colored by timepoint. **c**, UMAP of all DRG cells after clean-up gating, colored by primary Leiden clustering and labeled by presumptive cell type according to protein expression profiles. **d**, UMAP from **c**, colored by age. **e**, Violin plots of protein expression for clusters from **c**. **f**, The proportional abundance of major cell type classes across DRG development, created by combining the Leiden clusters from **c** into (1) leukocytes: $CD45^+$; (2) endothelia: $CD31^+$ and $CD133^+$; (3) smooth muscle: $p75NTR^+$, $PDGFR\alpha^+$, $TrkB^+$ and neuronal marker negative; (4) neurons: $Islet1^+$, $MAP2^+$, $NeuN^+$, $PGP9.5^+$ and $TuJ1^+$; (5) SGCs: $BFABP^+$, $Sox10^+$ and $Vimentin^+$; (6) phagocytic glial precursors: $BFABP^+$, $Sox10^+$ and $Vimentin^+$, plus a mixture of neuronal markers such as $Islet1^+$, $MAP2^+$, $NeuN^+$, $PGP9.5^+$ and $TuJ1^+$; (7) neural progenitors: $Ki67^+$, $Nestin^+$, $Sox10^+$ and $Vimentin^+$; and (8) Schwann cells: $CD9^+$, $cMet^+$ and $OligO4^+$. **g**, Changes in neuronal and glial abundance during periods of neuronal and SGC expansion, glial phagocytosis and postnatal Schwann cell proliferation. Data are presented as mean values ± s.e.m. with biologically independent samples consisting of pool litters including both sexes with $n = 2$ for E11.5–E13.5 and E18.5; $n = 3$ for E14.5–E16.5; and $n = 4$ for E18.5. Postnatal ages were biologically independent samples consisting of sex-separated litters with $n = 2$ female and $n = 2$ male for P2–P4 and $n = 2$ female and $n = 3$ male for P0–P1. Number of pups per litter for each sample is provided in Supplementary Table 2. phago, phagocytosis; prod, production.

After all samples were collected, they were thawed and barcode labeled (Zunder et al., 2015a), followed by pooling into barcode sets (Supplementary Table 2) for uniform staining and subsequent mass cytometry analysis (Fig. 1a). Preliminary inspection revealed that five samples had a low percentage of $Islet1^+$ cells, and two additional samples had low overall cell numbers, so additional litters were collected for these timepoints and run as a third barcode set (Supplementary Table 3). The resulting 4,974,302 events from three barcode sets were pre-processed by (1) bead normalization (Extended Data Fig. 2a) (Finck et al., 2013); (2) debarcoding (Fread et al., 2017); (3) clean-up gating to remove dead cells, aggregates and debris (Extended Data Fig. 2b; www.cytobank.org); (4) batch normalization (Schuyler et al., 2019); (5) marker scaling (Extended Data Fig. 2c); and (6) removal of low-complexity cells (Extended Data Fig. 3a–

f). After these pre-processing and clean-up steps, we were left with 2,768,945 high-quality, viable, singlet DRG cells for analysis (Fig. 1b and Supplementary Table 3).

To identify broad classes of DRG cell types, we performed Leiden clustering (Traag et al., 2019) on the full ~2.8 million cell dataset and visualized the resulting clusters, or developmental age, on a two-dimensional (2D) uniform manifold approximation and projection (UMAP) layout (Becht et al., 2019; McInnes et al., 2018) (Fig. 1c,d and Extended Data Fig. 3g–j). Cell type assignment for each cluster was determined by protein expression profiles matching neurons (23.09%), stem cells and glial progenitors (28.18%), satellite glial cells (SGCs) (12.21%), Schwann cells (11.87%), vascular smooth muscle cells (VSMCs) (11.51%), endothelial cells (5.17%) and leukocytes (3.07%) (Fig. 1e). Because glial precursors can act as 'non-professional' phagocytes (Wu et al., 2009), we assigned the identity of putative phagocytosing glial precursors (4.9%) to cells that express glial precursor markers along with additional markers of their presumptive phagocytosed cargo (Fig. 1e). In addition to clustering analysis, we also prepared a 2D gating hierarchy as an alternative method to identify key cell types (Extended Data Fig. 2d).

To investigate how the abundances of all DRG cell types change across development, we grouped the cell populations identified by Leiden clustering (Fig. 1c) by cell class and calculated their abundance and s.e.m. for sample replicates at each timepoint (Fig. 1f and Extended Data Fig. 3k,l). Generally, leukocytes, endothelia and VSMCs showed consistent abundance across development. Consistent with previous studies, we

observed that the relative abundance of neurons increases until E16.5 due to initial proliferation and migration waves and then diminishes due to apoptosis and concurrent increase in glial progenitors (Fig. 1f) (Cheng et al., 2018; Crowley et al., 1994; Fariñas et al., 1996; Patel et al., 2000; White et al., 1998, 1996). The proportion of neurons, SGCs, putative phagocytic glial precursors and Schwann cells across the time course correspond to the expected windows of neuronal proliferation and glial subtype expansion, as indicated in Fig. 1g.

Comparison of DRG mass cytometry with immunohistochemistry

Neuronal cell types have not previously been characterized by mass cytometry, so we sought to validate our results by comparison with immunohistochemistry (IHC), assessing the total abundance of neurons observed with each technique, plus the relative abundance of TrkA-, TrkB-, TrkC- and Ret-expressing neurons. These neurotrophic factor receptors are essential for somatosensory growth and survival, but they also delineate the broad neuronal cell types (Fig. 2a). First, we performed IHC on DRGs from E11.5, E12.5, E13.5, E14.5 and P0, using Islet1 as a global marker for somatosensory neurons; assessed the percentage of Islet1$^+$ cells out of total DAPI$^+$ cells by IHC; and compared this to the percentage of Islet1$^+$ cells observed by mass cytometry at the same ages, excluding non-DRG cells (blood, endothelia, VSMCs and Schwann cells) (Fig. 2b). In both our mass cytometry and IHC analysis, the percentage of Islet1$^+$ cells was relatively consistent across E11.5 to E14.5 and then dropped approximately 50% by P0, which is due to both neuron death and expansion of non-neuronal cell types (Cheng et al., 2018; Fariñas et al., 1996; White et al., 1998, 1996).

We next examined specific neuron subtypes by performing IHC on E11.5, E12.5, E13.5, E14.5 and P0 DRGs with antibodies against the receptor tyrosine kinases (RTKs) TrkA, TrkB, TrkC and Ret, to distinguish the major classes of somatosensory neurons[1]. To compare cell abundance and staining intensity between mass cytometry and IHC, the microscopy images are shown side by side with UMAP plots from the same respective timepoints, subset for Islet1$^+$ somatosensory neurons (Fig. 2c–e and Extended Data Fig. 4a–c). To quantify the abundance of somatosensory neuron subtypes observed by IHC, we counted the percentage of RTK$^+$DAPI$^+$ double-positive cells (Fig. 2c). To quantify the abundance of somatosensory neuron subtypes observed by mass cytometry, the percentage of cells positive for each RTK was counted and then normalized to the percentage of Islet1$^+$ cells from the same developmental age (Fig. 2d).

The patterns of cell abundance across this developmental window were similar for TrkA$^+$, TrkB$^+$ and Ret$^+$ neurons, but TrkC$^+$ neurons are more abundant in IHC than mass cytometry at E11.5–E12.5 (Fig. 2c,d). One potential explanation for this discrepancy is that only cell surface TrkC is detected by mass cytometry, whereas IHC detects total TrkC.

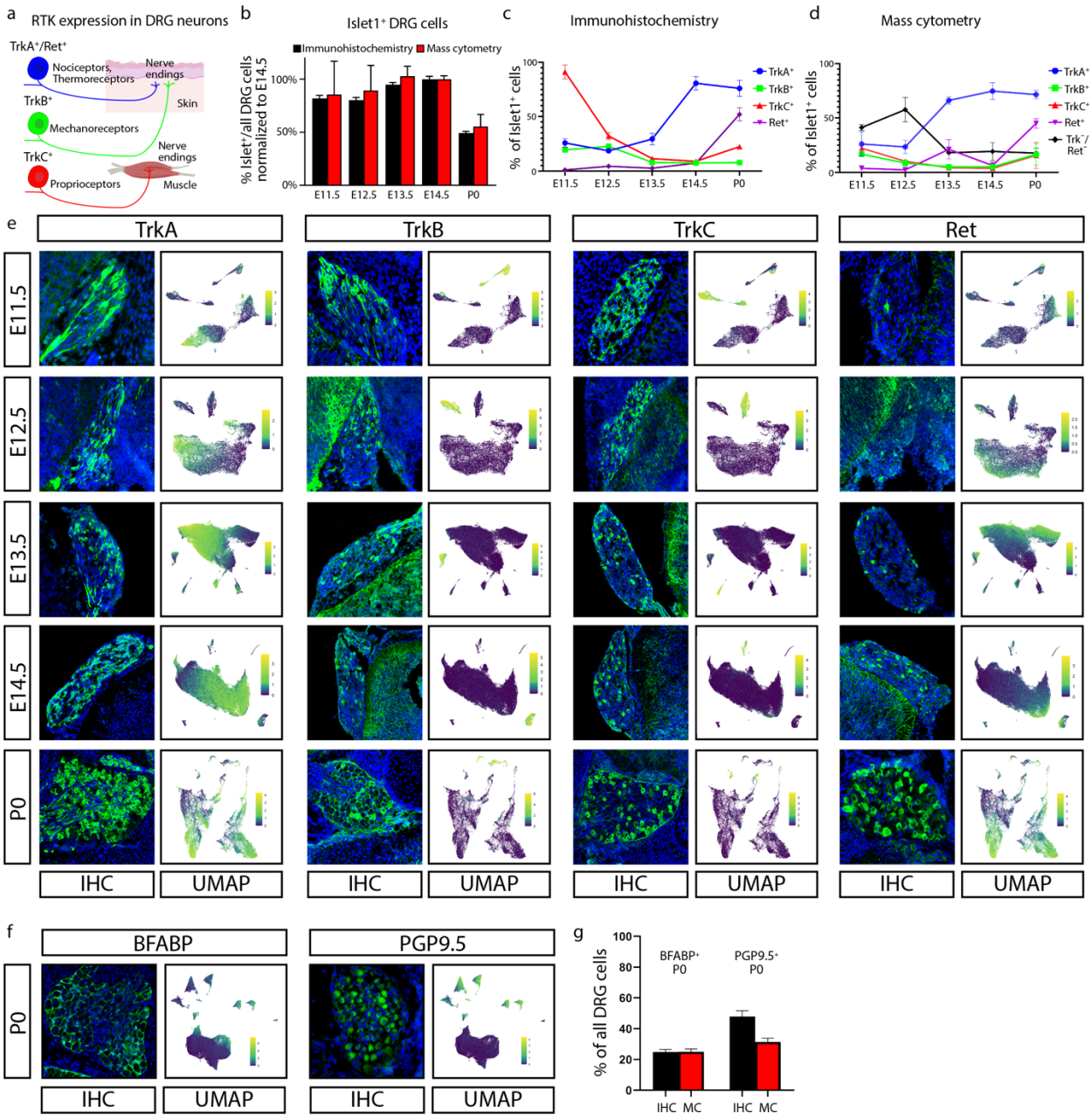

Figure 2. Comparison of DRG analysis by mass cytometry and IHC. **a**, Schematic illustration of somatosensory neuron subtypes divided by TrkA$^+$, TrkB$^+$, TrkC$^+$ and Ret$^+$ expression during development. Created with BioRender. **b**, Proportion of Islet1$^+$ cells out of all DRG cells, by IHC and mass cytometry. All ages are normalized to E14.5, the peak of Islet1$^+$ cell abundance by IHC. Data are presented as mean values ± s.e.m. with biologically independent samples as in Fig. 1g except just E11.5–E14.5 and P0 for the mass cytometry and one or two sections from the L4 DRG of three mice (sexes unknown) from three litters, thus 17 datapoints for IHC at each age. **c**,**d**, Proportion of TrkA$^+$, TrkB$^+$, TrkC$^+$ and/or Ret$^+$ neurons across matching timepoints between IHC (**c**) and mass cytometry (**d**), respectively. Mass cytometry also identifies the number of neurons that express Islet1 but none of TrkA, TrB, TrkC or Ret. Data are presented as mean

values ± s.e.m. with the same samples in **b**. **e**, Representative IHC of lower lumbar (L3–L6) DRGs stained for TrkA, TrkB, TrkC or Ret, at ages E11.5, E12.5, E13.5, E14.5 and P0 quantified in **c**,**d**. IHC images are paired with mass cytometry UMAP layouts from neurons of the corresponding age, colored by protein expression for each RTK. Scale bar, 100 µm. **f**, Representative IHC of P0 DRGs for BFABP and PGP9.5 quantified in **g** and UMAP layouts of all P0 DRG cells colored by expression of these two markers. Scale bar, 100 µm. **g**, Relative abundance of $BFABP^+$ and $PGP9.5^+$ DRG cells at P0 by IHC or mass cytometry. Data are presented as mean values ± s.e.m. with the same samples as in **b** except just P0. MC, mass cytometry.

We also compared IHC and mass cytometry with the glial marker BFABP and the neuronal marker PGP9.5 at P0 (Fig. 2f,g). At P0, the relative percentages of $BFABP^+$ cells are similar between techniques, although the proportion of PGP9.5-expressing cells is slightly lower by mass cytometry (Fig. 2f,g). This difference is likely due to the expansion of glial Schwann cell precursors in proximal nerve roots that can be spatially excluded by IHC but not when dissected for mass cytometry.

Glial cell subtypes and their developmental trajectories

To further investigate how glia mature in the DRG, we selected all cell clusters that expressed glial markers Sox10, Vimentin, BFABP, CD9, cMet, OligO4 and GFAP and then performed an additional round of Leiden clustering on this subset (Fig. 3a and Extended Data Fig. 5a–d), identifying four distinct glial cell types: (1) Schwann cells, (2) SGCs, (3) unspecified glial progenitors and (4) putative phagocytic glial precursors. We then performed URD pseudotime analysis (Farrell et al., 2018), which uses timepoint-biased random walk iterations to identify the most likely cellular trajectory from a manually selected ‘root’ cell type to manually selected ‘tip’ cell types. We selected all E11.5 cells in the glial subset as the root and each of the three mature cell types as tips (Fig. 3b,c and

Extended Data Fig. 5e–i). For finer cluster-level resolution, we performed an additional tertiary round of subclustering on the SGCs, Schwann cells and phagocytic glial precursors, producing 30 molecularly distinct clusters (Fig. 3d,e,h,i,l,m).

Glial precursors arrive in the DRG and start ensheathing somatosensory neuron cell bodies and phagocytosing dying neurons by E13.5 (Britsch et al., 2001; Fariñas et al., 1996; Maro et al., 2004; Taylor et al., 2007; Wu et al., 2009). The non-myelinating, presumptive SGCs that we observed here all express BFABP, N-cadherin, Sox2, Sox10 and Vimentin (Fig. 3d–g) and subcluster into 11 populations, four of which are retained at P4 (Fig. 3d). The early embryonic clusters express Nestin and a mix of Ki67, Ret and c-Kit, whereas the postnatal SGCs upregulate TrkB (Fig. 3d–g). GFAP is a commonly used marker for SGCs, but only a small percentage of glial cells expressed GFAP, first appearing as ~2% of all $BFABP^{+}$ glia at E16.5 and increasing to ~17% of $BFABP^{+}$ glia by P4 (Fig. 3d,e).

Schwann cells ($CD9^{+}$ and $Sox2^{low}$) appear around birth and rapidly expand into two distinct classes: immature/non-myelinating (Nestin, Sox10 and Vimentin) and maturing/myelinating (cMet, OligO4 and one subcluster still expressing Sox10 and Vimentin, suggesting a less mature state) (Fig. 3h). Each of these groups contains a subset of $TuJ1^{low}$ cells, which is likely not expressed by these cells but rather comes from axons wrapped by these Schwann cells and not removed by dissociation (Fig. 3h–k). The neurofilament NFH is also present in a subset of the maturing/myelinating cells. These subtypes do not simply transition from the immature/non-myelinating (clusters 2, 4 and 5)

to maturing/myelinating island (clusters 1, 3, 6 and 7), suggesting that the distinct islands are likely delineating between non-myelinating and myelinating pools of the same populations rather than a difference in developmental lineages or maturation state (Fig. 3h,i).

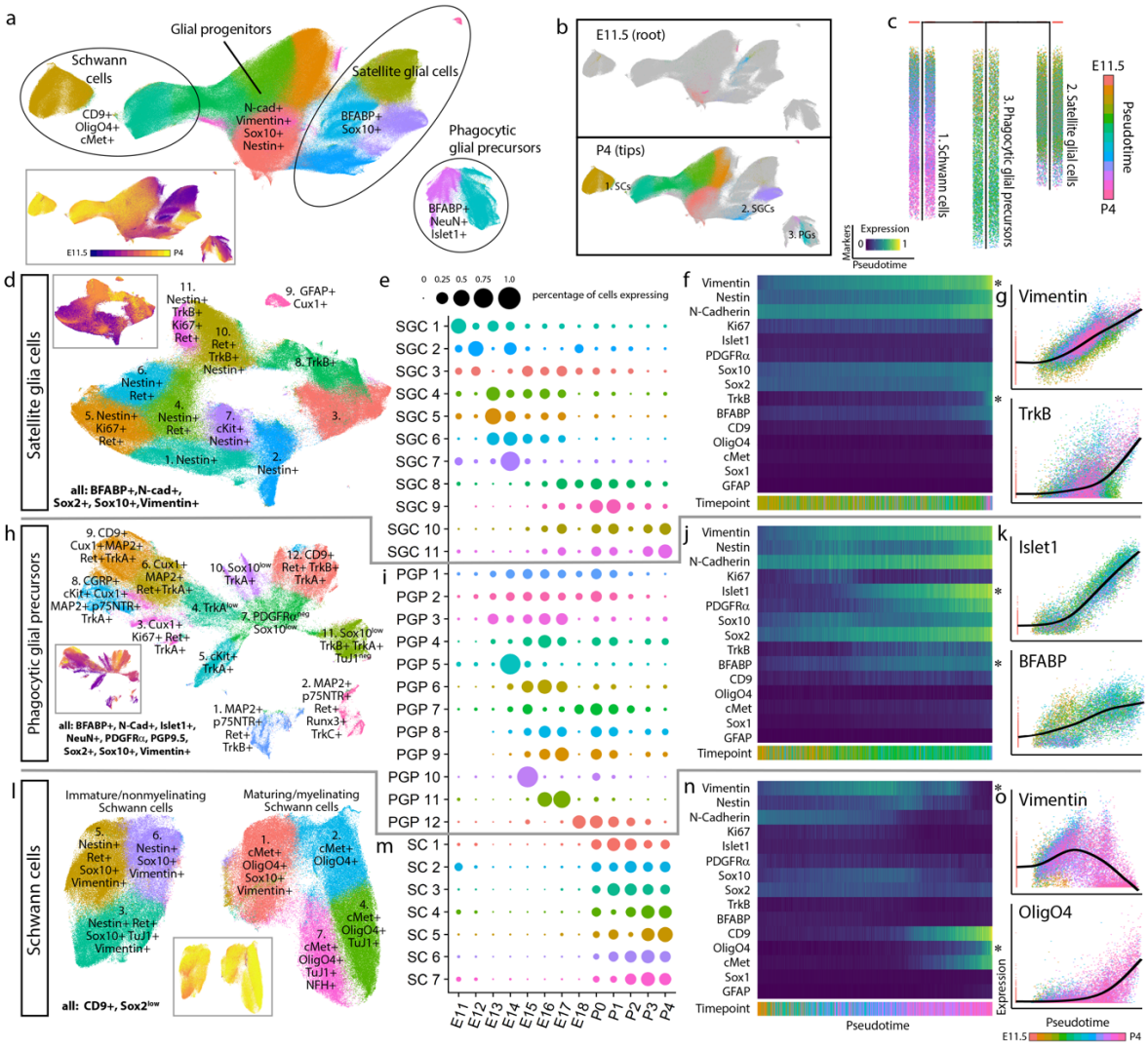

Figure 3. Glial subtypes show distinct developmental trajectories. **a**, Leiden clustering and UMAP of E11.5–P4 DRG glia and glial precursors, performed on all cells from the clusters in Fig. 1c that expressed glial markers BFABP, CD9, cMet, GFAP, OligO4, Sox10 and/or Vimentin, labeled by glial types and key markers. Inset: colored by age. **b**, E11.5 or P4 cells only, colored by Leiden clustering, overlaid on the full UMAP from **a**, colored gray. **c**, URD pseudotime hierarchy for SGCs, Schwann cells and putative phagocytic glial precursors, produced with E11.5 root (pooled) and P4 tips (individual clusters) from **b**, colored by pseudotime. **d**–**g**, SGC clusters were extracted from the glial dataset for an additional secondary

round of Leiden clustering and UMAP, with SGC subtypes labeled by their characteristic marker expression (**d**). Inset is colored by age. Relative abundances for each SGC subtype are plotted across sample collection ages (**e**), and changes in protein expression are plotted across the SGC pseudotime trajectory (**f**). Expression markers denoted by asterisks are also plotted by scatter plot (**g**) to illustrate the cells underlying the pseudotime heat map in **f**. Similar analysis was performed for Schwann cells (**h**–**k**) and putative phagocytic glial precursors (**l**–**o**). **p**, Percentage of doublets counted in the samples from ages E13.5, E15.5, E17.5, P1 and P3 from manual inspection under bright-field analysis with a hemocytometer. Data are biologically independent samples as in Fig. 1g for the ages used here. **q**, Percentage of phagocytic glia by mass cytometry after all clean-up gating. Data are biologically independent samples as in Fig. 1g for E13.5, E15.5, E17.5, P1 and P3. **r**, Representative IHC of E15.5 L4/L5 DRGs with anti-Islet1 (neuronal marker) and anti-BFABP (satellite glial marker). Similar results were obtained across three or more DRGs per litter and three separate litters. Scale bar, 20 μm. Insets i–iii show three phagocytic events as previously described (Wu et al., 2009).

Putative phagocytic glial precursors co-express non-myelinating glial markers (BFABP, Vimentin and Sox10) but also contain neuronal markers (for example, Islet1, NeuN and TuJ1) (Fig. 3l–o). Glial precursors have been shown to phagocytose dying neurons in the embryonic DRG before macrophages infiltrate and become the primary phagocytosing cell type (Wu et al., 2009). We identified these putative phagocytic cells and performed the following analyses to rule out false positives associated with doublets and aberrant association with debris: (1) DNA intercalator gating, (2) ‘barcode-negative’ filtering, (3) abundance comparisons, (4) expression intensity comparisons and (5) hemocytometer doublet analysis (Fig. 3p,q and Extended Data Fig. 5j). What are these glial precursors likely phagocytosing? Their subclustering is largely driven by the four RTKs that define somatosensory neuron types, TrkA, TrkB, TrkC and Ret, but other neuronal proteins are also present, including nuclear transcription factors that indicate entire cell engulfment (Fig. 3l and Extended Data Fig. 5k,l). These putative phagocytosis events are observed across embryonic and postnatal development but peak during the late embryonic stage (Fig. 3l,m). To validate these results, we performed IHC on E15.5 DRGs with anti-Islet1

and anti-BFABP antibodies and DNA-label DAPI to demonstrate phagocytosis as previously observed by others (Wu et al., 2009). Immature glial precursors were identified phagocytosing neuronal fragments (Fig. 3r).

Somatosensory neuron subtypes

To further investigate neuronal subtypes in the DRG, we extracted all clusters that expressed TuJ1, NeuN, Islet1, PGP9.5 and/or MAP2 and performed an additional round of clustering on this 637,744-cell subset. Specific subclusters were identified for removal as errant non-neurons, including putative phagocytic glia and spinal cord contamination (Extended Data Fig. 6a). After these clean-up steps, the remaining 533,488 cells were clustered again, dividing into three primary groups: $TrkA^{+}Ret^{+}$, $TrkB^{+}$ and $TrkC^{+}$ (Extended Data Fig. 6b–h). These three groups were separated for a final round of subclustering to identify, as completely as possible, the somatosensory neuronal subtypes present across the DRG time course (Fig. 4a–d and Extended Data Fig. 7a–v). From E11.5 to P4, we identified 41 neuronal cell types and/or cell states, each molecularly distinguished by at least one of the 41 markers measured, and included transient intermediates as well as all known somatosensory neuron subtypes, such as mechano-noxious heat peptidergic (PEP) neurons, itch-mechano-heat non-peptidergic (NP) neurons, cold-sensing neurons (which remain as a subpopulation within NP at P4; Extended Data Fig. 6i), C-low-threshold mechanoreceptors (C-LTMRs) (TH; Fig. 4f–n), A-low-threshold mechanoreceptors (NF1, NF2 and NF3) and proprioceptors (NF4) (Fig. 4d and Extended Data Fig. 6b–h). These previously reported subtypes are labeled ‘E&E’

in Fig. 4d, in reference to the review by Emery and Ernfors where they were described (Emery and Ernfors, 2020).

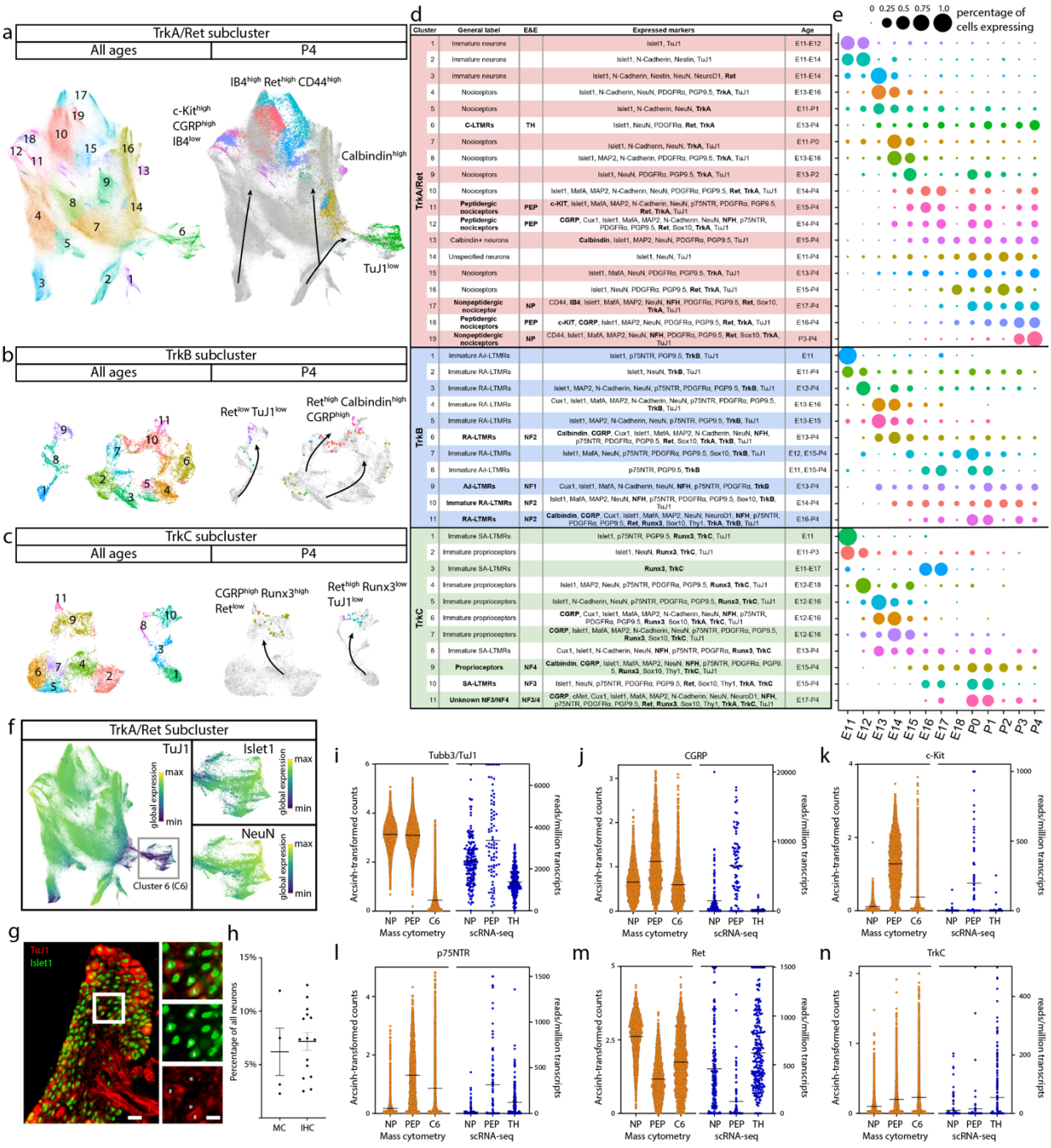

Figure 4. Distinct neuron subtypes emerge across development. a–c, Clusters from Fig. 1c expressing only neuronal markers (Islet1, MAP2, NeuN, PGP9.5 and/or TuJ1) were extracted for a secondary round of analysis (Extended Data Fig. 6), producing three groups of somatosensory

neurons characterized by TrkA/Ret, TrkB or TrkC expression. Each group was extracted for tertiary analysis on $TrkA^+Ret^+$ (**a**), $TrkB^+$ (**b**) and $TrkC^+$ (**c**) neurons. Cells from all ages are shown in the left UMAP, with clusters numbered by age of appearance. Black arrows denote population shifts across development from E11.5 to P4. In the right UMAP, all cells except P4 are colored gray to highlight the final timepoint populations. **d**, Table of all 41 neuron populations, listed in order of emergence. Cell types with protein expression that match designations from the recent Emery and Ernfors review are labeled[5]. Proteins expressed at a higher level relative to other neuronal populations are noted. Bolded proteins were used for subtype identification. The age range where each subtype was 1% or greater of all neurons in the TrkA/Ret, TrkB or TrkC group is indicated. **e**, Relative abundance for neuronal subtypes, from E11.5 to P4. **f**, TrkA/Ret UMAP from **a** colored by TuJ1 expression. Inset panels show cluster 6. **g**, Representative IHC of P3 DRGs stained for Islet1 (Alexa Fluor 488, green) and TuJ1 (Alexa Fluor 568, red) quantified in **h**. Scale bar, 50 µm. Inset highlighting $Islet1^+$ cells with corresponding high and low expression of TuJ1. Asterisk (*) denotes $Islet1^+TuJ1^{low}$ neurons, and pound sign (#) denotes $Islet1^+TuJ1^+$ neurons. **h**, Percentage of $TuJ1^{low}$ neurons observed by mass cytometry (left) and IHC (right) as shown in **g** at P3. For mass cytometry, two litters, sex-separated, were assessed (two litters, four samples). For IHC, L4/L5 DRGs were stained from five pups, 2–3 females and males per litter, from three litters and counted for TuJ1 expression (15 DRGs in total). **i**, On the left, protein expression of TuJ1 from mass cytometry from P4 mice (in orange) for non-peptidergic (NP) nociceptors, peptidergic (PEP) nociceptors and cluster 6 (C6) neurons. On the right, gene expression of *TUBB3* (TuJ1) from the scRNA-seq dataset from Usoskin et al.[2] for the same nociceptive populations and TH^+ C-LTMRs (TH) from P42–P56 mice[2] (in blue). Data are presented as mean values. **j**–**n**, Comparison of protein and mRNA transcript expression from the same datasets for CGRP, c-Kit, p75NTR, Ret and TrkC, respectively. Data are presented as mean values. MC, mass cytometry.

Separately clustering 493,544 $TrkA^+Ret^+$ neurons, 21,652 $TrkB^+$ neurons and 18,292 $TrkC^+$ neurons revealed 19, 11 and 11 distinct somatosensory subtypes and/or cell states, respectively, labeled by their order of appearance during development (Fig. 4e). The $TrkA^+Ret^+$ subtypes appear to emerge from three immature populations at E11.5 (clusters 1, 2 and 3) and diverge into four distinct subtypes: peptidergic nociceptors ($c\text{-}Kit^+$, $CGRP^+$

and IB4^{low}; clusters 11, 12 and 18), non-peptidergic nociceptors (IB4^{+}, Ret^{+} and CD44^{+}; TrkA/Ret clusters 17 and 19), Calbindin^{+} neurons (TrkA/Ret cluster 13) and TH^{+} C-LTMRs (TuJ1^{low}; TrkA/Ret cluster 6; Fig. 4f–n) (Fig. 4a,d). The TrkB^{+} neurons separated into two distinct groups: Aδ low-threshold mechanoreceptors (Aδ-LTMR) (TrkB^{+} and Ret^{low}) and rapidly adapting low-threshold mechanoreceptors (RA-LTMRs) (TrkB^{+}, Ret^{+}, Calbindin^{+} and CGRP^{+}). RA-LTMR clusters 2, 7 and 10 do not express the mature markers CGRP or Calbindin even at P4, indicating that these neurons do not mature until after P4 (Fig. 4b,d). TrkC^{+} neurons separate into two distinct groups: slowly adapting low-threshold mechanoreceptor (SA-LTMR) (TrkC^{+} and Ret^{+}) and proprioceptors (TrkC^{+} and Runx3^{+}). Interestingly, a small population of mostly postnatal TrkC^{+} neurons (TrkC cluster 11) express both Ret and Runx3 (Fig. 4c,d), indicating that these cells may undergo a period of cell fate plasticity during innervation of their final tissue targets, between SA-LTMR and proprioceptors.

We were initially surprised to find neuronal clusters with low TuJ1 expression, as TuJ1 is a widely accepted marker of somatosensory neurons (Fig. 4a–c) (Avraham et al., 2020; Guo et al., 2013; Levin et al., 2017). TrkB^{+} and TrkC^{+}TuJ1^{low} clusters were identified by their differential expression of Ret and other key markers (Aδ-LTMR$^{–}$: TrkB^{+}, Ret^{low}, Calbindin$^{–}$ and CGRP$^{–}$; SA-LTMR$^{–}$: TrkC^{+}, Ret^{+} and Runx3$^{–}$). However, no markers were uniquely expressed in the TrkA^{+}Ret^{+}TuJ1^{low} cluster 6 (Fig. 4f and Extended Data Fig. 6j–m). We verified that TuJ1^{low} neurons exist in P3 L4/L5 DRG cryosections stained with TuJ1 and Islet1. These two neuronal markers were co-expressed in most cells examined (Fig. 4g), but 7.16% (±0.8% s.e.m.) of the Islet1^{+} cells had faint or no TuJ1 signal

compared to 6.2% (±1.9% s.e.m.) by mass cytometry (Fig. 4h). In a publicly available scRNA-seq dataset on DRG neurons (Usoskin et al., 2015), we identified a single TuJ1^{low} population, C-LTMRs (Fig. 4i), which exhibited a similar expression pattern (CGRP, c-Kit, p75NTR, Ret and TrkC) to our TrkA^{+}Ret^{+}TuJ1^{low} cluster 6 (Fig. 4j–n and Extended Data Fig. 6n), and, therefore, we labeled cluster 6 as TH^{+} C-LTMRs.

Developmental trajectories of somatosensory neurons

The TrkA^{+}Ret^{+} and TrkB^{+}TrkC^{+} lineages are thought to be distinct as separate migration waves of specific progenitors, with a common progenitor in the neural crest (Lallemend and Ernfors, 2012). Because this common progenitor is present before our earliest collection, we performed URD pseudotime analysis (Farrell et al., 2018) on each lineage separately, with unique roots for TrkA^{+}Ret^{+} (TrkA/Ret clusters 1, 2 and 3 at E11.5) versus TrkB^{+}TrkC^{+} (TrkB clusters 1 and 2; TrkC clusters 1, 2 and 3; all at E11.5) (Fig. 4a–d and Extended Data Fig. 8a–f). Viewed together, these trajectories represent the maturation of 14 somatosensory cell types: mechanoreceptors (segments 1, 4, 7, 9, 14 and 17), proprioceptors (segments 10, 20 and 23), Th^{+} C-LTRMs (segment 6), peptidergic nociceptors (segments 11, 13, 15, 19 and 21) and non-peptidergic nociceptors (segments 12, 16, 18 and 22) (Fig. 5a and Extended Data Fig. 8e,f). As expected, these somatosensory subtype trajectories are distinguished by Trk paralog expression as well as markers such as Ret, IB4, CGRP and c-Kit. (Fig. 5b and Extended Data Fig. 8g–t).

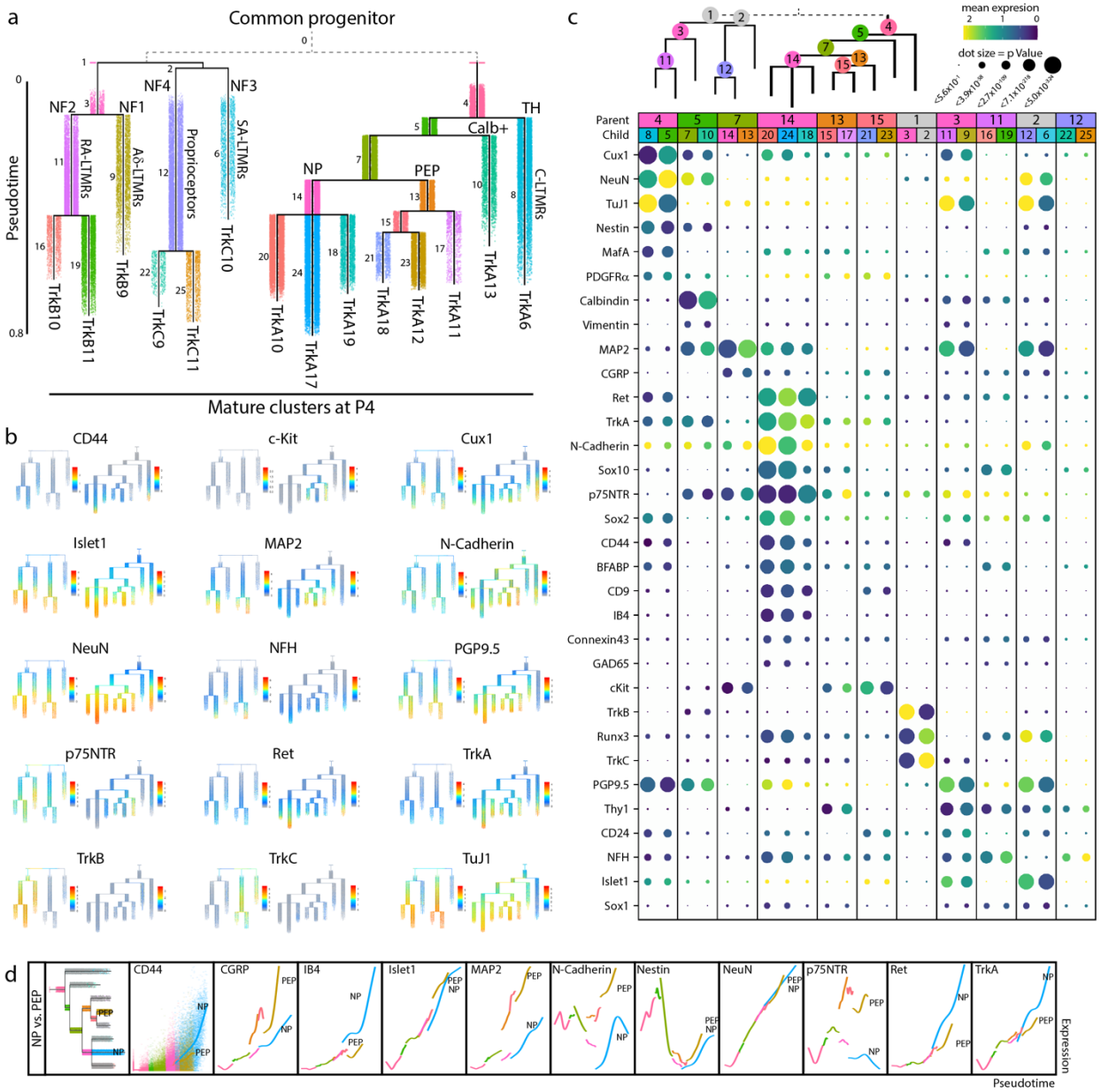

Figure 5. Pseudotime analysis of neuronal differentiation. a, URD pseudotime analysis of TrkB/TrkC neurons (39,944 cells) and TrkA/Ret neurons (64,997 cells downsampled from 493,544 total). These were run separately (gray dashed line), each with all E11.5 cells designated as root, and all mature P4 clusters were designated as tips (Extended Data Fig. 8). Cells are colored by their dendrogram segment, which are numbered by median pseudotime, from youngest to oldest. Key cell fate bifurcations are labeled at branch points. **b**, URD dendrograms from **a** colored by protein expression for key markers of somatosensory neurons and subtypes. **c**, Proteins with the highest URD branch point divergence, ranked by *P* value of the two-sample *t*-test between protein expression in the cell populations of each child segment. For branch points with more than two child segments, pairwise comparisons were made, and the most highly divergent *P* value was used for rank ordering. Circle size indicates these *P* values (log-transformed), and circle color

indicates marker expression in each child segment. **d**, Trajectory plots showing protein expression by pseudotime for non-peptidergic and peptidergic nociceptors. Each URD segment (colored in the grayed URD in the top-left box in **e**) is plotted with all cells from that segment overlaid with a smoothed spline (for example, CD44). For clarity, the dots representing the cells on both trajectories were removed from the subsequent markers.

To investigate cell fate decisions at URD branch points, we identified the most significant differences in protein expression between child segments at each branch point in the TrkBTrkC and TrkARet URDs (Fig. 5c). As expected, TrkB and TrkC are the key markers that divide TrkB$^+$ RA-LTMR and Aδ-LTMR from the TrkC$^+$ SA-LTMR and proprioceptors, along with Runx3 (Fig. 5b,c). Divergence between RA-LTMR and Aδ-LTMR trajectories (from parent segment 1 into child segments 7 and 9; Fig. 5a) corresponds to changes in expression of Thy1, Cux1, Islet1, CD24, Calbindin, p75NTR and NFH, among others (Fig. 5b,c). NeuN, Runx3 and N-Cadherin similarly show the largest shift in expression between SA-LTMRs and proprioceptors (Fig. 5b,c). In the TrkARet URD branchpoints, the split between peptidergic and non-peptidergic nociceptors corresponded to expression differences in MAP2, N-Cadherin, p75NTR and c-Kit, suggesting that peptidergic nociceptors mature earlier than non-peptidergic nociceptors (Fig. 5b,c).

We observed differences in the timing and expression level of neuronal maturation markers across both pseudotime dendrograms. For example, MAP2 increases across all somatosensory populations except for the presumptive non-peptidergic nociceptors, indicating that maturation for this subtype is delayed until after P4 (Fig. 5b,c). The TNFR family member p75NTR, a pro-growth signal in somatosensory development, is expressed broadly in both TrkB$^+$ and TrkC$^+$ types but only strongly in a single TrkA$^+$

branch, a presumptive peptidergic (CGRP$^+$ and c-Kit$^+$) cell type (Fig. 5b,c) (Cheng et al., 2018). CD44 signaling is involved in nociception, and we observed early expression of CD44 in non-peptidergic nociceptors as well as the TuJ1^{low} TH cluster (Ferrari et al., 2018) (Fig. 5b,c). Direct comparison of the peptidergic (PEP) and non-peptidergic (NP) trajectories revealed an increase in CGRP, c-Kit, MAP2, N-Cadherin and p75NTR for PEP and elevated CD44, IB4, Ret and TrkA for NP (Fig. 5d).

Multi-Trk$^+$ neurons with elevated pro-growth and stem markers

Because Trk receptors delineate somatosensory neuron subtypes and link a neuron's survival to proper innervation of targets (Lallemend and Ernfors, 2012), we investigated whether neurons could transiently express two or more Trks simultaneously before committing to a specific cell fate. This analysis revealed a small pool of multi-Trk$^+$ neurons that express two Trk receptors simultaneously (TrkA$^+$TrkB$^+$, TrkA$^+$TrkC$^+$ or TrkB$^+$TrkC$^+$, respectively) (Extended Data Fig. 9a–c). We also identified multi-Trk$^+$ neurons in publicly available scRNA-seq datasets (Sharma et al., 2020; Usoskin et al., 2015) (Extended Data Fig. 9d,e), although these were not highlighted or commented on in the publication of these datasets.

The abundance of multi-Trk$^+$ neurons begins to increase at E15.5 and peaks at P0 (Fig. 6a,c and Extended Data Fig. 9f). To confirm the presence of these multi-Trk$^+$ neurons, we performed IHC analysis before, during and after this peak, at E15.5, P0 and P4, respectively (Fig. 6b,d,e). This analysis suggests that P0 is a peak of abundance for all three types of multi-Trk$^+$ neurons within this time course (Fig. 6a–e).

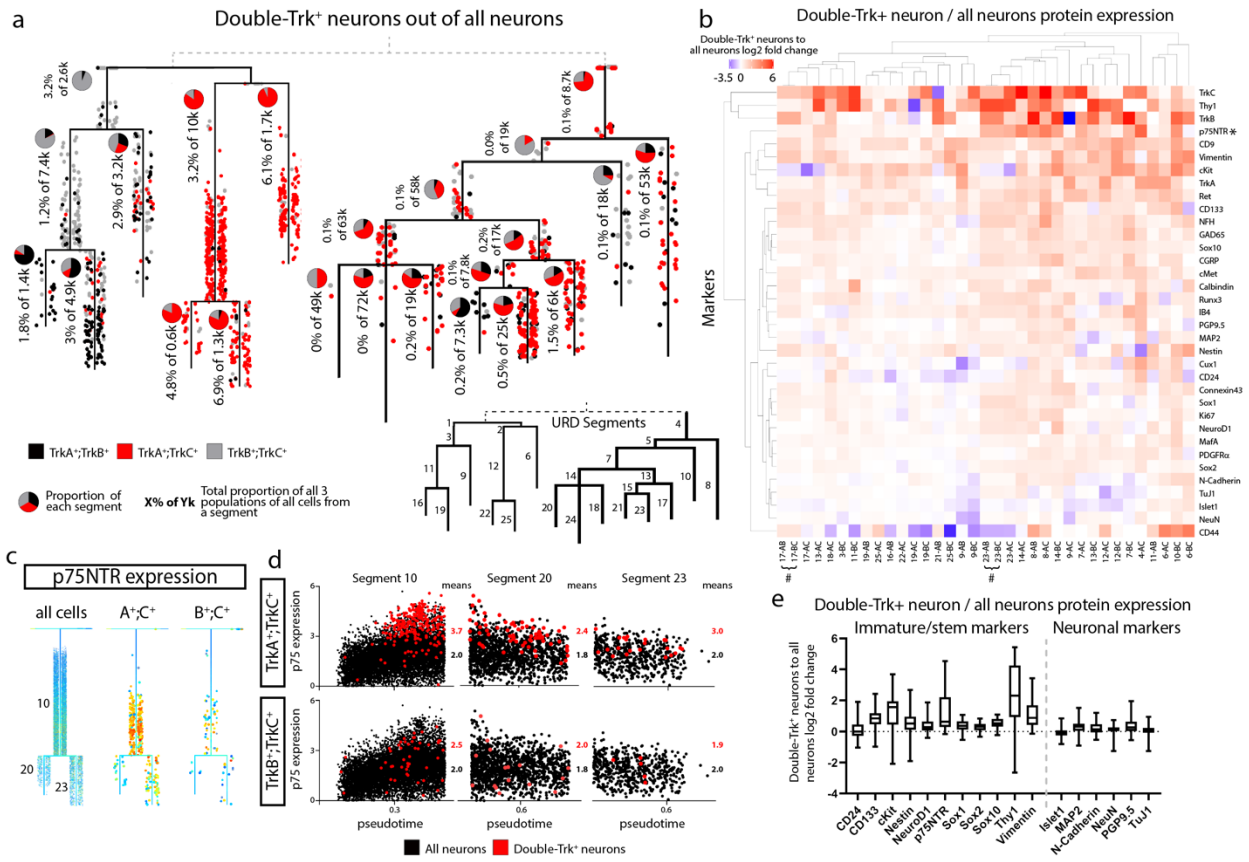

Figure 6. Elevated expression of stem cell and pro-growth markers in multi-Trk⁺ neurons. a, Proportion of multi-Trk⁺ neurons out of all Trk⁺ neurons (determined by thresholding expression values; TrkA > 2, TrkB > 3 and TrkC > 2) at E15.5, P0 and P4 by mass cytometry. Data are presented as mean values ± s.e.m. with sample size as in Fig. 1g for the relevant age. **b**, Proportion of multi-Trk⁺ neurons out of all Trk⁺ neurons at E15.5, P0 and P4 by IHC of individual L4/L5 DRG cryosections. Data are presented as mean values ± s.e.m. with three litters with multiple DRGs analyzed per age for a total of 10, 23 and 14 DRGs at E15.5, P0 and P4, respectively. **c**, Relative proportion of each multi-Trk population in each P0 mass cytometry sample from **a**. Data are presented as mean values ± s.e.m. with sample size as in Fig. 1g for only P0. **d**, Relative proportion of each multi-Trk population in individual L4/L5 DRG cryosections. Data are presented as mean values ± s.e.m. with three litters with 7–8 DRGs analyzed per litter, 23 DRGs in total. **e**, Representative IHC images of P0 L4/L5 DRGs with anti-TrkA, anti-TrkB and anti-TrkC quantified in **b** and **d**. Insets show a multi-Trk⁺ expressing neuron. Scale bar, 100 µm. **f**, All 1,480 multi-Trk⁺ neurons mapped onto the URD dendrogram from Fig. 5a by NNUTT (Methods). In each segment, the relative proportions of each type of multi-Trk⁺ cells are indicated by pie charts, and the total proportion for all multi-Trk⁺ neurons relative to total neurons is indicated as a percentage. **g**, $\log_2$ fold change of protein expression in the multi-Trk⁺ neurons versus total neurons in each URD dendrogram segment (Fig. 5a). Pound sign (#) denotes paired segments where all multiTrk⁺ neurons were, in fact, triple-Trk⁺ neurons producing identical expression profiles in both segments. **h**, URD dendrograms of the proprioceptor population colored by

p75NTR expression for the full dataset and two multi-Trk$^+$-expressing neuron types. **i**, Every cell in segments 12, 22 and 25, respectively, plotted by pseudotime value and p75NTR expression. All neurons colored in black with the multi-Trk$^+$ neurons are overlaid in red. **j**, $\log_2$ fold change multi-Trk$^+$ to all neuron comparisons of marker expressions for immature/stem markers (left) and for neuronal markers (right) for all segments. Data are presented as mean values with the minimum value shown as the lower whisker; the maximal value shown as the upper whisker; and the box bottom and top defines the first and third quartiles, respectively. Data are the marker expression comparisons for each URD segment, thus $n = 35$. **k**, Representative IHC of P4 L4/L5 DRG with anti-TrkA, anti-TrkC and anti-Vimentin. Dotted lines outline the indicated DRG neuron. Scale bar, 5 µm. **l**, Quantification of Vimentin IHC pixel intensity for single-Trk$^+$ and multi-Trk$^+$ neurons measured in Fiji. Three P4 litters with three L4/L5 DRGs (nine total) per litter were analyzed. Only four TrkA$^+$TrkB$^+$ neurons, five TrkA$^+$TrkC$^+$ and zero TrkB$^+$TrkC$^+$ neurons were detected in these DRGs. Statistical analysis: one-way ANOVA using Tukey's multiple comparison test and *P* value **<0.005. Exact *P* values for all comparisons are in Extended Data Fig. 9i. Data are presented as mean values ± s.e.m. **m**, Quantification of Vimentin expression from the mass cytometry dataset for single-Trk$^+$ and multi-Trk$^+$ neurons only from P4 samples. As in **a**, multi-Trk$^+$ neurons were determined by thresholding expression values; TrkA > 2, TrkB > 3 and TrkC > 2. Statistical analysis: one-way ANOVA using Tukey's multiple comparison test and *P* value *<0.05. Exact *P* values for all comparisons are in Extended Data Fig. 9j. All neurons from P4 samples ($n = 2$ biologically independent samples of pooled female and male litters) were included: 6,034 TrkA$^+$ neurons, 31 TrkB$^+$ neurons, 20 TrkC$^+$ neurons, ten TrkA$^+$TrkB$^+$ neurons, seven TrkA$^+$TrkC$^+$ neurons and one TrkB$^+$TrkC$^+$ neuron. Data are presented as mean values ± s.e.m. ND, not detected.

To assess whether the multi-Trk$^+$ neurons were concentrated at cell fate decision points, we mapped all multi-Trk$^+$ neurons from our analysis onto the URD dendrograms by Euclidean distance to estimate their trajectory and pseudotime position (Fig. 6f and Extended Data Fig. 9g,h). Interestingly, the incidence of these multi-Trk$^+$ neurons increases over pseudotime for many lineages (Fig. 6f and Extended Data Fig. 9g,h), and they exhibit characteristic shifts in the expression of pro-growth and stem cell markers when compared to single-Trk$^+$ neurons from the same URD segment (Fig. 6g).

p75NTR, a receptor that promotes progressive developmental signaling in somatosensory neurons (Z. Chen et al., 2017; Cheng et al., 2018; Fan et al., 1999; Lee et al., 1992; Murray et al., 1999), was expressed in TrkB$^+$ and TrkC$^+$ neurons from E11.5 to P4 and in peptidergic nociceptors and not in all non-peptidergic nociceptors (Fig. 4d and Extended Data Fig. 6f,h). In multi-Trk$^+$ neurons, however, expression of the pro-growth p75NTR was elevated in many URD segments, such as TrkA$^+$TrkC$^+$ neurons in the proprioceptor trajectory (Fig. 6h,i). Multi-Trk$^+$ neurons also showed increased expression of stem markers but remained largely unchanged for other marker types (Fig. 6j). IHC staining for Vimentin in all three types of multi-Trk$^+$ neurons confirms elevated Vimentin compared to single-Trk$^+$ neurons (Fig. 6k–m) These rare cells could represent a state of increased plasticity before cell fate decisions are made. Alternatively, they may be neurons with delayed cell fate or a residual pool of immature cells that is destined to act as neural stem cells in the adult DRG.

Comparison of DRG mass cytometry with scRNA-seq

To determine the degree of correlation between our protein-based mass cytometry measurements and mRNA abundances, we compared our results to an scRNA-seq study with closely overlapping timepoints: E11.5, E12.5, E15.5, P0 and P5 (Sharma et al., 2020). Our antibody panel has 36 proteins with directly comparable cognate mRNAs, but the other markers are not directly comparable, such as the lectin IB4 and Cleaved Caspase-3. Because mRNA and protein levels are not strictly related in a linear or predictable manner (see analysis below), we first compared the normalized mean expressions and the percentage of cells expressing these protein–mRNA cognate pairs.

This comparison was performed at each matching timepoint plus the close timepoints P4 (protein) and P5 (RNA) (Fig. 7a). In several cases, protein expression closely tracked RNA expression, but, for most protein–mRNA cognate pairs, there were large differences in the timing of relative trends in expression levels. For example, the transcription factors Cux1, Islet1, MafA, NeuN, Sox1, Sox2 and Sox10 all exhibited protein expression delayed by at least 5 days relative to RNA expression, and we saw similar patterns for BFABP, GAD65, PGP9.5, TrkA, cMet, CD133, c-Kit, MAP2 and GFAP. In rare cases, we even saw relative trends in protein expression levels occur before those for RNA, such as for Thy1 and CD31.

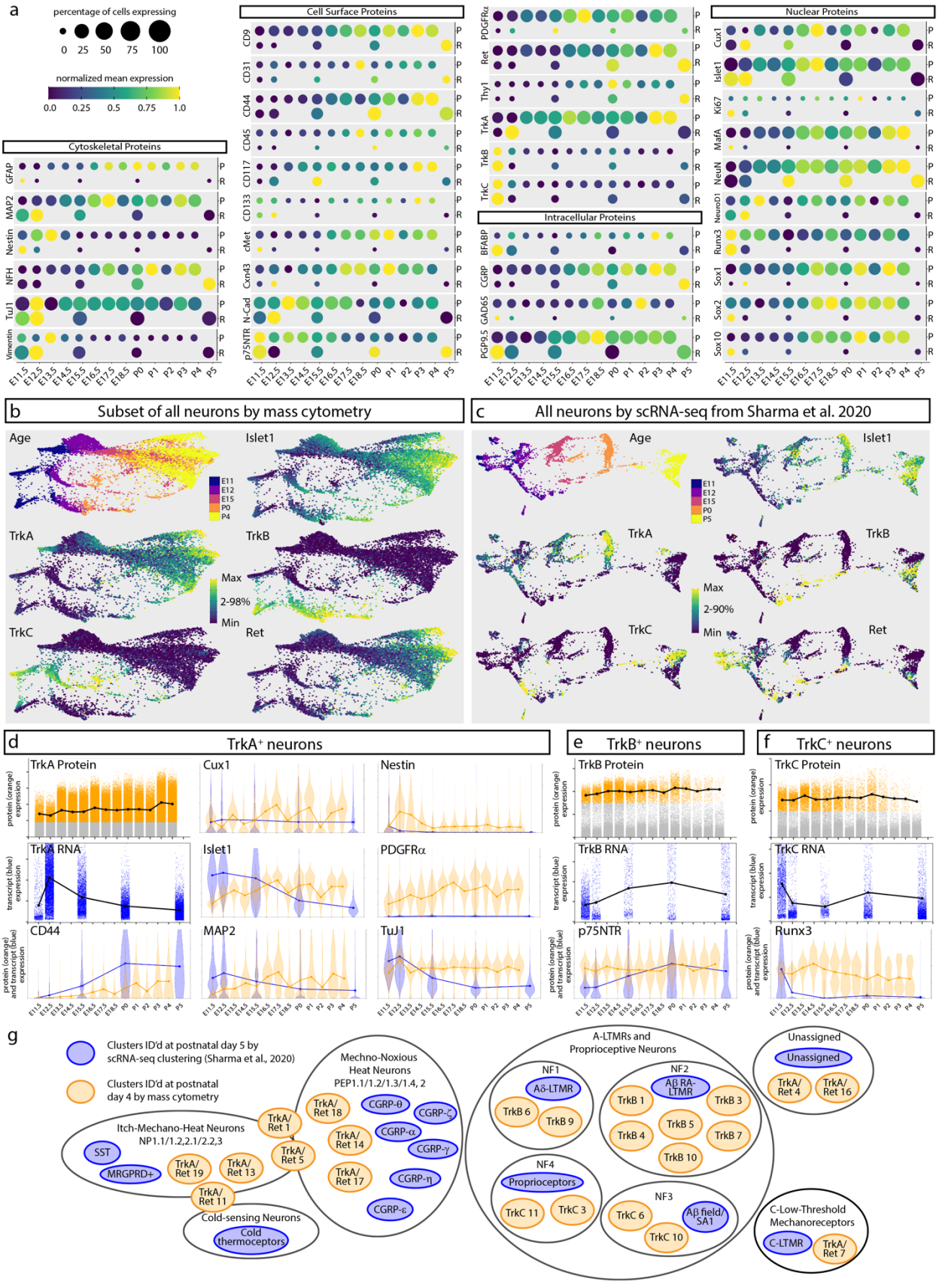
a
percentage of cells expressing
0 25 50 75 100
normalized mean expression
0.0 0.25 0.5 0.75 1.0
Cytoskeletal Proteins
GFAP
MAP2
Nestin
NFH
TuJ1
Vimentin
Cell Surface Proteins
CD9
CD31
CD44
CD45
CD117
CD133
cMet
Cxn43
N-Cad
p75NTR
PDGFRα
Ret
Thy1
TrkA
TrkB
TrkC
Intracellular Proteins
BFABP
CGRP
GAD65
PGP9.5
Nuclear Proteins
Cux1
Islet1
Ki67
MafA
NeuN
Neuro01
Runx3
Sox1
Sox2
Sox10
P
R
E11.5 E12.5 E13.5 E14.5 E15.5 E16.5 E17.5 E18.5 P0 P1 P2 P3 P4 P5
b Subset of all neurons by mass cytometry
Age
Islet1
TrkA
TrkB
TrkC
Ret
E11
E12
E15
P0
P4
Max
2-98%
Min
c All neurons by scRNA-seq from Sharma et al. 2020
Age
Islet1
TrkA
TrkB
TrkC
Ret
E11
E12
E15
P0
P5
Max
2-90%
Min
d TrkA+ neurons
TrkA Protein
Cux1
Nestin
TrkA RNA
Islet1
PDGFRα
CD44
MAP2
TuJ1
protein (orange) expression
transcript (blue) expression
protein (orange) and transcript (blue) expression
e TrkB+ neurons
TrkB Protein
TrkB RNA
p75NTR
f TrkC+ neurons
TrkC Protein
TrkC RNA
Runx3
g
Clusters ID'd at postnatal day 5 by scRNA-seq clustering (Sharma et al., 2020)
Clusters ID'd at postnatal day 4 by mass cytometry
Itch-Mechano-Heat Neurons
NP1.1/1.2,2.1/2.2,3
SST
MRGPRD+
TrkA/ Ret 19
TrkA/ Ret 13
TrkA/ Ret 11
TrkA/ Ret 1
TrkA/ Ret 5
Cold-sensing Neurons
Cold thermoceptors
Mechno-Noxious Heat Neurons
PEP1.1/1.2/1.3/1.4, 2
TrkA/ Ret 18
TrkA/ Ret 14
TrkA/ Ret 17
CGRP-θ
CGRP-ζ
CGRP-α
CGRP-γ
CGRP-η
CGRP-ε
A-LTMRs and Proprioceptive Neurons
NF1
Aδ-LTMR
TrkB 6
TrkB 9
NF2
Aβ RA-LTMR
TrkB 1
TrkB 3
TrkB 4
TrkB 5
TrkB 7
TrkB 10
NF4
Proprioceptors
TrkC 11
TrkC 3
NF3
TrkC 6
Aβ field/ SA1
TrkC 10
Unassigned
Unassigned
TrkA/ Ret 4
TrkA/ Ret 16
C-Low-Threshold Mechanoreceptors
C-LTMR
TrkA/ Ret 7

Figure 7. Comparison of DRG analysis by mass cytometry and scRNA-seq. a, Protein abundance measured by mass cytometry (E11.5 to P4) and mRNA transcript abundance measured by scRNA-seq (E11.5, E12.5, E15.5, P0 and P5; Sharma et al.[19]). Circle size indicates the percentage of cells with expression above marker-specific thresholds. For mass cytometry, the threshold was set at greater than the 99th percentile expression level of low-complexity cells. For scRNA-seq, the threshold was set at zero; all non-zero values were included. Circle color indicates mean intensity of expression within the positive expressing cells. Protein–mRNA pairs are grouped by protein subcellular localization. P, protein (mass cytometry measurements); R, mRNA (Sharma et al. scRNA-seq measurements[19]). **b**,**c**, FLOW-MAP layouts from mass cytometry (25,000 cells downsampled from all neuronal cells; Fig. 4a–c) (**a**) and scRNA-seq (full 32,169-cell dataset[19]) (**b**), colored by age and marker expression level. **d**–**f**, Comparison of protein and mRNA expression levels in TrkA$^+$, TrkB$^+$ or TrkC$^+$ neurons. Positive expressing cells for each RTK were separated from non-expressers (gray) by thresholding for mass cytometry (orange) and scRNA-seq (blue) as described above. Violin plot overlays compare the normalized protein and mRNA abundance in each Trk-expressing population. **g**, Comparison of IHC and RNAscope for TuJ1/*TUBB3* and TrkA/*NTRK1* of L4/L5 DRG at E12.5, E15.5 and P0. IHC scale bar, 100 µm; RNAscope scale bar, 200 µm. **h**–**k**, Quantification of the IHC (**h**,**j**) and RNAscope (**i**,**k**) in **g** for TuJ1/*TUBB3* and TrkA/*NTRK1*. Twenty cells from one or more DRGs per litter with three litters (60 total DRG neurons) were traced per age per technique, and pixel intensity was measured in Fiji for each marker. Statistical analysis: one-way ANOVA using Tukey's multiple comparison test and *P* values *<0.05, ***<0.001 and ****<0.0001. Exact *P* values for **h**: E12 versus E15 $P = 0.0745$, E12 versus P0 $P < 0.0001$, E15 versus P0 $P < 0.0001$; exact *P* values for **i**: E12 versus E15 $P = 0.0492$, E12 versus P0 $P < 0.0001$, E15 versus P0 $P < 0.0001$; exact *P* values for **j**: E12 versus E15 $P = 0.0003$, E12 versus P0 $P < 0.0001$, E15 versus P0 $P < 0.0001$; exact *P* values for **k**: E12 versus E15 $P = 0.0794$, E12 versus P0 $P < 0.0001$, E15 versus P0 $P < 0.0001$. Data are presented as mean values ± s.e.m.

We next compared mass cytometry and scRNA-seq DRG measurements across development at the population level. Due to the larger gaps in developmental time, FLOW-MAP was applied to promote connections between the most similar cells from adjacent timepoints (Ko et al., 2020). Along with the 32,169 scRNA-seq neurons, we analyzed approximately 25,000 mass cytometry neurons, evenly downsampled to approximately 5,000 cells per timepoint (Extended Data Fig. 10a). By mass cytometry, three distinct trajectories correspond to TrkA/Ret (top), TrkB (bottom) and TrkC (middle)

(Fig. 7b); and, by scRNA-seq, two distinct trajectories correspond to TrkA (top) and TrkB, TrkC and Ret (bottom) (Fig. 7c). Islet1 expression increases similarly with age along each trajectory for both datasets.

Because mRNA and protein levels are not well-correlated, one-to-one comparison of mass cytometry and scRNA-seq cell clusters was not feasible. Instead, we used the general and widely accepted TrkA$^+$, TrkB$^+$ and TrkC$^+$ populations (Extended Data Fig. 10b) to compare RNA and protein expression in a more cell-type-specific context (Fig. 7d–f). As in the bulk comparison, we observed markers where RNA and protein levels track closely together; markers where RNA expression precedes the protein (Islet1 in all cell types or CD44 in TrkA$^+$ neurons); markers where the RNA levels swiftly diminish but the protein expression remains high (TuJ1 in all cell types or Runx3 in TrkC$^+$ neurons); and even markers where protein expression precedes the RNA levels (for example, p75NTR in TrkB$^+$ neurons). In agreement with these findings, we observed the same discrepancy between protein and mRNA levels in the two cognate pairs that we selected for validation by IHC and RNAscope: TuJ1/*TUBB3* and TrkA/*NTRK1* (Fig. 7d).

Discussion

Seventy-one neural cell types were identified in this study by their protein expression profiles, using an antibody panel with canonical markers of somatosensory development (Lallemend and Ernfors, 2012) (Fig. 8a). Our panel provided sufficient intersectional coverage to identify cell types even when lacking canonical markers. For example, C-LTMRs could be identified by low TuJ1 expression, even without their canonical marker tyrosine hydroxylase. The high-throughput nature of our dataset, with over 550,000

neurons, revealed rare neurons that co-expressed multiple Trk receptors and over-expressed stem cell markers. Comparison between our mass cytometry results and previous scRNA-seq data highlighted the complex relationship between transcripts and proteins. Thus, this study illustrates that mass cytometry is a high-throughput, scalable platform for developing neural tissues.

An unexpected result of this study was the observation of putative phagocytic events, consistent with previous reports (Wu et al., 2009). We were not intending to investigate this phenomenon, so we did not include glial subtype markers or markers of phagocytosis, such as CD68 (da Silva and Gordon, 1999), Jedi-1 and MEGF10 (Wu et al., 2009), in our antibody staining panel. Based on our gating strategy (Extended Data Fig. 2b), it is unlikely that most putative phagocytic events result from cell doublets, larger aggregates or incomplete dissociation of debris sticking to cells (Extended Data Fig. 5). After additional validation, future studies could investigate whether glial subtypes have different patterns of phagocytic ‘food’ over the course of development and better characterize the molecular nature of these phagocytic events. This approach could provide additional insight into how the somatosensory nervous system is sculpted by axonal pruning and phagocytosis of whole cells and track the switch from phagocytosis by glial precursor cells to phagocytosis by macrophages later in development.

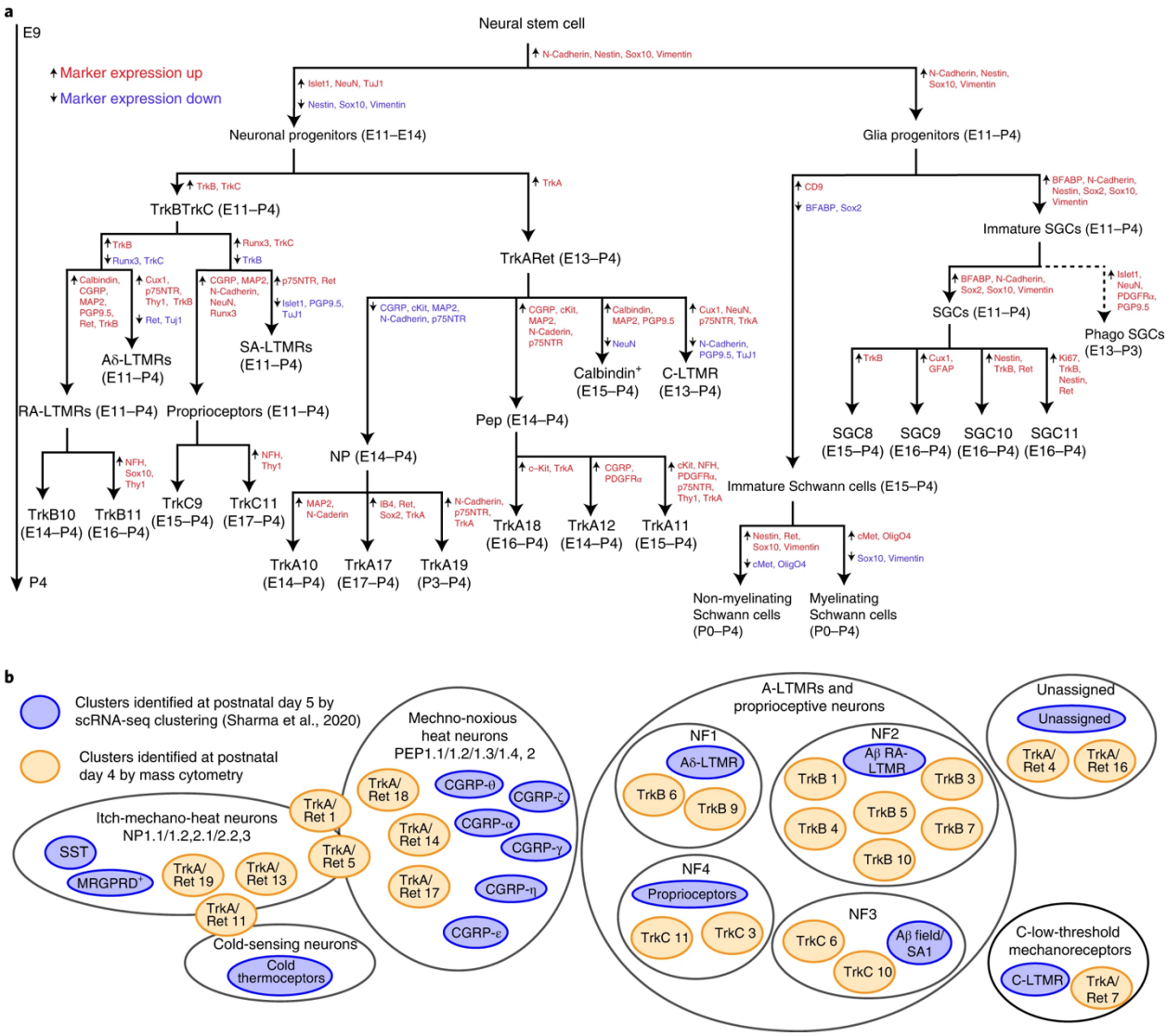

Figure 8. Somatosensory maturation and development in the DRG. a, Expression level overlap from analysis in Fig. 7 between the cell types identified by mass cytometry at P4 (orange) and scRNA-seq at P5 (ref. [19]) (blue). **b**, Summary diagram of DRG cell populations identified by mass cytometry analysis. Marker expression changes between segments are indicated by upward arrows, with red text denoting marker expression increases and downward arrows with blue text denoting marker expression decreases. The age range where each population comprises at least 1% of that cell type (for example, a neuronal cell type is at least 1% of all neurons, not all cells) is indicated beside each population label.

As illustrated in the discussion of putative phagocytic glia, an important caveat for single-cell analyses of neural tissue is that cell processes, such as axons, dendrites, glial feet and ensheathing membranes, can be ripped away during tissue dissociation. For cell identification of neurons, the loss of pre-synaptic markers is more problematic than post-synaptic markers, because the latter can also be detected in synapses on the cell body. Many axonal and dendritic proteins are synthesized in the cell body and can be detected here, too, although at lower levels. Glial process shearing can result in neurons appearing to express ensheathing membrane markers from glial cells, although neuronal identity can be confirmed by the lack of glial nuclear proteins. In this case, the wrapping membranes can be viewed as an additional level of characterization for the neuron's phenotype and maturity.

Another caveat for single-cell analysis of neural tissue is the potential for biased loss of specific cell types during dissociation and processing. This could be due to more fragile cell types lysing during cell dissociation or stickier cell types adhering to the inner walls of storage and processing tubes. Another potential source of biased cell loss is incomplete tissue dissociation, because the cells present in non-dissociated tissue are filtered out with a 40-μm strainer and lost to analysis. To validate the abundance levels of specific cell types, IHC can be applied to tissue slices (Fig. 2). Additionally, the metal-labeled antibodies described in this study can also be used for imaging mass cytometry (IMC) (Giesen et al., 2014) or multiplexed ion beam imaging (MIBI) (Angelo et al., 2014). The multi-Trk^{+} neurons that we identified in this study may represent transient cell states that can react to neurotrophic factors and switch cell fates if necessary, possibly related

to previous work that showed cell-state-specific differentiation outcomes from the same neurotrophin stimulus (Luo et al., 2007). A signaling mass cytometry approach that combines antibodies for cell identity markers with antibodies for cell signaling molecules, such as phospho-specific antibodies, could facilitate a mechanistic investigation of these downstream pathways and cell states in every somatosensory cell type simultaneously, to determine how the internal cell signaling response to neurotrophins, such as NGF, NT-3, BDNF and GDNF, differs between cell types and contributes to cell fate and survival decisions. Another aspect of cell state, receptor internalization, could be added to this analysis by staining with one antibody before permeabilization and the same antibody with a different metal label after permeabilization, to investigate the distinct roles of surface versus internalized receptors (Kuruvilla et al., 2004).

Expression profiles from scRNA-seq have previously been used to define DRG cell types, but mRNA expression cannot directly predict protein expression and functional cell states. For example, translational control, protein degradation and incomplete trafficking or internalization of surface proteins may result in high levels of mRNA but no protein present. On the other hand, mRNA degradation may result in high levels of long-lived proteins but no mRNA remaining present. The discrepancy between RNA and protein is thought to be largest during dynamic cell transitions (Liu et al., 2016; Reimegård et al., 2021), such as DRG development. We, therefore, sought to determine how well scRNA-seq could predict protein expression and functional cell states in the DRG (Sharma et al., 2020). In direct comparison, many protein–mRNA cognate pairs showed poor agreement across timepoints, highlighting the value of protein-level measurements by mass

cytometry to identify functional cell states in the DRG. The mechanisms that control these observed differences are likely to be different for each protein–mRNA cognate pair and could change considerably across developmental stages and between cell types. This could be investigated further by parallel measurement of split samples with scRNA-seq and mass cytometry and by performing CITE-seq to simultaneously detect protein and RNA at the single-cell level, although this technique is limited to cell surface proteins (Stoeckius et al., 2017).

Although the cell types defined by clustering of mass cytometry or scRNA-seq datasets are not expected to correspond perfectly, we were still interested to compare their similarities and differences. Because Ginty and colleagues found that early DRG timepoints were transcriptionally unspecialized (Sharma et al., 2020), we decided to focus on their P5 cell type clusters and manually compare these with our P4 mass cytometry-based clusters. The two methods identified similar cell types, but, interestingly, both methods found subpopulations not present in the other study (Fig. 8b). For example, although scRNA-seq identified six CGRP subtypes, mass cytometry discerned at least three. Alternatively, although scRNA-seq identified a single cluster of Aβ RA-LTMRs, mass cytometry identified six molecularly distinct Aβ RA-LTMRs at P4. These similar (yet complementary) results were obtained by mass cytometry with a panel of just 41 markers, compared to the transcriptome-level measurements by scRNA-seq. Although proper antibody selection and panel design is critical for successful identification of specific cell types by mass cytometry, these results suggest that the relatively limited number of measurement parameters is not an impediment to deep cell profiling, whereas the high

sample throughput of mass cytometry facilitates replicate analysis and characterization of rare populations, such as the multi-Trk neurons.

The neural mass cytometry platform developed in this study and the resulting cell atlas of somatosensory development will facilitate future mechanistic studies to characterize the effects of specific genetic or pharmacological perturbations on DRG development. Additionally, further optimization of tissue dissection and cell dissociation techniques for adult DRG tissues could expand our roadmap of embryonic and postnatal development to include DRG maturation and adult states, an important piece of the puzzle for studies linking animal behavior to cell population-level changes. Collectively, our mass cytometry analyses of the developing DRG demonstrate replicable ground truths associated with somatosensory development and provide a platform for future studies to ask fundamental developmental questions with enhanced speed and resolution.

Chapter IV: Conclusions, Perspectives and Future Directions

Figure 4 in this chapter was previously published in “Sexual dimorphism in the dorsal root ganglia of neonatal mice identified by protein expression profiling with single-cell mass cytometry.” Shayla Vradenburgh, Amy Van Deusen, Allison Beachum, Jacqueline Moats, Ashley Hirt, Christopher Deppmann, Austin Keeler, Eli Zunder. *Molecular and Cellular Neuroscience.* 2023;126:103866.

Development of the nervous system requires precisely controlled differentiation, maturation, and integration of neural and nonneural cell types. However, we are only beginning to understand the molecular and cellular complexity involved in orchestrating this developmental symphony. The most comprehensive databases of molecular expression in the nervous system, such as those maintained by the Allen Institute (http://brain-map.org) and National Institutes of Health (http://www.ncbi.nlm.nih.gov/geo), are heavily focused on mRNA expression. However, as our results show (Chapter II Figure 4 and Chapter III Figure 7), mRNA expression does not perfectly correlate with protein expression.

In this thesis, we leveraged the high throughput of mass cytometry to profile expression of 40 proteins in millions of cells in the mouse brain (i.e., telencephalon, diencephalon, mesencephalon, and rhombencephalon) and DRG at daily time points from embryonic E11.5 to P4. No previous study has molecularly profiled single cells from these tissues at daily time points across embryonic and postnatal development, and no single-cell omics study to date has quantified protein instead of mRNA abundance levels in the developing mouse nervous system.

In this chapter, we highlight our key conclusions and discuss mechanisms to expand our findings to a broader array of neuroscience applications. Finally, we conclude with thoughts on future efforts to generate a complete molecular and cellular atlas of the mammalian nervous system.

Mass Cytometry is a Validated Method to Analyze Neural Cells

Our first goal was to establish methodologies that would allow mass cytometry to be used for analysis of neural cells. To achieve this, we initially performed preliminary experiments with neural cell lines (i.e., Neuro2A, N1E-115, GL261, OPC-1052, and OPC-8713) to provide proof-of-principle. Next, to adapt mass cytometry for analysis of neural tissues, we optimized protocols for dissociation of mouse brain and DRG into single-cell suspensions. As demonstrated by the results presented in Chapters II and III, our protocols are capable of generating sample preparations with high percentages of single viable cells, low amounts of cellular debris, and relatively few cell aggregates.

We next used our optimized cell preparations to develop a library of primary antibodies suitable for identifying neural and nonneural cell types in neural tissues. In total, we validated over 150 surface and intracellular antibodies for neural tissues and cell lines, including transcription factors, neurofilaments, neurotrophic receptors, enzymes, and other factors relevant to cell identity and functions in neural tissues (Figure 1). Given the number of key markers for neural cell identity that were validated (e.g., Sox2 for NSCs, Tbr2 for INPs, NeuN for neurons, and Islet1 for sensory neurons), publication of this resource provides a strong foundation for researchers seeking to incorporate mass cytometry or IMC in the future.

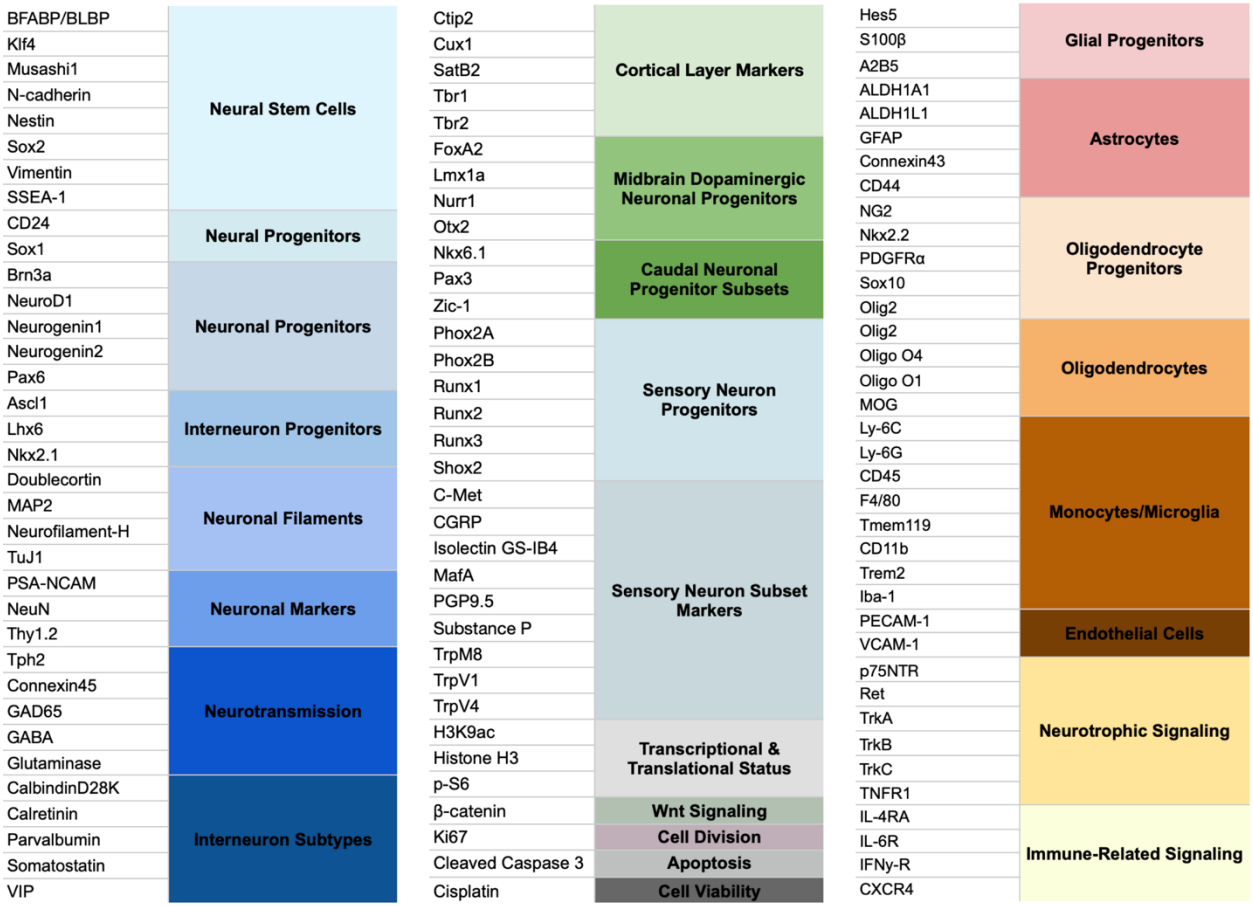

Figure 1. Validated antibody library for mass cytometry of neural cells and tissues. Primary antibodies are organized according to the cell type or process with which they are associated.

Next, we optimized parameters for isolating single-cell events from raw mass cytometry data. In addition to approaches generally applied for all mass cytometry studies (i.e., bead-based signal normalization, marker scaling, iridium-based identification of singlets, and removal of metal contaminants), we identified optimal strategies for previously reported barcoding, batch correction, and platinum-based viability staining protocols. Moreover, we defined neural tissue-specific parameters for cleanup gating, such as the removal of neurite debris, which is essential for faithfully isolating neuronal cells. We also describe observations of neural marker positivity for nonneural cells (e.g., microglia and

mural cells positive for TuJ1) and how interactions between different cell types must be taken into consideration when analyzing protein expression data using mass cytometry.

To further validate our observations of protein expression in cells isolated from neural tissues, we corroborated trends observed by mass cytometry with the more traditional approach of IHC and fluorescence microscopy. As shown in Figure 2 of Chapter II and Figure 2 of Chapter III, our results confirm that trends for relative proportions of marker-expressing cells were largely consistent between mass cytometry and IHC measurements for both the brain and DRG.

Altogether, the methods, materials, and analytical strategies published as part of this thesis provide the foundation for future mass cytometry-based studies of neural tissues.

First Protein-Based Atlas of Embryonic and Postnatal Mouse Brain Development

Our next goal was to generate a high-dimensional protein-based atlas of mouse brain development using mass cytometry. To achieve this, we selected a 40-antibody panel (Chapter II, Table 1) of markers relevant to CNS development from our validated antibody library and analyzed samples collected at daily time points from E13.5 to P4. As shown in Figure 1 of Chapter II, UMAP and Leiden clustering yielded 85 distinct clusters, including 49 neural cell clusters, 33 nonneural cell clusters, and three unidentifiable (apoptotic or low-complexity) clusters. In total, 97.84% of all cells examined in the brain were classified as specific cell types by their protein expression profile, localization (i.e., telencephalon, diencephalon, mesencephalon, or rhombencephalon), and age.

Our results also allowed us to observe changes in the abundances of neural and nonneural cells during brain development. The large proportions of NSCs and neuronal cells observed during embryonic ages decreased before birth, whereas glial cells expanded perinatally and nonneural cells steadily increased (Chapter II, Figure 3). However, as expected, trends for each of these cell types varied across the different regions of the developing brain. For example, proportions of neural progenitors were highest at early ages (E13.5–E16.5) in the telencephalon but steadily increased only after E15.5 in the rhombencephalon, consistent with high levels of postnatal neurogenesis in the cerebellum (Carter et al., 2018; Wizeman et al., 2019).

Because this is one of the first reported mass cytometry datasets for neural cells, we evaluated the robustness of our clustering results using several methods. Our examinations of both technical (Chapter II, Figure 3i–k) and biological (Chapter II, Figure 3b; Appendix I, Extended Data Figure 5) reproducibility show that our analytical approach employing UMAP and Leiden clustering is robust for mass cytometry analysis of brain tissues.

First Protein-Based Atlas of Embryonic and Postnatal Mouse DRG Development

Given our success evaluating cell populations in the developing mouse brain, we also generated a protein-based atlas of cells present in the developing mouse DRG from E11.5 to P4. By selecting a 41-antibody panel including markers of somatosensory neuron subtypes and tissue-resident nonneural cell populations, we identified 41 neuronal

populations, 30 glial populations, and 5 nonneural cell populations, together encompassing over 95% of cells examined. Approximately 75% of cells were identified as neural subtypes (i.e., neurons, stem cells/glial progenitors, SGCs, Schwann cells), approximately 20% were nonneural cells (i.e., VSMCs, endothelial cells, and leukocytes), and the remaining 5% were unidentifiable due to a lack of marker expression.

We also investigated how abundances of these cell types changed over the course of development. Consistent with previous studies (Cheng et al., 2018; Crowley et al., 1994; Fariñas et al., 1996; Patel et al., 2000; White et al., 1998, 1996), we observed increases in the relative abundances of neurons until E16.5, followed by a sustained decrease in neurons that coincided with increasing proportions of glial progenitors (Chapter III, Figure 1f). Similar to our observations for the mouse brain, nonneural cells such as leukocytes, endothelia, and VSMCs consistently increased in abundance as development proceeded.

Importantly, although our panel did not include TH or other markers frequently used to identify certain somatosensory neuron subtypes, we had sufficient intersectional coverage to identify cell types even in the absence of these markers. These results demonstrate both the benefit of having more than 40 biomarkers and power of thoughtful antibody panel design.

Mass Cytometry Permits Quantification of Rare Cell Populations in Neural Tissues

With the ability to assess up to 1×10^6 cells per hour, mass cytometry allows for characterization and quantification of rare cell populations in neural tissues. This feature is useful for evaluating cells undergoing molecular transitions, which may be infrequent or occur rapidly, and especially important for investigation of neural tissues given the uniqueness of certain neuronal subtypes.

As shown in Figure 1 of Chapter II, we were able to observe small populations of cells expressing Pax6 and Olig2, as well as a subset of dopaminergic neuronal progenitors in the mouse brain. Similarly, as shown in Figure 6 of Chapter III, we were able to discern small populations of sensory neurons positive for multiple tyrosine kinases (i.e., TrkA, TrkB, and TrkC), representing transient differentiation states, that were confirmed by IHC. Together, these results validate our ability to resolve small populations of cells with mass cytometry.

Although neither of the antibody panels used for these studies set out to identify rare cell types, we nonetheless were able to observe these populations with ease thanks to the number of cells we analyzed and our robust high-dimensional analysis pipeline. In the future, we hope to apply this functionality to distinguish molecular and cellular mechanisms underlying disease phenotypes, especially those believed to be driven by changes in transient or low-abundance cell types.

Protein and mRNA Expression Are Discordant During Nervous System Development

Both mRNA and protein expression are frequently used to characterize cells, however there is no universal method to accurately predict protein abundances from mRNA expression levels, or vice versa (Liu et al., 2016). To compare how protein and mRNA expression profiles vary in the developing mouse nervous system, we compared our protein-based mass cytometry results with mRNA-based measurements of scRNA-seq.

We first compared our antibody-based mass cytometry measurements of mouse brain tissues with age- and tissue-matched scRNA-seq measurements from Linnarsson and colleagues (La Manno et al., 2021). As shown in Chapter II Figure 4a, expression profiles of markers key for identifying specific cell types were mostly congruent, although the highest levels of mRNA expression tended to precede or coincide with the highest levels of protein expression for many markers.

To take a closer look at how evaluating cells by mRNA or protein positivity affects quantification of relative cell abundances in the developing brain, trends for relative percentages of nestin- and Tbr2-positive cells were confirmed by IHC and RNAscope in the mouse telencephalon (Chapter II, Figure 4b,c). At nearly every age examined, proportions of positive cells evaluated by mRNA expression were much lower than those measured by protein expression. Moreover, the localization of positive cells varied slightly, with *Tbr2*-positive cells being observed closer to the ventricle than Tbr2-positive cells (Chapter II, Figure 4c).

As shown in Figure 7 of Chapter III, direct comparison of many protein–mRNA cognate pairs in the DRG resulted in poor agreement across timepoints. A more refined analysis comparing our results for P4 DRG with those published by Ginty and colleagues for P5 DRG (Sharma et al., 2020) revealed that each method identified cell types not identified by the other method (Chapter III, Figure 8). These results suggest the using a limited number of measurement parameters does not necessarily impede the identification of cell subtypes in single-cell samples. Moreover, because mass cytometry can easily be used to quantify protein expression in millions of cells, it affords the ability to run numerous sample replicates and capture rare cell populations, as discussed above.

We did not expect our comparisons of mRNA and protein to perfectly match because of differences in mRNA and protein production, regulation, and trafficking, as well as artifacts associated with comparing tissue sections to dissociated samples of whole tissue. However, trends for mRNA expression were consistent between scRNA-seq and RNAScope, while trends for protein expression were consistent between mass cytometry and IHC (Chapter II, Figure 4).

In summary, our results highlight the need for protein-based measurements to corroborate the many findings reported from *in situ* hybridization, microarray, scRNA-seq, and other approaches quantifying mRNA. Future investigations would benefit from parallel measurement of split samples with scRNA-seq and mass cytometry, or use of an alternative method capable of simultaneously detecting protein and RNA at the single-cell level [e.g., CITE-seq (Stoeckius et al., 2017)].

Pseudotime-Based Trajectory Analysis Replicates Canonical Molecular Progressions of Neural Cell Differentiation

Mapping the molecular trajectories underlying cell fate decisions during brain development will facilitate understanding of neurodevelopmental disorders such as ASD (Courchesne et al., 2007) and epilepsy (Bozzi et al., 2012; Nickels et al., 2016), as well as neurological diseases that may originate during development, such as schizophrenia (Owen et al., 2011; Nour and Howes, 2015) and Alzheimer's disease (Bothwell and Giniger, 2000; Arendt et al., 2017). Therefore, we next sought to use our high-dimensional, single-cell protein expression profiles to evaluate the molecular trajectories underlying differentiation of specific neural cell types. To achieve this, we employed URD (Farrell et al., 2018), which is just one of many trajectory-inference approaches developed to predict molecular progressions based on scRNA-seq data (Saelens et al., 2019). Although we evaluated several of these approaches, we chose URD because of its tree-based approach, scalability, and user-friendliness.

Initially, we evaluated changes in protein expression associated with early specification of neuronal and glial progenitors/precursors in NSCs from all brain regions and ages. As shown in Figure 5 of Chapter II and Figure 7 of Chapter III, URD analysis of $Sox2^{high}nestin^{high}$ cells (excluding endothelial cells, nonneural cells, and microglia/macrophages) predicted early separation of neuronal and glial trajectories based on expression of Pax6, Tbr2, and DCX. Further separation of individual neuronal and glial trajectories was based on decreasing expression of stem/progenitor cell markers

(e.g., Pax6, CD24, and N-cadherin) and increasing expression of mature markers (e.g., NeuN for neuronal progenitors, GLAST for glial progenitors, and Olig2 for OPCs).

Next, we used URD to examine the molecular progressions underpinning differentiation and maturation of neural cells in the mouse telencephalon. As shown in Figure 6 of Chapter II, the predicted trajectories for cortical excitatory neurons displayed canonical (Englund et al., 2005) downregulation of Pax6 coinciding with upregulation of Tbr2, which subsequently decreased as NeuroD1, Tbr1, TuJ1, and NeuN increased. Similarly, the predicted trajectory for OPCs exhibited high Olig2 expression from an early age and sequential increases in PDGFRα, Sox10, and OligoO4, consistent with the reported molecular sequence for OPC specification and maturation into oligodendrocytes (Lu et al., 2000; Tekki-Kessaris et al., 2001; Zhou et al., 2000).

Similar results were observed for Schwann cells in URD analysis of the DRG. Initially, these cells expressed nestin, vimentin, and Sox10 before downregulating these markers in favor of cMet and OligoO4 (Chapter III, Figure 3). In addition, evaluation of somatosensory neuron differentiation with URD replicated the molecular trajectories of distinct Trk-positive progenitors (Chapter III, Figure 5) previously reported in the literature (Lallemend and Ernfors, 2012).

Based on these results, we conclude that analysis of protein expression levels along URD pseudotime trajectories can accurately predict the relative timing and sequence of molecular transitions contributing to neural cell specification.

Pseudotime-Based Trajectory Analysis Predicts Two Distinct Pathways for Generating OPCs

In addition to replicating canonical molecular progressions of neural cell differentiation, URD predicted two pathways by which OPCs can be generated from NSCs in the developing mouse brain (Chapter II, Figure 5). In the first pathway, NSCs directly differentiate into OPCs by increasing expression of Olig2, followed sequentially by PDGFRα and Sox10. In the second pathway, NSCs indirectly produce OPCs by proceeding through a $BLBP^{high}GLAST^{high}$ intermediate state before sequentially upregulating PDGFRα and Sox10. Although we have yet to validate these novel findings with an appropriate confirmatory method, they are consistent with previous reports of O2A cells (Baracskay et al., 2007).

Mass Cytometry is Useful for Evaluating Phagocytosis in Neural Tissues

Although mass cytometry has previously been employed to evaluate microglia and other hematopoietic lineages in the nervous system (Mrdjen et al., 2018; Ajami et al., 2018; Li et al., 2019; Böttcher et al., 2019; Fu et al., 2020b, 2020a; Ormel et al., 2020; Xie et al., 2022), none of the previous studies included markers for neural cells. In contrast, the antibody panels we applied to evaluate the brain and DRG only included a few markers of microglia/macrophages (e.g., CD45 and CD11b) and numerous neural markers. Fortuitously, this combination allowed us to observe populations of cells known to display phagocytic functions (e.g., macrophages, microglia, and glial progenitors) in both the brain and DRG.

As shown in Figure 7 of Chapter II and Extended Data Figure 9 (Appendix I), microglia and macrophages were observed from the earliest age examined (E11.5) in the brain and gradually increased in proportion. However, populations of microglia with engulfed neuronal cells and neurite debris displayed trends that coincided with peaks of neurogenesis in the forebrain and mesencephalon. Further, proportions of microglia with presumptive myelin cargo (OligoO4$^+$ microglia) increased in a caudal-to-rostral manner that mimics reported myelination patterns in the brain (Inder and Huppi, 2000; Jakovcevski and Zecevic, 2005; Kanfer et al., 1989; Verity and Campagnoni, 1988).

In the DRG, populations of cells containing presumptive phagocytosed cargoes were not just limited to hematopoietic lineages. Glial precursors, which were previously demonstrated to phagocytose dying neurons in the DRG prior to infiltration of macrophages into this tissue (Wu et al., 2009), were also positive neuronal markers (e.g., Islet1, NeuN and TuJ1) (Chapter III, Figure 3l–o). These results were confirmed by IHC, which showed BFABP$^+$ immature glial precursors phagocytosing Islet1$^+$ neuronal fragments (Chapter III, Figure 3r).

Future Directions

Current phenotyping approaches demand thousands of personnel hours for data collection and analysis, but often yield highly oversimplified depictions of cell identity, developmental origin, and behavior. By overcoming limitations accompanying fluorescence-based methods to examine protein expression (Bendall et al., 2011), mass cytometry allows one individual to do in an afternoon what previously would have taken years – conveying enormous potential to explore previously unidentified cell subtypes,

developmental pathways, and phenotypes. Given the successes and limitations described in this thesis, we believe that there are several avenues to move forward.

Profiling Cellular Phenotypes During Neurodevelopment Disorders

The antibody panels described Chapters II and III of this thesis permitted identification of over 97% of cells in the brain and over 95% of cells in the DRG of C57/BL6 mice from E11.5 to P4. In addition to providing baseline values for the abundances of major neural and nonneural cell types in this frequently used research model, our findings immediately enable quantification of global changes in cellular composition during mouse nervous system development. Application of our methodology to models of neurodevelopmental disorders promises to enhance and expedite these investigations.

Preliminary studies we performed in partnership with Dr. Noelle Dwyer (UVA Department of Cell Biology) demonstrate proof of this principle. Previously, the Dwyer laboratory showed that mice homozygous for a mutation in *Kif20b* (*Kif20b*^{magoo}) display reduced cortical thickness (Figure 2a) and size (Figure 2b) compared with their heterozygous littermates (Janisch et al., 2013). Our subsequent mass cytometry analysis reveals apparent reductions in BLBP^{high}GLAST^{high} cells and Olig2^{high} cells (corresponding to glial precursors and OPCs, respectively) in the telencephalon of *Kif20b*^{magoo} homozygous mice at P0 compared with their wild-type and heterozygous littermates (Figure 2c). Although further studies are necessary to verify these findings, they demonstrate the potential of mass cytometry to immediately improve our understanding of neurodevelopmental

phenotypes, especially those underlying structural abnormalities (e.g., microcephaly, macrocephaly, and cortical dysplasia).

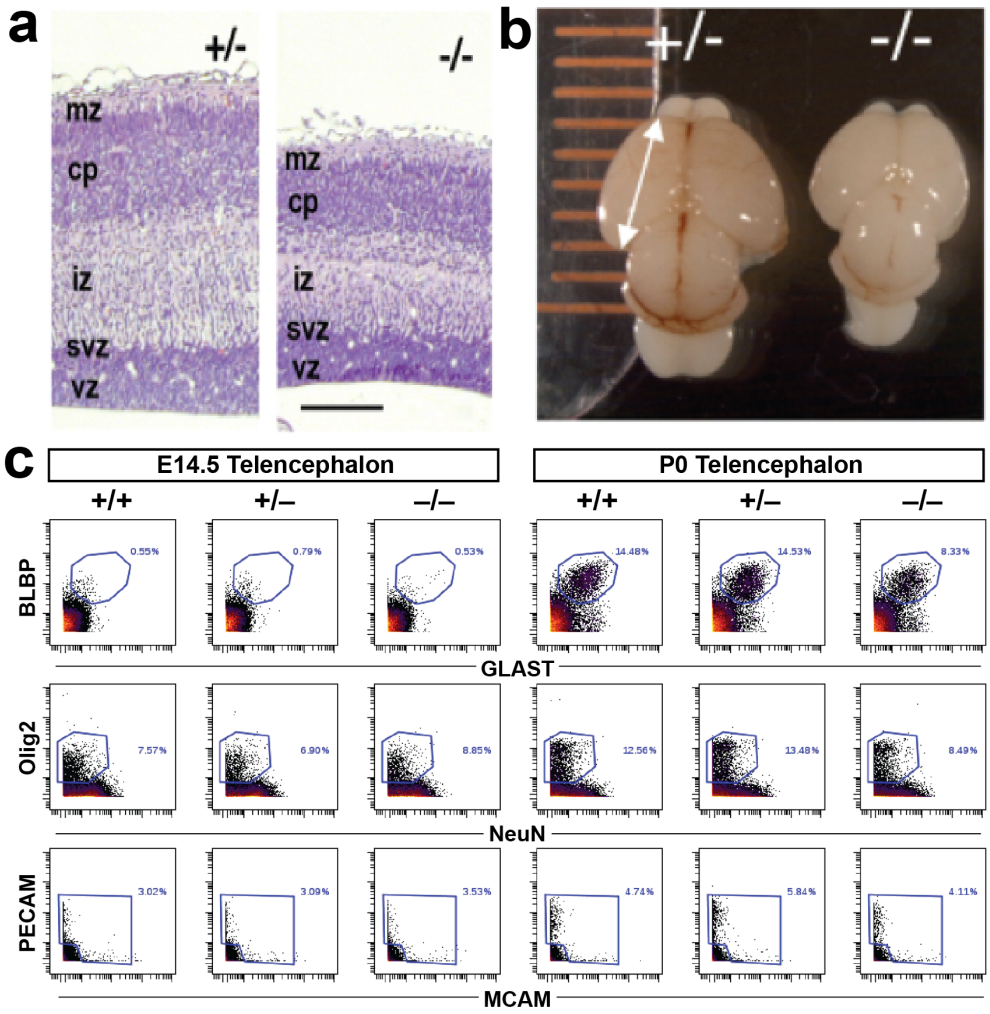

Figure 2. Evaluation of *Kif20b*^{magoo} mutant mice with mass cytometry. a, Dorsal view of *Kif20b*^{magoo} heterozygous control (+/-) and homozygous mutant (-/-) mouse cortices at E18.5. **b**, Cortical sections from comparable levels of P0 control and homozygous *Kif20b*^{magoo} mutant littermates stained with hematoxylin and eosin. mz, marginal zone; cp, cortical plate neurons; iz, intermediate zone; svz, subventricular zone; vz, ventricular zone. Scale bars, 100 μm. Panels **a** and **b** were originally published in Janisch, et al., 2013. The vertebrate-specific kinesin-6, Kif20b, is required for normal cytokinesis of polarized cortical stem cells and cerebral cortex size. *Development*. Reprinted with permission from The Company of Biologists Ltd. (License No. 1422232-1). **c**, Biaxial plots (cytobank.org) showing expression of glial markers BLBP and GLAST, OPC marker Olig2, neuronal marker NeuN, mural cell marker MCAM, and endothelial cell marker PECAM in E14.5 and P0 telencephalon, as measured by mass cytometry.

In addition, the broad approach afforded by mass cytometry will be useful to investigate more profound neurodevelopmental disorders, such as autism spectrum disorder (ASD). In partnership with Dr. John Lukens (UVA Department of Neuroscience), we performed experiments to evaluate mouse brain development in the context of maternal immune activation (MIA), a hypothesized cause of both ASD and schizophrenia. Modeling MIA in the laboratory can be achieved with application of either immunogenic approaches [e.g., infection, lipopolysaccharide, or polyinosinic:polycytidylic acid (polyI:C)] or valproic acid to pregnant mice at a critical period of development (around E12.5) (Woods et al., 2021). Although male mice display MIA-associated phenotypes at a higher rate than females (Xuan and Hampson, 2014), the mechanisms underpinning susceptibility of males (or conversely protection of females) are not well understood. Although preliminary, our results demonstrate increases in the relative proportions of NeuroD1^{high} and Tbr1^{high} cells at E14.5 in males from polyI:C-injected dams compared with their female littermates and control males from saline-injected dams (Figure 3), consistent with reports of increased numbers of neurons in male children diagnosed with ASD (Courchesne et al., 2007).

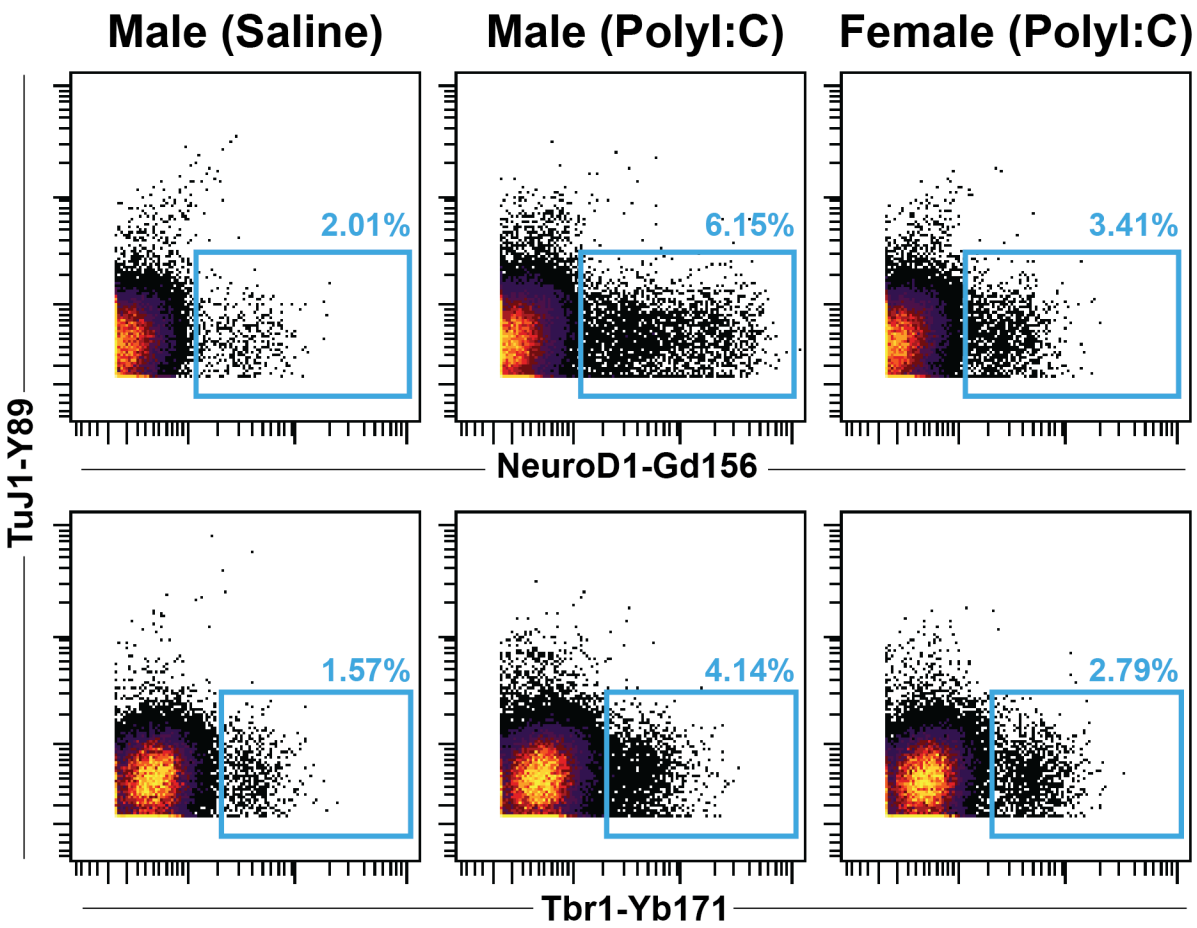

Figure 3. Comparison of neuronal cells in maternal immune activation model mice using mass cytometry. Biaxial gating (cytobank.org) of TuJ1, NeuroD1, and Tbr1 expression in sindividual telencephalic cells of E14.5 mice from saline-injected and polyI:C-injected dams.

Notably, although individuals with ASD experience can experience a diverse array of sensory effects [e.g., auditory sensitivity, hyperesthesia, increased tolerance to pain, oronasal effects, and visual disturbances (Leekam et al., 2007)], how transmission of this information is altered at cellular and tissue levels remains largely unknown. The antibody panel described in Chapter III permits quantification of the abundances and molecular profiles of somatosensory neurons, glia, and nonneural cells in the DRG. Applying our approach to ASD models may finally shed light on changes driving some of the sensory phenotypes observed in individuals with ASD.

Defining Sex-Related Differences in Nervous System Development and Disease

The contribution of sex to developmental and disease-related phenotypes is only beginning to be appreciated, primarily because the bulk of previous studies employed only male samples to save on cost and reduce complexity. Thanks to the high throughput and high dimensionality of mass cytometry, future studies of the CNS and PNS can more easily evaluate the differences between sexes that are important for health and disease.

Indeed, we have already used this atlas to design an antibody panel to evaluate sexual dimorphism in sensory neuron specification during mouse DRG development (Figure 4). These experiments, performed by Dr. Shayla Vradenburgh, show significant increases in the relative abundances of endothelial cells in males (Fig. 4d) and neuronal cells in females (Fig. 4f) that were confirmed by IHC (Fig. 4m, n) (Vradenburgh et al., 2023).

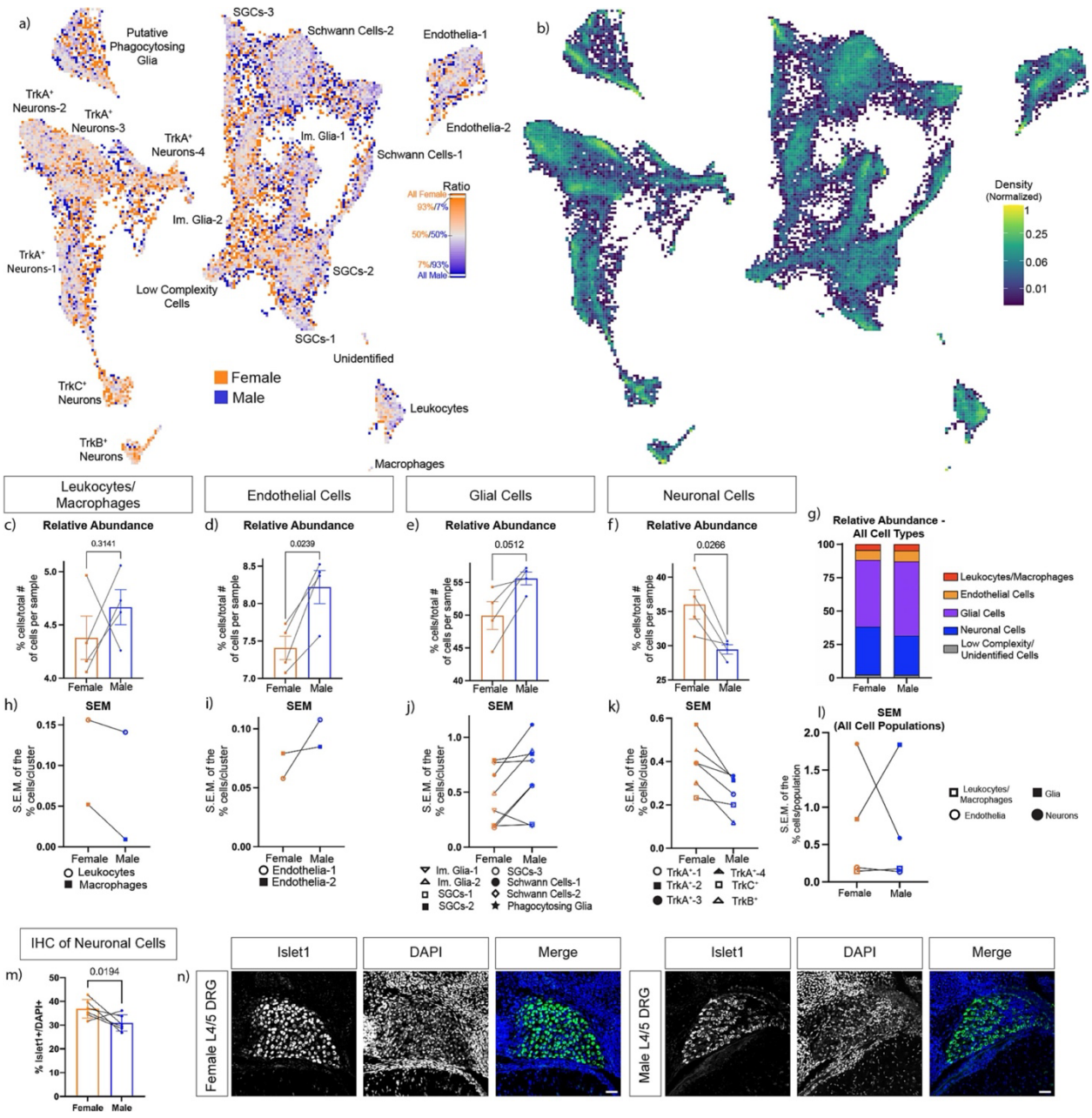

Figure 4. **Sexual dimorphism within general cell populations in the DRG.** a) Relative abundance UMAP of all cells colored by which sex has the highest relative abundance for each bin. b) Density UMAP showing the normalized density of cells within each bin. c-f) Graphs depicting the relative abundance in female and male pups of the four general cell populations identified in Fig. 1 – leukocytes/macrophages (c), endothelial cells (d), glial cells (e), and neuronal cells (f). g) Stacked bar graph depicting the average relative abundance for all females and all males colored by the different cell types. Low complexity and unidentified cells were included in this graph and are colored in gray. h–k) Graphs depicting the SEM of the relative percentage of

cells present for each male and female sample in distinct clusters within each cell population – leukocytes/macrophages (h), endothelial cells (i), glia (j), and neurons (k). l) Depiction of the SEM calculated on the combined relative percentage of cells for each male and female sample within the different clusters that form the four broad cell populations. m) Proportion of Islet1^{+} cells out of all DRG cells (DAPI^{+}) by IHC. One to eight DRG sections were imaged and analyzed for up to two animals per litter for six litters for each sex. Counts from all sections from a single litter were averaged. n) Representative IHC images of P0 L4/L5 DRGs with anti-Islet1 and DAPI quantified in (m). Scale bar = 50 μm Bins = 200 for subpanels (a) and (b). Connecting lines in subpanels (c)–(f) and (h)–(m) signify females and males from the same litter.

At present, it is difficult to predict the extent to which sex-related differences contribute to observed neurological phenotypes because so little information is available. However, recent technological advancements (e.g., omics and machine learning) and an increased focus on sex and gender equity in scientific research (Heidari et al., 2016) are helping to fill this void. Doing so will finally allow researchers to address such questions as:

- How are male and female brains different at a cellular level?
- Is there a molecular/cellular foundation for gender identity?
- Why are males more susceptible to dyslexia, autism, schizophrenia, Parkinson's disease, and brain cancer?
- Why are females more susceptible to migraines, chronic pain, and multiple sclerosis?
- Why does epilepsy manifest differently in males and females?
- How do females effectuate higher tolerances to pain than males?

The answers to these questions may substantially impact how we view the nervous system and potentially, human identity. In addition, better understanding of the molecular

and cellular differences between sexes may have significant implications for how we treat neurological disease.

Deep Profiling of Neural Cell Types

Perhaps the most obvious extension of the work described in this thesis is the performance of studies targeted at a specific cell type or differentiation pathway. As shown in Figure 1, we have already validated numerous antibodies to further refine the identities of neural and nonneural cells, as well as characterize their intracellular signaling (e.g., S6 phosphorylation, H3K9 acetylation, and caspase-3 cleavage). Based on our experience validating these antibodies and mapping cells in the developing mouse nervous system, we believe that some ideal applications of mass cytometry-based deep profiling include:

- Defining sequences of transcription factor expression underlying specification, differentiation, and maturation of specific neural cell types;
- Establishing specific biomarkers to distinguish astroglia from neural stem cells;
- High-dimensional profiling of cell surface receptors key for neuronal identity;
- Increasing molecular resolution of cells in established neural circuits (e.g., refining the identities of neurons involved in appetite control in the arcuate nucleus); and
- Multiplexed evaluations of developmental and pathological cell death in the nervous system (e.g., apoptosis, necroptosis, and pyroptosis).

Lineage-Tracing Studies to Probe Neurogenesis and Gliogenesis

The entire milieu of neuronal and glial cells found in the adult CNS and PNS originate from two relatively homogenous population of stem cells, NSCs (Götz and Huttner, 2005) and NCCs (Stemple and Anderson, 1992). However, the molecular pathways and transitions states predicating proper differentiation, maturation, and integration of neural cells are only beginning to be understood. Combining the advantages of mass cytometry with the power of modern lineage-tracing approaches, such as Cre- and/or CRISPR-based genetic recombination systems and genetically encoded markers, has the potential to exponentially enhance investigations of neural cell lineages.

For example, as described above and in Chapter II, our trajectory analyses both reproduced canonical molecular progressions underlying neural cell differentiation and predicted a somewhat novel finding: two distinct molecular pathways for OPC differentiation in the mouse forebrain. Based on these findings and localization data, we hypothesize that Olig2^{mid} NSCs are capable of directly producing OPCs early during development before switching to a progenitor phenotype capable of producing both OPCs and astrocytes, while Pax6^{high} NSCs in the dorsal telencephalon are incapable of directly producing OPCs, as outlined in Figure 5.

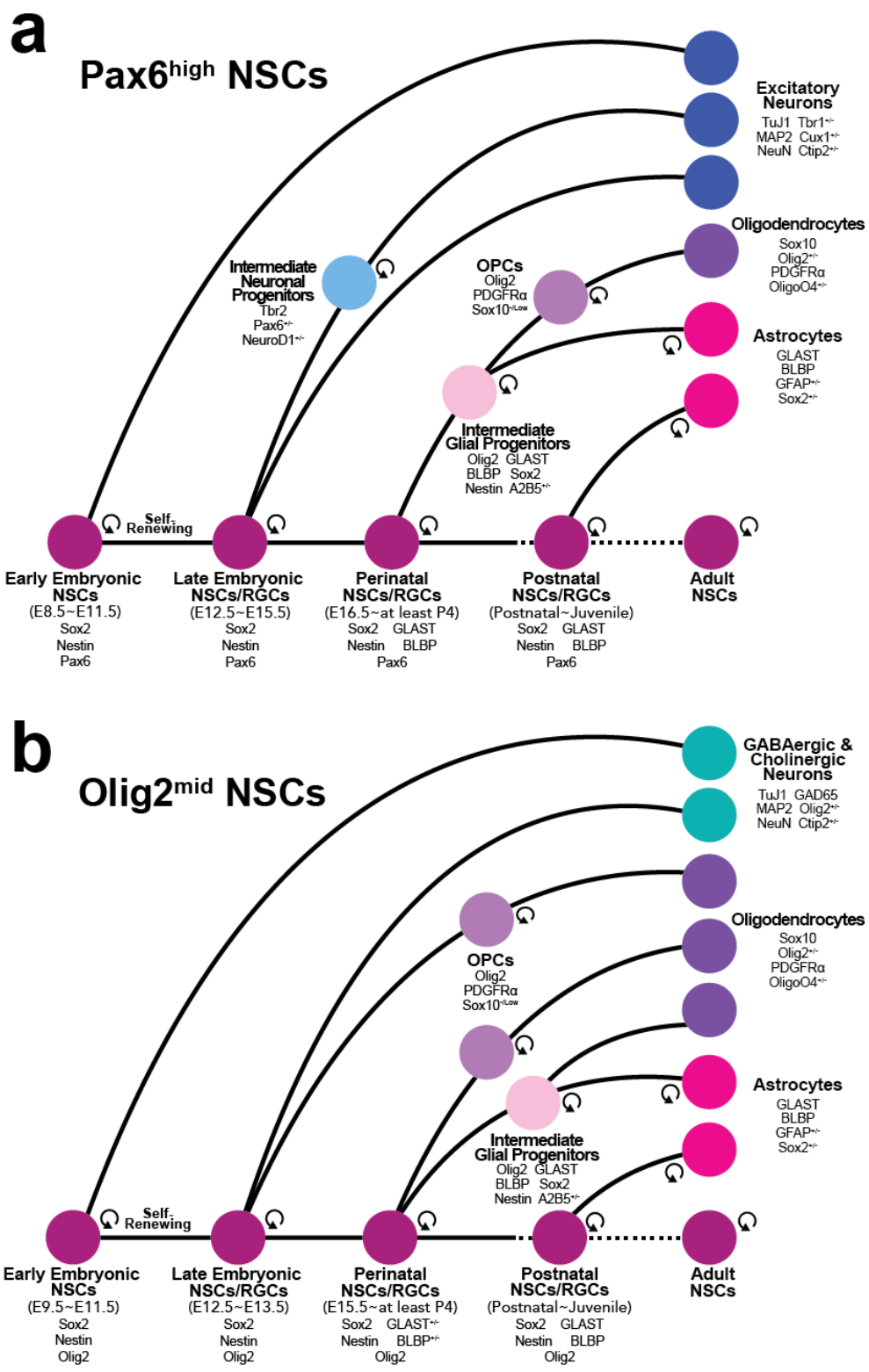

Figure 5. **Predicted model for generation of OPCs from Olig2^{mid} NSCs by two distinct pathways in the mouse forebrain**. Markers key for the identification of each cell subtype are indicated.

Although we have yet to validate these findings, which emulate previous reports of O2A cells (Baracskay et al., 2007), resolving two distinct trajectories for OPCs could help unlock some as yet unexplained mysteries about these cells, such as:

- Why do some OPCs mature into oligodendrocytes while others maintain a progenitor cell state?
- Are ventrally and dorsally derived OPCs functionally redundant?
- Why does the first wave of OPCs die off postnatally in all regions of the brain except the ventral forebrain and corpus callosum?
- How can we exploit OPCs *in vivo* to repair demyelination and nerve injury?

Moreover, because OPCs are the cell of origin for many glioblastoma (Zong et al., 2012), the ability to perform more detailed investigations of how their stemness and potency are regulated can have monumental implications for the treatment of brain cancers – especially glioblastoma, which has notoriously poor survival rates (American Cancer Society, 2020).

Profiling Phagocytic Phenotypes During Development and Disease

A diverse array of cell types can perform phagocytosis, including cells considered to be professional (e.g., microglia, macrophages, neutrophils, and osteoclasts) and non-professional phagocytes (e.g., glial precursors, endothelial cells, and fibroblasts) (Rabinovitch, 1995). However, because phagocytic cells are motile, highly dynamic, and sparsely localized in the absence of injury or inflammation (Silvin and Ginhoux, 2018), it is difficult to evaluate their homeostatic functions.

As described in Chapters II and III, we were able to capture microglia, macrophages, and glial precursors engulfing neural cells and debris in the mouse brain and DRG during development. Notably, our observations of microglia positive for OligoO4 provide evidence for microglial regulation of myelin at an earlier age than previously reported. Given their relative sparsity, it is unsurprising that these cells have previously eluded detection.

Importantly, our mass cytometry approach is agnostic to the both the type of cell performing engulfment and the engulfed cargo, meaning that it can be theoretically adapted to quantify any phagocytic cell type and target for which there is an antibody available. This includes the increasing number of cells identified to serve as 'non-professional' phagocytes (Wu et al., 2009), such as glial precursors, fibroblasts, endothelial cells, and mesenchymal cells (Ichimura et al., 2008; Juncadella et al., 2013; Z. Lu et al., 2011; Mesa et al., 2015; Wood et al., 2000).

We anticipate that future use of our approach will yield a greater appreciation of both the homeostatic and pathological functions of phagocytic cells, both within and outside the nervous system. Because the functions of phagocytic cells are increasingly implicated in neurological health and disease (Galloway et al., 2019), our approach represents a valuable new tool for investigators. Future use of this technique may facilitate understanding of the role of microglia in aggregation of amyloid β plaques in patients with

Alzheimer's disease or why myelin is degraded in the CNS of patients with multiple sclerosis but not their peripheral nerves.

Final Thoughts

Mass cytometry is a highly useful tool to quantify protein expression of single cells collected from neural tissues. The breadth and depth of the results it provides are an important complement to the growing number of scRNA-seq studies focused on the nervous system. Together, these single-cell approaches enable high-resolution delineation of molecular features that define specific cell types, which is absolutely required to build an atlas of the thousands of neuronal subtypes predicted to exist in the mammalian brain.

Although the findings described in this thesis focused on single-cell studies, mass cytometry can also be used to evaluate subcellular components such as synaptosomes (Gajera et al., 2022) and exosomes (Wang et al., 2020). Virtually all the analytical tools we developed to precisely identify cells, transition states, and molecular trajectories are also applicable for such studies, although strategies for data cleanup would need modification. We look forward to seeing future innovations of this methodology, especially for multiomic studies.

It is worth noting that there are many ways in which existing and future molecular probes can be combined with mass cytometry to immediately expand its capabilities for discerning molecular features of cells or subcellular components. For example, cell cycle

kinetics and proliferation can be examined at high-resolution using multiplexed IdU and EdU labels generated with Click chemistry (Tosevski et al., 2017). Furthermore, based on the molecular flexibility of Click chemistry, a wide array of reagents could presumably be adapted for mass cytometry.

In addition, based on some very preliminary experiments, we predict that circuit tracing studies can be performed using appropriate molecular tracers such as wheat germ agglutinin or viruses. In sum, virtually anything that can be targeted with an antibody – and many things that cannot – can be measured by mass cytometry. In the future, it will be exciting to see how this combinatorial power is wielded to advance our understanding of molecular and cellular biology.

IMC (Giesen et al., 2014) and MIBI (Angelo et al., 2014) represent important advancements of mass cytometry that can both resolve spatial information and quantify protein expression. Neuroscience-related studies employing these approaches have primarily focused on the very worthy target of human brain tumors (Ajaib et al., 2023; Surendran et al., 2023; van Hooren et al., 2023). At present, the Deppmann and Zunder laboratories are working to capitalize on our extensive library of validated antibodies to extend IMC/MIBI analyses to rodent models of neurodevelopmental disorders and neurodegeneration. Collectively, the methodologies and results of these studies have the potential to revolutionize pathology.

Building an atlas of the nervous system is an enormous but vastly important undertaking. Fortunately, the extraordinary intelligence afforded by our highly developed prefrontal cortex allows humans to develop the tools to solve such complex problems. The findings presented in this thesis represent only the beginning of our ability to harness high-dimensional, single-cell protein data to unravel the mysteries of the nervous system. I am honored to have played my small part.

References

Adams, M.D., Kelley, J.M., Gocayne, J.D., Dubnick, M., Polymeropoulos, M.H., Xiao, H., Merril, C.R., Wu, A., Olde, B., Moreno, R.F., 1991. Complementary DNA sequencing: expressed sequence tags and human genome project. Science 252, 1651–1656. https://doi.org/10.1126/science.2047873

Adrian, E.D., 1954. The basis of sensation; some recent studies of olfaction. Br. Med. J. 1, 287–290. https://doi.org/10.1136/bmj.1.4857.287

Ajaib, S., Lodha, D., Pollock, S., Hemmings, G., Finetti, M.A., Gusnanto, A., Chakrabarty, A., Ismail, A., Wilson, E., Varn, F.S., Hunter, B., Filby, A., Brockman, A.A., McDonald, D., Verhaak, R.G.W., Ihrie, R.A., Stead, L.F., 2023. GBMdeconvoluteR accurately infers proportions of neoplastic and immune cell populations from bulk glioblastoma transcriptomics data. Neuro-Oncol. 25, 1236–1248. https://doi.org/10.1093/neuonc/noad021

Ajami, B., Samusik, N., Wieghofer, P., Ho, P.P., Crotti, A., Bjornson, Z., Prinz, M., Fantl, W.J., Nolan, G.P., Steinman, L., 2018. Single-cell mass cytometry reveals distinct populations of brain myeloid cells in mouse neuroinflammation and neurodegeneration models. Nat. Neurosci. 21, 541–551. https://doi.org/10.1038/s41593-018-0100-x

AlJanahi, A.A., Danielsen, M., Dunbar, C.E., 2018. An Introduction to the Analysis of Single-Cell RNA-Sequencing Data. Mol. Ther. - Methods Clin. Dev. 10, 189–196. https://doi.org/10.1016/j.omtm.2018.07.003

Alliot, F., Godin, I., Pessac, B., 1999. Microglia derive from progenitors, originating from the yolk sac, and which proliferate in the brain. Brain Res. Dev. Brain Res. 117, 145–152. https://doi.org/10.1016/s0165-3806(99)00113-3

American Cancer Society, 2020. Survival Rates for Selected Adult Brain and Spinal Cord Tumors [WWW Document]. URL https://www.cancer.org/cancer/types/brain-spinal-cord-tumors-adults/detection-diagnosis-staging/survival-rates.html (accessed 12.1.23).

Angelo, M., Bendall, S.C., Finck, R., Hale, M.B., Hitzman, C., Borowsky, A.D., Levenson, R.M., Lowe, J.B., Liu, S.D., Zhao, S., Natkunam, Y., Nolan, G.P., 2014. Multiplexed ion beam imaging (MIBI) of human breast tumors. Nat. Med. 20, 436–442. https://doi.org/10.1038/nm.3488

Arai, Y., Funatsu, N., Numayama-Tsuruta, K., Nomura, T., Nakamura, S., Osumi, N., 2005. Role of Fabp7, a downstream gene of Pax6, in the maintenance of neuroepithelial cells during early embryonic development of the rat cortex. J. Neurosci. Off. J. Soc. Neurosci. 25, 9752–9761. https://doi.org/10.1523/JNEUROSCI.2512-05.2005

Arai, Y., Pierani, A., 2014. Development and evolution of cortical fields. Neurosci. Res., Neocortical Development and Evolution 86, 66–76. https://doi.org/10.1016/j.neures.2014.06.005

Arendt, T., Stieler, J., Ueberham, U., 2017. Is sporadic Alzheimer′s disease a developmental disorder? J. Neurochem. 143, 396–408. https://doi.org/10.1111/jnc.14036

Avilion, A.A., Nicolis, S.K., Pevny, L.H., Perez, L., Vivian, N., Lovell-Badge, R., 2003. Multipotent cell lineages in early mouse development depend on SOX2 function. Genes Dev. 17, 126–140. https://doi.org/10.1101/gad.224503

Avraham, O., Deng, P.-Y., Jones, S., Kuruvilla, R., Semenkovich, C.F., Klyachko, V.A., Cavalli, V., 2020. Satellite glial cells promote regenerative growth in sensory neurons. Nat. Commun. 11, 4891. https://doi.org/10.1038/s41467-020-18642-y

Azari, H., Reynolds, B.A., 2016. In Vitro Models for Neurogenesis. Cold Spring Harb. Perspect. Biol. 8, a021279. https://doi.org/10.1101/cshperspect.a021279

Azevedo, F.A.C., Carvalho, L.R.B., Grinberg, L.T., Farfel, J.M., Ferretti, R.E.L., Leite, R.E.P., Filho, W.J., Lent, R., Herculano-Houzel, S., 2009. Equal numbers of neuronal and

nonneuronal cells make the human brain an isometrically scaled-up primate brain. J. Comp. Neurol. 513, 532–541. https://doi.org/10.1002/cne.21974
Bandura, D.R., Baranov, V.I., Ornatsky, O.I., Antonov, A., Kinach, R., Lou, X., Pavlov, S., Vorobiev, S., Dick, J.E., Tanner, S.D., 2009. Mass cytometry: technique for real time single cell multitarget immunoassay based on inductively coupled plasma time-of-flight mass spectrometry. Anal. Chem. 81, 6813–6822. https://doi.org/10.1021/ac901049w
Bankhead, P., Loughrey, M.B., Fernández, J.A., Dombrowski, Y., McArt, D.G., Dunne, P.D., McQuaid, S., Gray, R.T., Murray, L.J., Coleman, H.G., James, J.A., Salto-Tellez, M., Hamilton, P.W., 2017. QuPath: Open source software for digital pathology image analysis. Sci. Rep. 7, 16878. https://doi.org/10.1038/s41598-017-17204-5
Baracskay, K.L., Kidd, G.J., Miller, R.H., Trapp, B.D., 2007. NG2-positive cells generate A2B5-positive oligodendrocyte precursor cells. Glia 55, 1001–1010. https://doi.org/10.1002/glia.20519
Bastian, M., Heymann, S., Jacomy, M., 2009. Gephi: An Open Source Software for Exploring and Manipulating Networks. Proc. Int. AAAI Conf. Web Soc. Media 3, 361–362. https://doi.org/10.1609/icwsm.v3i1.13937
Becht, E., McInnes, L., Healy, J., Dutertre, C.-A., Kwok, I.W.H., Ng, L.G., Ginhoux, F., Newell, E.W., 2019. Dimensionality reduction for visualizing single-cell data using UMAP. Nat. Biotechnol. 37, 38–44. https://doi.org/10.1038/nbt.4314
Bedogni, F., Hodge, R.D., Elsen, G.E., Nelson, B.R., Daza, R.A.M., Beyer, R.P., Bammler, T.K., Rubenstein, J.L.R., Hevner, R.F., 2010. Tbr1 regulates regional and laminar identity of postmitotic neurons in developing neocortex. Proc. Natl. Acad. Sci. U. S. A. 107, 13129–13134. https://doi.org/10.1073/pnas.1002285107
Beekhof, G.C., Osório, C., White, J.J., van Zoomeren, S., van der Stok, H., Xiong, B., Nettersheim, I.H., Mak, W.A., Runge, M., Fiocchi, F.R., Boele, H.-J., Hoebeek, F.E., Schonewille, M., 2021. Differential spatiotemporal development of Purkinje cell populations and cerebellum-dependent sensorimotor behaviors. eLife 10, e63668. https://doi.org/10.7554/eLife.63668
Behbehani, G.K., Bendall, S.C., Clutter, M.R., Fantl, W.J., Nolan, G.P., 2012. Single-cell mass cytometry adapted to measurements of the cell cycle. Cytometry A 81A, 552–566. https://doi.org/10.1002/cyto.a.22075
Bendall, S.C., Davis, K.L., Amir, E.D., Tadmor, M.D., Simonds, E.F., Chen, T.J., Shenfeld, D.K., Nolan, G.P., Pe'er, D., 2014. Single-Cell Trajectory Detection Uncovers Progression and Regulatory Coordination in Human B Cell Development. Cell 157, 714–725. https://doi.org/10.1016/j.cell.2014.04.005
Bendall, S.C., Simonds, E.F., Qiu, P., Amir, E.D., Krutzik, P.O., Finck, R., Bruggner, R.V., Melamed, R., Trejo, A., Ornatsky, O.I., Balderas, R.S., Plevritis, S.K., Sachs, K., Pe'er, D., Tanner, S.D., Nolan, G.P., 2011. Single-cell mass cytometry of differential immune and drug responses across a human hematopoietic continuum. Science 332, 687–696. https://doi.org/10.1126/science.1198704
Bessis, A., Béchade, C., Bernard, D., Roumier, A., 2007. Microglial control of neuronal death and synaptic properties. Glia 55, 233–238. https://doi.org/10.1002/glia.20459
Bifari, F., Decimo, I., Pino, A., Llorens-Bobadilla, E., Zhao, S., Lange, C., Panuccio, G., Boeckx, B., Thienpont, B., Vinckier, S., Wyns, S., Bouché, A., Lambrechts, D., Giugliano, M., Dewerchin, M., Martin-Villalba, A., Carmeliet, P., 2017. Neurogenic Radial Glia-like Cells in Meninges Migrate and Differentiate into Functionally Integrated Neurons in the Neonatal Cortex. Cell Stem Cell 20, 360-373.e7. https://doi.org/10.1016/j.stem.2016.10.020
Bothwell, M., Giniger, E., 2000. Alzheimer's disease: neurodevelopment converges with neurodegeneration. Cell 102, 271–273. https://doi.org/10.1016/s0092-8674(00)00032-5

Böttcher, C., Fernández-Zapata, C., Snijders, G.J.L., Schlickeiser, S., Sneeboer, M.A.M., Kunkel, D., De Witte, L.D., Priller, J., 2020a. Single-cell mass cytometry of microglia in major depressive disorder reveals a non-inflammatory phenotype with increased homeostatic marker expression. Transl. Psychiatry 10, 310. https://doi.org/10.1038/s41398-020-00992-2

Böttcher, C., Schlickeiser, S., Sneeboer, M.A.M., Kunkel, D., Knop, A., Paza, E., Fidzinski, P., Kraus, L., Snijders, G.J.L., Kahn, R.S., Schulz, A.R., Mei, H.E., NBB-Psy, Hol, E.M., Siegmund, B., Glauben, R., Spruth, E.J., de Witte, L.D., Priller, J., 2019. Human microglia regional heterogeneity and phenotypes determined by multiplexed single-cell mass cytometry. Nat. Neurosci. 22, 78–90. https://doi.org/10.1038/s41593-018-0290-2

Böttcher, C., van der Poel, M., Fernández-Zapata, C., Schlickeiser, S., Leman, J.K.H., Hsiao, C.-C., Mizee, M.R., Adelia, null, Vincenten, M.C.J., Kunkel, D., Huitinga, I., Hamann, J., Priller, J., 2020b. Single-cell mass cytometry reveals complex myeloid cell composition in active lesions of progressive multiple sclerosis. Acta Neuropathol. Commun. 8, 136. https://doi.org/10.1186/s40478-020-01010-8

Bozzi, Y., Casarosa, S., Caleo, M., 2012. Epilepsy as a Neurodevelopmental Disorder. Front. Psychiatry 3, 19. https://doi.org/10.3389/fpsyt.2012.00019

Britsch, S., Goerich, D.E., Riethmacher, D., Peirano, R.I., Rossner, M., Nave, K.A., Birchmeier, C., Wegner, M., 2001. The transcription factor Sox10 is a key regulator of peripheral glial development. Genes Dev. 15, 66–78. https://doi.org/10.1101/gad.186601

Cai, J., Chen, Y., Cai, W.-H., Hurlock, E.C., Wu, H., Kernie, S.G., Parada, L.F., Lu, Q.R., 2007. A crucial role for Olig2 in white matter astrocyte development. Development 134, 1887–1899. https://doi.org/10.1242/dev.02847

Carlén, M., Meletis, K., Göritz, C., Darsalia, V., Evergren, E., Tanigaki, K., Amendola, M., Barnabé-Heider, F., Yeung, M.S.Y., Naldini, L., Honjo, T., Kokaia, Z., Shupliakov, O., Cassidy, R.M., Lindvall, O., Frisén, J., 2009. Forebrain ependymal cells are Notch-dependent and generate neuroblasts and astrocytes after stroke. Nat. Neurosci. 12, 259–267. https://doi.org/10.1038/nn.2268

Carter, R.A., Bihannic, L., Rosencrance, C., Hadley, J.L., Tong, Y., Phoenix, T.N., Natarajan, S., Easton, J., Northcott, P.A., Gawad, C., 2018. A single-cell transcriptional atlas of the developing murine cerebellum. Curr. Biol. 28, 2910-2920.e2. https://doi.org/10.1016/j.cub.2018.07.062

Chai, H., Diaz-Castro, B., Shigetomi, E., Monte, E., Octeau, J.C., Yu, X., Cohn, W., Rajendran, P.S., Vondriska, T.M., Whitelegge, J.P., Coppola, G., Khakh, B.S., 2017. Neural circuit-specialized astrocytes: transcriptomic, proteomic, morphological and functional evidence. Neuron 95, 531-549.e9. https://doi.org/10.1016/j.neuron.2017.06.029

Chen, B., Wang, S.S., Hattox, A.M., Rayburn, H., Nelson, S.B., McConnell, S.K., 2008. The Fezf2–Ctip2 genetic pathway regulates the fate choice of subcortical projection neurons in the developing cerebral cortex. Proc. Natl. Acad. Sci. U. S. A. 105, 11382–11387. https://doi.org/10.1073/pnas.0804918105

Chen, C., Xing, D., Tan, L., Li, H., Zhou, G., Huang, L., Xie, X.S., 2017. Single-cell whole-genome analyses by Linear Amplification via Transposon Insertion (LIANTI). Science 356, 189–194. https://doi.org/10.1126/science.aak9787

Chen, V.S., Morrison, J.P., Southwell, M.F., Foley, J.F., Bolon, B., Elmore, S.A., 2017. Histology atlas of the developing prenatal and postnatal mouse central nervous system, with emphasis on prenatal days E7.5 to E18.5. Toxicol. Pathol. 45, 705–744. https://doi.org/10.1177/0192623317728134

Chen, Y.-J.J., Friedman, B.A., Ha, C., Durinck, S., Liu, J., Rubenstein, J.L., Seshagiri, S., Modrusan, Z., 2017. Single-cell RNA sequencing identifies distinct mouse medial ganglionic eminence cell types. Sci. Rep. 7, 45656. https://doi.org/10.1038/srep45656

Chen, Z., Donnelly, C.R., Dominguez, B., Harada, Y., Lin, W., Halim, A.S., Bengoechea, T.G., Pierchala, B.A., Lee, K.-F., 2017. p75 Is Required for the Establishment of Postnatal Sensory Neuron Diversity by Potentiating Ret Signaling. Cell Rep. 21, 707–720. https://doi.org/10.1016/j.celrep.2017.09.037
Cheng, I., Jin, L., Rose, L.C., Deppmann, C.D., 2018. Temporally restricted death and the role of p75NTR as a survival receptor in the developing sensory nervous system. Dev. Neurobiol. 78, 701–717. https://doi.org/10.1002/dneu.22591
Chevrier, S., Crowell, H.L., Zanotelli, V.R.T., Engler, S., Robinson, M.D., Bodenmiller, B., 2018. Compensation of signal spillover in suspension and imaging mass cytometry. Cell Syst. 6, 612-620.e5. https://doi.org/10.1016/j.cels.2018.02.010
Chiu, I.M., Barrett, L.B., Williams, E.K., Strochlic, D.E., Lee, S., Weyer, A.D., Lou, S., Bryman, G.S., Roberson, D.P., Ghasemlou, N., Piccoli, C., Ahat, E., Wang, V., Cobos, E.J., Stucky, C.L., Ma, Q., Liberles, S.D., Woolf, C.J., n.d. Transcriptional profiling at whole population and single cell levels reveals somatosensory neuron molecular diversity. eLife 3, e04660. https://doi.org/10.7554/eLife.04660
Chu, W.K., Edge, P., Lee, H.S., Bansal, V., Bafna, V., Huang, X., Zhang, K., 2017. Ultraaccurate genome sequencing and haplotyping of single human cells. Proc. Natl. Acad. Sci. U. S. A. 114, 12512–12517. https://doi.org/10.1073/pnas.1707609114
Colombo, E., Farina, C., 2016. Astrocytes: Key Regulators of Neuroinflammation. Trends Immunol. 37, 608–620. https://doi.org/10.1016/j.it.2016.06.006
Coons, A.H., Creech, H.J., Jones, R.N., 1941. Immunological Properties of an Antibody Containing a Fluorescent Group. Proc. Soc. Exp. Biol. Med. 47, 200–202. https://doi.org/10.3181/00379727-47-13084P
Cornell-Bell, A.H., Finkbeiner, S.M., 1991. Ca2+ waves in astrocytes. Cell Calcium 12, 185–204. https://doi.org/10.1016/0143-4160(91)90020-f
Coulter, D.A., Steinhäuser, C., 2015. Role of Astrocytes in Epilepsy. Cold Spring Harb. Perspect. Med. 5, a022434. https://doi.org/10.1101/cshperspect.a022434
Courchesne, E., Pierce, K., Schumann, C.M., Redcay, E., Buckwalter, J.A., Kennedy, D.P., Morgan, J., 2007. Mapping Early Brain Development in Autism. Neuron 56, 399–413. https://doi.org/10.1016/j.neuron.2007.10.016
Crowley, C., Spencer, S.D., Nishimura, M.C., Chen, K.S., Pitts-Meek, S., Armanini, M.P., Ling, L.H., McMahon, S.B., Shelton, D.L., Levinson, A.D., 1994. Mice lacking nerve growth factor display perinatal loss of sensory and sympathetic neurons yet develop basal forebrain cholinergic neurons. Cell 76, 1001–1011. https://doi.org/10.1016/0092-8674(94)90378-6
Cuevas-Diaz Duran, R., Wei, H., Wu, J.Q., 2017. Single-cell RNA-sequencing of the brain. Clin. Transl. Med. 6, 20. https://doi.org/10.1186/s40169-017-0150-9
Curtis, H.J., Cole, K.S., 1940. Membrane action potentials from the squid giant axon. J. Cell. Comp. Physiol. 15, 147–157. https://doi.org/10.1002/jcp.1030150204
da Silva, R.P., Gordon, S., 1999. Phagocytosis stimulates alternative glycosylation of macrosialin (mouse CD68), a macrophage-specific endosomal protein. Biochem. J. 338, 687–694.
Darmanis, S., Sloan, S.A., Zhang, Y., Enge, M., Caneda, C., Shuer, L.M., Hayden Gephart, M.G., Barres, B.A., Quake, S.R., 2015. A survey of human brain transcriptome diversity at the single cell level. Proc. Natl. Acad. Sci. U. S. A. 112, 7285–7290. https://doi.org/10.1073/pnas.1507125112
Davalos, D., Grutzendler, J., Yang, G., Kim, J.V., Zuo, Y., Jung, S., Littman, D.R., Dustin, M.L., Gan, W.-B., 2005. ATP mediates rapid microglial response to local brain injury in vivo. Nat. Neurosci. 8, 752–758. https://doi.org/10.1038/nn1472
De Juan Romero, C., Borrell, V., 2015. Coevolution of radial glial cells and the cerebral cortex. Glia 63, 1303–1319. https://doi.org/10.1002/glia.22827

Decimo, I., Fumagalli, G., Berton, V., Krampera, M., Bifari, F., 2012. Meninges: from protective membrane to stem cell niche. Am. J. Stem Cells 1, 92–105.
DeFelipe, J., 2011. The Evolution of the Brain, the Human Nature of Cortical Circuits, and Intellectual Creativity. Front. Neuroanat. 5.
Dent, K.A., Christie, K.J., Bye, N., Basrai, H.S., Turbic, A., Habgood, M., Cate, H.S., Turnley, A.M., 2015. Oligodendrocyte Birth and Death following Traumatic Brain Injury in Adult Mice. PLoS ONE 10, e0121541. https://doi.org/10.1371/journal.pone.0121541
Derecki, N.C., Cronk, J.C., Lu, Z., Xu, E., Abbott, S.B.G., Guyenet, P.G., Kipnis, J., 2012. Wild-type microglia arrest pathology in a mouse model of Rett syndrome. Nature 484, 105–109. https://doi.org/10.1038/nature10907
Di Bella, D.J., Habibi, E., Stickels, R.R., Scalia, G., Brown, J., Yadollahpour, P., Yang, S.M., Abbate, C., Biancalani, T., Macosko, E.Z., Chen, F., Regev, A., Arlotta, P., 2021. Molecular logic of cellular diversification in the mouse cerebral cortex. Nature 595, 554–559. https://doi.org/10.1038/s41586-021-03670-5
Djannatian, M., Weikert, U., Safaiyan, S., Wrede, C., Deichsel, C., Kislinger, G., Ruhwedel, T., Campbell, D.S., Ham, T. van, Schmid, B., Hegermann, J., Möbius, W., Schifferer, M., Simons, M., 2021. Myelin biogenesis is associated with pathological ultrastructure that is resolved by microglia during development. https://doi.org/10.1101/2021.02.02.429485
Doetsch, F., 2003. The glial identity of neural stem cells. Nat. Neurosci. 6, 1127–1134. https://doi.org/10.1038/nn1144
Domenech, P., Koechlin, E., 2015. Executive control and decision-making in the prefrontal cortex. Curr. Opin. Behav. Sci., Cognitive control 1, 101–106. https://doi.org/10.1016/j.cobeha.2014.10.007
Dusoswa, S.A., Verhoeff, J., Abels, E., Méndez-Huergo, S.P., Croci, D.O., Kuijper, L.H., de Miguel, E., Wouters, V.M.C.J., Best, M.G., Rodriguez, E., Cornelissen, L.A.M., van Vliet, S.J., Wesseling, P., Breakefield, X.O., Noske, D.P., Würdinger, T., Broekman, M.L.D., Rabinovich, G.A., van Kooyk, Y., Garcia-Vallejo, J.J., 2020. Glioblastomas exploit truncated O-linked glycans for local and distant immune modulation via the macrophage galactose-type lectin. Proc. Natl. Acad. Sci. 117, 3693–3703. https://doi.org/10.1073/pnas.1907921117
Dwyer, N.D., Chen, B., Chou, S.-J., Hippenmeyer, S., Nguyen, L., Ghashghaei, H.T., 2016. Neural stem cells to cerebral cortex: emerging mechanisms regulating progenitor behavior and productivity. J. Neurosci. 36, 11394–11401. https://doi.org/10.1523/JNEUROSCI.2359-16.2016
Eccles, J.C., Eccles, R.M., Lundberg, A., 1957. Synaptic actions on motoneurones caused by impulses in Golgi tendon organ afferents. J. Physiol. 138, 227–252.
Edlund, T., Jessell, T.M., 1999. Progression from Extrinsic to Intrinsic Signaling in Cell Fate Specification: A View from the Nervous System. Cell 96, 211–224. https://doi.org/10.1016/S0092-8674(00)80561-9
Ellis, P., Fagan, B.M., Magness, S.T., Hutton, S., Taranova, O., Hayashi, S., McMahon, A., Rao, M., Pevny, L., 2004. SOX2, a Persistent Marker for Multipotential Neural Stem Cells Derived from Embryonic Stem Cells, the Embryo or the Adult. Dev. Neurosci. 26, 148–165. https://doi.org/10.1159/000082134
Emery, E.C., Ernfors, P., 2020. Dorsal Root Ganglion Neuron Types and Their Functional Specialization, in: Wood, J.N. (Ed.), The Oxford Handbook of the Neurobiology of Pain. Oxford University Press, p. 0. https://doi.org/10.1093/oxfordhb/9780190860509.013.4
Engelhardt, B., Liebner, S., 2014. Novel insights into the development and maintenance of the blood–brain barrier. Cell Tissue Res. 355, 687–699. https://doi.org/10.1007/s00441-014-1811-2

Engelhardt, B., Sorokin, L., 2009. The blood-brain and the blood-cerebrospinal fluid barriers: function and dysfunction. Semin. Immunopathol. 31, 497–511. https://doi.org/10.1007/s00281-009-0177-0
Englund, C., Fink, A., Lau, C., Pham, D., Daza, R.A.M., Bulfone, A., Kowalczyk, T., Hevner, R.F., 2005. Pax6, Tbr2, and Tbr1 are expressed sequentially by radial glia, intermediate progenitor cells, and postmitotic neurons in developing neocortex. J. Neurosci. 25, 247–251. https://doi.org/10.1523/JNEUROSCI.2899-04.2005
Fan, G., Jaenisch, R., Kucera, J., 1999. A role for p75 receptor in neurotrophin-3 functioning during the development of limb proprioception. Neuroscience 90, 259–268. https://doi.org/10.1016/s0306-4522(98)00432-1
Fancy, S.P.J., Baranzini, S.E., Zhao, C., Yuk, D.-I., Irvine, K.-A., Kaing, S., Sanai, N., Franklin, R.J.M., Rowitch, D.H., 2009. Dysregulation of the Wnt pathway inhibits timely myelination and remyelination in the mammalian CNS. Genes Dev. 23, 1571. https://doi.org/10.1101/gad.1806309
Fantin, A., Vieira, J.M., Gestri, G., Denti, L., Schwarz, Q., Prykhozhij, S., Peri, F., Wilson, S.W., Ruhrberg, C., 2010. Tissue macrophages act as cellular chaperones for vascular anastomosis downstream of VEGF-mediated endothelial tip cell induction. Blood 116, 829–840. https://doi.org/10.1182/blood-2009-12-257832
Fariñas, I., Yoshida, C.K., Backus, C., Reichardt, L.F., 1996. Lack of neurotrophin-3 results in death of spinal sensory neurons and premature differentiation of their precursors. Neuron 17, 1065–1078. https://doi.org/10.1016/s0896-6273(00)80240-8
Farrell, J.A., Wang, Y., Riesenfeld, S.J., Shekhar, K., Regev, A., Schier, A.F., 2018. Single-cell reconstruction of developmental trajectories during zebrafish embryogenesis. Science 360, eaar3131. https://doi.org/10.1126/science.aar3131
Faure, L., Wang, Y., Kastriti, M.E., Fontanet, P., Cheung, K.K.Y., Petitpré, C., Wu, H., Sun, L.L., Runge, K., Croci, L., Landy, M.A., Lai, H.C., Consalez, G.G., de Chevigny, A., Lallemend, F., Adameyko, I., Hadjab, S., 2020. Single cell RNA sequencing identifies early diversity of sensory neurons forming via bi-potential intermediates. Nat. Commun. 11, 4175. https://doi.org/10.1038/s41467-020-17929-4
Ferrari, L.F., Khomula, E.V., Araldi, D., Levine, J.D., 2018. CD44 Signaling Mediates High Molecular Weight Hyaluronan-Induced Antihyperalgesia. J. Neurosci. Off. J. Soc. Neurosci. 38, 308–321. https://doi.org/10.1523/JNEUROSCI.2695-17.2017
Fienberg, H.G., Simonds, E.F., Fantl, W.J., Nolan, G.P., Bodenmiller, B., 2012. A platinum-based covalent viability reagent for single-cell mass cytometry. Cytometry A 81A, 467–475. https://doi.org/10.1002/cyto.a.22067
Finck, R., Simonds, E.F., Jager, A., Krishnaswamy, S., Sachs, K., Fantl, W., Pe'er, D., Nolan, G.P., Bendall, S.C., 2013. Normalization of mass cytometry data with bead standards. Cytom. Part J. Int. Soc. Anal. Cytol. 83, 483–494. https://doi.org/10.1002/cyto.a.22271
Finno, C.J., Peterson, J., Kang, M., Park, S., Bordbari, M.H., Durbin-Johnson, B., Settles, M., Perez-Flores, M.C., Lee, J.H., Yamoah, E.N., 2019. Single-Cell RNA-seq Reveals Profound Alterations in Mechanosensitive Dorsal Root Ganglion Neurons with Vitamin E Deficiency. iScience 21, 720–735. https://doi.org/10.1016/j.isci.2019.10.064
Fisher, D. a. C., Malkova, O., Engle, E.K., Miner, C.A., Fulbright, M.C., Behbehani, G.K., Collins, T.B., Bandyopadhyay, S., Zhou, A., Nolan, G.P., Oh, S.T., 2017. Mass cytometry analysis reveals hyperactive NF Kappa B signaling in myelofibrosis and secondary acute myeloid leukemia. Leukemia 31, 1962–1974. https://doi.org/10.1038/leu.2016.377
Fix, E., Hodges, J.L., 1989. Discriminatory Analysis. Nonparametric Discrimination: Consistency Properties. Int. Stat. Rev. Rev. Int. Stat. 57, 238–247. https://doi.org/10.2307/1403797
Florio, M., Huttner, W.B., 2014. Neural progenitors, neurogenesis and the evolution of the neocortex. Development 141, 2182–2194. https://doi.org/10.1242/dev.090571

Fluidigm, 2015. Guidelines for mass cytometry panel design. PN 13-01_150711.
Franco, S.J., Müller, U., 2013. Shaping Our Minds: Stem and Progenitor Cell Diversity in the Mammalian Neocortex. Neuron 77, 19–34. https://doi.org/10.1016/j.neuron.2012.12.022
Frazer, S., Prados, J., Niquille, M., Cadilhac, C., Markopoulos, F., Gomez, L., Tomasello, U., Telley, L., Holtmaat, A., Jabaudon, D., Dayer, A., 2017. Transcriptomic and anatomic parcellation of 5-HT3AR expressing cortical interneuron subtypes revealed by single-cell RNA sequencing. Nat. Commun. 8, 14219. https://doi.org/10.1038/ncomms14219
Fread, K.I., Strickland, W.D., Nolan, G.P., Zunder, E.R., 2017. An updated barcoding tool for mass cytometry with cell type-specific and cell-sample specific stringency adjustment. Pac. Symp. Biocomput. Pac. Symp. Biocomput. 22, 588–598. https://doi.org/10.1142/9789813207813_0054
Frei, A.P., Bava, F.-A., Zunder, E.R., Hsieh, E.W.Y., Chen, S.-Y., Nolan, G.P., Gherardini, P.F., 2016. Highly multiplexed simultaneous detection of RNAs and proteins in single cells. Nat. Methods 13, 269–275. https://doi.org/10.1038/nmeth.3742
Friebel, E., Kapolou, K., Unger, S., Núñez, N.G., Utz, S., Rushing, E.J., Regli, L., Weller, M., Greter, M., Tugues, S., Neidert, M.C., Becher, B., 2020. Single-Cell Mapping of Human Brain Cancer Reveals Tumor-Specific Instruction of Tissue-Invading Leukocytes. Cell 181, 1626-1642.e20. https://doi.org/10.1016/j.cell.2020.04.055
Fu, W., Wang, W., Li, H., Jiao, Y., Huo, R., Yan, Z., Wang, Jie, Wang, S., Wang, Jiangfei, Chen, D., Cao, Y., Zhao, J., 2020a. Single-cell atlas reveals complexity of the immunosuppressive microenvironment of initial and recurrent glioblastoma. Front. Immunol. 11, 835. https://doi.org/10.3389/fimmu.2020.00835
Fu, W., Wang, W., Li, H., Jiao, Y., Weng, J., Huo, R., Yan, Z., Wang, Jie, Xu, H., Wang, S., Wang, Jiangfei, Chen, D., Cao, Y., Zhao, J., 2020b. High dimensional mass cytometry analysis reveals characteristics of the immunosuppressive microenvironment in diffuse astrocytomas. Front. Oncol. 10.
Fu, Y., Li, C., Lu, S., Zhou, W., Tang, F., Xie, X.S., Huang, Y., 2015. Uniform and accurate single-cell sequencing based on emulsion whole-genome amplification. Proc. Natl. Acad. Sci. U. S. A. 112, 11923–11928. https://doi.org/10.1073/pnas.1513988112
Fu, Y., Yang, M., Yu, H., Wang, Y., Wu, X., Yong, J., Mao, Y., Cui, Y., Fan, X., Wen, L., Qiao, J., Tang, F., 2021. Heterogeneity of glial progenitor cells during the neurogenesis-to-gliogenesis switch in the developing human cerebral cortex. Cell Rep. 34, 108788. https://doi.org/10.1016/j.celrep.2021.108788
Fuentealba, L.C., Rompani, S.B., Parraguez, J.I., Obernier, K., Romero, R., Cepko, C.L., Alvarez-Buylla, A., 2015. Embryonic origin of postnatal neural stem cells. Cell 161, 1644–1655. https://doi.org/10.1016/j.cell.2015.05.041
Furusho, M., Ono, K., Takebayashi, H., Masahira, N., Kagawa, T., Ikeda, K., Ikenaka, K., 2006. Involvement of the Olig2 transcription factor in cholinergic neuron development of the basal forebrain. Dev. Biol. 293, 348–357. https://doi.org/10.1016/j.ydbio.2006.01.031
Furutachi, S., Miya, H., Watanabe, T., Kawai, H., Yamasaki, N., Harada, Y., Imayoshi, I., Nelson, M., Nakayama, K.I., Hirabayashi, Y., Gotoh, Y., 2015. Slowly dividing neural progenitors are an embryonic origin of adult neural stem cells. Nat. Neurosci. 18, 657–665. https://doi.org/10.1038/nn.3989
Gage, F.H., 2000. Mammalian Neural Stem Cells. Science 287, 1433–1438. https://doi.org/10.1126/science.287.5457.1433
Gajera, C.R., Fernandez, R., Postupna, N., Montine, K.S., Keene, C.D., Bendall, S.C., Montine, T.J., 2022. Mass Synaptometry: Applying Mass Cytometry to Single Synapse Analysis. Methods Mol. Biol. Clifton NJ 2417, 69–88. https://doi.org/10.1007/978-1-0716-1916-2_6
Galdieri, L., Jash, A., Malkova, O., Mao, D.D., DeSouza, P., Chu, Y.E., Salter, A., Campian, J.L., Naegle, K.M., Brennan, C.W., Wakimoto, H., Oh, S.T., Kim, A.H., Chheda, M.G.,

2021. Defining phenotypic and functional heterogeneity of glioblastoma stem cells by mass cytometry. JCI Insight 6, 128456. https://doi.org/10.1172/jci.insight.128456
Gall, J.G., Pardue, M.L., 1969. Formation and detection of RNA-DNA hybrid molecules in cytological preparations. Proc. Natl. Acad. Sci. U. S. A. 63, 378–383. https://doi.org/10.1073/pnas.63.2.378
Galloway, D.A., Phillips, A.E.M., Owen, D.R.J., Moore, C.S., 2019. Phagocytosis in the Brain: Homeostasis and Disease. Front. Immunol. 10.
Gao, P., Postiglione, M.P., Krieger, T.G., Hernandez, L., Wang, C., Han, Z., Streicher, C., Papusheva, E., Insolera, R., Chugh, K., Kodish, O., Huang, K., Simons, B.D., Luo, L., Hippenmeyer, S., Shi, S.-H., 2014. Deterministic progenitor behavior and unitary production of neurons in the neocortex. Cell 159, 775–788. https://doi.org/10.1016/j.cell.2014.10.027
Garcia-Lopez, P., Garcia-Marin, V., Freire, M., 2010. The Histological Slides and Drawings of Cajal. Front. Neuroanat. 4, 9. https://doi.org/10.3389/neuro.05.009.2010
Gehrmann, J., Matsumoto, Y., Kreutzberg, G.W., 1995. Microglia: Intrinsic immuneffector cell of the brain. Brain Res. Rev. 20, 269–287. https://doi.org/10.1016/0165-0173(94)00015-H
Geisler, S., 2018. The Neurogenesis of Thought. Cell 173, 1061. https://doi.org/10.1016/j.cell.2018.05.001
Gewers, F.L., Ferreira, G.R., Arruda, H.F.D., Silva, F.N., Comin, C.H., Amancio, D.R., Costa, L.D.F., 2021. Principal Component Analysis: A Natural Approach to Data Exploration. ACM Comput. Surv. 54, 70:1-70:34. https://doi.org/10.1145/3447755
Giesen, C., Wang, H.A.O., Schapiro, D., Zivanovic, N., Jacobs, A., Hattendorf, B., Schüffler, P.J., Grolimund, D., Buhmann, J.M., Brandt, S., Varga, Z., Wild, P.J., Günther, D., Bodenmiller, B., 2014. Highly multiplexed imaging of tumor tissues with subcellular resolution by mass cytometry. Nat. Methods 11, 417–422. https://doi.org/10.1038/nmeth.2869
Ginhoux, F., Greter, M., Leboeuf, M., Nandi, S., See, P., Gokhan, S., Mehler, M.F., Conway, S.J., Ng, L.G., Stanley, E.R., Samokhvalov, I.M., Merad, M., 2010. Fate Mapping Analysis Reveals That Adult Microglia Derive from Primitive Macrophages. Science 330, 841–845. https://doi.org/10.1126/science.1194637
Ginhoux, F., Lim, S., Hoeffel, G., Low, D., Huber, T., 2013. Origin and differentiation of microglia. Front. Cell. Neurosci. 7.
Goldmann, T., Prinz, M., 2013. Role of Microglia in CNS Autoimmunity. Clin. Dev. Immunol. 2013, 208093. https://doi.org/10.1155/2013/208093
Gong, H., Holcomb, I., Ooi, A., Wang, X., Majonis, D., Unger, M.A., Ramakrishnan, R., 2016. Simple Method To Prepare Oligonucleotide-Conjugated Antibodies and Its Application in Multiplex Protein Detection in Single Cells. Bioconjug. Chem. 27, 217–225. https://doi.org/10.1021/acs.bioconjchem.5b00613
González-Hernández, T., Barroso-Chinea, P., Acevedo, A., Salido, E., Rodríguez, M., 2001. Colocalization of tyrosine hydroxylase and GAD65 mRNA in mesostriatal neurons. Eur. J. Neurosci. 13, 57–67.
Goswami, S., Walle, T., Cornish, A.E., Basu, S., Anandhan, S., Fernandez, I., Vence, L., Blando, J., Zhao, H., Yadav, S.S., Ott, M., Kong, L.Y., Heimberger, A.B., de Groot, J., Sepesi, B., Overman, M., Kopetz, S., Allison, J.P., Pe'er, D., Sharma, P., 2020. Immune profiling of human tumors identifies CD73 as a combinatorial target in glioblastoma. Nat. Med. 26, 39–46. https://doi.org/10.1038/s41591-019-0694-x
Götz, M., Huttner, W.B., 2005. The cell biology of neurogenesis. Nat. Rev. Mol. Cell Biol. 6, 777–788. https://doi.org/10.1038/nrm1739
Götz, M., Stoykova, A., Gruss, P., 1998. Pax6 controls radial glia differentiation in the cerebral cortex. Neuron 21, 1031–1044. https://doi.org/10.1016/S0896-6273(00)80621-2

Gray, E.G., 1959. Axo-somatic and axo-dendritic synapses of the cerebral cortex. J. Anat. 93, 420–433.
Guo, Q., Li, J.Y.H., 2019. Defining developmental diversification of diencephalon neurons through single cell gene expression profiling. Dev. Camb. Engl. 146, dev174284. https://doi.org/10.1242/dev.174284
Guo, W., Zhang, Z., Liu, X., Burnstock, G., Xiang, Z., He, C., 2013. Developmental expression of P2X5 receptors in the mouse prenatal central and peripheral nervous systems. Purinergic Signal. 9, 239–248. https://doi.org/10.1007/s11302-012-9346-z
Gusel'nikova, V.V., Korzhevskiy, D.E., 2015. NeuN as a neuronal nuclear antigen and neuron differentiation marker. Acta Naturae 7, 42–47.
Habib, N., Li, Y., Heidenreich, M., Swiech, L., Avraham-Davidi, I., Trombetta, J.J., Hession, C., Zhang, F., Regev, A., 2016. Div-Seq: Single-nucleus RNA-Seq reveals dynamics of rare adult newborn neurons. Science 353, 925–928. https://doi.org/10.1126/science.aad7038
Hammond, T.R., Dufort, C., Dissing-Olesen, L., Giera, S., Young, A., Wysoker, A., Walker, A.J., Gergits, F., Segel, M., Nemesh, J., Marsh, S.E., Saunders, A., Macosko, E., Ginhoux, F., Chen, J., Franklin, R.J.M., Piao, X., McCarroll, S.A., Stevens, B., 2019. Single-cell RNA sequencing of microglia throughout the mouse lifespan and in the injured brain reveals complex cell-state changes. Immunity 50, 253-271.e6. https://doi.org/10.1016/j.immuni.2018.11.004
Hanani, M., Spray, D.C., 2020. Emerging importance of satellite glia in nervous system function and dysfunction. Nat. Rev. Neurosci. 21, 485–498. https://doi.org/10.1038/s41583-020-0333-z
Hanisch, U.-K., Kettenmann, H., 2007. Microglia: active sensor and versatile effector cells in the normal and pathologic brain. Nat. Neurosci. 10, 1387–1394. https://doi.org/10.1038/nn1997
Hart, I.K., Richardson, W.D., Heldin, C.H., Westermark, B., Raff, M.C., 1989. PDGF receptors on cells of the oligodendrocyte-type-2 astrocyte (O-2A) cell lineage. Dev. Camb. Engl. 105, 595–603. https://doi.org/10.1242/dev.105.3.595
Hartfuss, E., Galli, R., Heins, N., Götz, M., 2001. Characterization of CNS precursor subtypes and radial glia. Dev. Biol. 229, 15–30. https://doi.org/10.1006/dbio.2000.9962
Hartline, D.K., 2011. The evolutionary origins of glia. Glia 59, 1215–1236. https://doi.org/10.1002/glia.21149
He, L., Vanlandewijck, M., Raschperger, E., Andaloussi Mäe, M., Jung, B., Lebouvier, T., Ando, K., Hofmann, J., Keller, A., Betsholtz, C., 2016. Analysis of the brain mural cell transcriptome. Sci. Rep. 6, 35108. https://doi.org/10.1038/srep35108
Heidari, S., Babor, T.F., De Castro, P., Tort, S., Curno, M., 2016. Sex and Gender Equity in Research: rationale for the SAGER guidelines and recommended use. Res. Integr. Peer Rev. 1, 2. https://doi.org/10.1186/s41073-016-0007-6
Heins, N., Malatesta, P., Cecconi, F., Nakafuku, M., Tucker, K.L., Hack, M.A., Chapouton, P., Barde, Y.-A., Götz, M., 2002. Glial cells generate neurons: the role of the transcription factor Pax6. Nat. Neurosci. 5, 308–315. https://doi.org/10.1038/nn828
Heng, X., Guo, Q., Leung, A.W., Li, J.Y., 2017. Analogous mechanism regulating formation of neocortical basal radial glia and cerebellar Bergmann glia. eLife 6, e23253. https://doi.org/10.7554/eLife.23253
Herbomel, P., Thisse, B., Thisse, C., 2001. Zebrafish Early Macrophages Colonize Cephalic Mesenchyme and Developing Brain, Retina, and Epidermis through a M-CSF Receptor-Dependent Invasive Process. Dev. Biol. 238, 274–288. https://doi.org/10.1006/dbio.2001.0393
Herculano-Houzel, S., Collins, C.E., Wong, P., Kaas, J.H., 2007. Cellular scaling rules for primate brains. Proc. Natl. Acad. Sci. U. S. A. 104, 3562–3567. https://doi.org/10.1073/pnas.0611396104

Herculano-Houzel, S., Lent, R., 2005. Isotropic fractionator: a simple, rapid method for the quantification of total cell and neuron numbers in the brain. J. Neurosci. 25, 2518–2521. https://doi.org/10.1523/JNEUROSCI.4526-04.2005
Herculano-Houzel, S., Manger, P.R., Kaas, J.H., 2014. Brain scaling in mammalian evolution as a consequence of concerted and mosaic changes in numbers of neurons and average neuronal cell size. Front. Neuroanat. 8.
Herculano-Houzel, S., Mota, B., Lent, R., 2006. Cellular scaling rules for rodent brains. Proc. Natl. Acad. Sci. 103, 12138–12143. https://doi.org/10.1073/pnas.0604911103
Hockley, J.R.F., Taylor, T.S., Callejo, G., Wilbrey, A.L., Gutteridge, A., Bach, K., Winchester, W.J., Bulmer, D.C., McMurray, G., Smith, E.S.J., 2019. Single-cell RNAseq reveals seven classes of colonic sensory neuron. Gut 68, 633–644. https://doi.org/10.1136/gutjnl-2017-315631
Hu, A.X., Adams, J.J., Vora, P., Qazi, M., Singh, S.K., Moffat, J., Sidhu, S.S., 2019. EPH profiling of BTIC populations in glioblastoma mutiforme using CyTOF, in: Singh, S.K., Venugopal, C. (Eds.), Brain Tumor Stem Cells: Methods and Protocols, Methods in Molecular Biology. Springer, New York, NY, pp. 155–168. https://doi.org/10.1007/978-1-4939-8805-1_14
Hu, X.-L., Chen, G., Zhang, S., Zheng, J., Wu, J., Bai, Q.-R., Wang, Y., Li, Ji, Wang, H., Feng, H., Li, Jia, Sun, X., Xia, Q., Yang, F., Hang, J., Qi, C., Phoenix, T.N., Temple, S., Shen, Q., 2017. Persistent Expression of VCAM1 in Radial Glial Cells Is Required for the Embryonic Origin of Postnatal Neural Stem Cells. Neuron 95, 309-325.e6. https://doi.org/10.1016/j.neuron.2017.06.047
Huang, W., Zhao, N., Bai, X., Karram, K., Trotter, J., Goebbels, S., Scheller, A., Kirchhoff, F., 2014. Novel NG2-CreERT2 knock-in mice demonstrate heterogeneous differentiation potential of NG2 glia during development. Glia 62, 896–913. https://doi.org/10.1002/glia.22648
Hughes, A.N., Appel, B., 2020. Microglia phagocytose myelin sheaths to modify developmental myelination. Nat. Neurosci. 23, 1055–1066. https://doi.org/10.1038/s41593-020-0654-2
Hutton, S.R., Pevny, L.H., 2011. SOX2 expression levels distinguish between neural progenitor populations of the developing dorsal telencephalon. Dev. Biol. 352, 40–47. https://doi.org/10.1016/j.ydbio.2011.01.015
Ichimura, T., Asseldonk, E.J.P.V., Humphreys, B.D., Gunaratnam, L., Duffield, J.S., Bonventre, J.V., 2008. Kidney injury molecule-1 is a phosphatidylserine receptor that confers a phagocytic phenotype on epithelial cells. J. Clin. Invest. 118, 1657–1668. https://doi.org/10.1172/JCI34487
Inder, T.E., Huppi, P.S., 2000. In vivo studies of brain development by magnetic resonance techniques. Ment. Retard. Dev. Disabil. Res. Rev. 6, 59–67. https://doi.org/10.1002/(SICI)1098-2779(2000)6:1<59::AID-MRDD8>3.0.CO;2-E
Ivell, R., Teerds, K., Hoffman, G.E., 2014. Proper Application of Antibodies for Immunohistochemical Detection: Antibody Crimes and How to Prevent Them. Endocrinology 155, 676–687. https://doi.org/10.1210/en.2013-1971
Jacomy, M., Venturini, T., Heymann, S., Bastian, M., 2014. ForceAtlas2, a continuous graph layout algorithm for handy network visualization designed for the Gephi software. PloS One 9, e98679. https://doi.org/10.1371/journal.pone.0098679
Jakovcevski, I., Filipovic, R., Mo, Z., Rakic, S., Zecevic, N., 2009. Oligodendrocyte Development and the Onset of Myelination in the Human Fetal Brain. Front. Neuroanat. 3, 5. https://doi.org/10.3389/neuro.05.005.2009
Jakovcevski, I., Zecevic, N., 2005. Sequence of oligodendrocyte development in the human fetal telencephalon. Glia 49, 480–491. https://doi.org/10.1002/glia.20134

Jang, E.S., Goldman, J.E., 2011. Pax6 expression is sufficient to induce a neurogenic fate in glial progenitors of the neonatal subventricular zone. PloS One 6, e20894. https://doi.org/10.1371/journal.pone.0020894
Janisch, K.M., Vock, V.M., Fleming, M.S., Shrestha, A., Grimsley-Myers, C.M., Rasoul, B.A., Neale, S.A., Cupp, T.D., Kinchen, J.M., Liem, K.F., Dwyer, N.D., 2013. The vertebrate-specific Kinesin-6, Kif20b, is required for normal cytokinesis of polarized cortical stem cells and cerebral cortex size. Dev. Camb. Engl. 140, 4672–4682. https://doi.org/10.1242/dev.093286
Jessen, K.R., Mirsky, R., Lloyd, A.C., 2015. Schwann Cells: Development and Role in Nerve Repair. Cold Spring Harb. Perspect. Biol. 7, a020487. https://doi.org/10.1101/cshperspect.a020487
Johansson, C.B., Momma, S., Clarke, D.L., Risling, M., Lendahl, U., Frisén, J., 1999. Identification of a neural stem cell in the adult mammalian central nervous system. Cell 96, 25–34. https://doi.org/10.1016/s0092-8674(00)80956-3
Ju, J., Liu, Q., Zhang, Y., Liu, Y., Jiang, M., Zhang, L., He, X., Peng, C., Zheng, T., Lu, Q.R., Li, H., 2016. Olig2 regulates Purkinje cell generation in the early developing mouse cerebellum. Sci. Rep. 6, 30711. https://doi.org/10.1038/srep30711
Juncadella, I.J., Kadl, A., Sharma, A.K., Shim, Y.M., Hochreiter-Hufford, A., Borish, L., Ravichandran, K.S., 2013. Apoptotic cell clearance by bronchial epithelial cells critically influences airway inflammation. Nature 493, 547–551. https://doi.org/10.1038/nature11714
Kaiser, Y., Lakshmikanth, T., Chen, Y., Mikes, J., Eklund, A., Brodin, P., Achour, A., Grunewald, J., 2017. Mass Cytometry Identifies Distinct Lung CD4+ T Cell Patterns in Löfgren's Syndrome and Non-Löfgren's Syndrome Sarcoidosis. Front. Immunol. 8, 1130. https://doi.org/10.3389/fimmu.2017.01130
Kamil, K., Yazid, M.D., Idrus, R.B.H., Das, S., Kumar, J., 2019. Peripheral Demyelinating Diseases: From Biology to Translational Medicine. Front. Neurol. 10.
Kanfer, J., Parenty, M., Goujet-Zalc, C., Monge, M., Bernier, L., Campagnoni, A.T., Dautigny, A., Zalc, B., 1989. Developmental expression of myelin proteolipid, basic protein, and 2′,3′-cyclic nucleotide 3′-phosphodiesterase transcripts in different rat brain regions. J. Mol. Neurosci. 1, 39–46. https://doi.org/10.1007/BF02918889
Kaufman, D.L., Houser, C.R., Tobin, A.J., 1991. Two forms of the gamma-aminobutyric acid synthetic enzyme glutamate decarboxylase have distinct intraneuronal distributions and cofactor interactions. J. Neurochem. 56, 720–723. https://doi.org/10.1111/j.1471-4159.1991.tb08211.x
Kee, N., Volakakis, N., Kirkeby, A., Dahl, L., Storvall, H., Nolbrant, S., Lahti, L., Björklund, Å.K., Gillberg, L., Joodmardi, E., Sandberg, R., Parmar, M., Perlmann, T., 2017. Single-Cell Analysis Reveals a Close Relationship between Differentiating Dopamine and Subthalamic Nucleus Neuronal Lineages. Cell Stem Cell 20, 29–40. https://doi.org/10.1016/j.stem.2016.10.003
Keeler, A.B., Van Deusen, A.L., Gadani, I.C., Williams, C.M., Goggin, S.M., Hirt, A.K., Vradenburgh, S.A., Fread, K.I., Puleo, E.A., Jin, L., Calhan, O.Y., Deppmann, C.D., Zunder, E.R., 2022. A developmental atlas of somatosensory diversification and maturation in the dorsal root ganglia by single-cell mass cytometry. Nat. Neurosci. 25, 1543–1558. https://doi.org/10.1038/s41593-022-01181-8
Kessaris, N., Fogarty, M., Iannarelli, P., Grist, M., Wegner, M., Richardson, W.D., 2006. Competing waves of oligodendrocytes in the forebrain and postnatal elimination of an embryonic lineage. Nat. Neurosci. 9, 173–179. https://doi.org/10.1038/nn1620
Khakh, B.S., Sofroniew, M.V., 2015. Diversity of astrocyte functions and phenotypes in neural circuits. Nat. Neurosci. 18, 942–952. https://doi.org/10.1038/nn.4043

Kharchenko, P.V., Silberstein, L., Scadden, D.T., 2014. Bayesian approach to single-cell differential expression analysis. Nat. Methods 11, 740–742. https://doi.org/10.1038/nmeth.2967
Kim, D.W., Washington, P.W., Wang, Z.Q., Lin, S.H., Sun, C., Ismail, B.T., Wang, H., Jiang, L., Blackshaw, S., 2020. The cellular and molecular landscape of hypothalamic patterning and differentiation from embryonic to late postnatal development. Nat. Commun. 11, 4360. https://doi.org/10.1038/s41467-020-18231-z
Kim, J., Lo, L., Dormand, E., Anderson, D.J., 2003. SOX10 Maintains Multipotency and Inhibits Neuronal Differentiation of Neural Crest Stem Cells. Neuron 38, 17–31. https://doi.org/10.1016/S0896-6273(03)00163-6
Knapp, D.J.H.F., Kannan, N., Pellacani, D., Eaves, C.J., 2017. Mass Cytometric Analysis Reveals Viable Activated Caspase-3+ Luminal Progenitors in the Normal Adult Human Mammary Gland. Cell Rep. 21, 1116–1126. https://doi.org/10.1016/j.celrep.2017.09.096
Ko, M.E., Williams, C.M., Fread, K.I., Goggin, S.M., Rustagi, R.S., Fragiadakis, G.K., Nolan, G.P., Zunder, E.R., 2020. FLOW-MAP: a graph-based, force-directed layout algorithm for trajectory mapping in single-cell time course datasets. Nat. Protoc. 15, 398–420. https://doi.org/10.1038/s41596-019-0246-3
Koch, M.S., Zdioruk, M., Nowicki, M.O., Griffith, A.M., Aguilar, E., Aguilar, L.K., Guzik, B.W., Barone, F., Tak, P.P., Tabatabai, G., Lederer, J.A., Chiocca, E.A., Lawler, S., 2022. Systemic high-dose dexamethasone treatment may modulate the efficacy of intratumoral viral oncolytic immunotherapy in glioblastoma models. J. Immunother. Cancer 10, e003368. https://doi.org/10.1136/jitc-2021-003368
Kondo, N., Hikida, M., Nakada, M., Sakurai, Y., Hirata, E., Takeno, S., Suzuki, M., 2020. Glioma stem-like cells can be targeted in boron neutron capture therapy with boronophenylalanine. Cancers 12, E3040. https://doi.org/10.3390/cancers12103040
Korzhevskii, D.E., Kirik, O.V., 2016. Brain Microglia and Microglial Markers. Neurosci. Behav. Physiol. 46, 284–290. https://doi.org/10.1007/s11055-016-0231-z
Kreutzberg, G.W., 1996. Microglia: a sensor for pathological events in the CNS. Trends Neurosci. 19, 312–318. https://doi.org/10.1016/0166-2236(96)10049-7
Krieg, C., Nowicka, M., Guglietta, S., Schindler, S., Hartmann, F.J., Weber, L.M., Dummer, R., Robinson, M.D., Levesque, M.P., Becher, B., 2018. High-dimensional single-cell analysis predicts response to anti-PD-1 immunotherapy. Nat. Med. 24, 144–153. https://doi.org/10.1038/nm.4466
Kriegstein, A., Alvarez-Buylla, A., 2009. The Glial Nature of Embryonic and Adult Neural Stem Cells. Annu. Rev. Neurosci. 32, 149–184. https://doi.org/10.1146/annurev.neuro.051508.135600
Krutzik, P.O., Clutter, M.R., Trejo, A., Nolan, G.P., 2011. Fluorescent Cell Barcoding for Multiplex Flow Cytometry. Curr. Protoc. Cytom. 55, 6.31.1-6.31.15. https://doi.org/10.1002/0471142956.cy0631s55
Kuhlbrodt, K., Herbarth, B., Sock, E., Hermans-Borgmeyer, I., Wegner, M., 1998. Sox10, a Novel Transcriptional Modulator in Glial Cells. J. Neurosci. 18, 237–250. https://doi.org/10.1523/JNEUROSCI.18-01-00237.1998
Kupari, J., Usoskin, D., Parisien, M., Lou, D., Hu, Y., Fatt, M., Lönnerberg, P., Spångberg, M., Eriksson, B., Barkas, N., Kharchenko, P.V., Loré, K., Khoury, S., Diatchenko, L., Ernfors, P., 2021. Single cell transcriptomics of primate sensory neurons identifies cell types associated with chronic pain. Nat. Commun. 12, 1510. https://doi.org/10.1038/s41467-021-21725-z
Kurtz, A., Zimmer, A., Schnütgen, F., Brüning, G., Spener, F., Müller, T., 1994. The expression pattern of a novel gene encoding brain-fatty acid binding protein correlates with neuronal and glial cell development. Dev. Camb. Engl. 120, 2637–2649. https://doi.org/10.1242/dev.120.9.2637

Kuruvilla, R., Zweifel, L.S., Glebova, N.O., Lonze, B.E., Valdez, G., Ye, H., Ginty, D.D., 2004. A neurotrophin signaling cascade coordinates sympathetic neuron development through differential control of TrkA trafficking and retrograde signaling. Cell 118, 243–255. https://doi.org/10.1016/j.cell.2004.06.021

La Manno, G., Gyllborg, D., Codeluppi, S., Nishimura, K., Salto, C., Zeisel, A., Borm, L.E., Stott, S.R.W., Toledo, E.M., Villaescusa, J.C., Lönnerberg, P., Ryge, J., Barker, R.A., Arenas, E., Linnarsson, S., 2016. Molecular Diversity of Midbrain Development in Mouse, Human, and Stem Cells. Cell 167, 566-580.e19. https://doi.org/10.1016/j.cell.2016.09.027

La Manno, G., Siletti, K., Furlan, A., Gyllborg, D., Vinsland, E., Mossi Albiach, A., Mattsson Langseth, C., Khven, I., Lederer, A.R., Dratva, L.M., Johnsson, A., Nilsson, M., Lönnerberg, P., Linnarsson, S., 2021. Molecular architecture of the developing mouse brain. Nature 596, 92–96. https://doi.org/10.1038/s41586-021-03775-x

Lallemend, F., Ernfors, P., 2012. Molecular interactions underlying the specification of sensory neurons. Trends Neurosci. 35, 373–381. https://doi.org/10.1016/j.tins.2012.03.006

Lauritsen, M.B., 2013. Autism spectrum disorders. Eur. Child Adolesc. Psychiatry 22, 37–42. https://doi.org/10.1007/s00787-012-0359-5

Lavdas, A.A., Grigoriou, M., Pachnis, V., Parnavelas, J.G., 1999. The Medial Ganglionic Eminence Gives Rise to a Population of Early Neurons in the Developing Cerebral Cortex. J. Neurosci. 19, 7881–7888. https://doi.org/10.1523/JNEUROSCI.19-18-07881.1999

Le Douarin, N.M., Creuzet, S., Couly, G., Dupin, E., 2004. Neural crest cell plasticity and its limits. Development 131, 4637–4650. https://doi.org/10.1242/dev.01350

Lee, D.R., Rhodes, C., Mitra, A., Zhang, Y., Maric, D., Dale, R.K., Petros, T.J., 2022. Transcriptional heterogeneity of ventricular zone cells in the ganglionic eminences of the mouse forebrain. eLife 11, e71864. https://doi.org/10.7554/eLife.71864

Lee, K.F., Li, E., Huber, L.J., Landis, S.C., Sharpe, A.H., Chao, M.V., Jaenisch, R., 1992. Targeted mutation of the gene encoding the low affinity NGF receptor p75 leads to deficits in the peripheral sensory nervous system. Cell 69, 737–749. https://doi.org/10.1016/0092-8674(92)90286-l

Lee, S.-K., Jurata, L.W., Funahashi, J., Ruiz, E.C., Pfaff, S.L., 2004. Analysis of embryonic motoneuron gene regulation: derepression of general activators function in concert with enhancer factors. Development 131, 3295–3306. https://doi.org/10.1242/dev.01179

Leekam, S.R., Nieto, C., Libby, S.J., Wing, L., Gould, J., 2007. Describing the Sensory Abnormalities of Children and Adults with Autism. J. Autism Dev. Disord. 37, 894–910. https://doi.org/10.1007/s10803-006-0218-7

Leelatian, N., Doxie, D.B., Greenplate, A.R., Mobley, B.C., Lehman, J.M., Sinnaeve, J., Kauffmann, R.M., Werkhaven, J.A., Mistry, A.M., Weaver, K.D., Thompson, R.C., Massion, P.P., Hooks, M.A., Kelley, M.C., Chambless, L.B., Ihrie, R.A., Irish, J.M., 2017. Single cell analysis of human tissues and solid tumors with mass cytometry. Cytometry B Clin. Cytom. 92, 68–78. https://doi.org/10.1002/cyto.b.21481

Leelatian, N., Sinnaeve, J., Mistry, A.M., Barone, S.M., Brockman, A.A., Diggins, K.E., Greenplate, A.R., Weaver, K.D., Thompson, R.C., Chambless, L.B., Mobley, B.C., Ihrie, R.A., Irish, J.M., 2020. Unsupervised machine learning reveals risk stratifying glioblastoma tumor cells. eLife 9, e56879. https://doi.org/10.7554/eLife.56879

Lehmann, H.C., Höke, A., 2010. Schwann cells as a therapeutic target for peripheral neuropathies. CNS Neurol. Disord. Drug Targets 9, 801–806.

Lehnardt, S., 2010. Innate immunity and neuroinflammation in the CNS: the role of microglia in Toll-like receptor-mediated neuronal injury. Glia 58, 253–263. https://doi.org/10.1002/glia.20928

Leid, M., Ishmael, J.E., Avram, D., Shepherd, D., Fraulob, V., Dollé, P., 2004. CTIP1 and CTIP2 are differentially expressed during mouse embryogenesis. Gene Expr. Patterns GEP 4, 733. https://doi.org/10.1016/j.modgep.2004.03.009
Lendahl, U., Zimmerman, L.B., McKay, R.D., 1990. CNS stem cells express a new class of intermediate filament protein. Cell 60, 585–595. https://doi.org/10.1016/0092-8674(90)90662-x
Leone, D.P., Srinivasan, K., Chen, B., Alcamo, E., McConnell, S.K., 2008. The determination of projection neuron identity in the developing cerebral cortex. Curr. Opin. Neurobiol. 18, 28–35. https://doi.org/10.1016/j.conb.2008.05.006
Leto, K., Carletti, B., Williams, I.M., Magrassi, L., Rossi, F., 2006. Different Types of Cerebellar GABAergic Interneurons Originate from a Common Pool of Multipotent Progenitor Cells. J. Neurosci. 26, 11682–11694. https://doi.org/10.1523/JNEUROSCI.3656-06.2006
Levin, E., Andreadaki, A., Gobrecht, P., Bosse, F., Fischer, D., 2017. Nociceptive DRG neurons express muscle lim protein upon axonal injury. Sci. Rep. 7, 643. https://doi.org/10.1038/s41598-017-00590-1
Levine, J.H., Simonds, E.F., Bendall, S.C., Davis, K.L., Amir, E.D., Tadmor, M.D., Litvin, O., Fienberg, H.G., Jager, A., Zunder, E.R., Finck, R., Gedman, A.L., Radtke, I., Downing, J.R., Pe'er, D., Nolan, G.P., 2015. Data-Driven Phenotypic Dissection of AML Reveals Progenitor-like Cells that Correlate with Prognosis. Cell 162, 184–197. https://doi.org/10.1016/j.cell.2015.05.047
Li, C., Wang, S., Chen, Y., Zhang, X., 2018. Somatosensory Neuron Typing with High-Coverage Single-Cell RNA Sequencing and Functional Analysis. Neurosci. Bull. 34, 200–207. https://doi.org/10.1007/s12264-017-0147-9
Li, C.-L., Li, K.-C., Wu, D., Chen, Y., Luo, H., Zhao, J.-R., Wang, S.-S., Sun, M.-M., Lu, Y.-J., Zhong, Y.-Q., Hu, X.-Y., Hou, R., Zhou, B.-B., Bao, L., Xiao, H.-S., Zhang, X., 2016. Somatosensory neuron types identified by high-coverage single-cell RNA-sequencing and functional heterogeneity. Cell Res. 26, 83–102. https://doi.org/10.1038/cr.2015.149
Li, Q., Cheng, Z., Zhou, L., Darmanis, S., Neff, N.F., Okamoto, J., Gulati, G., Bennett, M.L., Sun, L.O., Clarke, L.E., Marschallinger, J., Yu, G., Quake, S.R., Wyss-Coray, T., Barres, B.A., 2019. Developmental Heterogeneity of Microglia and Brain Myeloid Cells Revealed by Deep Single-Cell RNA Sequencing. Neuron 101, 207-223.e10. https://doi.org/10.1016/j.neuron.2018.12.006
Li, S., Liao, Y., Dong, Y., Li, X., Li, J., Cheng, Y., Cheng, J., Yuan, Z., 2021. Microglial deletion and inhibition alleviate behavior of post-traumatic stress disorder in mice. J. Neuroinflammation 18, 7. https://doi.org/10.1186/s12974-020-02069-9
Li, Z., Tyler, W.A., Zeldich, E., Santpere Baró, G., Okamoto, M., Gao, T., Li, M., Sestan, N., Haydar, T.F., 2020. Transcriptional priming as a conserved mechanism of lineage diversification in the developing mouse and human neocortex. Sci. Adv. 6, eabd2068. https://doi.org/10.1126/sciadv.abd2068
Linington, C., Lassmann, H., 1987. Antibody responses in chronic relapsing experimental allergic encephalomyelitis: correlation of serum demyelinating activity with antibody titre to the myelin/oligodendrocyte glycoprotein (MOG). J. Neuroimmunol. 17, 61–69. https://doi.org/10.1016/0165-5728(87)90031-2
Lister, R., O'Malley, R.C., Tonti-Filippini, J., Gregory, B.D., Berry, C.C., Millar, A.H., Ecker, J.R., 2008. Highly Integrated Single-Base Resolution Maps of the Epigenome in Arabidopsis. Cell 133, 523–536. https://doi.org/10.1016/j.cell.2008.03.029
Liu, Y., Beyer, A., Aebersold, R., 2016. On the dependency of cellular protein levels on mRNA abundance. Cell 165, 535–550. https://doi.org/10.1016/j.cell.2016.03.014
Lozovaya, N., Eftekhari, S., Cloarec, R., Gouty-Colomer, L.A., Dufour, A., Riffault, B., Billon-Grand, M., Pons-Bennaceur, A., Oumar, N., Burnashev, N., Ben-Ari, Y., Hammond, C., 2018. GABAergic inhibition in dual-transmission cholinergic and GABAergic striatal

interneurons is abolished in Parkinson disease. Nat. Commun. 9, 1422. https://doi.org/10.1038/s41467-018-03802-y
Lu, P., Takai, K., Weaver, V.M., Werb, Z., 2011. Extracellular Matrix Degradation and Remodeling in Development and Disease. Cold Spring Harb. Perspect. Biol. 3, a005058. https://doi.org/10.1101/cshperspect.a005058
Lu, Q.R., Yuk, D., Alberta, J.A., Zhu, Z., Pawlitzky, I., Chan, J., McMahon, A.P., Stiles, C.D., Rowitch, D.H., 2000. Sonic hedgehog–regulated oligodendrocyte lineage genes encoding bHLH proteins in the mammalian central nervous system. Neuron 25, 317–329. https://doi.org/10.1016/S0896-6273(00)80897-1
Lu, Z., Elliott, M.R., Chen, Y., Walsh, J.T., Klibanov, A.L., Ravichandran, K.S., Kipnis, J., 2011. Phagocytic activity of neuronal progenitors regulates adult neurogenesis. Nat. Cell Biol. 13, 1076–1083. https://doi.org/10.1038/ncb2299
Lujan, E., Zunder, E.R., Ng, Y.H., Goronzy, I.N., Nolan, G.P., Wernig, M., 2015. Early reprogramming regulators identified by prospective isolation and mass cytometry. Nature 521, 352–356. https://doi.org/10.1038/nature14274
Luo, W., Lin, G.N., Song, W., Zhang, Y., Lai, H., Zhang, M., Miao, J., Cheng, X., Wang, Y., Li, W., Wei, W., Gao, W.-Q., Yang, R., Wang, J., 2021. Single-cell spatial transcriptomic analysis reveals common and divergent features of developing postnatal granule cerebellar cells and medulloblastoma. BMC Biol. 19, 135. https://doi.org/10.1186/s12915-021-01071-8
Luo, W., Wickramasinghe, S.R., Savitt, J.M., Griffin, J.W., Dawson, T.M., Ginty, D.D., 2007. A hierarchical NGF signaling cascade controls Ret-dependent and Ret-independent events during development of nonpeptidergic DRG neurons. Neuron 54, 739–754. https://doi.org/10.1016/j.neuron.2007.04.027
Ma, Q., Fode, C., Guillemot, F., Anderson, D.J., 1999. NEUROGENIN1 and NEUROGENIN2 control two distinct waves of neurogenesis in developing dorsal root ganglia. Genes Dev. 13, 1717–1728.
Macaulay, I.C., Ponting, C.P., Voet, T., 2017. Single-Cell Multiomics: Multiple Measurements from Single Cells. Trends Genet. 33, 155–168. https://doi.org/10.1016/j.tig.2016.12.003
Macosko, E.Z., Basu, A., Satija, R., Nemesh, J., Shekhar, K., Goldman, M., Tirosh, I., Bialas, A.R., Kamitaki, N., Martersteck, E.M., Trombetta, J.J., Weitz, D.A., Sanes, J.R., Shalek, A.K., Regev, A., McCarroll, S.A., 2015. Highly Parallel Genome-wide Expression Profiling of Individual Cells Using Nanoliter Droplets. Cell 161, 1202–1214. https://doi.org/10.1016/j.cell.2015.05.002
Magistretti, P.J., Allaman, I., 2015. A Cellular Perspective on Brain Energy Metabolism and Functional Imaging. Neuron 86, 883–901. https://doi.org/10.1016/j.neuron.2015.03.035
Mair, F., Hartmann, F.J., Mrdjen, D., Tosevski, V., Krieg, C., Becher, B., 2016. The end of gating? An introduction to automated analysis of high dimensional cytometry data. Eur. J. Immunol. 46, 34–43. https://doi.org/10.1002/eji.201545774
Manzini, M.C., Walsh, C.A., 2011. What disorders of cortical development tell us about the cortex: one plus one does not always make two. Curr. Opin. Genet. Dev., Molecular and genetic bases of disease 21, 333–339. https://doi.org/10.1016/j.gde.2011.01.006
Mapps, A.A., Thomsen, M.B., Boehm, E., Zhao, H., Hattar, S., Kuruvilla, R., 2022. Diversity of satellite glia in sympathetic and sensory ganglia. Cell Rep. 38, 110328. https://doi.org/10.1016/j.celrep.2022.110328
Maro, G.S., Vermeren, M., Voiculescu, O., Melton, L., Cohen, J., Charnay, P., Topilko, P., 2004. Neural crest boundary cap cells constitute a source of neuronal and glial cells of the PNS. Nat. Neurosci. 7, 930–938. https://doi.org/10.1038/nn1299
Marques, S., van Bruggen, D., Vanichkina, D.P., Floriddia, E.M., Munguba, H., Väremo, L., Giacomello, S., Falcão, A.M., Meijer, M., Björklund, Å.K., Hjerling-Leffler, J., Taft, R.J., Castelo-Branco, G., 2018. Transcriptional convergence of oligodendrocyte lineage

progenitors during development. Dev. Cell 46, 504-517.e7. https://doi.org/10.1016/j.devcel.2018.07.005
Mayer, C., Hafemeister, C., Bandler, R.C., Machold, R., Batista Brito, R., Jaglin, X., Allaway, K., Butler, A., Fishell, G., Satija, R., 2018. Developmental diversification of cortical inhibitory interneurons. Nature 555, 457–462. https://doi.org/10.1038/nature25999
McCormick, D.A., 1989. GABA as an inhibitory neurotransmitter in human cerebral cortex. J. Neurophysiol. 62, 1018–1027. https://doi.org/10.1152/jn.1989.62.5.1018
McInnes, L., Healy, J., Saul, N., Großberger, L., 2018. UMAP: Uniform Manifold Approximation and Projection. J. Open Source Softw. 3, 861. https://doi.org/10.21105/joss.00861
Merkle, F.T., Tramontin, A.D., García-Verdugo, J.M., Alvarez-Buylla, A., 2004. Radial glia give rise to adult neural stem cells in the subventricular zone. Proc. Natl. Acad. Sci. U. S. A. 101, 17528–17532. https://doi.org/10.1073/pnas.0407893101
Mesa, K.R., Rompolas, P., Zito, G., Myung, P., Sun, T.Y., Brown, S., Gonzalez, D.G., Blagoev, K.B., Haberman, A.M., Greco, V., 2015. Niche-induced cell death and epithelial phagocytosis regulate hair follicle stem cell pool. Nature 522, 94–97. https://doi.org/10.1038/nature14306
Mi, D., Li, Z., Lim, L., Li, M., Moissidis, M., Yang, Y., Gao, T., Hu, T.X., Pratt, T., Price, D.J., Sestan, N., Marín, O., 2018. Early emergence of cortical interneuron diversity in the mouse embryo. Science 360, 81–85. https://doi.org/10.1126/science.aar6821
Miale, I.L., Sidman, R.L., 1961. An autoradiographic analysis of histogenesis in the mouse cerebellum. Exp. Neurol. 4, 277–296. https://doi.org/10.1016/0014-4886(61)90055-3
Mignone, J.L., Kukekov, V., Chiang, A.-S., Steindler, D., Enikolopov, G., 2004. Neural stem and progenitor cells in nestin-GFP transgenic mice. J. Comp. Neurol. 469, 311–324. https://doi.org/10.1002/cne.10964
Miller, E.K., 2000. The prefontral cortex and cognitive control. Nat. Rev. Neurosci. 1, 59–65. https://doi.org/10.1038/35036228
Miller, J.A., Horvath, S., Geschwind, D.H., 2010. Divergence of human and mouse brain transcriptome highlights Alzheimer disease pathways. Proc. Natl. Acad. Sci. 107, 12698–12703. https://doi.org/10.1073/pnas.0914257107
Minghetti, L., Levi, G., 1998. Microglia as effector cells in brain damage and repair: focus on prostanoids and nitric oxide. Prog. Neurobiol. 54, 99–125. https://doi.org/10.1016/S0301-0082(97)00052-X
Miyoshi, G., Hjerling-Leffler, J., Karayannis, T., Sousa, V.H., Butt, S.J.B., Battiste, J., Johnson, J.E., Machold, R.P., Fishell, G., 2010. Genetic Fate Mapping Reveals That the Caudal Ganglionic Eminence Produces a Large and Diverse Population of Superficial Cortical Interneurons. J. Neurosci. 30, 1582–1594. https://doi.org/10.1523/JNEUROSCI.4515-09.2010
Molnár, Z., Pollen, A., 2014. How unique is the human neocortex? Development 141, 11–16. https://doi.org/10.1242/dev.101279
Molofsky, A.V., Krenick, R., Ullian, E., Tsai, H., Deneen, B., Richardson, W.D., Barres, B.A., Rowitch, D.H., 2012. Astrocytes and disease: a neurodevelopmental perspective. Genes Dev. 26, 891–907. https://doi.org/10.1101/gad.188326.112
Morimoto, K., Nakajima, K., 2019. Role of the Immune System in the Development of the Central Nervous System. Front. Neurosci. 13.
Mountcastle, V.B., 1997. The columnar organization of the neocortex. Brain J. Neurol. 120 (Pt 4), 701–722. https://doi.org/10.1093/brain/120.4.701
Mrdjen, D., Pavlovic, A., Hartmann, F.J., Schreiner, B., Utz, S.G., Leung, B.P., Lelios, I., Heppner, F.L., Kipnis, J., Merkler, D., Greter, M., Becher, B., 2018. High-dimensional single-cell mapping of central nervous system immune cells reveals distinct myeloid subsets in health, aging, and disease. Immunity 48, 380-395.e6. https://doi.org/10.1016/j.immuni.2018.01.011

Mueller, S., Taitt, J.M., Villanueva-Meyer, J.E., Bonner, E.R., Nejo, T., Lulla, R.R., Goldman, S., Banerjee, A., Chi, S.N., Whipple, N.S., Crawford, J.R., Gauvain, K., Nazemi, K.J., Watchmaker, P.B., Almeida, N.D., Okada, K., Salazar, A.M., Gilbert, R.D., Nazarian, J., Molinaro, A.M., Butterfield, L.H., Prados, M.D., Okada, H., 2020. Mass cytometry detects H3.3K27M-specific vaccine responses in diffuse midline glioma. J. Clin. Invest. 130, 6325–6337. https://doi.org/10.1172/JCI140378

Muhl, L., Genové, G., Leptidis, S., Liu, J., He, L., Mocci, G., Sun, Y., Gustafsson, S., Buyandelger, B., Chivukula, I.V., Segerstolpe, Å., Raschperger, E., Hansson, E.M., Björkegren, J.L.M., Peng, X.-R., Vanlandewijck, M., Lendahl, U., Betsholtz, C., 2020. Single-cell analysis uncovers fibroblast heterogeneity and criteria for fibroblast and mural cell identification and discrimination. Nat. Commun. 11, 3953. https://doi.org/10.1038/s41467-020-17740-1

Murray, S.S., Bartlett, P.F., Cheema, S.S., 1999. Differential loss of spinal sensory but not motor neurons in the p75NTR knockout mouse. Neurosci. Lett. 267, 45–48. https://doi.org/10.1016/s0304-3940(99)00330-4

Nemes-Baran, A.D., White, D.R., DeSilva, T.M., 2020. Fractalkine-dependent microglial pruning of viable oligodendrocyte progenitor cells regulates myelination. Cell Rep. 32, 108047. https://doi.org/10.1016/j.celrep.2020.108047

Newell, E.W., Sigal, N., Bendall, S.C., Nolan, G.P., Davis, M.M., 2012. Cytometry by time-of-flight shows combinatorial cytokine expression and virus-specific cell niches within a continuum of CD8+ T cell phenotypes. Immunity 36, 142–152. https://doi.org/10.1016/j.immuni.2012.01.002

Nguyen, M.Q., von Buchholtz, L.J., Reker, A.N., Ryba, N.J., Davidson, S., 2021. Single-nucleus transcriptomic analysis of human dorsal root ganglion neurons. eLife 10, e71752. https://doi.org/10.7554/eLife.71752

Nickels, K.C., Zaccariello, M.J., Hamiwka, L.D., Wirrell, E.C., 2016. Cognitive and neurodevelopmental comorbidities in paediatric epilepsy. Nat. Rev. Neurol. 12, 465–476. https://doi.org/10.1038/nrneurol.2016.98

Nikouei, K., Muñoz-Manchado, A.B., Hjerling-Leffler, J., 2016. BCL11B/CTIP2 is highly expressed in GABAergic interneurons of the mouse somatosensory cortex. J. Chem. Neuroanat. 71, 1–5. https://doi.org/10.1016/j.jchemneu.2015.12.004

Nimmerjahn, A., Kirchhoff, F., Helmchen, F., 2005. Resting microglial cells are highly dynamic surveillants of brain parenchyma in vivo. Science 308, 1314–1318. https://doi.org/10.1126/science.1110647

Noble, M., Murray, K., Stroobant, P., Waterfield, M.D., Riddle, P., 1988. Platelet-derived growth factor promotes division and motility and inhibits premature differentiation of the oligodendrocyte/type-2 astrocyte progenitor cell. Nature 333, 560–562. https://doi.org/10.1038/333560a0

Noctor, S.C., Flint, A.C., Weissman, T.A., Wong, W.S., Clinton, B.K., Kriegstein, A.R., 2002. Dividing Precursor Cells of the Embryonic Cortical Ventricular Zone Have Morphological and Molecular Characteristics of Radial Glia. J. Neurosci. 22, 3161–3173. https://doi.org/10.1523/JNEUROSCI.22-08-03161.2002

Nour, M.M., Howes, O.D., 2015. Interpreting the neurodevelopmental hypothesis of schizophrenia in the context of normal brain development and ageing. Proc. Natl. Acad. Sci. 112, E2745–E2745. https://doi.org/10.1073/pnas.1502170112

Oberheim, N.A., Goldman, S.A., Nedergaard, M., 2012. Heterogeneity of Astrocytic Form and Function. Methods Mol. Biol. Clifton NJ 814, 23–45. https://doi.org/10.1007/978-1-61779-452-0_3

Oberheim, N.A., Takano, T., Han, X., He, W., Lin, J.H.C., Wang, F., Xu, Q., Wyatt, J.D., Pilcher, W., Ojemann, J.G., Ransom, B.R., Goldman, S.A., Nedergaard, M., 2009. Uniquely

Hominid Features of Adult Human Astrocytes. J. Neurosci. 29, 3276–3287. https://doi.org/10.1523/JNEUROSCI.4707-08.2009
Ogrodnik, M., Zhu, Y., Langhi, L.G.P., Tchkonia, T., Krüger, P., Fielder, E., Victorelli, S., Ruswhandi, R.A., Giorgadze, N., Pirtskhalava, T., Podgorni, O., Enikolopov, G., Johnson, K.O., Xu, M., Inman, C., Palmer, A.K., Schafer, M., Weigl, M., Ikeno, Y., Burns, T.C., Passos, J.F., von Zglinicki, T., Kirkland, J.L., Jurk, D., 2019. Obesity-induced cellular senescence drives anxiety and impairs neurogenesis. Cell Metab. 29, 1061-1077.e8. https://doi.org/10.1016/j.cmet.2018.12.008
Ohtaka-Maruyama, C., Okado, H., 2015. Molecular Pathways Underlying Projection Neuron Production and Migration during Cerebral Cortical Development. Front. Neurosci. 9.
Okita, K., Ichisaka, T., Yamanaka, S., 2007. Generation of germline-competent induced pluripotent stem cells. Nature 448, 313–317. https://doi.org/10.1038/nature05934
Ono, K., Takebayashi, H., Ikeda, K., Furusho, M., Nishizawa, T., Watanabe, K., Ikenaka, K., 2008. Regional- and temporal-dependent changes in the differentiation of Olig2 progenitors in the forebrain, and the impact on astrocyte development in the dorsal pallium. Dev. Biol. 320, 456–468. https://doi.org/10.1016/j.ydbio.2008.06.001
Orefice, L.L., Mosko, J.R., Morency, D.T., Wells, M.F., Tasnim, A., Mozeika, S.M., Ye, M., Chirila, A.M., Emanuel, A.J., Rankin, G., Fame, R.M., Lehtinen, M.K., Feng, G., Ginty, D.D., 2019. Targeting Peripheral Somatosensory Neurons to Improve Tactile-Related Phenotypes in ASD Models. Cell 178, 867-886.e24. https://doi.org/10.1016/j.cell.2019.07.024
Orefice, L.L., Zimmerman, A.L., Chirila, A.M., Sleboda, S.J., Head, J.P., Ginty, D.D., 2016. Peripheral Mechanosensory Neuron Dysfunction Underlies Tactile and Behavioral Deficits in Mouse Models of ASDs. Cell 166, 299–313. https://doi.org/10.1016/j.cell.2016.05.033
Ormel, P.R., Böttcher, C., Gigase, F.A.J., Missall, R.D., van Zuiden, W., Fernández Zapata, M.C., Ilhan, D., de Goeij, M., Udine, E., Sommer, I.E.C., Priller, J., Raj, T., Kahn, R.S., Hol, E.M., de Witte, L.D., 2020. A characterization of the molecular phenotype and inflammatory response of schizophrenia patient-derived microglia-like cells. Brain. Behav. Immun. 90, 196–207. https://doi.org/10.1016/j.bbi.2020.08.012
Ornatsky, O.I., Lou, X., Nitz, M., Schäfer, S., Sheldrick, W.S., Baranov, V.I., Bandura, D.R., Tanner, S.D., 2008. Study of cell antigens and intracellular DNA by identification of element-containing labels and metallointercalators using inductively coupled plasma mass spectrometry. Anal. Chem. 80, 2539–2547. https://doi.org/10.1021/ac702128m
Orr, M.E., Garbarino, V.R., Salinas, A., Buffenstein, R., 2016. Extended Postnatal Brain Development in the Longest-Lived Rodent: Prolonged Maintenance of Neotenous Traits in the Naked Mole-Rat Brain. Front. Neurosci. 10.
Osman, A.M., Rodhe, J., Shen, X., Dominguez, C.A., Joseph, B., Blomgren, K., 2019. The Secretome of Microglia Regulate Neural Stem Cell Function. Neuroscience, Microglia-Neuron interactions in health and disease - novel perspectives for translational research 405, 92–102. https://doi.org/10.1016/j.neuroscience.2017.10.034
Owen, M.J., O'Donovan, M.C., Thapar, A., Craddock, N., 2011. Neurodevelopmental hypothesis of schizophrenia. Br. J. Psychiatry 198, 173–175. https://doi.org/10.1192/bjp.bp.110.084384
Özkaya, A.K., Güler, E., Arık, E., Namlı, A.R., Cevizli, D., Güngör, O., 2014. A case of congenital insensitivity to pain with anhidrosis. Turk. Arch. Pediatr. Pediatri Arş. 49, 177–179. https://doi.org/10.5152/tpa.2014.1549
Paolicelli, R.C., Bolasco, G., Pagani, F., Maggi, L., Scianni, M., Panzanelli, P., Giustetto, M., Ferreira, T.A., Guiducci, E., Dumas, L., Ragozzino, D., Gross, C.T., 2011. Synaptic pruning by microglia is necessary for normal brain development. Science 333, 1456–1458. https://doi.org/10.1126/science.1202529

Park, D., Xiang, A.P., Mao, F.F., Zhang, L., Di, C.-G., Liu, X.-M., Shao, Y., Ma, B.-F., Lee, J.-H., Ha, K.-S., Walton, N., Lahn, B.T., 2010. Nestin is required for the proper self-renewal of neural stem cells. Stem Cells Dayt. Ohio 28, 2162–2171. https://doi.org/10.1002/stem.541

Patel, J., Balabanov, R., 2012. Molecular Mechanisms of Oligodendrocyte Injury in Multiple Sclerosis and Experimental Autoimmune Encephalomyelitis. Int. J. Mol. Sci. 13, 10647–10659. https://doi.org/10.3390/ijms130810647

Patel, T.D., Jackman, A., Rice, F.L., Kucera, J., Snider, W.D., 2000. Development of sensory neurons in the absence of NGF/TrkA signaling in vivo. Neuron 25, 345–357. https://doi.org/10.1016/s0896-6273(00)80899-5

Paul, A., Crow, M., Raudales, R., He, M., Gillis, J., Huang, Z.J., 2017. Transcriptional Architecture of Synaptic Communication Delineates GABAergic Neuron Identity. Cell 171, 522-539.e20. https://doi.org/10.1016/j.cell.2017.08.032

Pelvig, D.P., Pakkenberg, H., Stark, A.K., Pakkenberg, B., 2008. Neocortical glial cell numbers in human brains. Neurobiol. Aging 29, 1754–1762. https://doi.org/10.1016/j.neurobiolaging.2007.04.013

Perea, G., Navarrete, M., Araque, A., 2009. Tripartite synapses: astrocytes process and control synaptic information. Trends Neurosci. 32, 421–431. https://doi.org/10.1016/j.tins.2009.05.001

Pfenninger, C.V., Roschupkina, T., Hertwig, F., Kottwitz, D., Englund, E., Bengzon, J., Jacobsen, S.E., Nuber, U.A., 2007. CD133 is not present on neurogenic astrocytes in the adult subventricular zone, but on embryonic neural stem cells, ependymal cells, and glioblastoma cells. Cancer Res. 67, 5727–5736. https://doi.org/10.1158/0008-5472.CAN-07-0183

Pilz, D.T., Matsumoto, N., Minnerath, S., Mills, P., Gleeson, J.G., Allen, K.M., Walsh, C.A., Barkovich, A.J., Dobyns, W.B., Ledbetter, D.H., Ross, M.E., 1998. LIS1 and XLIS (DCX) Mutations Cause Most Classical Lissencephaly, but Different Patterns of Malformation. Hum. Mol. Genet. 7, 2029–2037. https://doi.org/10.1093/hmg/7.13.2029

Plein, A., Fantin, A., Denti, L., Pollard, J.W., Ruhrberg, C., 2018. Erythro-myeloid progenitors contribute endothelial cells to blood vessels. Nature 562, 223–228. https://doi.org/10.1038/s41586-018-0552-x

Polikowsky, H.G., Drake, K.A., 2019. Supervised Machine Learning with CITRUS for Single Cell Biomarker Discovery. Methods Mol. Biol. Clifton NJ 1989, 309–332. https://doi.org/10.1007/978-1-4939-9454-0_20

Ponath, G., Park, C., Pitt, D., 2018. The Role of Astrocytes in Multiple Sclerosis. Front. Immunol. 9, 217. https://doi.org/10.3389/fimmu.2018.00217

Porpiglia, E., Samusik, N., Ho, A.T.V., Cosgrove, B.D., Mai, T., Davis, K.L., Jager, A., Nolan, G.P., Bendall, S.C., Fantl, W.J., Blau, H.M., 2017. High-resolution Myogenic Lineage Mapping by Single-Cell Mass Cytometry. Nat. Cell Biol. 19, 558–567. https://doi.org/10.1038/ncb3507

Qian, X., Shen, Q., Goderie, S.K., He, W., Capela, A., Davis, A.A., Temple, S., 2000. Timing of CNS cell generation: a programmed sequence of neuron and glial cell production from isolated murine cortical stem cells. Neuron 28, 69–80. https://doi.org/10.1016/S0896-6273(00)00086-6

Qiu, P., Simonds, E.F., Bendall, S.C., Gibbs, K.D., Bruggner, R.V., Linderman, M.D., Sachs, K., Nolan, G.P., Plevritis, S.K., 2011. Extracting a cellular hierarchy from high-dimensional cytometry data with SPADE. Nat. Biotechnol. 29, 886–891. https://doi.org/10.1038/nbt.1991

Rabinovitch, M., 1995. Professional and non-professional phagocytes: an introduction. Trends Cell Biol. 5, 85–87. https://doi.org/10.1016/s0962-8924(00)88955-2

Rakic, P., 1982. Early developmental events: cell lineages, acquisition of neuronal positions, and areal and laminar development. Neurosci. Res. Program Bull. 20, 439–451.
Ransohoff, R.M., Perry, V.H., 2009. Microglial physiology: unique stimuli, specialized responses. Annu. Rev. Immunol. 27, 119–145. https://doi.org/10.1146/annurev.immunol.021908.132528
Reimegård, J., Tarbier, M., Danielsson, M., Schuster, J., Baskaran, S., Panagiotou, S., Dahl, N., Friedländer, M.R., Gallant, C.J., 2021. A combined approach for single-cell mRNA and intracellular protein expression analysis. Commun. Biol. 4, 1–11. https://doi.org/10.1038/s42003-021-02142-w
Renshaw, B., Forbes, A., Morison, B.R., 1940. Activity of the isocortex and hippocampus: electrical studies with micro-electrodes. J. Neurophysiol. 3, 74–105.
Riccio, O., Murthy, S., Szabo, G., Vutskits, L., Kiss, J.Z., Vitalis, T., Lebrand, C., Dayer, A.G., 2012. New pool of cortical interneuron precursors in the early postnatal dorsal white matter. Cereb. Cortex N. Y. N 1991 22, 86–98. https://doi.org/10.1093/cercor/bhr086
Richard, L., Topilko, P., Magy, L., Decouvelaere, A.-V., Charnay, P., Funalot, B., Vallat, J.-M., 2012. Endoneurial Fibroblast-Like Cells. J. Neuropathol. Exp. Neurol. 71, 938–947. https://doi.org/10.1097/NEN.0b013e318270a941
Richardson, W.D., Pringle, N., Mosley, M.J., Westermark, B., Dubois-Dalcq, M., 1988. A role for platelet-derived growth factor in normal gliogenesis in the central nervous system. Cell 53, 309–319. https://doi.org/10.1016/0092-8674(88)90392-3
Robinson, M.H., Vasquez, J., Kaushal, A., MacDonald, T.J., Vega, J.E.V., Schniederjan, M., Dhodapkar, K., 2020. Subtype and grade-dependent spatial heterogeneity of T-cell infiltration in pediatric glioma. J. Immunother. Cancer 8, e001066. https://doi.org/10.1136/jitc-2020-001066
Romanov, R.A., Tretiakov, E.O., Kastriti, M.E., Zupancic, M., Häring, M., Korchynska, S., Popadin, K., Benevento, M., Rebernik, P., Lallemend, F., Nishimori, K., Clotman, F., Andrews, W.D., Parnavelas, J.G., Farlik, M., Bock, C., Adameyko, I., Hökfelt, T., Keimpema, E., Harkany, T., 2020. Molecular design of hypothalamus development. Nature 582, 246–252. https://doi.org/10.1038/s41586-020-2266-0
Romanov, R.A., Zeisel, A., Bakker, J., Girach, F., Hellysaz, A., Tomer, R., Alpár, A., Mulder, J., Clotman, F., Keimpema, E., Hsueh, B., Crow, A.K., Martens, H., Schwindling, C., Calvigioni, D., Bains, J.S., Máté, Z., Szabó, G., Yanagawa, Y., Zhang, M.-D., Rendeiro, A., Farlik, M., Uhlén, M., Wulff, P., Bock, C., Broberger, C., Deisseroth, K., Hökfelt, T., Linnarsson, S., Horvath, T.L., Harkany, T., 2017. Molecular interrogation of hypothalamic organization reveals distinct dopamine neuronal subtypes. Nat. Neurosci. 20, 176–188. https://doi.org/10.1038/nn.4462
Romero, D.M., Bahi-Buisson, N., Francis, F., 2018. Genetics and mechanisms leading to human cortical malformations. Semin. Cell Dev. Biol., Neocortical development 76, 33–75. https://doi.org/10.1016/j.semcdb.2017.09.031
Rosenberg, A.B., Roco, C.M., Muscat, R.A., Kuchina, A., Sample, P., Yao, Z., Graybuck, L.T., Peeler, D.J., Mukherjee, S., Chen, W., Pun, S.H., Sellers, D.L., Tasic, B., Seelig, G., 2018. Single-cell profiling of the developing mouse brain and spinal cord with split-pool barcoding. Science 360, 176–182. https://doi.org/10.1126/science.aam8999
Ross, M.E., Walsh, C.A., 2001. Human Brain Malformations and Their Lessons for Neuronal Migration. Annu. Rev. Neurosci. 24, 1041–1070. https://doi.org/10.1146/annurev.neuro.24.1.1041
Rowitch, D.H., Kriegstein, A.R., 2010. Developmental genetics of vertebrate glial–cell specification. Nature 468, 214–222. https://doi.org/10.1038/nature09611
Ruan, X., Kang, B., Qi, C., Lin, W., Wang, J., Zhang, X., 2021. Progenitor cell diversity in the developing mouse neocortex. Proc. Natl. Acad. Sci. U. S. A. 118, e2018866118. https://doi.org/10.1073/pnas.2018866118

Rudy, B., Fishell, G., Lee, S., Hjerling-Leffler, J., 2011. Three groups of interneurons account for nearly 100% of neocortical GABAergic neurons. Dev. Neurobiol. 71, 45–61. https://doi.org/10.1002/dneu.20853
Ruhrberg, C., Bautch, V.L., 2013. Neurovascular development and links to disease. Cell. Mol. Life Sci. 70, 1675–1684. https://doi.org/10.1007/s00018-013-1277-5
Saelens, W., Cannoodt, R., Todorov, H., Saeys, Y., 2019. A comparison of single-cell trajectory inference methods. Nat. Biotechnol. 37, 547–554. https://doi.org/10.1038/s41587-019-0071-9
Salzer, J.L., 2015. Schwann Cell Myelination. Cold Spring Harb. Perspect. Biol. 7, a020529. https://doi.org/10.1101/cshperspect.a020529
Sankowski, R., Böttcher, C., Masuda, T., Geirsdottir, L., Sagar, Sindram, E., Seredenina, T., Muhs, A., Scheiwe, C., Shah, M.J., Heiland, D.H., Schnell, O., Grün, D., Priller, J., Prinz, M., 2019. Mapping microglia states in the human brain through the integration of high-dimensional techniques. Nat. Neurosci. 22, 2098–2110. https://doi.org/10.1038/s41593-019-0532-y
Sarropoulos, I., Sepp, M., Frömel, R., Leiss, K., Trost, N., Leushkin, E., Okonechnikov, K., Joshi, P., Giere, P., Kutscher, L.M., Cardoso-Moreira, M., Pfister, S.M., Kaessmann, H., 2021. Developmental and evolutionary dynamics of cis-regulatory elements in mouse cerebellar cells. Science 373, eabg4696. https://doi.org/10.1126/science.abg4696
Schindelin, J., Arganda-Carreras, I., Frise, E., Kaynig, V., Longair, M., Pietzsch, T., Preibisch, S., Rueden, C., Saalfeld, S., Schmid, B., Tinevez, J.-Y., White, D.J., Hartenstein, V., Eliceiri, K., Tomancak, P., Cardona, A., 2012. Fiji - an Open Source platform for biological image analysis. Nat. Methods 9, 10.1038/nmeth.2019. https://doi.org/10.1038/nmeth.2019
Schlegelmilch, T., Henke, K., Peri, F., 2011. Microglia in the developing brain: from immunity to behaviour. Curr. Opin. Neurobiol., Developmental neuroscience 21, 5–10. https://doi.org/10.1016/j.conb.2010.08.004
Schmidt, T., Carmeliet, P., 2010. Blood-vessel formation: Bridges that guide and unite. Nature 465, 697–699. https://doi.org/10.1038/465697a
Schüller, U., Heine, V.M., Mao, J., Kho, A.T., Dillon, A.K., Han, Y.-G., Huillard, E., Sun, T., Ligon, A.H., Qian, Y., Ma, Q., Alvarez-Buylla, A., McMahon, A.P., Rowitch, D.H., Ligon, K.L., 2008. Acquisition of granule neuron precursor identity is a critical determinant of progenitor cell competence to form Shh-induced medulloblastoma. Cancer Cell 14, 123–134. https://doi.org/10.1016/j.ccr.2008.07.005
Schuyler, R.P., Jackson, C., Garcia-Perez, J.E., Baxter, R.M., Ogolla, S., Rochford, R., Ghosh, D., Rudra, P., Hsieh, E.W.Y., 2019. Minimizing batch effects in mass cytometry data. Front. Immunol. 10, 2367. https://doi.org/10.3389/fimmu.2019.02367
Sessa, A., Ciabatti, E., Drechsel, D., Massimino, L., Colasante, G., Giannelli, S., Satoh, T., Akira, S., Guillemot, F., Broccoli, V., 2017. The Tbr2 molecular network controls cortical neuronal differentiation through complementary genetic and epigenetic pathways. Cereb. Cortex 27, 3378–3396. https://doi.org/10.1093/cercor/bhw270
Seto, Y., Ishiwata, S., Hoshino, M., 2014. Characterization of Olig2 expression during cerebellar development. Gene Expr. Patterns GEP 15, 1–7. https://doi.org/10.1016/j.gep.2014.02.001
Shaim, H., Shanley, M., Basar, R., Daher, M., Gumin, J., Zamler, D.B., Uprety, N., Wang, F., Huang, Y., Gabrusiewicz, K., Miao, Q., Dou, J., Alsuliman, A., Kerbauy, L.N., Acharya, S., Mohanty, V., Mendt, M., Li, S., Lu, J., Wei, J., Fowlkes, N.W., Gokdemir, E., Ensley, E.L., Kaplan, M., Kassab, C., Li, L., Ozcan, G., Banerjee, P.P., Shen, Y., Gilbert, A.L., Jones, C.M., Bdiwi, M., Nunez-Cortes, A.K., Liu, E., Yu, J., Imahashi, N., Muniz-Feliciano, L., Li, Y., Hu, J., Draetta, G., Marin, D., Yu, D., Mielke, S., Eyrich, M., Champlin, R.E., Chen, K., Lang, F.F., Shpall, E.J., Heimberger, A.B., Rezvani, K., 2021.

Targeting the αv integrin/TGF-β axis improves natural killer cell function against glioblastoma stem cells. J. Clin. Invest. 131. https://doi.org/10.1172/JCI142116
Shaklee, J., Srivastava, K., Brown, H., Arriaga, E.A., Pierre, V.C., van Berlo, J.H., 2018. Development of a Click-Chemistry Reagent Compatible with Mass Cytometry. Sci. Rep. 8, 6657. https://doi.org/10.1038/s41598-018-25000-y
Sharma, N., Flaherty, K., Lezgiyeva, K., Wagner, D.E., Klein, A.M., Ginty, D.D., 2020. The emergence of transcriptional identity in somatosensory neurons. Nature 577, 392–398. https://doi.org/10.1038/s41586-019-1900-1
Shen, Q., Wang, Y., Dimos, J.T., Fasano, C.A., Phoenix, T.N., Lemischka, I.R., Ivanova, N.B., Stifani, S., Morrisey, E.E., Temple, S., 2006. The timing of cortical neurogenesis is encoded within lineages of individual progenitor cells. Nat. Neurosci. 9, 743–751. https://doi.org/10.1038/nn1694
Shendure, J., Ji, H., 2008. Next-generation DNA sequencing. Nat. Biotechnol. 26, 1135–1145. https://doi.org/10.1038/nbt1486
Shigemoto-Mogami, Y., Hoshikawa, K., Goldman, J.E., Sekino, Y., Sato, K., 2014. Microglia enhance neurogenesis and oligodendrogenesis in the early postnatal subventricular zone. J. Neurosci. Off. J. Soc. Neurosci. 34, 2231–2243. https://doi.org/10.1523/JNEUROSCI.1619-13.2014
Silvin, A., Ginhoux, F., 2018. Microglia heterogeneity along a spatio–temporal axis: More questions than answers. Glia 66, 2045–2057. https://doi.org/10.1002/glia.23458
Simonds, E.F., Lu, E.D., Badillo, O., Karimi, S., Liu, E.V., Tamaki, W., Rancan, C., Downey, K.M., Stultz, J., Sinha, M., McHenry, L.K., Nasholm, N.M., Chuntova, P., Sundström, A., Genoud, V., Shahani, S.A., Wang, L.D., Brown, C.E., Walker, P.R., Swartling, F.J., Fong, L., Okada, H., Weiss, W.A., Hellström, M., 2021. Deep immune profiling reveals targetable mechanisms of immune evasion in immune checkpoint inhibitor-refractory glioblastoma. J. Immunother. Cancer 9, e002181. https://doi.org/10.1136/jitc-2020-002181
Sofroniew, M.V., Vinters, H.V., 2010. Astrocytes: biology and pathology. Acta Neuropathol. (Berl.) 119, 7–35. https://doi.org/10.1007/s00401-009-0619-8
Sommer, I., Schachner, M., 1981. Monoclonal antibodies (O1 to O4) to oligodendrocyte cell surfaces: An immunocytological study in the central nervous system. Dev. Biol. 83, 311–327. https://doi.org/10.1016/0012-1606(81)90477-2
Spassky, N., Heydon, K., Mangatal, A., Jankovski, A., Olivier, C., Queraud-Lesaux, F., Goujet-Zalc, C., Thomas, J.L., Zalc, B., 2001. Sonic hedgehog-dependent emergence of oligodendrocytes in the telencephalon: evidence for a source of oligodendrocytes in the olfactory bulb that is independent of PDGFRα signaling. Development 128, 4993–5004. https://doi.org/10.1242/dev.128.24.4993
Spitzer, M.H., Nolan, G.P., 2016. Mass Cytometry: Single Cells, Many Features. Cell 165, 780–791. https://doi.org/10.1016/j.cell.2016.04.019
Squarzoni, P., Oller, G., Hoeffel, G., Pont-Lezica, L., Rostaing, P., Low, D., Bessis, A., Ginhoux, F., Garel, S., 2014. Microglia modulate wiring of the embryonic forebrain. Cell Rep. 8, 1271–1279. https://doi.org/10.1016/j.celrep.2014.07.042
Stemple, D.L., Anderson, D.J., 1992. Isolation of a stem cell for neurons and glia from the mammalian neural crest. Cell 71, 973–985. https://doi.org/10.1016/0092-8674(92)90393-Q
Stoeckius, M., Hafemeister, C., Stephenson, W., Houck-Loomis, B., Chattopadhyay, P.K., Swerdlow, H., Satija, R., Smibert, P., 2017. Simultaneous epitope and transcriptome measurement in single cells. Nat. Methods 14, 865–868. https://doi.org/10.1038/nmeth.4380
Suh, H., Consiglio, A., Ray, J., Sawai, T., D'Amour, K.A., Gage, F.H., 2007. In vivo fate analysis reveals the multipotent and self-renewal capacities of Sox2+ neural stem cells in the

adult hippocampus. Cell Stem Cell 1, 515–528. https://doi.org/10.1016/j.stem.2007.09.002
Sun, T., Hevner, R.F., 2014. Growth and folding of the mammalian cerebral cortex: from molecules to malformations. Nat. Rev. Neurosci. 15, 217–232. https://doi.org/10.1038/nrn3707
Sun, Y., Dykes, I.M., Liang, X., Eng, S.R., Evans, S.M., Turner, E.E., 2008. A central role for Islet1 in sensory neuron development linking sensory and spinal gene regulatory programs. Nat. Neurosci. 11, 1283–1293. https://doi.org/10.1038/nn.2209
Surendran, A., Jenner, A.L., Karimi, E., Fiset, B., Quail, D.F., Walsh, L.A., Craig, M., 2023. Agent-Based Modelling Reveals the Role of the Tumor Microenvironment on the Short-Term Success of Combination Temozolomide/Immune Checkpoint Blockade to Treat Glioblastoma. J. Pharmacol. Exp. Ther. 387, 66–77. https://doi.org/10.1124/jpet.122.001571
Svaren, J., Meijer, D., 2008. The molecular machinery of myelin gene transcription in Schwann cells. Glia 56, 1541–1551. https://doi.org/10.1002/glia.20767
Swinnen, N., Smolders, S., Avila, A., Notelaers, K., Paesen, R., Ameloot, M., Brône, B., Legendre, P., Rigo, J.-M., 2013. Complex invasion pattern of the cerebral cortex bymicroglial cells during development of the mouse embryo. Glia 61, 150–163. https://doi.org/10.1002/glia.22421
Tang, F., Barbacioru, C., Wang, Y., Nordman, E., Lee, C., Xu, N., Wang, X., Bodeau, J., Tuch, B.B., Siddiqui, A., Lao, K., Surani, M.A., 2009. mRNA-Seq whole-transcriptome analysis of a single cell. Nat. Methods 6, 377–382. https://doi.org/10.1038/nmeth.1315
Tasic, B., Menon, V., Nguyen, T.N., Kim, T.K., Jarsky, T., Yao, Z., Levi, B., Gray, L.T., Sorensen, S.A., Dolbeare, T., Bertagnolli, D., Goldy, J., Shapovalova, N., Parry, S., Lee, C., Smith, K., Bernard, A., Madisen, L., Sunkin, S.M., Hawrylycz, M., Koch, C., Zeng, H., 2016. Adult mouse cortical cell taxonomy revealed by single cell transcriptomics. Nat. Neurosci. 19, 335–346. https://doi.org/10.1038/nn.4216
Tata, M., Ruhrberg, C., Fantin, A., 2015. Vascularisation of the central nervous system. Mech. Dev. 138, 26–36. https://doi.org/10.1016/j.mod.2015.07.001
Tata, M., Wall, I., Joyce, A., Vieira, J.M., Kessaris, N., Ruhrberg, C., 2016. Regulation of embryonic neurogenesis by germinal zone vasculature. Proc. Natl. Acad. Sci. U. S. A. 113, 13414–13419. https://doi.org/10.1073/pnas.1613113113
Tatsumi, K., Isonishi, A., Yamasaki, M., Kawabe, Y., Morita-Takemura, S., Nakahara, K., Terada, Y., Shinjo, T., Okuda, H., Tanaka, T., Wanaka, A., 2018. Olig2-lineage astrocytes: a distinct subtype of astrocytes that differs from GFAP astrocytes. Front. Neuroanat. 12, 8. https://doi.org/10.3389/fnana.2018.00008
Taylor, M.K., Yeager, K., Morrison, S.J., 2007. Physiological Notch signaling promotes gliogenesis in the developing peripheral and central nervous systems. Dev. Camb. Engl. 134, 2435–2447. https://doi.org/10.1242/dev.005520
Teh, C.E., Gong, J.-N., Segal, D., Tan, T., Vandenberg, C.J., Fedele, P.L., Low, M.S.Y., Grigoriadis, G., Harrison, S.J., Strasser, A., Roberts, A.W., Huang, D.C.S., Nolan, G.P., Gray, D.H.D., Ko, M.E., 2020. Deep profiling of apoptotic pathways with mass cytometry identifies a synergistic drug combination for killing myeloma cells. Cell Death Differ. 27, 2217–2233. https://doi.org/10.1038/s41418-020-0498-z
Tekki-Kessaris, N., Woodruff, R., Hall, A.C., Gaffield, W., Kimura, S., Stiles, C.D., Rowitch, D.H., Richardson, W.D., 2001. Hedgehog-dependent oligodendrocyte lineage specification in the telencephalon. Dev. Camb. Engl. 128, 2545–2554. https://doi.org/10.1242/dev.128.13.2545
Telley, L., Govindan, S., Prados, J., Stevant, I., Nef, S., Dermitzakis, E., Dayer, A., Jabaudon, D., 2016. Sequential transcriptional waves direct the differentiation of newborn neurons

in the mouse neocortex. Science 351, 1443–1446. https://doi.org/10.1126/science.aad8361
Tiklová, K., Björklund, Å.K., Lahti, L., Fiorenzano, A., Nolbrant, S., Gillberg, L., Volakakis, N., Yokota, C., Hilscher, M.M., Hauling, T., Holmström, F., Joodmardi, E., Nilsson, M., Parmar, M., Perlmann, T., 2019. Single-cell RNA sequencing reveals midbrain dopamine neuron diversity emerging during mouse brain development. Nat. Commun. 10, 581. https://doi.org/10.1038/s41467-019-08453-1
Tosevski, V., Ulashchik, E., Trovato, A., Cappella, P., 2017. CyTOF Mass Cytometry for Click Proliferation Assays. Curr. Protoc. Cytom. 81, 7.50.1-7.50.14. https://doi.org/10.1002/cpcy.25
Traag, V.A., Waltman, L., van Eck, N.J., 2019. From Louvain to Leiden: guaranteeing well-connected communities. Sci. Rep. 9, 5233. https://doi.org/10.1038/s41598-019-41695-z
Tsai, H.-H., Li, H., Fuentealba, L.C., Molofsky, A.V., Taveira-Marques, R., Zhuang, H., Tenney, A., Murnen, A.T., Fancy, S.P.J., Merkle, F., Kessaris, N., Alvarez-Buylla, A., Richardson, W.D., Rowitch, D.H., 2012. Regional Astrocyte Allocation Regulates CNS Synaptogenesis and Repair. Science 337, 358–362. https://doi.org/10.1126/science.1222381
Tsai, H.-H., Niu, J., Munji, R., Davalos, D., Chang, J., Zhang, H., Tien, A.-C., Kuo, C.J., Chan, J.R., Daneman, R., Fancy, S.P.J., 2016. Oligodendrocyte precursors migrate along vasculature in the developing nervous system. Science 351, 379–384. https://doi.org/10.1126/science.aad3839
Turrero García, M., Stegmann, S.K., Lacey, T.E., Reid, C.M., Hrvatin, S., Weinreb, C., Adam, M.A., Nagy, M.A., Harwell, C.C., 2021. Transcriptional profiling of sequentially generated septal neuron fates. eLife 10, e71545. https://doi.org/10.7554/eLife.71545
Usoskin, D., Furlan, A., Islam, S., Abdo, H., Lönnerberg, P., Lou, D., Hjerling-Leffler, J., Haeggström, J., Kharchenko, O., Kharchenko, P.V., Linnarsson, S., Ernfors, P., 2015. Unbiased classification of sensory neuron types by large-scale single-cell RNA sequencing. Nat. Neurosci. 18, 145–153. https://doi.org/10.1038/nn.3881
van Hooren, L., Handgraaf, S.M., Kloosterman, D.J., Karimi, E., van Mil, L.W.H.G., Gassama, A.A., Solsona, B.G., de Groot, M.H.P., Brandsma, D., Quail, D.F., Walsh, L.A., Borst, G.R., Akkari, L., 2023. CD103+ regulatory T cells underlie resistance to radio-immunotherapy and impair CD8+ T cell activation in glioblastoma. Nat. Cancer 4, 665–681. https://doi.org/10.1038/s43018-023-00547-6
van Tilborg, E., de Theije, C.G.M., van Hal, M., Wagenaar, N., de Vries, L.S., Benders, M.J., Rowitch, D.H., Nijboer, C.H., 2018. Origin and dynamics of oligodendrocytes in the developing brain: Implications for perinatal white matter injury. Glia 66, 221–238. https://doi.org/10.1002/glia.23256
VanRyzin, J.W., 2021. Phagocytic microglia in development: Are they what they eat? Brain Behav. Immun. - Health 18, 100373. https://doi.org/10.1016/j.bbih.2021.100373
Vasquez, J.C., Huttner, A., Zhang, L., Marks, A., Chan, A., Baehring, J.M., Kahle, K.T., Dhodapkar, K.M., 2017. SOX2 immunity and tissue resident memory in children and young adults with glioma. J. Neurooncol. 134, 41–53. https://doi.org/10.1007/s11060-017-2515-8
Vasudevan, A., Long, J.E., Crandall, J.E., Rubenstein, J.L.R., Bhide, P.G., 2008. Compartment-specific transcription factors orchestrate angiogenesis gradients in the embryonic brain. Nat. Neurosci. 11, 429–439. https://doi.org/10.1038/nn2074
Verity, A.N., Campagnoni, A.T., 1988. Regional expression of myelin protein genes in the developing mouse brain: In situ hybridization studies. J. Neurosci. Res. 21, 238–248. https://doi.org/10.1002/jnr.490210216
Verney, C., Monier, A., Fallet-Bianco, C., Gressens, P., 2010. Early microglial colonization of the human forebrain and possible involvement in periventricular white-matter injury of

preterm infants. J. Anat. 217, 436–448. https://doi.org/10.1111/j.1469-7580.2010.01245.x
Vogenstahl, J., Parrilla, M., Acker-Palmer, A., Segarra, M., 2022. Vascular Regulation of Developmental Neurogenesis. Front. Cell Dev. Biol. 10, 890852. https://doi.org/10.3389/fcell.2022.890852
Volovitz, I., Shapira, N., Ezer, H., Gafni, A., Lustgarten, M., Alter, T., Ben-Horin, I., Barzilai, O., Shahar, T., Kanner, A., Fried, I., Veshchev, I., Grossman, R., Ram, Z., 2016. A non-aggressive, highly efficient, enzymatic method for dissociation of human brain-tumors and brain-tissues to viable single-cells. BMC Neurosci. 17, 30. https://doi.org/10.1186/s12868-016-0262-y
Vradenburgh, S.A., Van Deusen, A.L., Beachum, A.N., Moats, J.M., Hirt, A.K., Deppmann, C.D., Keeler, A.B., Zunder, E.R., 2023. Sexual dimorphism in the dorsal root ganglia of neonatal mice identified by protein expression profiling with single-cell mass cytometry. Mol. Cell. Neurosci. 126, 103866. https://doi.org/10.1016/j.mcn.2023.103866
Wang, H., Xu, L., Lai, C., Hou, K., Chen, J., Guo, Y., Sambangi, A., Swaminathan, S., Xie, C., Wu, Z., Chen, G., 2021. Region-specific distribution of Olig2-expressing astrocytes in adult mouse brain and spinal cord. Mol. Brain 14, 36. https://doi.org/10.1186/s13041-021-00747-0
Wang, K., Wang, S., Chen, Y., Wu, D., Hu, X., Lu, Y., Wang, L., Bao, L., Li, C., Zhang, X., 2021. Single-cell transcriptomic analysis of somatosensory neurons uncovers temporal development of neuropathic pain. Cell Res. 31, 904–918. https://doi.org/10.1038/s41422-021-00479-9
Wang, P.L., Yim, A.K.Y., Kim, K.-W., Avey, D., Czepielewski, R.S., Colonna, M., Milbrandt, J., Randolph, G.J., 2020. Peripheral nerve resident macrophages share tissue-specific programming and features of activated microglia. Nat. Commun. 11, 2552. https://doi.org/10.1038/s41467-020-16355-w
Wegner, M., Stolt, C.C., 2005. From stem cells to neurons and glia: a Soxist's view of neural development. Trends Neurosci. 28, 583–588. https://doi.org/10.1016/j.tins.2005.08.008
Wei, Z., Fei, Y., Su, W., Chen, G., 2019. Emerging Role of Schwann Cells in Neuropathic Pain: Receptors, Glial Mediators and Myelination. Front. Cell. Neurosci. 13.
Weisheit, G., Gliem, M., Endl, E., Pfeffer, P.L., Busslinger, M., Schilling, K., 2006. Postnatal development of the murine cerebellar cortex: formation and early dispersal of basket, stellate and Golgi neurons. Eur. J. Neurosci. 24, 466–478. https://doi.org/10.1111/j.1460-9568.2006.04915.x
Weng, Q., Wang, Jincheng, Wang, Jiajia, He, D., Cheng, Z., Zhang, F., Verma, R., Xu, L., Dong, X., Liao, Y., He, X., Potter, A., Zhang, L., Zhao, C., Xin, M., Zhou, Q., Aronow, B.J., Blackshear, P.J., Rich, J.N., He, Q., Zhou, W., Suvà, M.L., Waclaw, R.R., Potter, S.S., Yu, G., Lu, Q.R., 2019. Single-cell transcriptomics uncovers glial progenitor diversity and cell fate determinants during development and gliomagenesis. Cell Stem Cell 24, 707-723.e8. https://doi.org/10.1016/j.stem.2019.03.006
Wheeler, M.A., Heffner, D.L., Kim, S., Espy, S.M., Spano, A.J., Cleland, C.L., Deppmann, C.D., 2014. TNF-α/TNFR1 signaling is required for the development and function of primary nociceptors. Neuron 82, 587–602. https://doi.org/10.1016/j.neuron.2014.04.009
White, F.A., Keller-Peck, C.R., Knudson, C.M., Korsmeyer, S.J., Snider, W.D., 1998. Widespread elimination of naturally occurring neuronal death in Bax-deficient mice. J. Neurosci. Off. J. Soc. Neurosci. 18, 1428–1439. https://doi.org/10.1523/JNEUROSCI.18-04-01428.1998
White, F.A., Silos-Santiago, I., Molliver, D.C., Nishimura, M., Phillips, H., Barbacid, M., Snider, W.D., 1996. Synchronous onset of NGF and TrkA survival dependence in developing dorsal root ganglia. J. Neurosci. Off. J. Soc. Neurosci. 16, 4662–4672. https://doi.org/10.1523/JNEUROSCI.16-15-04662.1996

Wilsch-Bräuninger, M., Florio, M., Huttner, W.B., 2016. Neocortex expansion in development and evolution — from cell biology to single genes. Curr. Opin. Neurobiol., Cellular neuroscience 39, 122–132. https://doi.org/10.1016/j.conb.2016.05.004
Wizeman, J.W., Guo, Q., Wilion, E.M., Li, J.Y., 2019. Specification of diverse cell types during early neurogenesis of the mouse cerebellum. eLife 8, e42388. https://doi.org/10.7554/eLife.42388
Woldring, S., Dirken, M.N.J., 1950. Spontaneous unit-activity in the superficial cortical layers. Acta Physiol. Pharmacol. Neerl. 1, 369–379.
Wood, W., Turmaine, M., Weber, R., Camp, V., Maki, R.A., McKercher, S.R., Martin, P., 2000. Mesenchymal cells engulf and clear apoptotic footplate cells in macrophageless PU.1 null mouse embryos. Dev. Camb. Engl. 127, 5245–5252. https://doi.org/10.1242/dev.127.24.5245
Woods, R.M., Lorusso, J.M., Potter, H.G., Neill, J.C., Glazier, J.D., Hager, R., 2021. Maternal immune activation in rodent models: A systematic review of neurodevelopmental changes in gene expression and epigenetic modulation in the offspring brain. Neurosci. Biobehav. Rev. 129, 389–421. https://doi.org/10.1016/j.neubiorev.2021.07.015
Wu, H., Petitpré, C., Fontanet, P., Sharma, A., Bellardita, C., Quadros, R.M., Jannig, P.R., Wang, Y., Heimel, J.A., Cheung, K.K.Y., Wanderoy, S., Xuan, Y., Meletis, K., Ruas, J., Gurumurthy, C.B., Kiehn, O., Hadjab, S., Lallemend, F., 2021. Distinct subtypes of proprioceptive dorsal root ganglion neurons regulate adaptive proprioception in mice. Nat. Commun. 12, 1026. https://doi.org/10.1038/s41467-021-21173-9
Wu, H.-H., Bellmunt, E., Scheib, J.L., Venegas, V., Burkert, C., Reichardt, L.F., Zhou, Z., Fariñas, I., Carter, B.D., 2009. Glial precursors clear sensory neuron corpses during development via Jedi-1, an engulfment receptor. Nat. Neurosci. 12, 1534–1541. https://doi.org/10.1038/nn.2446
Xie, M., Liu, Y.U., Zhao, S., Zhang, L., Bosco, D.B., Pang, Y.-P., Zhong, J., Sheth, U., Martens, Y.A., Zhao, N., Liu, C.-C., Zhuang, Y., Wang, L., Dickson, D.W., Mattson, M.P., Bu, G., Wu, L.-J., 2022. TREM2 interacts with TDP-43 and mediates microglial neuroprotection against TDP-43-related neurodegeneration. Nat. Neurosci. 25, 26–38. https://doi.org/10.1038/s41593-021-00975-6
Xing, D., Tan, L., Chang, C.-H., Li, H., Xie, X.S., 2021. Accurate SNV detection in single cells by transposon-based whole-genome amplification of complementary strands. Proc. Natl. Acad. Sci. U. S. A. 118, e2013106118. https://doi.org/10.1073/pnas.2013106118
Xu, Q., Cobos, I., De La Cruz, E., Rubenstein, J.L., Anderson, S.A., 2004. Origins of Cortical Interneuron Subtypes. J. Neurosci. 24, 2612–2622. https://doi.org/10.1523/JNEUROSCI.5667-03.2004
Xuan, I.C.Y., Hampson, D.R., 2014. Gender-Dependent Effects of Maternal Immune Activation on the Behavior of Mouse Offspring. PLoS ONE 9, e104433. https://doi.org/10.1371/journal.pone.0104433
Yan, J., Zhao, Q., Wang, Jian, Tian, X., Wang, Jing, Xia, X., Ott, M., Rao, G., Heimberger, A.B., Li, S., 2021. FGL2-wired macrophages secrete CXCL7 to regulate the stem-like functionality of glioma cells. Cancer Lett. 506, 83–94. https://doi.org/10.1016/j.canlet.2021.02.021
Yao, Y., Li, Y., Ni, W., Li, Z., Feng, L., Wang, Y., Meng, J., Zhao, H., 2021. Systematic Study of Immune Cell Diversity in ischemic postconditioning Using High-Dimensional Single-Cell Analysis with Mass Cytometry. Aging Dis. 12, 812–825. https://doi.org/10.14336/AD.2020.1115
Yoon, K.-J., Vissers, C., Ming, G.-L., Song, H., 2018. Epigenetics and epitranscriptomics in temporal patterning of cortical neural progenitor competence. J. Cell Biol. 217, 1901–1914. https://doi.org/10.1083/jcb.201802117

Yu, J., Vodyanik, M.A., Smuga-Otto, K., Antosiewicz-Bourget, J., Frane, J.L., Tian, S., Nie, J., Jonsdottir, G.A., Ruotti, V., Stewart, R., Slukvin, I.I., Thomson, J.A., 2007. Induced Pluripotent Stem Cell Lines Derived from Human Somatic Cells. Science 318, 1917–1920. https://doi.org/10.1126/science.1151526

Yuste, R., Hawrylycz, M., Aalling, N., Aguilar-Valles, A., Arendt, D., Armañanzas, R., Ascoli, G.A., Bielza, C., Bokharaie, V., Bergmann, T.B., Bystron, I., Capogna, M., Chang, Y., Clemens, A., de Kock, C.P.J., DeFelipe, J., Dos Santos, S.E., Dunville, K., Feldmeyer, D., Fiáth, R., Fishell, G.J., Foggetti, A., Gao, X., Ghaderi, P., Goriounova, N.A., Güntürkün, O., Hagihara, K., Hall, V.J., Helmstaedter, M., Herculano-Houzel, S., Hilscher, M.M., Hirase, H., Hjerling-Leffler, J., Hodge, R., Huang, J., Huda, R., Khodosevich, K., Kiehn, O., Koch, H., Kuebler, E.S., Kühnemund, M., Larrañaga, P., Lelieveldt, B., Louth, E.L., Lui, J.H., Mansvelder, H.D., Marin, O., Martinez-Trujillo, J., Chameh, H.M., Mohapatra, A.N., Munguba, H., Nedergaard, M., Němec, P., Ofer, N., Pfisterer, U.G., Pontes, S., Redmond, W., Rossier, J., Sanes, J.R., Scheuermann, R.H., Serrano-Saiz, E., Staiger, J.F., Somogyi, P., Tamás, G., Tolias, A.S., Tosches, M.A., García, M.T., Wozny, C., Wuttke, T.V., Liu, Y., Yuan, J., Zeng, H., Lein, E., 2020. A community-based transcriptomics classification and nomenclature of neocortical cell types. Nat. Neurosci. 23, 1456–1468. https://doi.org/10.1038/s41593-020-0685-8

Yuzwa, S.A., Borrett, M.J., Innes, B.T., Voronova, A., Ketela, T., Kaplan, D.R., Bader, G.D., Miller, F.D., 2017. Developmental Emergence of Adult Neural Stem Cells as Revealed by Single-Cell Transcriptional Profiling. Cell Rep. 21, 3970–3986. https://doi.org/10.1016/j.celrep.2017.12.017

Zeisel, A., Hochgerner, H., Lönnerberg, P., Johnsson, A., Memic, F., van der Zwan, J., Häring, M., Braun, E., Borm, L.E., La Manno, G., Codeluppi, S., Furlan, A., Lee, K., Skene, N., Harris, K.D., Hjerling-Leffler, J., Arenas, E., Ernfors, P., Marklund, U., Linnarsson, S., 2018. Molecular Architecture of the Mouse Nervous System. Cell 174, 999-1014.e22. https://doi.org/10.1016/j.cell.2018.06.021

Zeisel, A., Muñoz-Manchado, A.B., Codeluppi, S., Lönnerberg, P., La Manno, G., Juréus, A., Marques, S., Munguba, H., He, L., Betsholtz, C., Rolny, C., Castelo-Branco, G., Hjerling-Leffler, J., Linnarsson, S., 2015. Brain structure. Cell types in the mouse cortex and hippocampus revealed by single-cell RNA-seq. Science 347, 1138–1142. https://doi.org/10.1126/science.aaa1934

Zhang, T., Liu, T., Mora, N., Guegan, J., Bertrand, M., Contreras, X., Hansen, A.H., Streicher, C., Anderle, M., Danda, N., Tiberi, L., Hippenmeyer, S., Hassan, B.A., 2021. Generation of excitatory and inhibitory neurons from common progenitors via Notch signaling in the cerebellum. Cell Rep. 35, 109208. https://doi.org/10.1016/j.celrep.2021.109208

Zhang, Y., Liu, G., Guo, T., Liang, X.G., Du, H., Yang, L., Bhaduri, A., Li, X., Xu, Z., Zhang, Z., Li, Z., He, M., Tsyporin, J., Kriegstein, A.R., Rubenstein, J.L., Yang, Z., Chen, B., 2020. Cortical Neural Stem Cell Lineage Progression Is Regulated by Extrinsic Signaling Molecule Sonic Hedgehog. Cell Rep. 30, 4490-4504.e4. https://doi.org/10.1016/j.celrep.2020.03.027

Zheng, K., Wang, C., Yang, J., Huang, H., Zhao, X., Zhang, Z., Qiu, M., 2018. Molecular and genetic evidence for the PDGFRα-independent population of oligodendrocyte progenitor cells in the developing mouse brain. J. Neurosci. 38, 9505–9513. https://doi.org/10.1523/JNEUROSCI.1510-18.2018

Zhou, Q., Wang, S., Anderson, D.J., 2000. Identification of a novel family of oligodendrocyte lineage-specific basic helix–loop–helix transcription factors. Neuron 25, 331–343. https://doi.org/10.1016/S0896-6273(00)80898-3

Zhou, X., Zhong, S., Peng, H., Liu, J., Ding, W., Sun, L., Ma, Q., Liu, Z., Chen, R., Wu, Q., Wang, X., 2020. Cellular and molecular properties of neural progenitors in the

developing mammalian hypothalamus. Nat. Commun. 11, 4063. https://doi.org/10.1038/s41467-020-17890-2
Zhu, Y., Crowley, S.C., Latimer, A.J., Lewis, G.M., Nash, R., Kucenas, S., 2019. Migratory neural crest cells phagocytose dead cells in the developing nervous system. Cell 179, 74-89.e10. https://doi.org/10.1016/j.cell.2019.08.001
Zilkha-Falb, R., Rachutin-Zalogin, T., Cleaver, L., Gurevich, M., Achiron, A., 2020. RAM-589.555 favors neuroprotective and anti-inflammatory profile of CNS-resident glial cells in acute relapse EAE affected mice. J. Neuroinflammation 17, 313. https://doi.org/10.1186/s12974-020-01983-2
Zimmer, C., Tiveron, M.-C., Bodmer, R., Cremer, H., 2004. Dynamics of Cux2 expression suggests that an early pool of SVZ precursors is fated to become upper cortical layer neurons. Cereb. Cortex N. Y. N 1991 14, 1408–1420. https://doi.org/10.1093/cercor/bhh102
Zong, C., Lu, S., Chapman, A.R., Xie, X.S., 2012. Genome-Wide Detection of Single Nucleotide and Copy Number Variations of a Single Human Cell. Science 338, 1622–1626. https://doi.org/10.1126/science.1229164
Zunder, E.R., Finck, R., Behbehani, G.K., Amir, E.D., Krishnaswamy, S., Gonzalez, V.D., Lorang, C.G., Bjornson, Z., Spitzer, M.H., Bodenmiller, B., Fantl, W.J., Pe'er, D., Nolan, G.P., 2015a. Palladium-based mass tag cell barcoding with a doublet-filtering scheme and single-cell deconvolution algorithm. Nat. Protoc. 10, 316–333. https://doi.org/10.1038/nprot.2015.020
Zunder, E.R., Lujan, E., Goltsev, Y., Wernig, M., Nolan, G.P., 2015b. A Continuous Molecular Roadmap to iPSC Reprogramming through Progression Analysis of Single-Cell Mass Cytometry. Cell Stem Cell 16, 323–337. https://doi.org/10.1016/j.stem.2015.01.015

Appendix I: Extended Data for Mass Cytometry Analysis of Mouse Brain Development

The contents of this chapter, corresponding to Chapter II, have been accepted for publication as “A developmental atlas of the mouse brain by single-cell mass cytometry.” Amy Van Deusen, Sushanth Kumar, O. Yipkin Calhan, Sarah Goggin, Jiachen Shi, Corey Williams, Austin Keeler, Kristen Fread, Irene Gadani, Christopher Deppmann, Eli Zunder. *Nature Neuroscience* [Accepted Jan 8 2024].

Metal	Reagent	Full Name(s)	Cell Types	Reference	Vendor	Catalog No.	Host	Clone	[CyTOF]	Localization	Reactivity
Y89	TuJ1	Beta 3-tubulin	Neurons	Caccamo, 1989	Gift (A. Spano)	–	Mouse	TuJ1	1000 ng/mL	Intracellular	Hu, Ms, Rt
In113	Olig2	Oligodendrocyte transcription factor 2	OPCs, Cholinergic Neuron and Interneuron Progenitor	Lu, 2000; Zhou, 2000	Millipore	MABN50	Mouse	211F1.1	1000 ng/mL	Intracellular	Hu, Ms, Rt
In115	A2B5	–	O2A Progenitors, Type 2 Astrocytes	Eisenbarth, 1979; Raff, 1983	Biolegend	150702	Mouse	105/A2B5	300 ng/mL	Surface	Hu, Ms
La139	PSA-NCAM	Polysialylated-neural cell adhesion molecule	Neuronal Progenitors	Theiry, 1979	eBioscience	14-9118-82	Mouse	12E3	300 ng/mL	Surface	Hu, Ms, Rt
Pr141	CD140b	Platelet-derived growth factor beta	OPCs, Fibroblasts	Richardson, 1988; Noble, 1988	eBioscience	14-1402-82	Rat	APB5	10 ng/mL	Surface	Hu, Ms, Fish
Nd142	VCAM1	CD106, Vascular cell adhesion molecule	NSCs, Glial Progenitors, and Neurovascular Cells	Osborn, 1989; Kokovay, 2012	Biolegend	105702	Mouse	429 (MVCAM.A)	100 ng/mL	Surface	Ms
Nd143	CD31	PECAM-1, Endothelial cell adhesion molecule	Endothelial cells	Newman, 1990; Vasudevan, 2008	Biolegend	102425	Rat	390	50 ng/mL	Surface	Ms
Nd144	Nestin	–	NSCs, Glial Progenitors, and Neurovascular Cells	Dahlstrand, 1992	R&D Systems	MAB2736	Mouse	307501	30 ng/mL	Intracellular	Ms, Rt
Nd145	Sox1	SRY-box transcription factor 1	Neural stem cells (especially striatal neuronal)	Gubbay, 1990; Pevny, 1998	R&D Systems	AF3369	Goat	Polyclonal	300 ng/mL	Intracellular	Hu, Ms, Rt
Nd146	Tbr2	T-box brain gene 2, EOMES, eomesdermin	Intermediate neuronal progenitors	Russ, 2000	Thermo Fisher	14-4875-82	Mouse	Dan11mag	1000 ng/mL	Intracellular	Ms
Sm147	CD140a	Platelet-derived growth factor alpha	OPCs and brain fibroblasts	Pringle, 1989	Biolegend	135902	Rat	APA5	30 ng/mL	Surface	Ms
Nd148	CD133	Prominin	Ependymal cells; apical neural progenitors	Weigmann, 1997	Biolegend	141202	Rat	315-2C11	100 ng/mL	Surface	Ms
Sm149	CD45	Tyrosine phosphatase receptor type C	Microglia and other leukocytes	Akiyama, 1988	Fluidigm	3089005B	Mouse	30-F11	10 ng/mL	Surface	Ms
Nd150	NeuN	Neuronal Nuclei	Neurons	Mullen, 1992	Novus	NBP1-92693	Mouse	1B7	100 ng/mL	Intracellular	Hu, Ms, Rt
Eu151	Sox10	Sex-determining region Y box 10	OPCs	Hu, 2009	Gift (S. Kucenas)	–	Rabbit	Monoclonal	3000 ng/mL	Intracellular	Ms, Rt, Fish
Sm152	Ki67	MKI67, Marker of proliferation Ki-67	Proliferative cells	Gerdes, 1983	BD Biosciences	550609	Mouse	B56	1000 ng/mL	Intracellular	Hu, Ms
Eu153	Oligo O4	Oligodendrocyte marker O4	Oligodendrocytes, Microglia?	Yokoyama, 2003	R&D Systems	MAB1326	Mouse	O4	300 ng/mL	Surface	Hu, Ms, Rt, Ck
Sm154	Pax6	Paired box 6	Neural stem cells, dorsal endothelial progenitors	Walther, 1991; Vasudevan, 2008	BD Biosciences	561462	Mouse	O18-1330	50 ng/mL	Intracellular	Hu, Ms
Gd155	MCAM	CD146, Melanoma cell adhersion molecule	Neurovascular cells	Schwarz, 1998	eBioscience	14-1469-80	Mouse	P1H12	30 ng/mL	Surface	Hu, Ms, Rb
Gd156	NeuroD1	Neurogenic differentiation 1	Differentiating neurons	Lee, 1998	R&D Systems	AF2746	Goat	Polyclonal	1000 ng/mL	Intracellular	Hu, Ms
Gd157	SSEA-1	CD15, Stage-specific embryonic antigen, Sialyl LewisX	Stem cells	Knowles, 1978	eBioscience	14-8813-80	Mouse	MC-480	10 ng/mL	Surface	Hu, Ms
Gd158	CD11b	Integrin aN, Mac-1	Microglia and monocytes	Perry, 1985	Biolegend	101249	Rat	M1/70	100 ng/mL	Surface	Hu, Ms
Tb159	CD24	Heat stable antigen	Postmitotic neural cells	Shirasawa, 1993	BD Biosciences	557436	Rat	m1/69	30 ng/mL	Surface	Ms
Gd160	Sox2	Sex-determining region Y box 2	Neural stem cells	Uwanogho, 1995	R&D Systems	MAB2018	Mouse	245610	1000 ng/mL	Intracellular	Hu, Ms, Rt
Dy161	CD325	N-cadherin	Most neural cells	Hatta, 1985	Biolegend	844702	Mouse	13A9	100 ng/mL	Surface	Hu, Ms, Rt
Dy162	GAD65	Glutamic acid decarboxylase 65-kD, glutamate decarboxylase	Interneurons	Kaufman, 1991	Biolegend	844502	Mouse	N-GAD65	300 ng/mL	Intracellular	Hu, Ms, Rt
Dy163	DCX	Doublecortin	Newborn neurons	des Portes, 1998	Thermo Fisher	481200	Rabbit	Polyclonal	500 ng/mL	Intracellular	Hu, Ms, Rt
Dy164	MAP2	Microtubule-associated protein 2	Differentiated neurons	Izant and McIntosh, 1980	Novus	NBP2-25156	Mouse	4H5	500 ng/mL	Intracellular	Hu, Ms
Ho165	ALDH1A1	Aldehyde dehydrogenase 1A1	Dopaminergic neurons, astrocyte progenitors	Galter, 2003; Adam, 2012	R&D Systems	AF5869	Goat	Polyclonal	100 ng/mL	Intracellular	Hu, Ms
Er166	Ly-6C	Lymphocyte antigen 6 complex, locus C	T cells	LeClair, 1989	Biolegend	128002	Rat	HK1.4	30 ng/mL	Surface	Ms
Er167	GLAST	Glutamate asparate transporter	Glial cells	Storck, 1992	Novus	NB100-1869	Rabbit	Polyclonal	1000 ng/mL	Surface	Hu, Ms, Rt
Er168	Ctip2	COUP-TF-interacting protein 2, Bcl11b	Developing neurons	Yamamato, 1999	Abcam	ab18465	Rat	25B6	200 ng/mL	Intracellular	Hu, Ms
Tm169	GFAP	Glial fibrillary acidic protein	Astrocytes	Uyeda, 1972	BD Biosciences	556330	Mouse	102	100 ng/mL	Intracellular	Hu, Ms, Rt
Er170	Cux1	Cut-like homeobox 1	Neural cells	Quaggin, 1996	Abcam	ab54583	Mouse	2A10	10 ng/mL	Intracellular	Hu, Ms
Yb171	Tbr1	T-box brain gene 1	Neurons (predominantly cortical)	Bulfone, 1995	Abcam	ab31940	Rabbit	Polyclonal	1000 ng/mL	Intracellular	Hu, Ms, Rt
Yb172	BLBP	Brain lipid-binding protein, fatty acid binding protein 7	Radial glial cells	Feng, 1994; Kurtz, 1994	Gift (C. Birchmeier & T. Müller)		Rabbit	Polyclonal	1000 ng/mL	Intracellular	Hu, Ms, Rt, Fish
Yb173	Cl. Casp-3	Caspase 3 (Cleaved Form)	Apoptotic Cells	Fernandes-Alnemri, 1994	BD Biosciences	559565	Rabbit	C92-605	500 ng/mL	Intracellular	Hu, Ms
Yb174	TrkB	Neurotrophic tyrosine kinase receptor type 2	Developing neural cells	Klein, 1989	Thermo Fisher	AF1494	Goat	Polyclonal	100 ng/mL	Surface	Ms
Yb175	F4/80	EMR1, Ly-71	Macrophages	Austyn, 1981	Biolegend	123101	Rat	BM8	100 ng/mL	Surface	Ms
Yb176	p75NTR	P75 neurotrophic receptor, TNF receptor 16	Neural cells	Herrup, 1973	R&D Systems	AF1157	Goat	Polyclonal	300 ng/mL	Surface	Ms
Ir191/193	DNA Intercalator	Cell-ID Intercalator-Ir	All fixed cells	–	Fluidigm	201192A	-	-	(1:5000)	Intracellular	Eukaryotic cells
Pt195/198	Cisplatin	Cisplatin	Dead cells	Fienberg, 2012	EMD Millipore	23120	-	-	5 uM	-	-

Ext. Data Fig. 1. Validation of single-cell processing of mouse brain tissue and titration of antibodies for mass cytometry. a–**d**, Biaxial plots (CytoBank) comparing single-cell P3 telencephalon samples prepared with no enzyme and the optimized combination of collagenase IV and dispase II. Samples were first characterized by flow cytometry (**a**) for proportions of DRAQ7^{+} single cells (gate and percentage of events in gate are shown), DRAQ7^{+++} cell doublets/aggregates, and DRAQ7^{-} debris. Expression of a neuronal marker (TuJ1) is shown to indicate the inclusion of neurons in samples. Subsequent analysis of samples by mass cytometry shows similar results for Cell-ID™ Intercalator-Ir (DNA-Ir191) and TuJ1-Pr141 (**b**), as well as percentages of viable cells [DNA-Ir191^{+} events negative for cisplatin (Pt195) viability stain] (**c**, gate and percentage of events in gate are shown). In addition, DNA-Ir191^{-}TuJ1-Pr141^{+} events observed in samples prepared without enzymes were confirmed to be negative for the nuclear marker Histone H3-In113 (**d**). **e**,**f** Flow cytometry analysis of supernatants from the five washes that occur during single-cell processing of brain tissue. Biaxial plots (**e**) and quantification (**f**) of a pan-cellular marker (DAPI) versus two markers of neural stem cells (Sox2-AlexaFluor488 and nestin-AlexaFluor647), a neuronal marker (TuJ1-PE/Cy7), and an oligodendroglia marker (Olig2-AlexaFluor568). **g**, Biaxial plots showing 1 µg/mL GLAST-Gd156 antibody versus known-negative (TuJ1-Pr141) and known-positive (GFAP-Tm169 and Sox2-Gd160) markers in primary cells harvested from P2 and P17 brain, and the GL261 mouse glioma cell line. **h**, Results for titration of GLAST-Gd156 antibody in primary cells harvested from mice [E12.5 head, E13.5/E14.5/E18.5/P2/P17 brain, E15.5 dorsal root ganglia (DRG)], mouse cell lines [Neuro2a (neuroblastoma), GL261 (glioma), N1E-115 (neuroblastoma), E14Tg2a (embryonic stem cells)], and a human cell line [HEK293T (embryonic kidney)]. **i**, Biaxial plots showing protein expression of the neuronal marker TuJ1 versus every antibody included in the panel in a single replicate of each age from the first mass cytometry run (barcode sets 1–3) for the telencephalon.

Ext. Data Fig. 2. Pre-processing of mass cytometry data for the developing mouse brain. a, Normalization of raw data (.fcs files) with calibration beads using the Matlab software described in Finck, et al. *Cytometry A*, 2013. **b**, Three-on/three-off palladium metal barcoding scheme. **c**, Biaxial plots (CytoBank) showing levels of each palladium metal used for barcoding in representative samples stained with the indicated barcode combination (1–20). **d**, Results of debarcoding normalized .fcs files using the R package described in Fread, et al. *Pac Symp Biocomput*, 2017. Bar graphs on top show numbers of events with each normalized barcode separation threshold value for all samples. Line graphs on bottom show yields of events for each debarcoded sample. **e**–**j**, Biaxial plots (CytoBank) showing gating (indicated in red) used to isolate single cells from developing mouse brains. Percentages in the top right corner of each plot indicate the ratio of ungated cells within the gate. **k**, Mean signal intensity and variance in pre- and post-batch corrected debarcoded .fcs files, as processed with the R package described in Schuyler, et al. *Front Immunol*, 2019. Markers not shown had a mean signal variance < 0.01 and were not corrected. **l**,**m**, Expression levels of each marker in all cells (l) and positive cells (m) of the seven universal samples used to correct for batch artifacts using the process described in Schulyer, et al. *Frontiers in Immunology*, 2019. Positive cells were thresholded for expression using the values shown in Extended Data Fig. 6b. **n**, Biaxial plots (CytoBank) comparing default (ASinH = 5) and manually optimized ASinH values in E14.5 or P4 cortex. ASinH values for markers on the x-axis are indicated at the top right corner of each panel. Markers not shown were transformed using the default value. **o**, P values assessed by Kruskal–Wallis test to evaluate variances in marker expression for each of the 46 sample types examined. Sample types for which expression of a marker significantly varied [$p < 0.05$; 94/1840 (5.1%) of samples] are labeled.

Ext. Data Fig. 3. Classification of cells in the developing mouse brain by mass cytometry. a, Overview of primary and secondary clustering of all 112 sample replicates. Groups were manually assigned according to molecular expression profile and UMAP layout. **b**, UMAP colored and labeled according to Round 1 Leiden clustering of all 112 sample replicates. **c**, Violin plot showing expression of all 40 protein markers in Round 1 Leiden clustering of all 112 sample replicates. **d**, Original UMAP layout and shifts used for compression into the final UMAP layout (corresponding to Fig. 1b). **e**, UMAPs showing Round 2 Leiden clustering of each group. **f**,**g**, Round 2 UMAPs for each group colored according to the (**f**) developmental age (E11.5–P4) from which each cell originated and (**g**) dbrain region of samples. **h**, UMAPs (corresponding to Fig. 1b) colored by sample replicate for all 46 sample types examined. **i**,**j**, UMAP of cells in seven universal samples colored by replicate (**i**) and Leiden cluster (**j**). **k**, Violin plot showing expression of all 40 protein markers in Leiden clustering of seven universal samples.

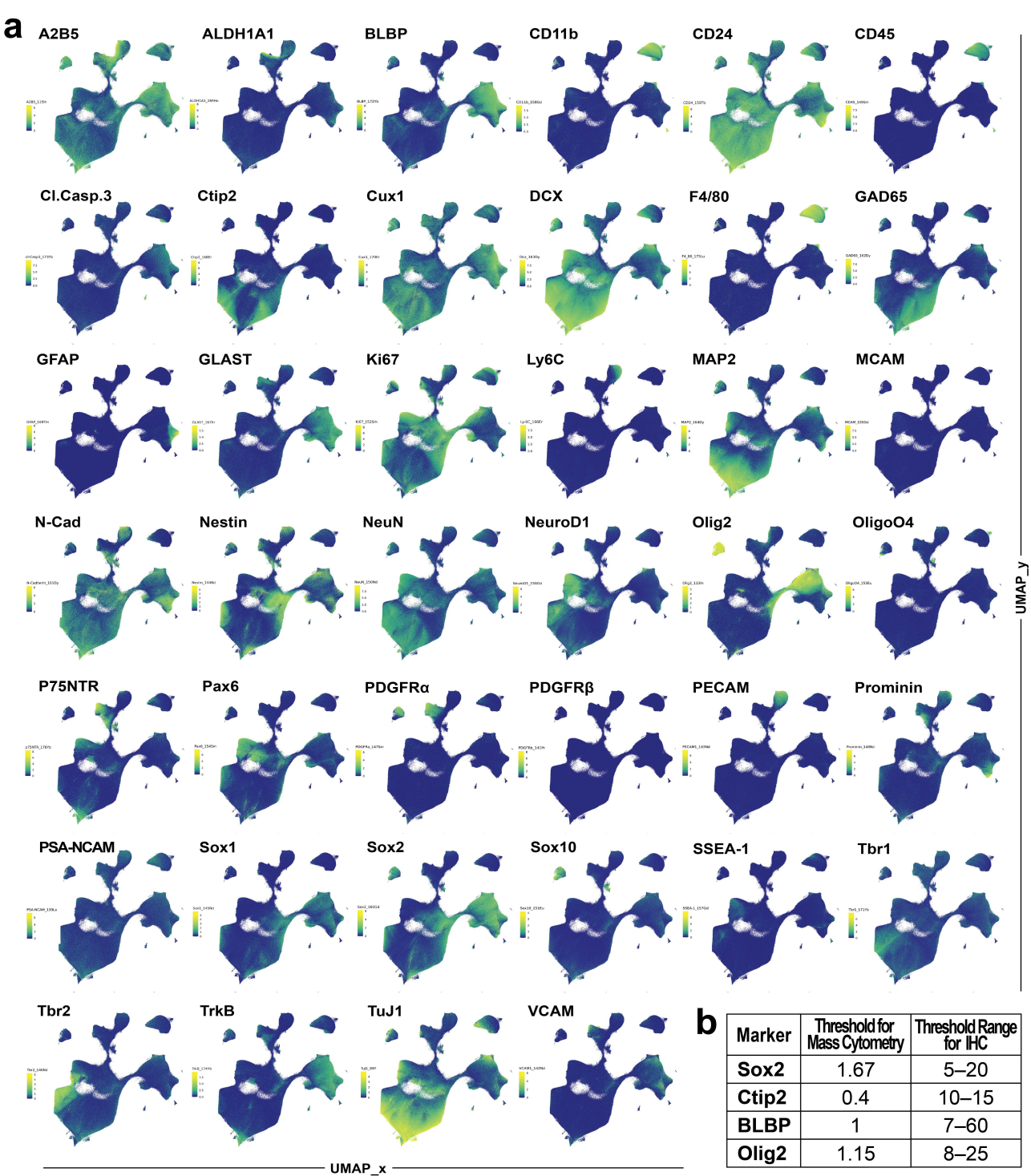

b

Marker	Threshold for Mass Cytometry	Threshold Range for IHC
Sox2	1.67	5–20
Ctip2	0.4	10–15
BLBP	1	7–60
Olig2	1.15	8–25

Ext. Data Fig. 4. Comparison of protein expression in mouse brain measured by mass cytometry and immunohistochemistry. a, UMAPs (corresponding to Figs. 1b, 2a) colored according to expression of the indicated proteins. **b**, Biaxial plots (CytoBank) showing two-dimensional gating of E13.5, E15.5, E17.5, P0, and P3 telencephalon for positive expression of the indicated markers.

Ext. Data Fig. 5. Spatiotemporal profile of cell abundances in the developing mouse brain. a, Relative abundances of major cell classes (not shown in Fig. 3b) in each brain region from E11.5–P4. Individual replicates are shown along with Loess curve fitting of the data. **b**, Heatmap of cluster variance for each sample type (e.g. E11.5 whole brain, P4 telencephalon). Low-abundance sample types (one or more replicate with < 5 cells) were excluded from variance analysis and are shown in grey. **c**,**d**, Scatter plots showing relative abundances of each cluster for each sample type for corresponding clusters in (b). Three clusters are highlighted in c, while the remaining clusters are shown in d.

a

Age	Tissue in Figure	Tissue(s) in La Manno, 2021	Age(s) in La Manno, 2021
E11.5	Whole Brain	Forebrain, Midbrain, Hindbrain	E11.0
E12.5	Whole Brain	Forebrain (Dorsal), Forebrain (Ventral), Midbrain, Hindbrain	E12.0, E12.5
E13.5	Telencephalon	Forebrain (Dorsal)	E13.0, E13.5
E14.5	Telencephalon	Forebrain (Dorsal)	E14.0, E14.5
E15.5	Telencephalon	Forebrain (Dorsal)	E15.0, E15.5
E16.5	Telencephalon	Forebrain (Dorsal)	E16.0, E16.25, E16.5
E17.5	Telencephalon	Forebrain (Dorsal)	E17.0, E17.5
E18.5	Telencephalon	Forebrain (Dorsal)	E18.0
E13.5	Diencephalon	Forebrain (Ventral)	E13.0, E13.5
E14.5	Diencephalon	Forebrain (Ventral)	E14.0, E14.5
E15.5	Diencephalon	Forebrain (Ventral)	E15.0, E15.5
E16.5	Diencephalon	Forebrain (Ventrothalamic), Forebrain (Ventrolateral)	E16.0, E16.5
E17.5	Diencephalon	Forebrain (Ventrothalamic), Forebrain (Ventrolateral)	E17.5
E18.5	Diencephalon	Forebrain (Ventrothalamic), Forebrain (Ventrolateral)	E18.0
E13.5	Mesencephalon	Midbrain	E13.0, E13.5
E14.5	Mesencephalon	Midbrain, Midbrain (Dorsal), Midbrain (Ventral)	E14.0, E14.5
E15.5	Mesencephalon	Midbrain, Midbrain (Dorsal), Midbrain (Ventral)	E15.0, E15.5
E16.5	Mesencephalon	Midbrain	E16.0, E16.5
E17.5	Mesencephalon	Midbrain	E17.5
E18.5	Mesencephalon	Midbrain	E18.0
E13.5	Rhombencephalon	Hindbrain	E13.0, E13.5
E14.5	Rhombencephalon	Hindbrain	E14.0, E14.5
E15.5	Rhombencephalon	Hindbrain	E15.0, E15.5
E16.5	Rhombencephalon	Hindbrain	E16.0, E16.5
E17.5	Rhombencephalon	Hindbrain	E17.0, E17.5
E18.5	Rhombencephalon	Hindbrain	E18.0

b

Marker	% Positive Threshold for Mass Cytometry	Common Gene Name
Sox2	1.67	*Sox2*
Pax6	0.8	*Pax6*
Tbr2	0.8	*Eomes*
NeuroD1	1.5	*Neurod1*
Tbr1	0.75	*Tbr1*
Ctip2	0.4	*Bcl11b*
Cux1	3	*Cux1*
Olig2	1.15	*Olig2*
Sox10	2.7	*Sox10*
Sox1	0.6	*Sox1*
Nestin	0.45	*Nes*
DCX	1.3	*Dcx*
TuJ1	3.3	*Tubb3*
MAP2	0.7	*Map2*
GFAP	2	*Gfap*
PDGFRa	0.6	*Pdgfra*
PDGFRb	0.7	*Pdgfrb*
TrkB	1	*Ntrk2*
P75NTR	1.3	*Ngfr*
Prominin	0.5	*Prom1*
GLAST	2.8	*Slc1a3*
CD45	1.5	*Ptprc*
F4/80	2	*Adgre1*
N-Cad	1	*Cdh2*
CD11b	2	*Cdk11b*
VCAM1	1.2	*Vcam1*
MCAM	4	*Mcam*
PECAM1	2	*Pecam1*
GAD65	0.5	*Gad2*
ALDH1A1	2	*Aldh1a1*
SSEA-1	2	*Fut4*
NeuN	1.5	*Rbfox3*
BLBP	1	*Fabp7*
Ki67	4	*Mki67*
A2B5	–	RNA Data Unavailable
CD24	–	RNA Data Unavailable
Cl.Casp.3	–	RNA Data Unavailable
Ly-6C	–	RNA Data Unavailable
OligoO4	–	RNA Data Unavailable
PSA-NCAM	–	RNA Data Unavailable

c

Dissociation Feature	Van Deusen et al., 2022	La Manno et al., 2021
Enzyme Utilized	Collagenase IV, dispase II, hyaluronidase, DNAse I	TrypLE Express, papain, DNase I
Buffer for Enzymatic Dissociation	Dulbecco's Modified Eagle's Medium	Cutting solution and Neurobasal Medium
Total Incubation Time at 37°C	30 min	45–50 min
Mechnical Filtration Pore Size	75 µm and 45 µm	20 µm
Molecular Filtration Method	None	OptiPrep™ Density Gradient
Centrifugation (Live Cells)	300 × g (3 min)	100 × g (4 min) and 80 × g (10 min)

d

Cell Class	Tissue	Clusters (La Manno, 2021)	Clusters (Van Deusen, 2022)
Angioblast	All	152,153	85
Astrocyte	All	172,296–302	39
Commited OPCs	All	318–320	48,49,50,55,56
Dopa. Neurons	Midbrain	662,663	33
Endothelial Cells	All	139–151	62,64,66,70,71
Glutamatergic Neurons	Forebrain	492–528,665,667–673,680–685,688–690,715–725,727,732–734,741–745,750-754	18,25,32
	Diencephalon	647–649,727,732–734,743,750,752,783–796	17,18,25,32
	Midbrain	654–662,702–714,727,732–734,743,750,752,771,772	17,18,25,32
	Hindbrain	625–646,727,732–734,743,750,752,759–761,767,776–782	17,18,25,32
Hematopoietic	All	97–106,171	80,83
Inhibitory Neurons	Forebrain	529–575,746–748,666,674–679,686,687,735–740,749	20,21,26
	Diencephalon	663,664,691–696,735–740,749	19,20,21,26
	Midbrain	576–589,591–595,735–740,749	19,20,21,26
	Hindbrain	597,598,608–611,615,616,618,619,735–740,749,762–766	19,20,21,26
Inhibitory Neuron Progenitors	Forebrain	327–333,449–452,454–458	22
	Diencephalon	327–333,449–452,454–458	22
	Midbrain	321,322	29
	Hindbrain	402,403,409	29
INPs	All	425,428,430,433,434,436–447	13,23,30
Microglia	Diencephalon	157,158,159	74,77,78,79,81
Neuronal Progenitors	Forebrain	325,326,339,342,349,355–360,362,364,374,426,427,429,431,432,435,453,470–472	24
	Diencephalon	209,226,229,235,259,251–254,269,270	27
	Midbrain	323,324,336–339,342,344–347,349,356,362,364–366,371,386–392,410–420,470–472	27
	Hindbrain	339–343,348–354,356,361–363,367,368,372,373,383,390,400,459–464,470–491	4,7,8,14,15,27,58
Nonneural Cells	All	115,116,120,122–125	63,65,67,68,69,72
Neural Stem Cells	Forebrain	180–195,210,211,214,216–227,229,235,259,271	6,9,11
	Diencephalon	209,226,229,235,259,251–254,269,270	6,9,11
	Midbrain	196–199,201,202,206,207,229–235,259	6,9,11
	Hindbrain	200,203–205,208,229,235–237,256–260,263–266	6,9,11
OPCs	All	313–317	51,52,54
Pre-OPCs	All	306–308	3,34,36,41,42,43,45
Glioblasts	Forebrain	173–179,285–290,309,310	35,37,38,46
	Diencephalon	290,309,310	35,37,38,46
	Midbrain	282–284,290,309,310	35,37,38,46
	Hindbrain	290–297,303,309,310	35,37,38,46

Ext. Data Fig. 6. Comparison of protein and mRNA expression patterns in the developing mouse brain. **a**, Overview of how results from the present study were compared sample-by-sample with the scRNA-seq results of La Manno, et al. *Nature*, 2021. **b**, Overview of genes included in the antibody panel and, if used in comparative analyses, the threshold value applied to calculate relative abundances of positive and negative cells for scRNA-seq and mass cytometry datasets (additional detailed in Methods section). **c**, Comparison of single-cell dissociation protocols used in the current study and La Manno, et al. *Nature*, 2021. **d**, Matching of the 85 clusters identified in the current study to the 798 clusters described in La Manno, et al. *Nature*, 2021 performed by comparing expression of key markers in addition to age and tissue information.

Ext. Data Fig. 7. Differentiation trajectories of Sox2^{+}Nestin^{+} cells in the developing mouse brain. a, UMAP colored and labeled according to R1 Leiden clustering assignment. Inset shows UMAP colored according to the five groups of Round 1 clusters that were subjected to a second round of Leiden clustering. **b**, Violin plot showing expression of all 40 protein markers in Round 1 Leiden clusters. **c**, Violin plot showing expression of all 40 protein markers in Round 2 Leiden clusters. **d**, Dot plot showing relative abundances of clusters at each developmental age for all brain regions together. **e**, UMAPs colored according to expression levels of all 40 protein markers. **f**, UMAP of Sox2^{+}Nestin^{+} cells chosen at the root and tips for analysis with the URD alogrithm (Farrell et al., *Science*, 2018). **g**, Change in total stability of URD pseudotime calculations with number of simulations. **h**, Histogram showing relative cell density for each developmental age (E11.5–P4) for each URD pseudotime bin. **i**, UMAP generated by the URD algorithm [6.1 × 10^4 cells (1.9% of total Sox2^{+}Nestin^{+} cells) included in URD analysis] colored according to pseudotime. **j**, UMAP generated by URD algorithm colored according to URD dendrogram tree segment. **k**, Dot plot showing expression of markers key for the division of each branchpoint in URD analysis. **l**, URD dendrogram with branch numbers indicated (corresponding to **k**). **m**, URD dendrograms colored according to protein expression levels of the indicated markers.

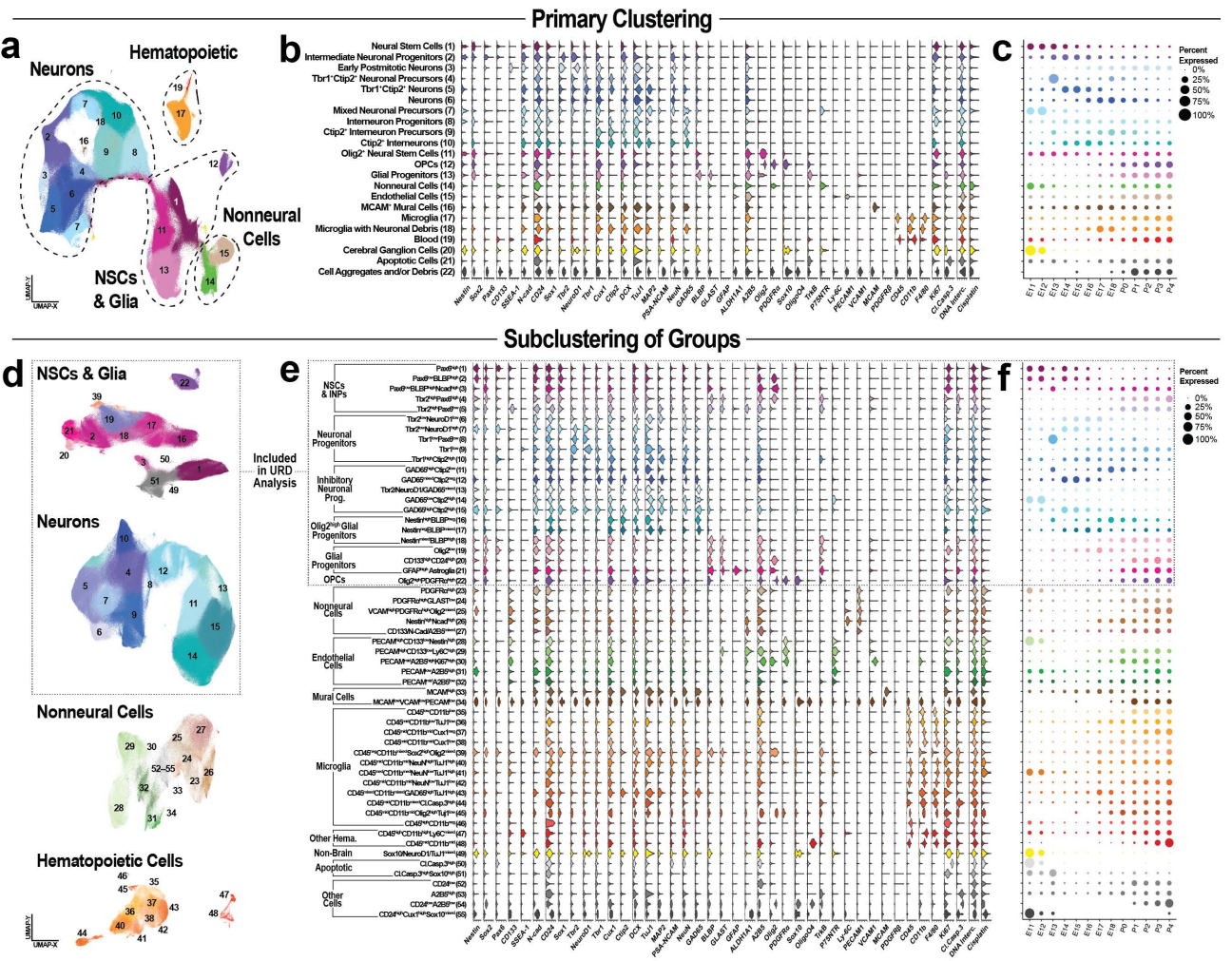

Ext. Data Fig. 8. Differentiation trajectories and molecular dynamics in the telencephalon. a, UMAP colored according to Round 1 Leiden clustering assignment. Dashed lines indicate four groups of Round 1 clusters that were subjected to a second round of Leiden clustering. **b**, Violin plot showing expression of all 40 protein markers in Round 1 Leiden clusters. **c**, Dot plot showing relative abundances of Round 1 Leiden clusters at each developmental age. **d**, UMAPs showing Round 2 Leiden clustering of each group. **e**, Violin plot showing expression of all 40 protein markers in Round 2 Leiden clusters. **f**, Dot plot showing relative abundances of Round 2 Leiden clusters at each developmental age. **g**, Change in total stability of URD pseudotime calculations with number of simulations. **h**, Histogram showing relative cell density for each developmental age (E11.5–P4) for each URD pseudotime bin. **i**, UMAP generated by the URD algorithm (6.1×10^4 cells included in URD analysis) colored according to pseudotime. **j**, UMAP generated by the URD algorithm colored according to the URD dendrogram tree segment. **k**, Heatmaps colored by protein expression of all 40 markers for select trajectories identified by URD analysis.

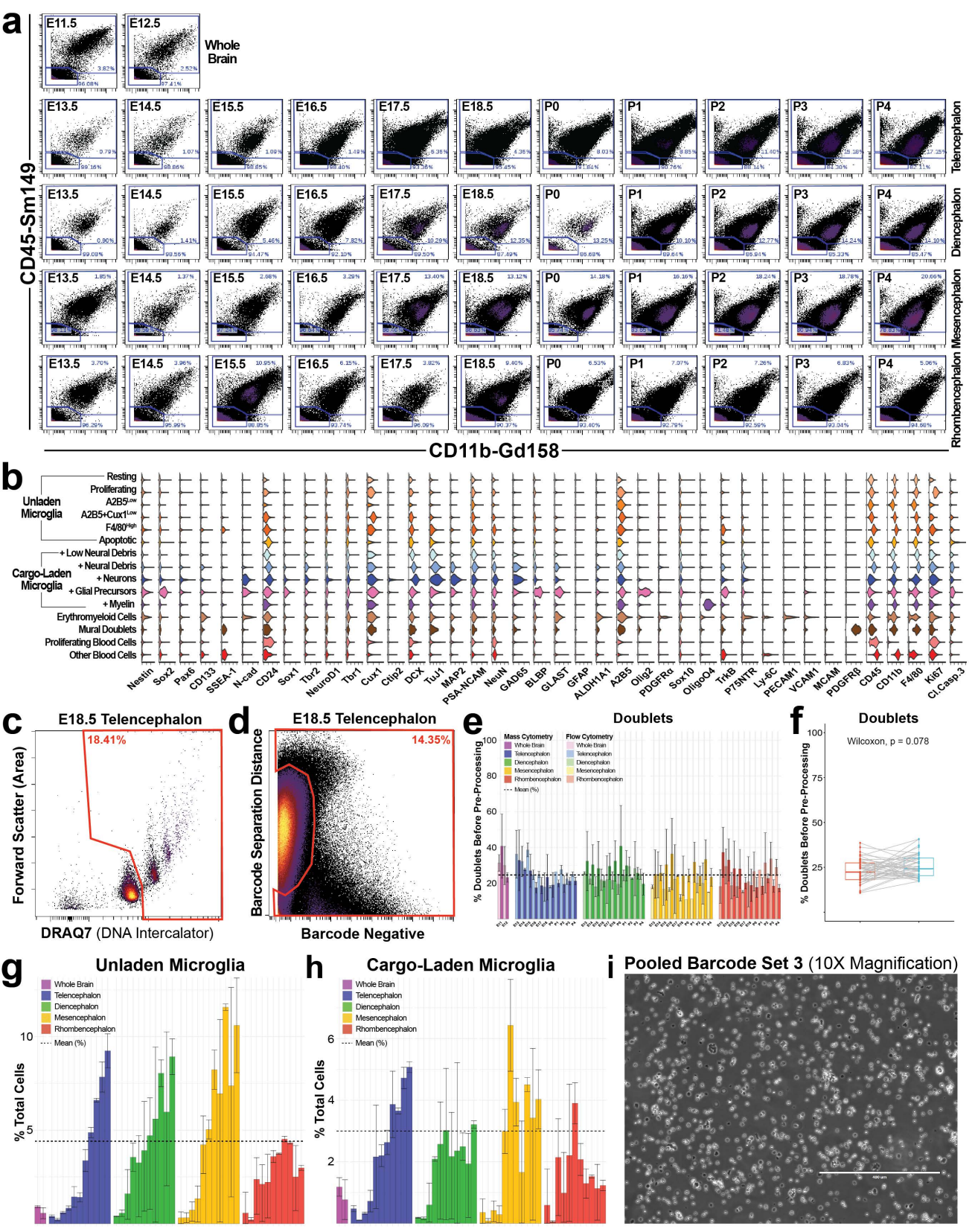

Ext. Data Fig. 9. Microglia/macrophage expansion and putative phagocytic cargoes in the developing mouse brain. a, Biaxial plots showing gating of all single-cell events from one replicate of each sample type. Cells in upper gate were retained as CD45$^+$ cells. **b**, Violin plot showing expression of all 40 protein markers for Leiden clustering of CD45$^+$ cells in the developing mouse brain. **c**, Biaxial plot showing gate used to isolate cell doublets and aggregates by flow cytometry in a single sample. **d**, Biaxial plot showing gate used to isolate cell doublets and aggregates by mass cytometry in the same sample shown in (c). **e**, Relative percentages of doublets identified in each sample by flow cytometry and mass cytometry. Error bars indicate standard deviation. **f**, Wilcoxon test for significant difference in relative percentages of doublets identified for each sample by flow cytometry and mass cytometry. **g**,**h**, Relative percentages of unladen (g) and cargo-laden (h) microglia identified by mass cytometry. Error bars indicate standard deviation. **i**, Brightfield image of pooled Barcode Set 3 (containing P1–P4 samples) prior to mass cytometry analysis (10× magnification, scale bar = 400 μm).

Extended Data Bibliography

Adam, S. *et al*. ALDH1A1 is a marker of astrocytic differentiation during brain development and correlates with better survival in glioblastoma patients. *Brain Pathology* (Zurich, Switzerland) **22**, 788–797 (2012).

Akiyama, H. *et al*. Major histocompatibility complex antigen expression on rat microglia following epidural kainic acid lesions. *Journal of Neuroscience Research* **20**, 147–157 (1988).

Arnold, D., et al. A strategy for the analysis of gene expression during neural development. *PNAS* **91**, 9970–9974 (1994).

Austyn, J. M. & Gordon, S. F4/80, a monoclonal antibody directed specifically against the mouse macrophage. *Europ. J. Immunology* **11**, 805–815 (1981).

Boström, K. I. *et al*. Endothelial cells may have tissue-specific origins. *J. Cell Bio. and Histol*. **1**, 104 (2018).

Bulfone, A. *et al*. T-Brain-1: a homolog of brachyury whose expression defines molecularly distinct domains within the cerebral cortex. *Neuron* **15**, 63–78 (1995).

Caccamo, D. V. *et al*. Primitive neuroepithelium displays immunoreactivity for neuropeptides and neuron-associated beta-tubulin isotype. *Am. J. Pathology* **135**, 801–813 (1989).

Dahlstrand, J. *et al*. Characterization of the human nestin gene reveals a close evolutionary relationship to neurofilaments. *J. Cell Sci.* **103**, 589–97 (1992).

des Portes, V. *et al*. A novel CNS gene required for neuronal migration and involved in x-linked subcortical laminar heterotopia and lissencephaly syndrome. *Cell* **92**, 51–61 (1998).

Eisenbarth, G. S. *et al*. Monoclonal antibody to a plasma membrane antigen of neurons. *PNAS* **76**, 4913–4917 (1979).

Farrell, J. A. *et al*. Single-cell reconstruction of developmental trajectories during zebrafish embryogenesis. *Science* **360**, ear3131 (2018).

Feng, L. *et al*. Brain lipid-binding protein (BLBP): a novel signaling system in the developing mammalian CNS. *Neuron* **12**, 895–908 (1994).

Fernandes-Alnemri, T. *et al*. CPP32, a novel human apoptotic protein with homology to caenorhabditis elegans cell death protein ced-3 and mammalian interleukin-1 beta-converting enzyme. *J. Biol. Chem.* **269**, 30761–30764 (1994).

Fienberg, H. G. *et al*. A platinum-based covalent viability reagent for single-cell mass cytometry. *Cytometry A* **81**, 467–475 (2012).

Finck, R. *et al.* Normalization of mass cytometry data with bead standards. *Cytom. Part J. Int. Soc. Anal. Cytol.* **83**, 483–494 (2013).

Fread, K. I. *et al*. An updated debarcoding tool for mass cytometry with cell type-specific and cell sample-specific stringency adjustment. *Pac. Symp. Biocomput. Pac. Symp. Biocomput.* **22**, 588–598 (2017).

Galter, D. *et al*. ALDH1 mRNA: presence in human dopamine neurons and decreases in substantia nigra in parkinson's disease and in the ventral tegmental area in schizophrenia. *Neurobio. Disease* **14**, 637–647 (2003).

Gerdes, J. *et al*. Production of a mouse monoclonal antibody reactive with a human nuclear antigen associated with cell proliferation. *Int. J. Cancer* **31**, 13–20 (1983).

Gubbay, J. *et al*. A gene mapping to the sex-determining region of the mouse y chromosome is a member of a novel family of embryonically expressed genes. *Nature* **346**, 245–250 (1990).

Hatta, K. *et al*. a monoclonal antibody disrupting calcium-dependent cell-cell adhesion of brain tissues: possible role of its target antigen in animal pattern formation. *PNAS* **82**, 2789–2793 (1985).

Herrup, K. & Shooter, E. M. properties of the beta nerve growth factor receptor of avian dorsal root ganglia. *PNAS* **70**, 3884–3888 (1973).

Hu, B. Y. *et al*. Human oligodendrocytes from embryonic stem cells: conserved shh signaling networks and divergent FGF effects. *Development* **136**, 1443–1452 (2009).

Izant, J. G. & McIntosh, J. R. Microtubule-associated proteins: a monoclonal antibody to MAP2 binds to differentiated neurons. *PNAS* **77**, 4741–4475 (1980).

Kaufman, D. L. *et al*. Two forms of the gamma-aminobutyric acid synthetic enzyme glutamate decarboxylase have distinct intraneuronal distributions and cofactor interactions. *J. Neurochem.* **56**, 720–723 (1991).

Klein, R. *et al*. TrkB, a novel tyrosine protein kinase receptor expressed during mouse neural development. *EMBO* **8**, 3701–3709 (1989).

Kokovay, E. *et al*. VCAM1 is essential to maintain the structure of the SVZ niche and acts as an environmental sensor to regulate SVZ lineage progression. *Cell Stem Cell* **11**, 220–230 (2012).

Kurtz, A. *et al*. The expression pattern of a novel gene encoding brain-fatty acid binding protein correlates with neuronal and glial cell development. *Development* **120**, 2637-49 (1994).

La Manno, G. *et al*. Molecular diversity of midbrain development in mouse, human, and stem cells. *Cell* **167**, 566–580 (2016).

LeClair, K. P. *et al*. Kinetic analysis of Ly-6 gene induction in a T lymphoma by interferons and interleukin 1, and demonstration of Ly-6 inducibility in diverse cell types. *Eur. J. Immunology* **19**, 1233–1239 (1989).

Lee, J. E. *et al*. Conversion of xenopus ectoderm into neurons by NeuroD, a basic helix-loop-helix protein. *Science* 268, 836–844 (1995).

Lu, Q. R. *et al*. Sonic hedgehog-regulated oligodendrocyte lineage genes encoding bHLH proteins in the mammalian central nervous system. *Neuron* **25**, 317–329 (2000).

Mullen, R. J. *et al*. NeuN, a neuronal specific nuclear protein in vertebrates. *Development* **116**, 201–211 (1992).

Noble, M. *et al*. Platelet-derived growth factor promotes division and motility and inhibits premature differentiation of the oligodendrocyte/type-2 astrocyte progenitor cell. *Nature* **333**, 560–562 (1988).

Osborn, L. *et al*. Direct expression cloning of vascular cell adhesion molecule 1, a cytokine-induced endothelial protein that binds to lymphocytes. *Cell* **59**, 1203–1211 (1989).

Newman, P. J. *et al*. PECAM-1 (CD31) cloning and relation to adhesion molecules of the immunoglobulin gene superfamily. *Science* **247**, 1219–1222 (1990).

Perry, V. H. *et al*. Immunohistochemical localization of macrophages and microglia in the adult and developing mouse brain. *Neuroscience* **15**, 313–326 (1985).

Pevny, L. H. *et al*. A role for SOX1 in neural determination. *Development* **125**, 1967–1978 (1998).

Pringle, N. *et al*. PDGF A chain homodimers drive proliferation of bipotential (O-2A) glial progenitor cells in the developing rat optic nerve. *EMBO* **8**, 1049–1056 (1989).

Quaggin, S. E. *et al*. Primary structure, neural-specific expression, and chromosomal localization of Cux-2, a second murine homeobox gene related to drosophila cut. *J. Biol. Chem*. **271**, 22624–22634 (1996).

Raff, M. C. *et al*. Two types of astrocytes in cultures of developing rat white matter: differences in morphology, surface gangliosides, and growth characteristics. *J. Neurosci.* **3**, 1289–1300 (1983).

Riccio, O. *et al*. New pool of cortical interneuron precursors in the early postnatal dorsal white matter. *Cereb. Cortex* **22**, 86–98 (2012).

Richardson, W. D. *et al*. A role for platelet-derived growth factor in normal gliogenesis in the central nervous system. *Cell* **53**, 309–319 (1988).

Russ, A. P. *et al*. Eomesodermin is required for mouse trophoblast development and mesoderm formation. *Nature* **404**, 95–99 (2000).

Schwarz, M. J. *et al*. Melanoma-associated adhesion molecule MUC18/MCAM (CD146) and transcriptional regulator mader in normal human CNS. *Neuroimmunomod.* **5**, 270–276 (1998).

Schuyler, R. P. *et al.* minimizing batch effects in mass cytometry data. *Front. Immunol.* **10**, 2367 (2019).

Shirasawa, T. *et al*. Gene expression of CD24 core peptide molecule in developing brain and developing non-neural tissues. *Dev. Dynamics* **198**, 1–13 (1993).

Solter, D. & Knowles, B. B. Monoclonal antibody defining a stage-specific mouse embryonic antigen (SSEA-1). *PNAS* **75**, 5565–5569 (1978).

Storck, T. *et al*. Structure, expression, and functional analysis of a Na(+)-dependent glutamate/aspartate transporter from rat brain. *PNAS* **89**, 10955–10959 (1992).

Thiery, J. P. *et al*. Adhesion among neural cells of the chick embryo. II. Purification and characterization of a cell adhesion molecule from neural retina. *J. Biol. Chem.* **252**, 6841–6845 (1977).

Uwanogho, D. *et al*. Embryonic expression of the chicken *Sox2*, *Sox3* and *Sox11* genes suggests an interactive role in neuronal development. *Mechanisms Dev.* **49**, 23–36 (1995).

Uyeda, C. T. *et al*. Immunological study of the glial fibrillary acidic protein. *Brain Res.* **37**, 81–89 (1972).

Vasudevan, A. *et al*. Compartment-specific transcription factors orchestrate angiogenesis gradients in the embryonic brain. *Nature Neurosci.* **11**, 429–439 (2008).

Vouyiouklis, D. A. & Brophy, P. J. Microtubule-associated proteins in developing oligodendrocytes: transient expression of a MAP2c isoform in oligodendrocyte precursors. *J. Neurosci. Res.* **42**, 803–817 (1995).

Walther, C. & Gruss P. Pax-6, a murine paired box gene, is expressed in the developing CNS. *Development* **113**, 1435–1449 (1991).

Weigmann, A. *et al*. Prominin, a novel microvilli-specific polytopic membrane protein of the apical surface of epithelial cells, is targeted to plasmalemmal protrusions of non-epithelial cells. *PNAS* **94**, 12425–12430 (1997).

Yamamoto, M. *et al*. Sagittal band expression of COUP-TF2 gene in the developing cerebellum. *Mechanisms Dev.* **84**, 143–146 (1999).

Yokoyama, A. *et al*. Microglia, a potential source of neurons, astrocytes, and oligodendrocytes. *Glia* **45**, 96–104 (2004).

Zhou, Q. *et al*. Identification of a novel family of oligodendrocyte lineage-specific basic helix-loop-helix transcription factors. *Neuron* **25**, 331–343 (2000).

Appendix II: Extended Data for Mass Cytometry Analysis of Mouse DRG Development

The contents of this chapter, corresponding to Chapter III, were previously published as “A developmental atlas of somatosensory diversification in the dorsal root ganglia by single-cell mass cytometry.” Austin Keeler*, Amy Van Deusen*, Irene Gadani, Corey Williams, Sarah Goggin, Ashley Hirt, Shayla Vradenburgh, Kristen Fread, Emily Puleo, Lucy Jin, O. Yipkin Calhan, Christopher Deppmann, Eli Zunder. *Nature Neuroscience*. 2022;25(11):1543–1558.

EXTENDED DATA FIGURE 1

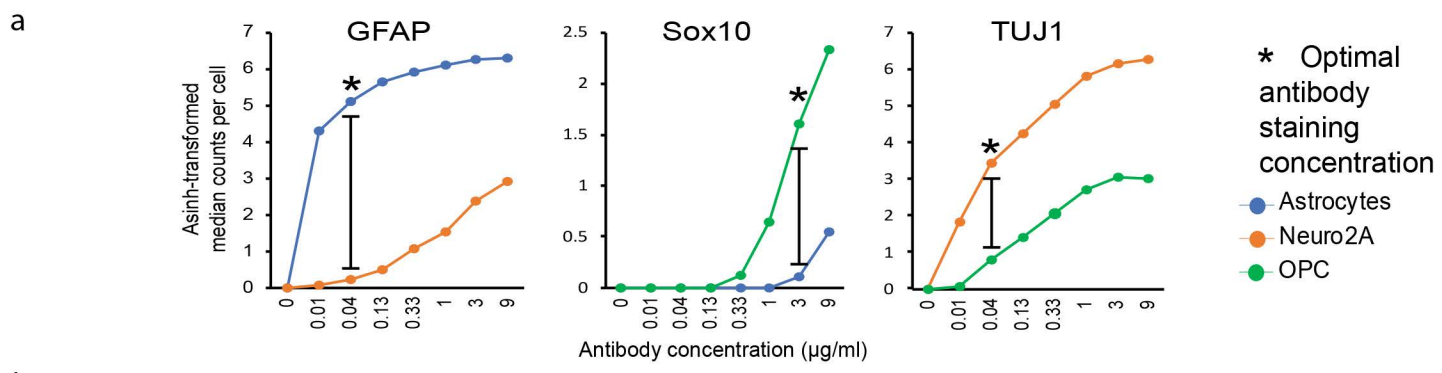

Extended Data Fig. 1 Validation of antibodies for mass cytometry. All antibodies validated and included in the DRG mass cytometry antibody panel. **a)** Each antibody was titrated across a range of concentrations (for example 9 µg/ml to 0.01 µg/ml). Known-positive and known-negative control cell samples were tailored for each antibody. Sometimes these were separate samples, and sometimes the known-positive and known-negative cells coexisted in a single sample, distinguishable by a separate antibody counterstain. Optimal staining concentrations for each antibody were determined by identifying the largest difference in signal intensity between known-positive and known-negative cells. **b)** Biaxials scatterplots for each antibody except for anti-Islet1 (y-axis) in the panel at each age by Islet1 (x-axis), demonstrating positive and negative staining across the DRG developmental time course. Samples were selected from Set 1. For postnatal ages the female sample from Set 1 was used. Full data available in Data Availability.

EXTENDED DATA FIGURE 2

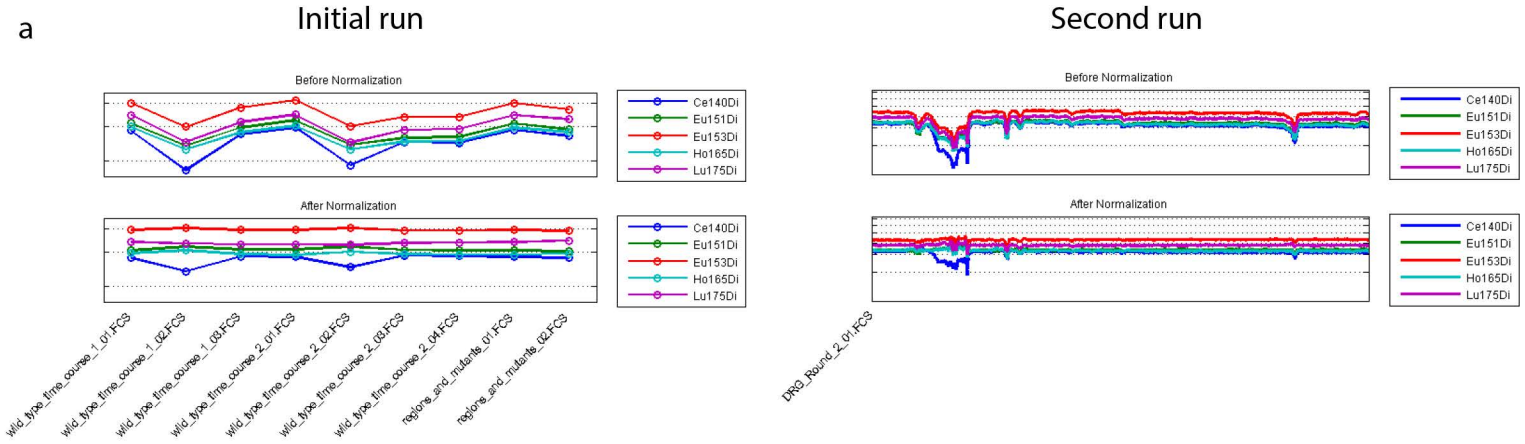

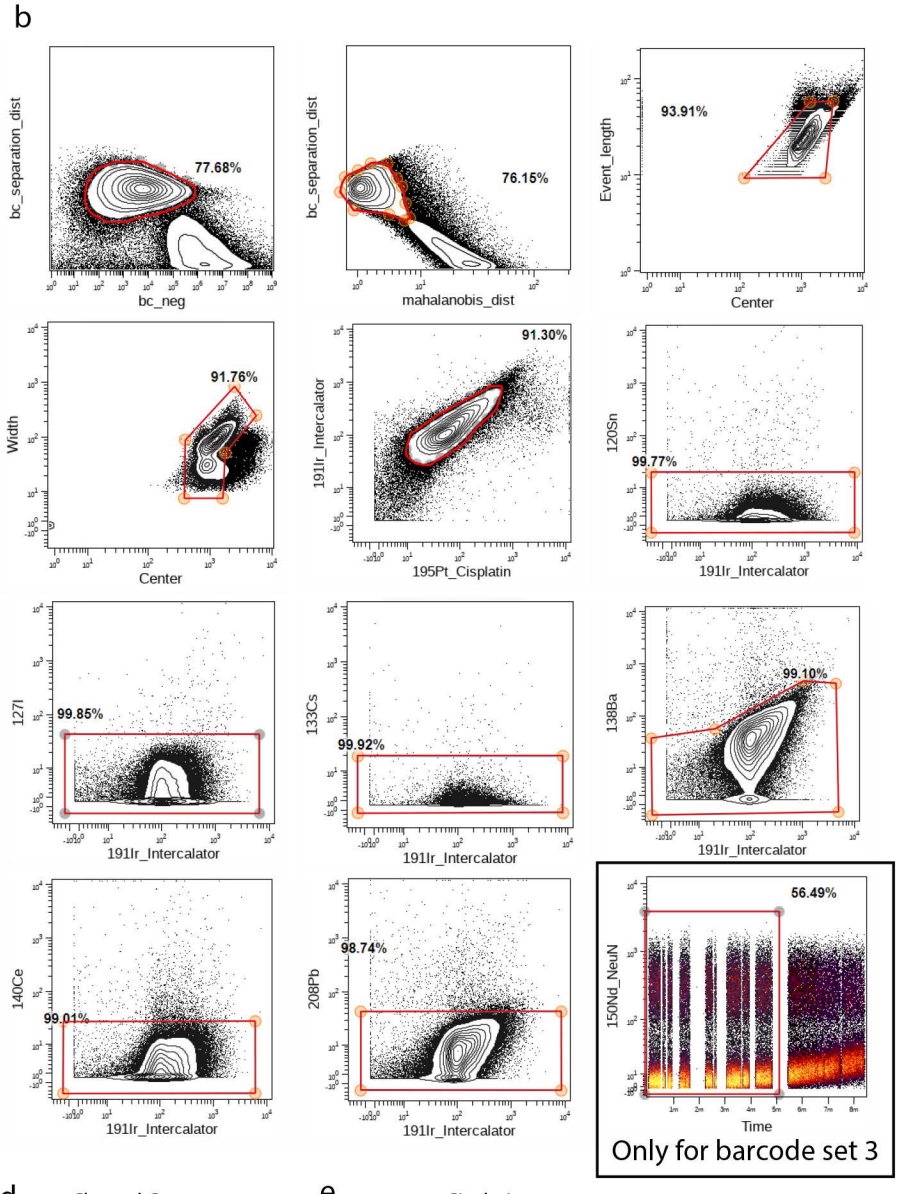

c

Metal	All Antibodies	Batch Adjust	ArcSinh Value
Y89	TuJ1	50p	30
In113	GFAP	NONE	10
In115	cMet	50p	20
La139	Connexin43	50p	50
Pr141	Sox2	50p	30
Nd142	CD9	50p	20
Nd143	CD117	50p	20
Nd144	Nestin	50p	20
Nd145	Sox1	50p	100
Nd146	CD24	50p	20
Sm147	NFH	50p	10
Nd148	CD133	50p	10
Sm149	CGRP	50p	20
Nd150	NeuN	50p	20
Eu151	Sox10	50p	30
Sm152	Ki67	50p	20
Eu153	OligO4	85p	10
Sm154	Vimentin	50p	20
Gd155	CD31	65p	20
Gd156	NeuroD1	50p	20
Gd157	CD45	65p	30
Gd158	Thy1.2	50p	20
Tb159	TrkC	50p	15
Gd160	Runx3	50p	50
Dy161	N-Cadherin	50p	5
Dy162	GAD65	50p	50
Dy163	Cabindin	50p	20
Dy164	MAP2	50p	10
Ho165	TrkA	50p	15
Er166	MafA	50p	20
Er167	Islet1	50p	100
Er168	PDGFRα	50p	5
Tm169	Ret	50p	20
Er170	Cux1	50p	30
Yb171	CD44	NONE	10
Yb172	BFABP/BLBP	50p	50
Yb173	Cleaved Caspase 3	50p	20
Yb174	TrkB	50p	10
Lu175	PGP9.5	50p	20
Yb176	p75NTR	50p	10
Os190	IB4	50p	15

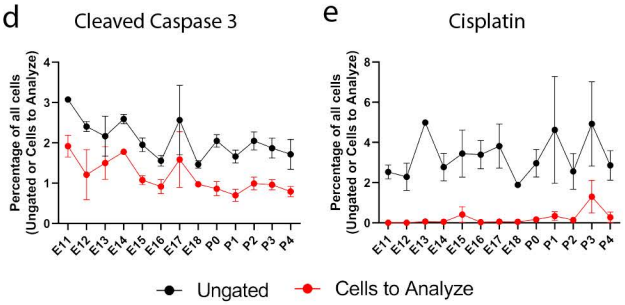

Extended Data Fig. 2 Pre-processing of DRG samples for mass cytometry. a) Calibration bead normalization of the raw mass cytometry data (stored as .fcs files) using the Matlab software described in Finck. et al[35]. **b)** Clean up gating done with Cytobank (cytobank.org) to remove low quality events from the dataset. Biaxial gates as follows (from left to right, top to bottom): 1) barcode_separation x barcode_negative and 2) barcode_separation x malahoidis_distance removes events that cannot be confidently separated by barcode label; 3) event_length x center and 4) width x center remove events that fall outside of normal Gaussian parameter distribution – these events are often enriched for cell doublets; 5) intercalator x cisplatin removes both non-cell events (for example cellular debris) and dying cells; 6–11) unused metals x intercalator removes high background events. A twelfth clean up gate was required for samples from barcode Set 3 to remove a runtime-dependent increase in background in a subset of channels: time x NeuN. **c)** Batch correction was run to normalize signal strength between runs (Schuyler et al.)[37]. Each barcode set included a 'universal' sample consisting of excess samples from across the DRG time course. These excess cells were pooled together, and then aliquoted and stored at −80 °C, to be included with each mass cytometry run as an unvarying control. After all samples were run, the universal samples between barcode sets were batch corrected to be as similar as possible on a per-marker basis, and then the batch adjustment process corrected the rest of the samples in that barcode set based on its corresponding universal sample. Arcsinh transformation values were manually adjusted to provide the greatest contrast between background and physiological values. **d)** A gating hierarchy of major populations found by high dimensional analysis of the whole time course. This gating hierarchy recapitulates the delineation of general cell types identified through high dimensional analysis with UMAP and leiden clustering.

EXTENDED DATA FIGURE 3

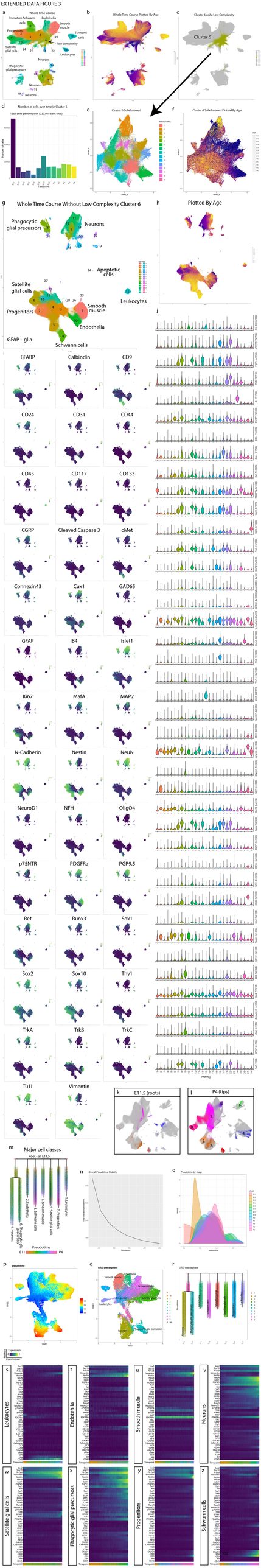

Extended Data Fig. 3 High dimensional analysis of the entire somatosensory time course data set. **a)** UMAP embedding of all 'Cells to Analyze' (cleanup gating applied) from the whole DRG time course. **b)** UMAP plot from (a) colored by age. **c)** UMAP plot grayed out except for low complexity Cluster 6. **d)** Cells from all ages in Cluster 6, with predominant contribution from E11.5. **e)** UMAP embedding of Cluster 6 after extraction and secondary Leiden clustering. **f)** UMAP plot from (e), colored by age. **g)** Unmodified UMAP embedding from Fig. 1c. UMAP layout was rotated and white space removed for improved visualization. **h)** UMAP plot from (g) colored by age. **i)** UMAP plot from (g) colored by expression level for every marker in the DRG antibody panel. **j)** Violin plots of all markers for all clusters; Fig. 1e is truncated to show just the most salient markers for the general populations. **k)** Analysis of the variability of each cluster by each sample at each age. The number of cells assigned to each cluster in each sample at each age was determined and the relative abundance of each cluster per sample per age calculated. Line and error bars denote the standard error of the mean. **l)** The standard error of the mean of the percentage of all cells for each cluster is shown, but only during the ages where the average abundance of that cluster comprised 1% or more of the cells at that age. Note, three clusters (Endothelia 3, Unassigned cells 1, and Unassigned cells 2) never reached that threshold.

EXTENDED DATA FIGURE 4

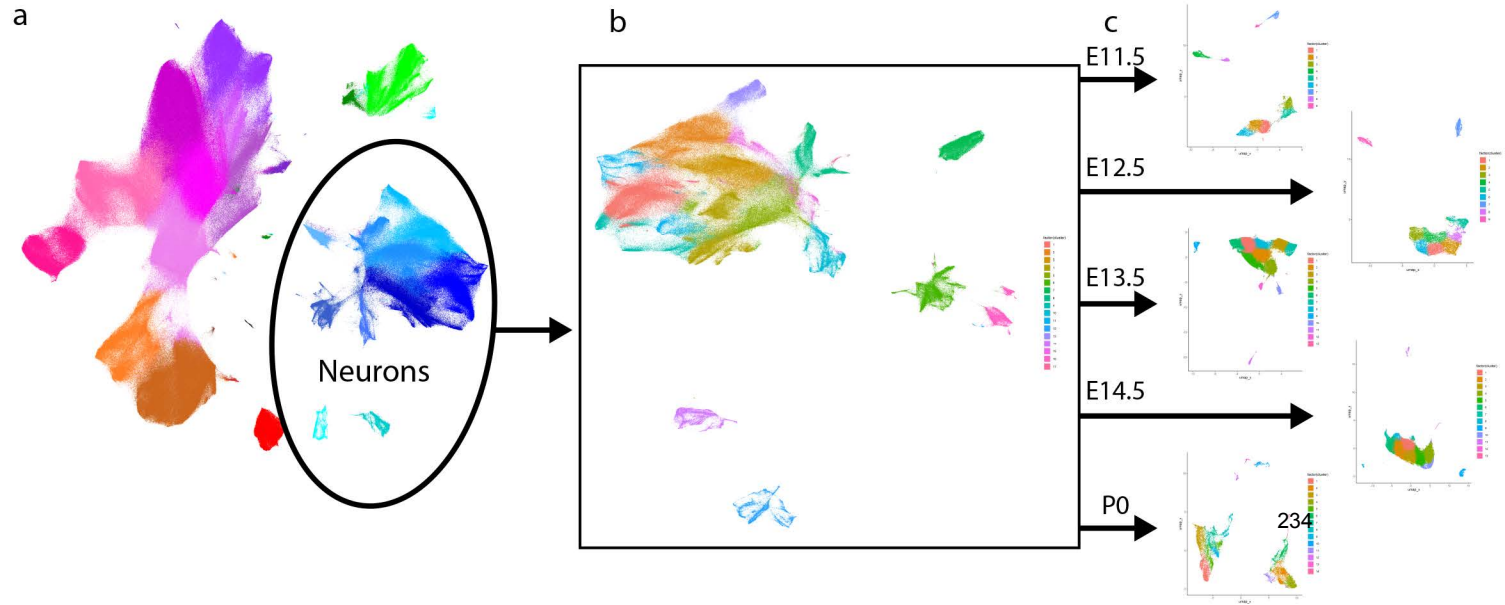

Extended Data Fig. 4 Extraction of single age neuron sets for comparison to IHC. a) Neuronal clusters were extracted from the DRG time course (Fig. 1c), **b)** and then subjected to secondary Leiden clustering and UMAP embedding. **c)** Then, individual ages matched to IHC samples were further extracted and subjected to tertiary Leiden clustering and UMAP embedding.

EXTENDED DATA FIGURE 5

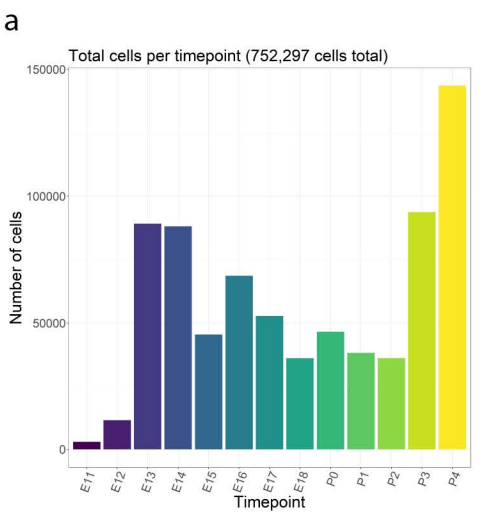

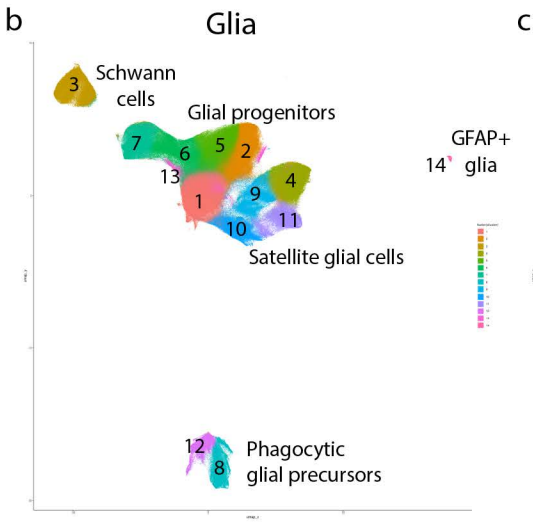

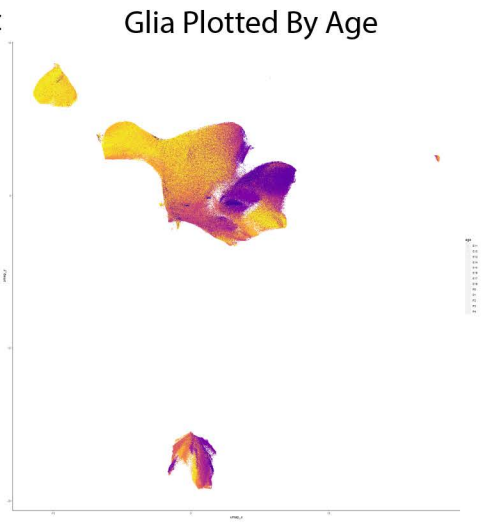

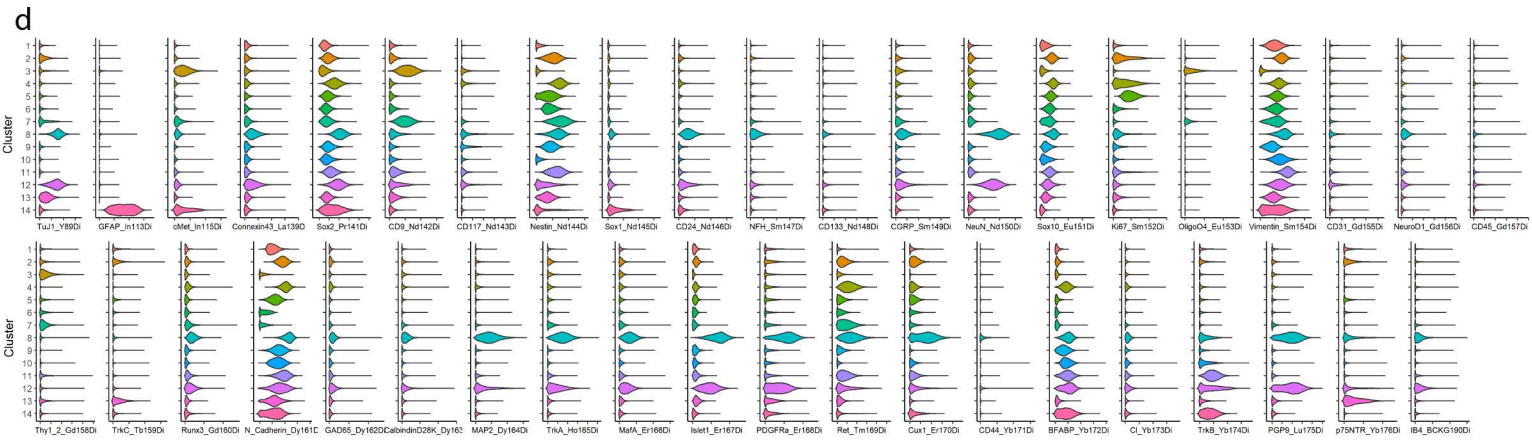

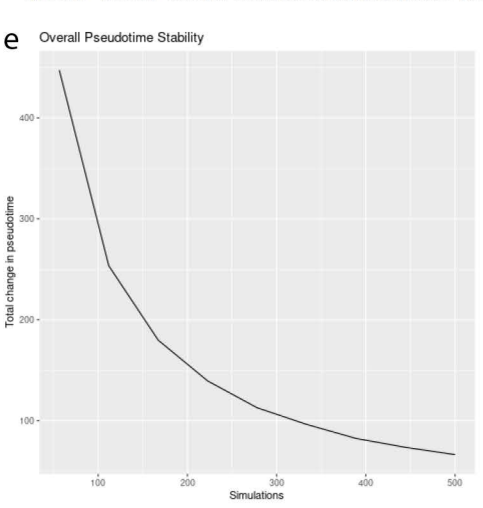

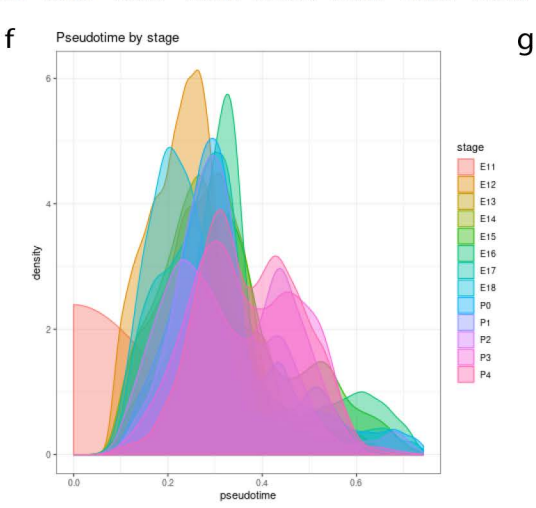

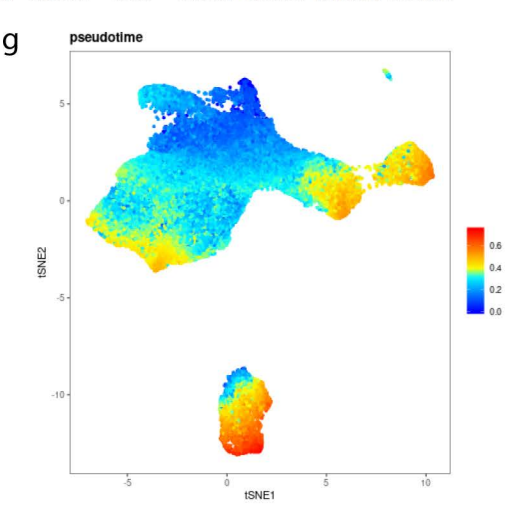

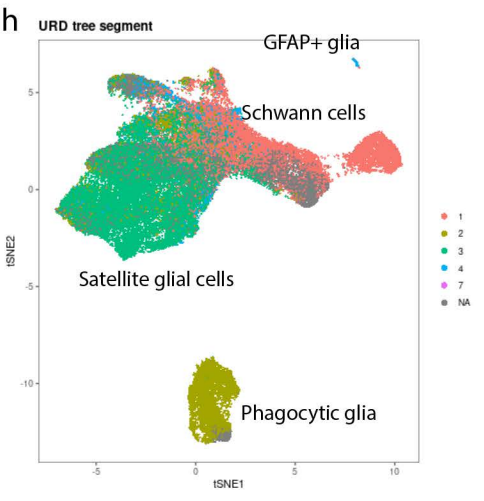

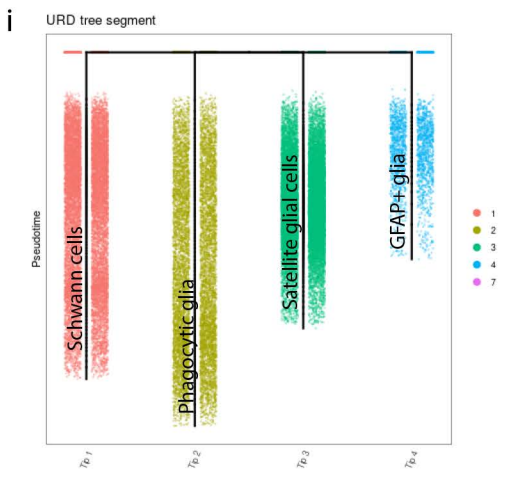

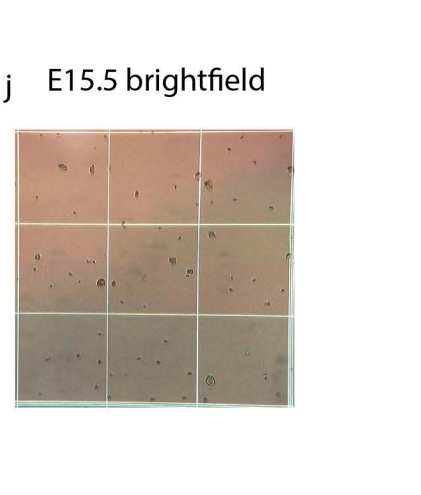

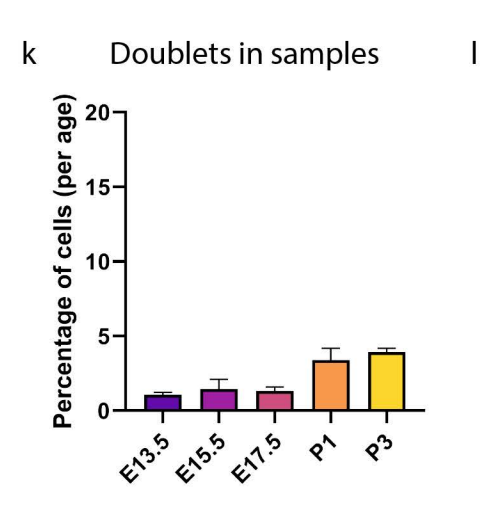

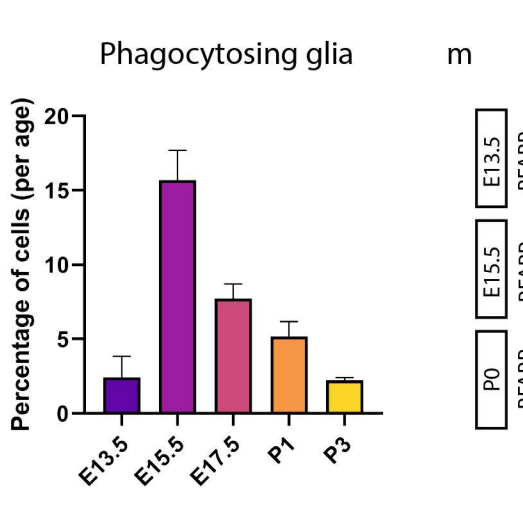

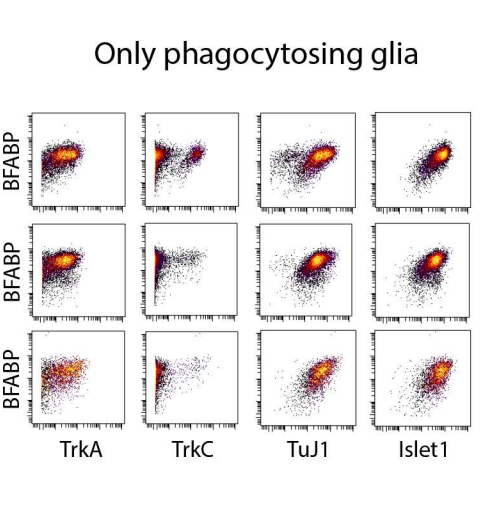

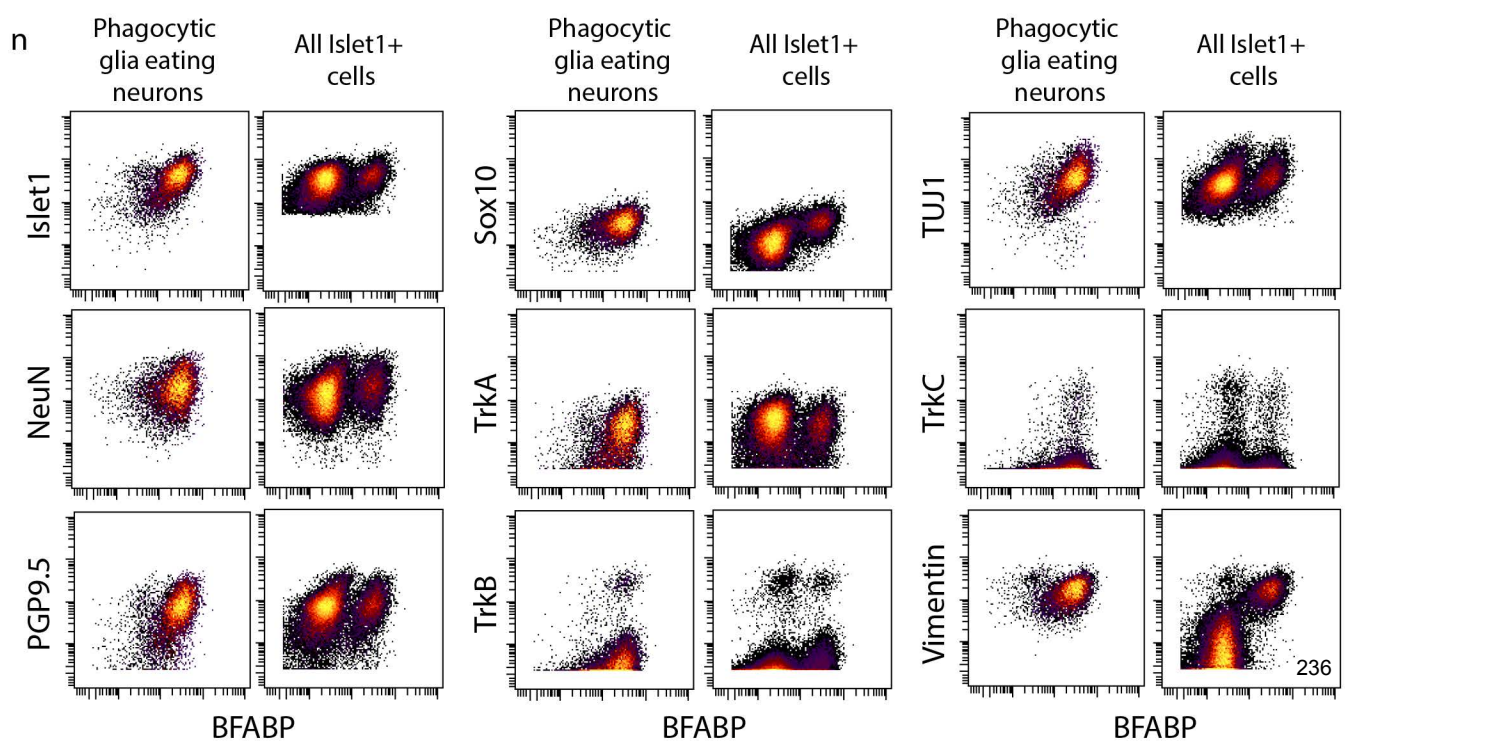

Extended Data Fig. 5 High dimensional analysis of all glial cells and precursors. a) Cell number per age for all glia and glial precursors. **b)** Unmodified UMAP embedding from Fig. 3a. White space was trimmed for ease of visualization. **c)** UMAP plot from (b) colored by age. **d)** Violin plot of all markers for the glial clusters (from Fig. 3a) **e)** During pseudotime calculation, several simulations are run, allowing pseudotime to be calculated from these iterations. For ideal pseudotime stability (for example decreased change in cell pseudotime with increasing runs) we assessed the number of runs required to approach an asymptote. We determined 500 simulations was sufficient to reach a stability asymptote. **f)** We next assessed the distribution of pseudotime by real age (E11.5 to P4). There is a general progression across pseudotime with age with overlap between stages, as expected. **g)** UMAP plot colored by pseudotime value for all 63,796 downsampled cells included in this analysis. **h)** UMAP plot from (g) colored by URD segment. **i)** URD dendrogram of the 4 general populations colored by segment. **j)** Representative brightfield image of E15.5 sample on a hemocytometer quantified in Fig. 3p. Scale bar, 500 μm.**k)** Biaxial scatterplots from only putative phagocytic glia showing expression of 4 neuronal markers (TrkA,TrkC, TuJ1, and Islet1), by satellite glial cell marker BFABP at E13.5, E15.5, and P0. **l)** Biaxial scatterplots comparing marker expression for several neuronally expressed markers (Islet1, NeuN, PGP9.5, TuJ1, TrkA, TrkB, and TrkC) and glial markers (Sox10, TrkB, and Vimentin) by BFABP between only putative phagocytic glia and all Islet1^{+} cells (neurons and putative phagocytic glia) from all ages.

EXTENDED DATA FIGURE 6

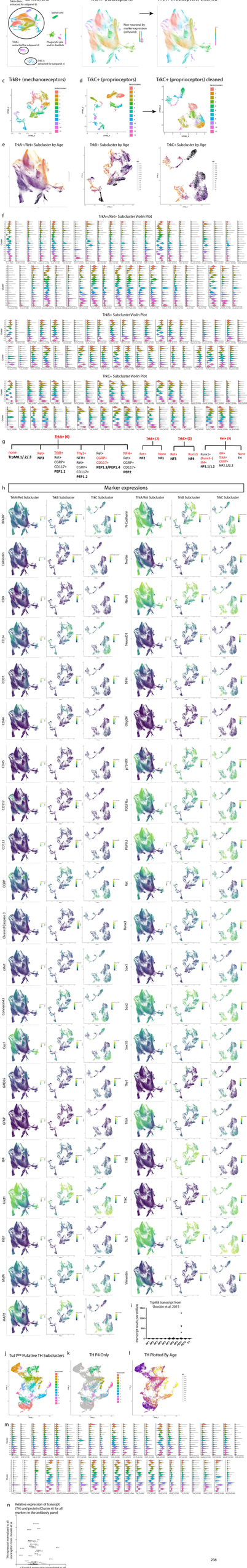

Extended Data Fig. 6 High dimensional analysis of all neurons. a) Leiden clustering (LC) and UMAP embedding of neurons extracted from the whole time course, labeled by cell type. Circles indicate the 3 main neuronal subtypes by RTK expression: $TrkA^+$;Ret^+, $TrkB^+$, and $TrkC^+$, respectively. **b)** LC and UMAP of the $TrkA^+$;Ret^+ neurons, extracted from a). Three clusters that did not exhibit neuronal markers were removed from the dataset before a final round of LC and UMAP (plot on right). **c)** LC and UMAP of the $TrkB^+$ neurons extracted from a). **d)** LC and UMAP of the $TrkC^+$ neurons extracted from a). Putative phagocytic glia expressing $TrkC^+$ could not be removed from $TrkC^+$ neurons in previous analytic iterations, but this could be done at this resolution resulting in a 'cleaned' $TrkC^+$ neuronal clustering and UMAP (plot on right). **e)** $TrkA^+$;Ret^+, $TrkB^+$, and $TrkC^+$ UMAP plots colored by age. **f)** Violin plots of all markers for $TrkA^+$;Ret^+, $TrkB^+$, and $TrkC^+$ neurons. **g)** Key markers in our panel that allow identification of somatosensory DRG populations[5]. **h)** UMAP plots colored by expression for all panel markers for $TrkA^+$;Ret^+, $TrkB^+$, and $TrkC^+$ neurons. **i)** TrpM8 transcript data from Usoskin et al.[2] showing that TrpM8-expressing neurons are a subset of peptidergic nociceptors. **j)** UMAP plot of TH^+ cells that were extracted from Fig. 4a (Cluster 6) and reclustered. **k)** UMAP plot of the TH^+ cells from P4 overlaid on the grayed out UMAP plot from j). These were the cells used in the comparison to the Usoskin et al[2] transcript data in Fig. 4i-n. **l)** UMAP plot from j) colored by age. **m)** Violin plot of marker expression of all clusters from j). **n)** Comparison of TH^+ C-LTMR transcripts expression to protein expression for all markers in the mass cytometry panel[2]. In both cases, transcript or protein expression in C-LTMRs was normalized to all nociceptors.

EXTENDED DATA FIGURE 7

a TrkB+;TrkC+

b TrkA+;Ret+

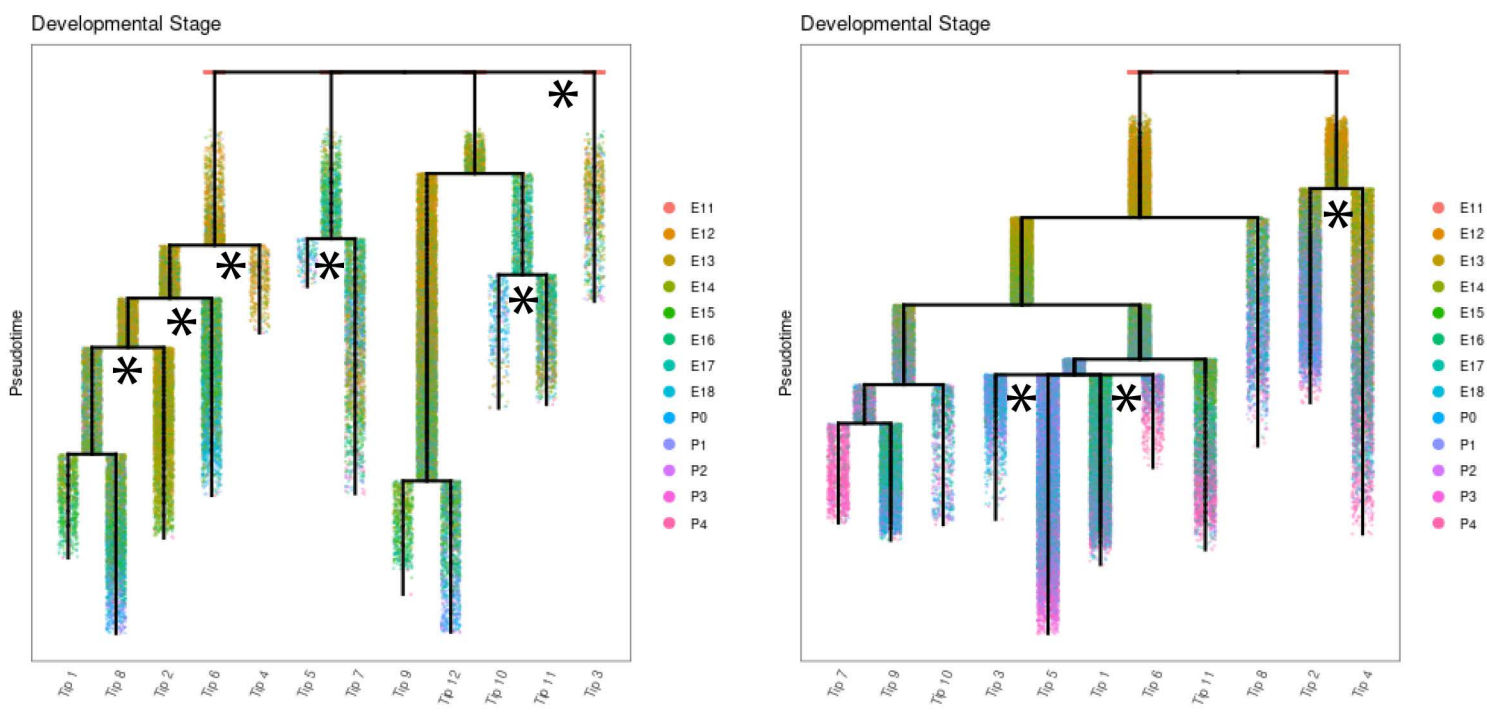

c

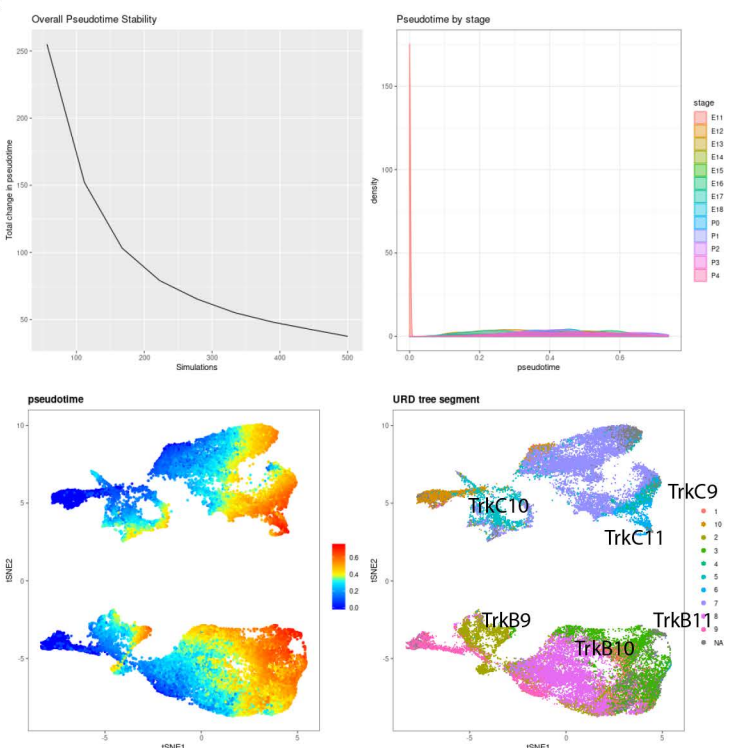

d

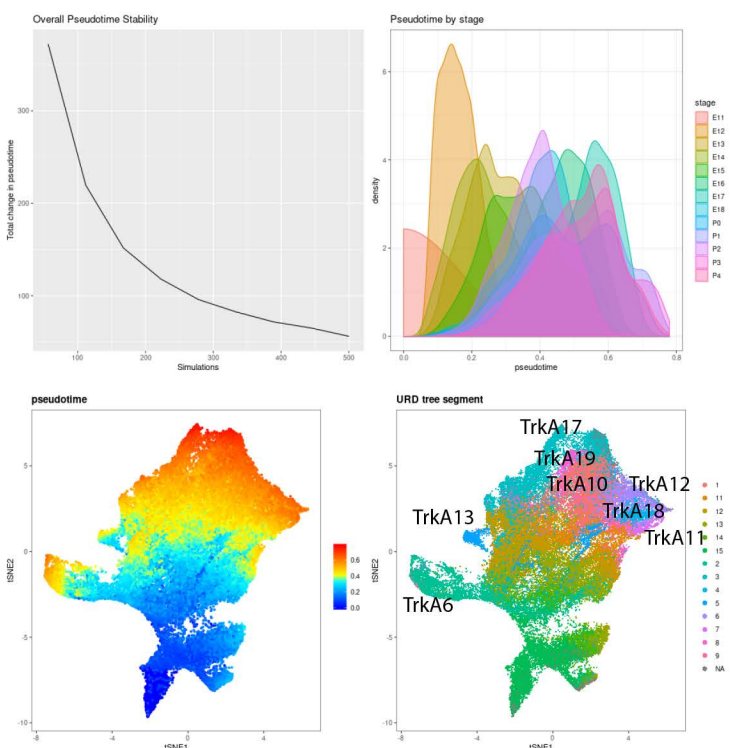

e

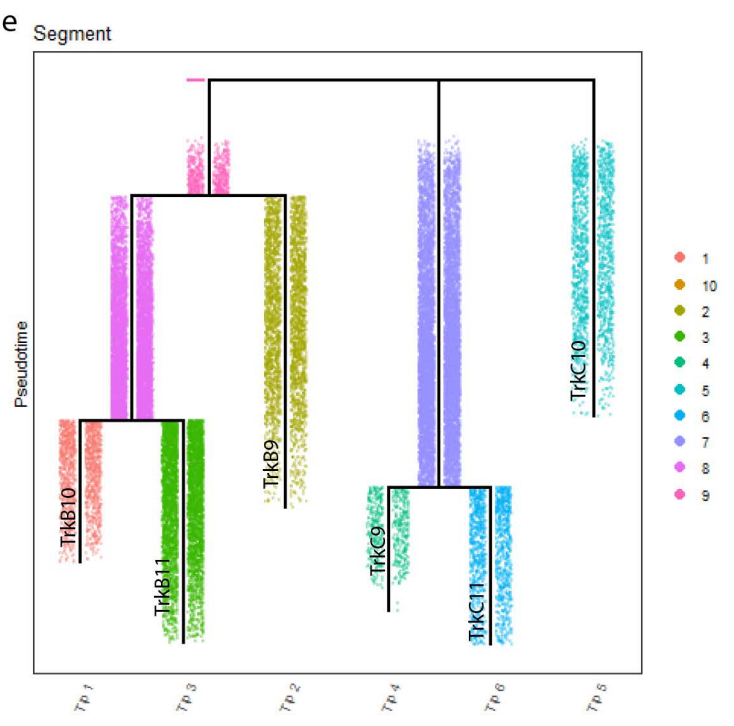

f

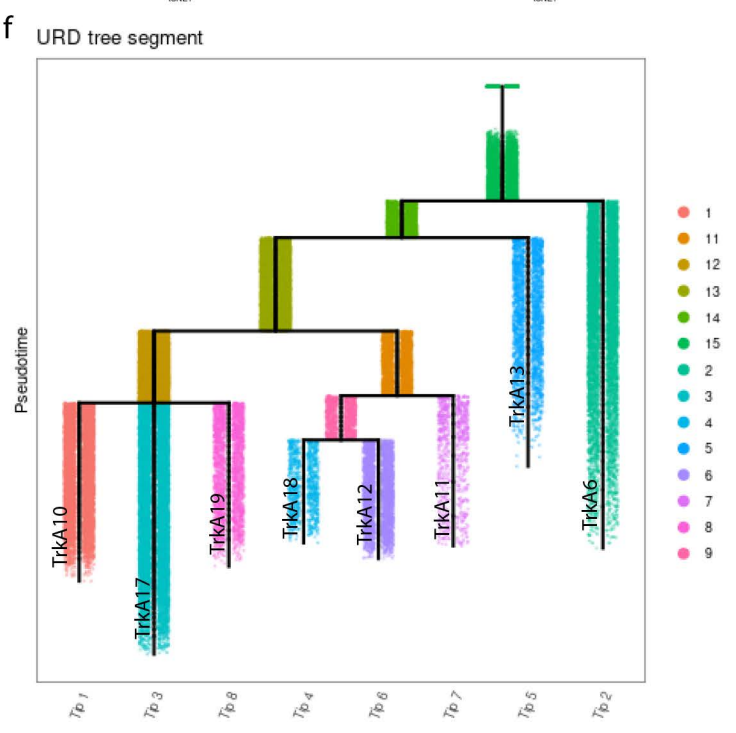

g

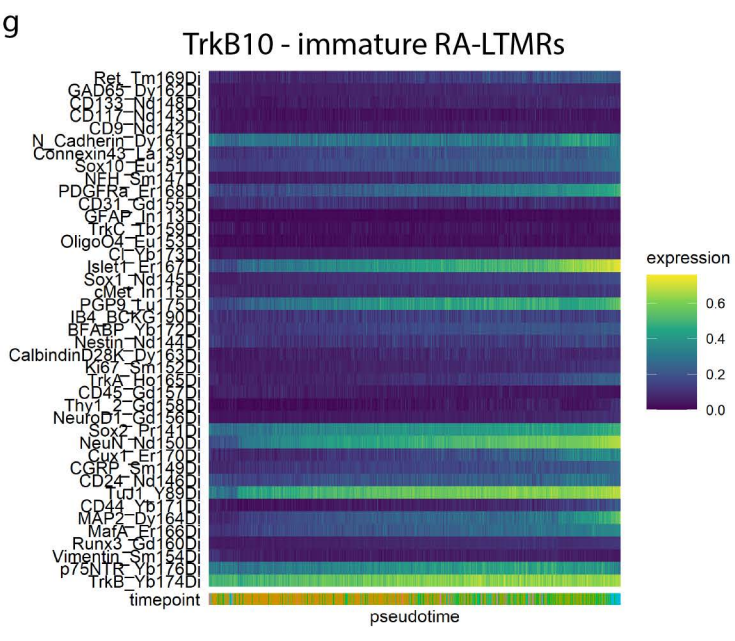

m

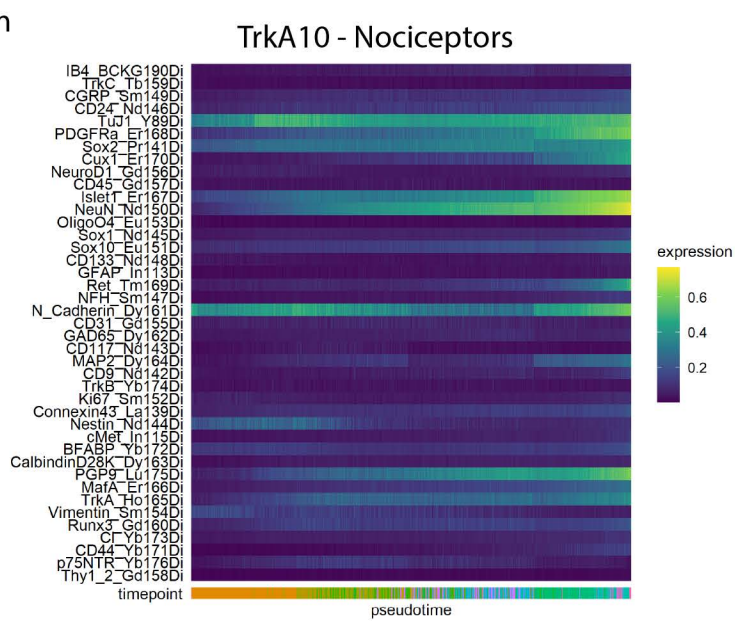

h

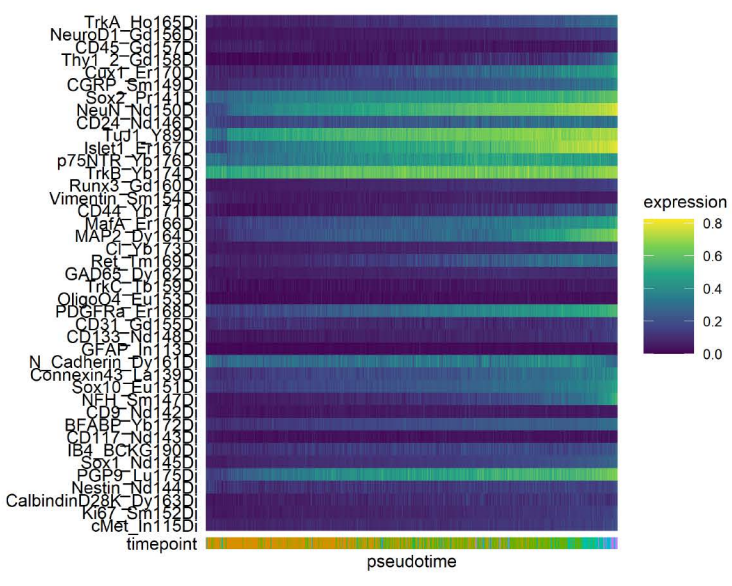

n

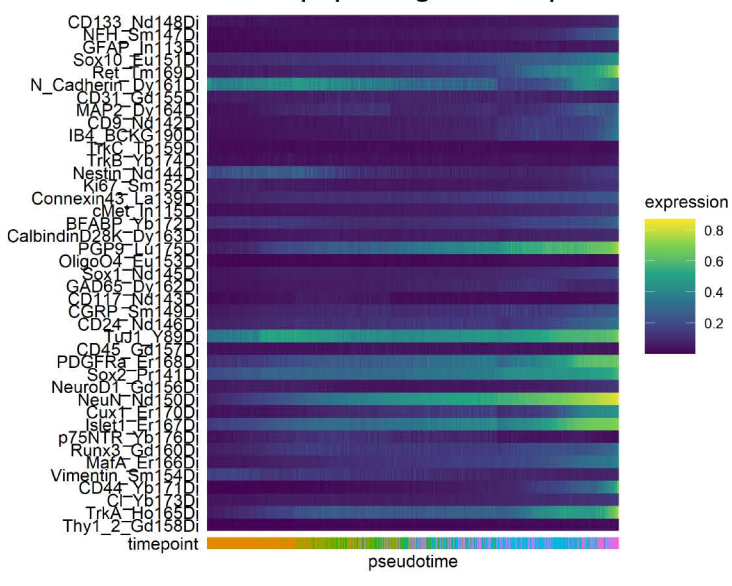

i

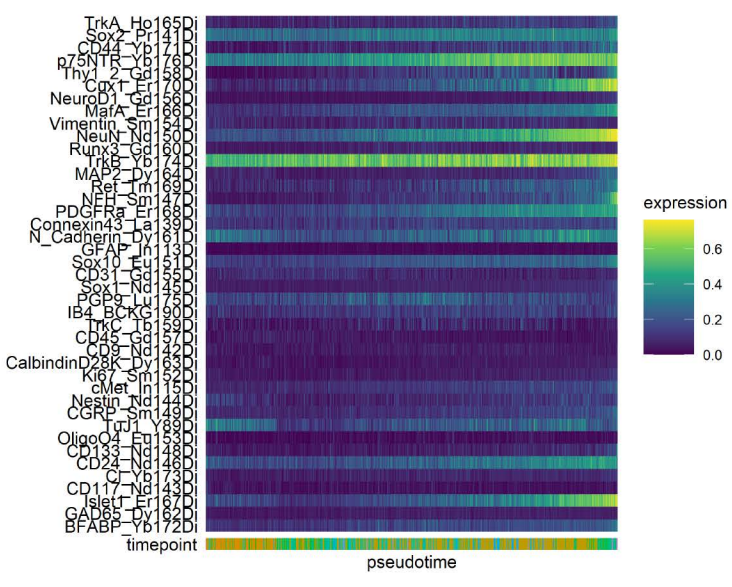

o

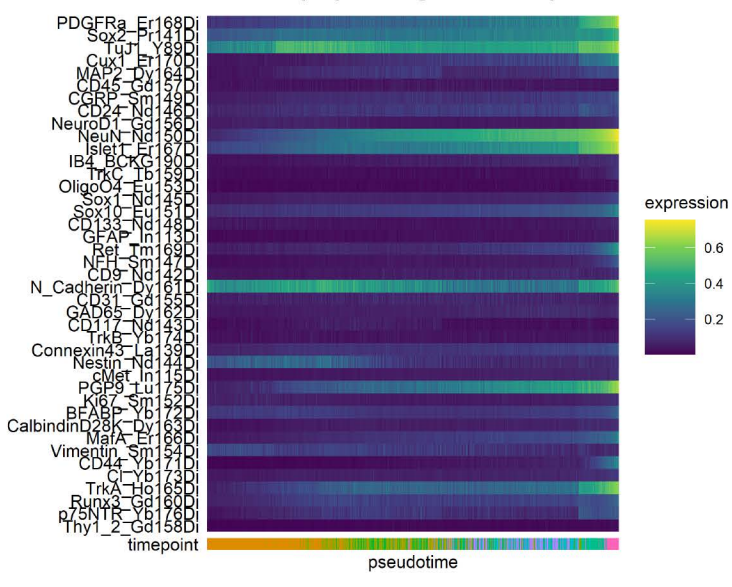

j

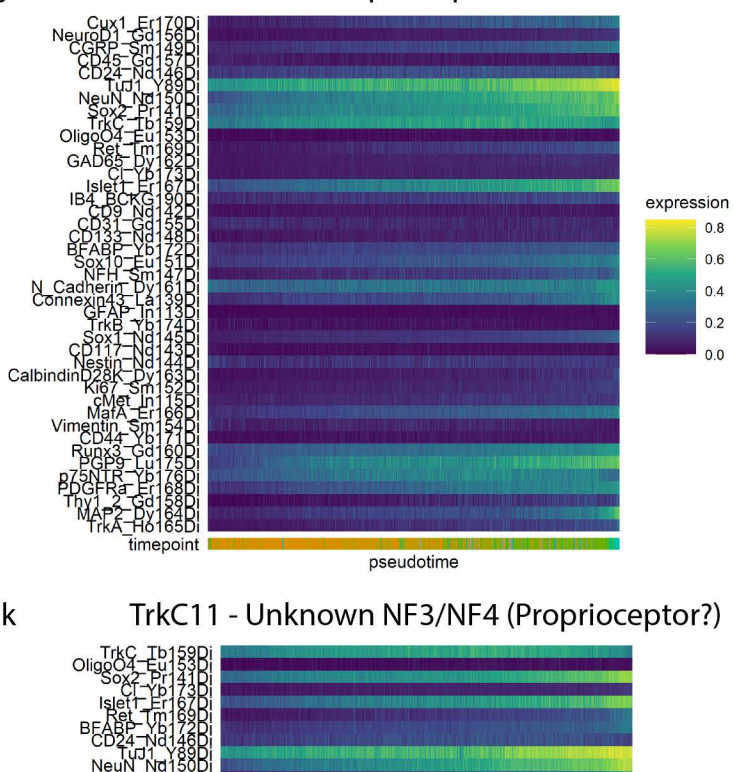

p

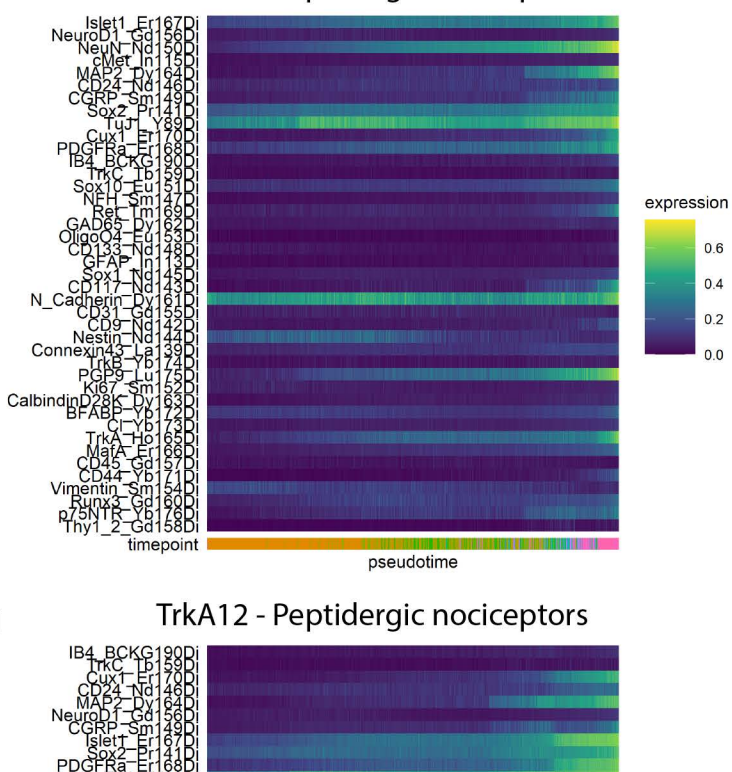

k

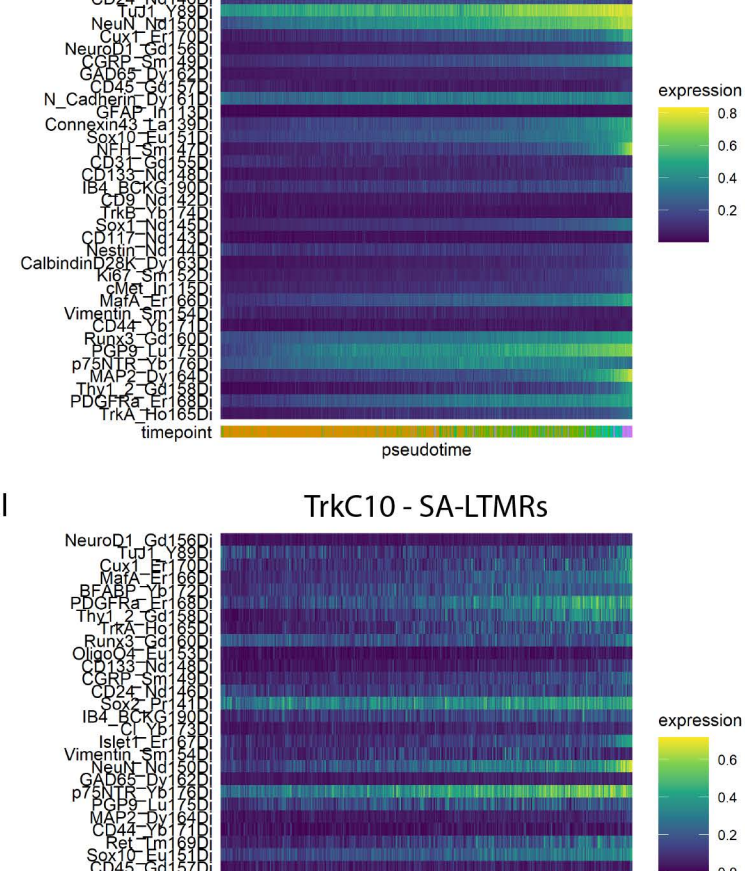

q

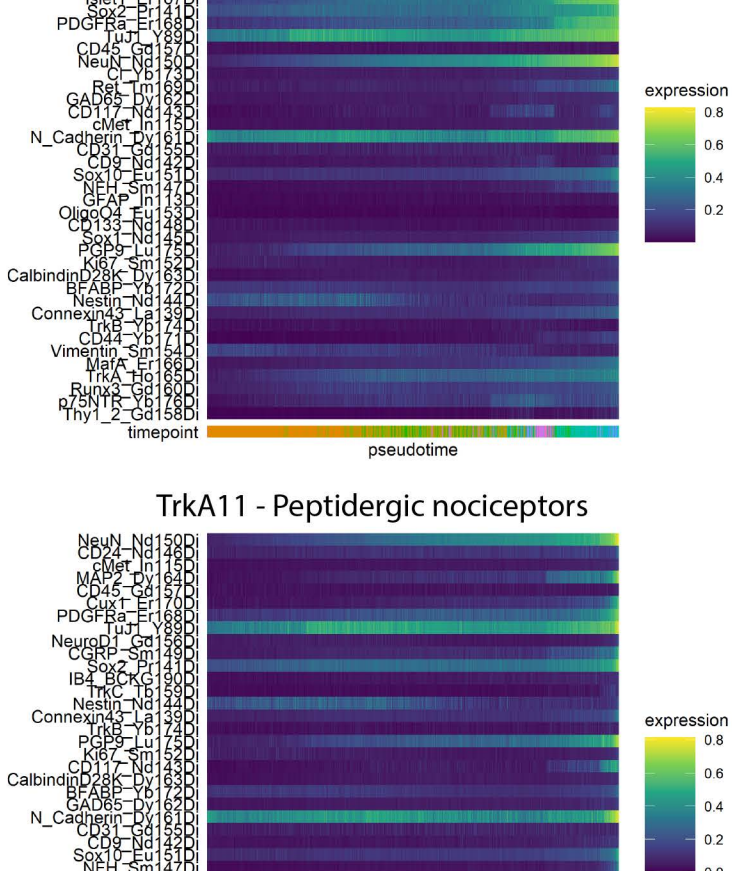

l

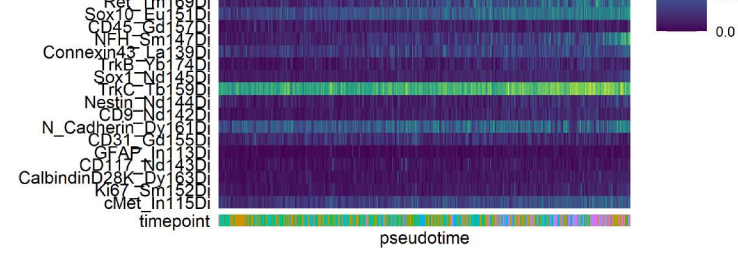

r

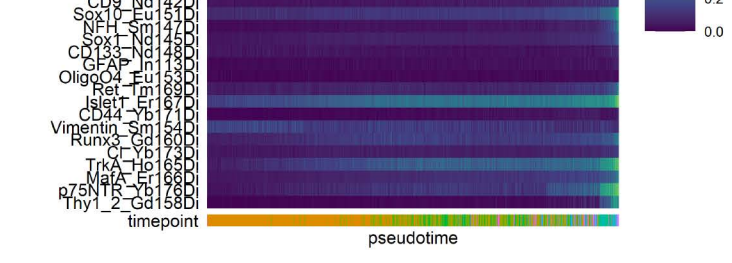

s

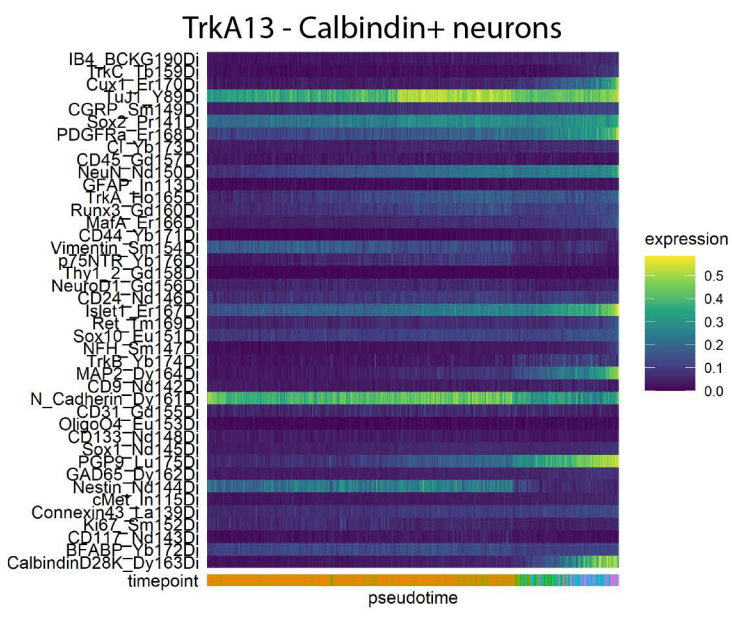

t

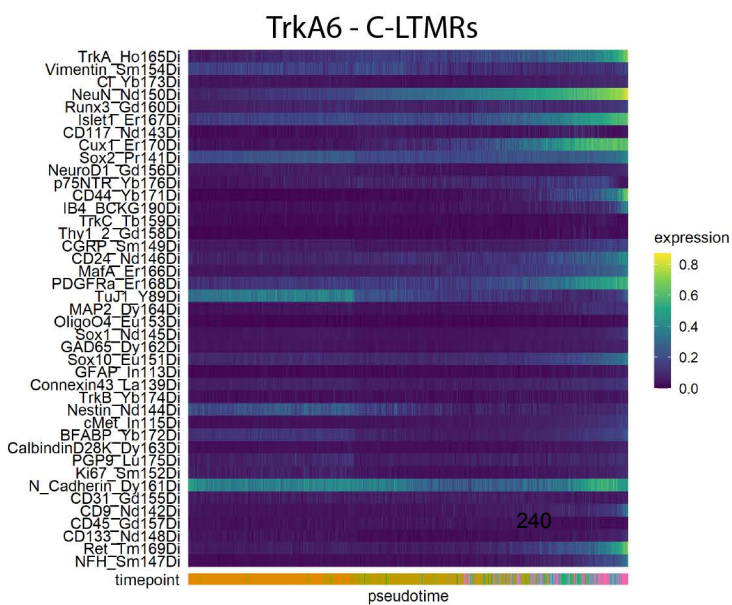

Extended Data Fig. 7 Analysis of inter-replicate variability for TrkA+, TrkB+, and TrkC+ neuron subclusters. a) Analysis of the variability of each cluster by each sample for each age for the $TrkA^+/Ret^+$ neuron subcluster. The number of cells assigned to each cluster in each sample at each age was determined and the relative abundance of each compared to all neurons in the $TrkA^+/Ret^+$ cluster was calculated. **b)** The standard error of the mean of the percentage of all neurons from the $TrkA^+/Ret^+$ dataset for each $TrkA^+/Ret^+$ cluster is shown, but only during the ages where the average proportion of that cluster comprised 1% or more of the cells at that age. **c)** UMAP where $TrkA^+/Ret^+$ subclusters have been grouped together by similar expression of markers into a more general cell type. **d)** UMAP where $TrkA^+/Ret^+$ subclusters were recolored by general groups expressing similar markers as denoted in (c). **e)** The relative abundance for the general groups created in (d) are shown with the samples deemed 'poorer quality' (see Supplementary Table 3) indicated as a red circle. **f)** The relative abundance for the general groups created in (d) shown without the 'poorer quality' samples. **g)** The standard error of the mean of the percentage of all neurons from the grouped $TrkA^+/Ret^+$ dataset with the 'poorer quality' samples data removed for each $TrkA^+/Ret^+$ cluster is shown, but only during the ages where the average proportion of that cluster comprised 1% or more of the cells at that age. **h-n)** The same analysis as (a-g) except for $TrkB^+$ neurons. (**o-u)** The same analysis as (a-g) except for $TrkC^+$ neurons. **v)** Frequency distribution of the S.E.M % of either all cells or neurons for 1) the whole time course (from Extended Data Fig. 3k, l), 2) all neuron subclusters, 3) subclusters grouped by general cell types, and 4) these general cell types with the 'poorer quality' samples removed.

EXTENDED DATA FIGURE 8

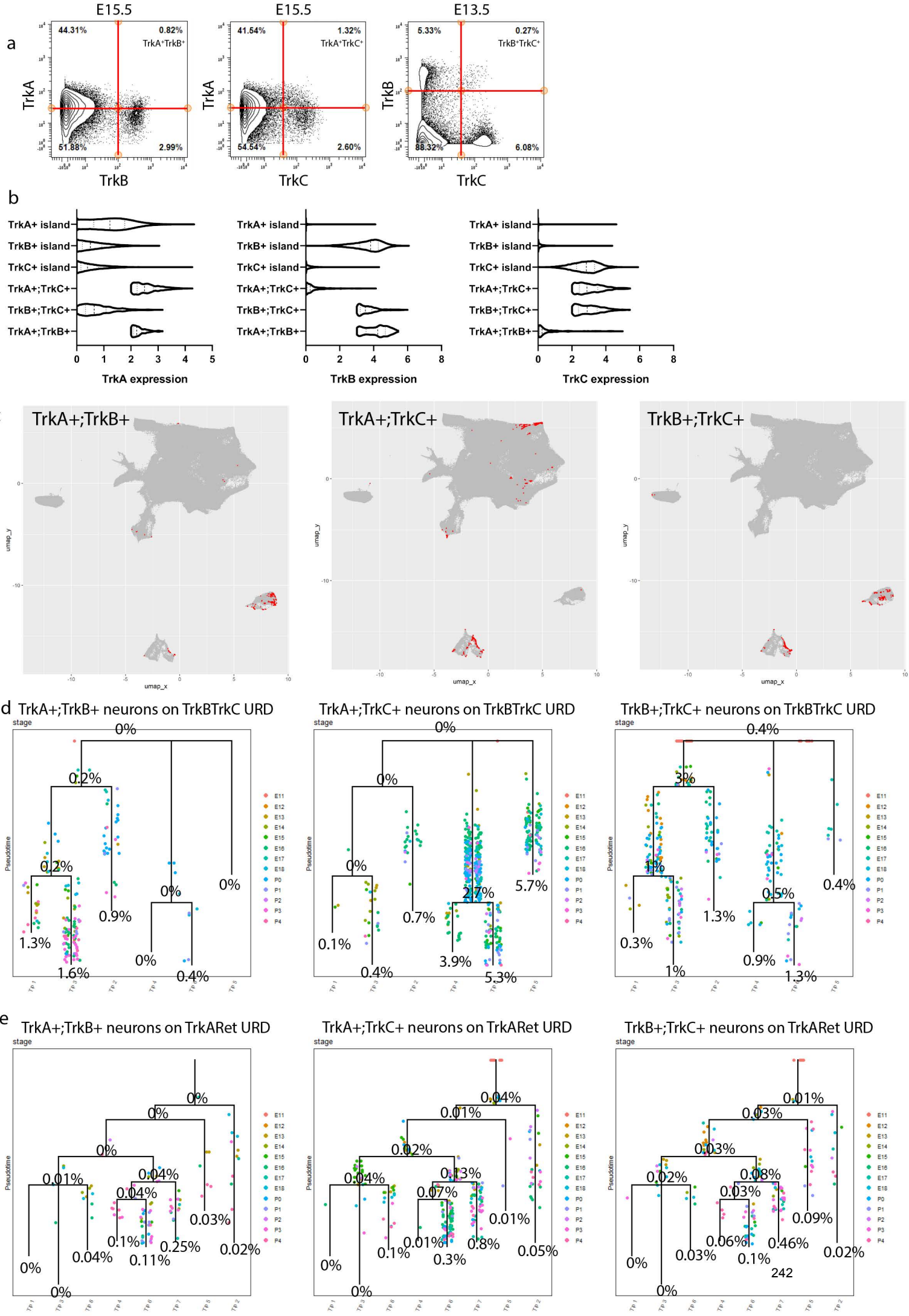

Extended Data Fig. 8 URD pseudotime analysis of all neurons. We initially defined tips as clusters present with ≥ 1% at P4 and all clusters at E11.5 as the root. However, this produced excessively branched pseudotime dendrograms for both a) $TrkB^+;TrkC^+$ and b) $TrkA^+;Ret^+$ where intermediate and more mature cell states were paired as tips. For instance, $TrkA^+/Ret^+$ clusters 5 and 13 are presumptively immature nonpeptidergic nociceptors. The presence of these immature cell types at P4 is expected as cell populations mature over development. By removing presumptive intermediates as tips, we were able to produce the most appropriate molecular trajectory across pseudotime, such as Fig. 5a. **c-f)** Supplemental URD analysis, same as in Extended Data Fig. 5: **c, d)** pseudotime stability to calculate simulation number, pseudotime by stage, UMAP of pseudotime value for all 39,944 ($TrkB^+;TrkC^+$) not downsampled and 64,997 ($TrkA^+/Ret^+$) downsampled cells included in this analysis, UMAP colored by URD segment, for $TrkB^+;TrkC^+$ and $TrkA^+/Ret^+$ datasets, respectively, and **e**, **f)** URD dendrogram colored by URD segment for $TrkB^+;TrkC^+$ and $TrkA^+/Ret^+$ datasets, respectively. **g-t)** Heatmaps for all URD tips from $TrkB^+;TrkC^+$ and $TrkA^+/Ret^+$ datasets, respectively, for all markers.

EXTENDED DATA FIGURE 9

a Mass cytometry scRNAseq Mass cytometry scRNAseq Mass cytometry scRNAseq

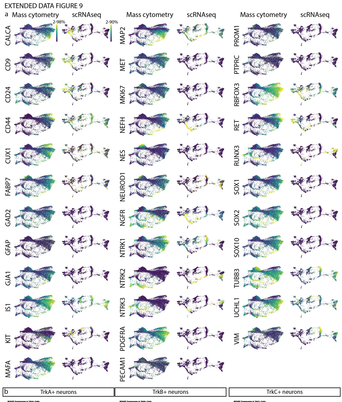

b

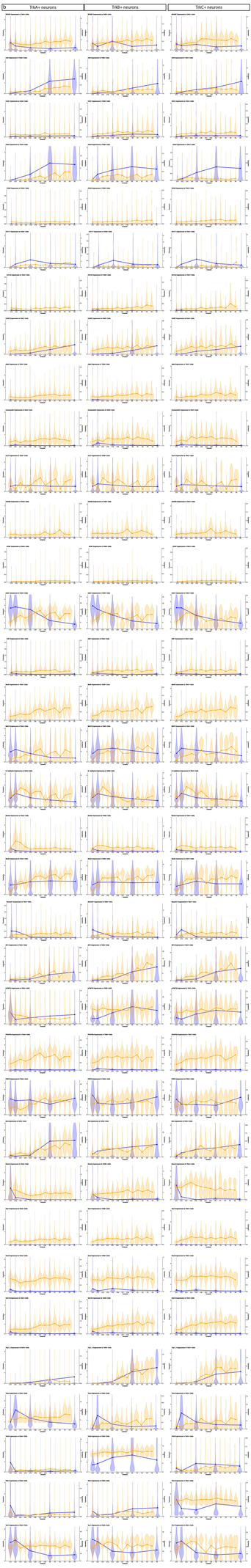

Extended Data Fig. 9 Multi-Trk+ neurons exhibit altered protein expression. a) Biaxial scatterplots showing the neurons that express at least two Trks for all 3 combinations: TrkA;TrkB, TrkA;TrkC, and TrkB;TrkC. **b)** Violin plots of Trk expression for all single-Trk$^+$ neurons (Fig. 4a-c) compared to multi-Trk$^+$ neurons. **c)** Proportion of TrkA$^+$;TrkB$^+$, TrkA$^+$;TrkC$^+$, and TrkB$^+$;TrkC$^+$ populations at different threshold values: left, TrkA>1.5, TrkB>2.5, TrkC>1.5 and right, TrkA>2, TrkB>3, TrkC>2. **d)** Proportion of TrkA$^+$;TrkB$^+$, TrkA$^+$;TrkC$^+$, and TrkB$^+$;TrkC$^+$ populations at E11, E12, E15, P0, P5, and P40 from Sharma et al[19] scRNA-seq. All cells with transcript expression values >0 were designated as expressing the given transcript. **e)** Proportion of TrkA$^+$;TrkB$^+$, TrkA$^+$;TrkC$^+$, and TrkB$^+$;TrkC$^+$ populations at P42-56 from Usoskin et al[2]. Transcript expression was determined by thresholding as in Usoskin et al[2]: briefly, the three cells with the highest expression for a given transcript were averaged and then multiplied by 5%. Cells with transcript expression greater than this threshold are designated as expressors. **f)** Proportion of all multi-Trk$^+$ neurons combined at each age across the whole time course from the mass cytometry dataset. **g**, **h)** URD dendrograms from Fig. 5a without the URD dataset cells. Instead, each multi-Trk$^+$ neuron type are mapped on the URDs, colored by the age of each cell, over the TrkB;TrkC URD (d) and the TrkA;Ret URD (e). Multi-Trk$^+$ neuron numbers were counted and compared to the number of cells within each TrkB;TrkC URD segment (d). However, the TrkA$^+$ and Ret$^+$ neurons were downsampled (64,997 out of 492,982 neurons). Thus we multiplied the number of neurons in each segment of the TrkA;Ret URD by the downsampling coefficient (7.584689) before determining the proportion of multi-Trk$^+$ neurons over the URD (e). **i, j)** All p Values for Fig. 6l, m, respectively.